

Tutorial : 2-D and 3-D electrical imaging surveys

By

Dr. M.H.Loke
Copyright (1996-2015)

email : drmhloke@yahoo.com, geotomo@gmail.com
Web : www.geotomosoft.com

(All rights reserved)

(Revision date : 17th October 2015)

Copyright and disclaimer notice

The author, M.H.Loke, retains the copyright to this set of notes. Users may print a copy of the notes, but may not alter the contents in any way. The copyright notices must be retained. For public distribution, prior approval by the author is required.

It is hoped that the information provided will prove useful for those carrying out 2-D and 3-D field surveys, but the author will not assume responsibility for any damage or loss caused by any errors in the information provided. If you find any errors, please inform me by email and I will make every effort to correct it in the next edition.

You can download the programs mentioned in the text (RES2DMOD, RES2DINV, RES3DMOD, RES3DINV) from the following Web site

www.geotomosoft.com

M.H.Loke

Table of Contents

1	Introduction to resistivity surveys	1
1.1	Introduction and basic resistivity theory	1
1.2	Electrical properties of earth materials	5
1.3	1-D resistivity surveys and inversions – applications, limitations and pitfalls	6
1.4	Basic Inverse Theory	11
1.5	2-D model discretization methods	15
2	2-D electrical surveys – Data acquisition, presentation and arrays.....	18
2.1	Introduction	18
2.2	Field survey method - instrumentation and measurement procedure.....	18
2.3	Available field instruments.....	21
2.4	Pseudosection data plotting method	24
2.5	A comparison of the different electrode arrays	26
2.5.1	The Frechet derivative for a homogeneous half-space	26
2.5.2	A 1-D view of the sensitivity function - depth of investigation	27
2.5.3	A 2-D view of the sensitivity function.....	30
2.5.4	Wenner array.....	31
2.5.5	Dipole-dipole array	31
2.5.6	Wenner-Schlumberger array	35
2.5.7	Pole-pole array	37
2.5.8	Pole-dipole array	38
2.5.9	Multiple gradient array	41
2.5.10	High-resolution electrical surveys with overlapping data levels	44
2.5.11	Summary of array types.....	45
2.5.12	Use of the sensitivity values for multi-channel measurements or streamers....	46
3	A 2-D forward modeling program	48
3.1	Finite-difference and finite-element methods.....	48
3.2	Using the forward modeling program RES2DMOD	49
3.3	Forward modeling exercises	50
4	A 2-D inversion program	52
4.1	Introduction	52
4.2	Pre-inversion and post-inversion methods to remove bad data points	52
4.3	Selecting the proper inversion settings	55
4.4	Using the model sensitivity and uncertainty values	61
4.5	Methods to handle topography	66
4.6	Incorporating information from borehole logs and seismic surveys	68
4.7	Model refinement	72
4.8	Fast inversion of long 2-D survey lines.....	76
4.8.1	Preprocessing steps	76
4.8.2	Data set and computer system used for tests	76
4.8.3	Finite-element mesh size.....	77
4.8.4	Limit calculation of Jacobian matrix values	77
4.8.5	Use sparse inversion techniques	78
4.8.6	Use wider cells.....	78
4.8.7	Overview of methods to reduce the calculation time.....	79
4.9	Model resolution and automatic array optimization methods	81
4.9.1	Concept of model resolution	81
4.9.2	A heuristic explanation of model resolution – through a glass darkly	81
4.9.3	Examples of model resolution with standard arrays	82
4.9.4	Array optimization methods	83

4.9.5	DOI versus model resolution?	87
4.9.6	The streamer design problem using a model resolution approach.....	87
4.10	Pitfalls in 2-D resistivity surveys and inversion.....	89
4.11	The pole-pole inversion paradox.....	94
5	I.P. inversion	96
5.1	Introduction	96
5.2	The IP effect	96
5.3	IP data types.....	98
5.4	IP mathematical models.....	100
5.5	I.P. surveys with multi-electrode systems	101
6	Cross-borehole imaging	103
6.1	Introduction	103
6.2	Electrode configurations for cross-borehole surveys	103
6.2.1	Two electrodes array – the pole-pole	103
6.2.2	Three electrodes array – the pole-bipole.....	105
6.2.3	Four electrodes array – the bipole-bipole	107
6.3	Single borehole surveys.....	110
6.4	Cross-borehole optimized arrays	112
6.5	Optimized arrays with subsurface electrodes	112
7	2-D field examples	116
7.1	Introduction	116
7.2	Landslide - Cangkat Jering, Malaysia	116
7.3	Old Tar Works - U.K.	116
7.4	Holes in clay layer - U.S.A.....	117
7.5	Time-lapse water infiltration survey - U.K.	119
7.6	Pumping test, U.K.	121
7.7	Wenner Gamma array survey - Nigeria.....	122
7.8	Mobile underwater survey - Belgium.....	123
7.9	Floating electrodes survey – U.S.A.....	125
7.10	Oil Sands, Canada	125
8	3-D electrical imaging surveys.....	127
8.1	Introduction to 3-D surveys.....	127
8.2	Array types for 3-D surveys	127
8.2.1	The pole-pole array	127
8.2.2	The pole-dipole array	130
8.2.3	The dipole-dipole, Wenner and Schlumberger arrays	130
8.2.4	Summary of array types	132
8.3	3-D roll-along techniques	135
8.4	A 3-D forward modeling program.....	137
8.5	3-D inversion algorithms and 3-D data sets	139
8.6	A 3-D inversion program.....	140
8.7	Banding effects in 3-D inversion models	141
8.8	The use of long electrodes in 3-D surveys	144
8.9	Data grid formats and model discretizations	146
8.9.1	Types of surveys and model grids	146
8.9.2	Model grid optimization for large surveys with arbitrary electrodes positions .	147
8.10	3-D array optimization – grids and perimeters.....	151
8.11	Unstable arrays and the geometric factor relative error	158
8.12	Not on firm foundations – inversion with shifting electrodes in 2-D and 3-D	160
8.13	Examples of 3-D field surveys	163

8.13.1	Birmingham field test survey - U.K.	163
8.13.2	Sludge deposit - Sweden.....	165
8.13.4	Copper Hill - Australia	168
8.13.5	Athabasca Basin – Canada	170
8.13.6	Cripple Creek and Victor Gold Mine, Colorado – USA	172
8.13.7	Burra copper deposit, South Australia : Model reliability determination	173
8.14	Closing remarks on the 3-D method	176
	Acknowledgments.....	177
	References.....	178

List of Figures

Figure 1. The flow of current from a point current source and the resulting potential distribution.....	3
Figure 2. The potential distribution caused by a pair of current electrodes. The electrodes are 1 m apart with a current of 1 ampere and a homogeneous half-space with resistivity of 1 $\Omega \cdot m$	3
Figure 3. A conventional array with four electrodes to measure the subsurface resistivity.....	4
Figure 4. Common arrays used in resistivity surveys and their geometric factors. Note that the dipole-dipole, pole-dipole and Wenner-Schlumberger arrays have two parameters, the dipole length "a" and the dipole separation factor "n". While the "n" factor is commonly an integer value, non-integer values can also be used.....	4
Figure 5. The resistivity of rocks, soils and minerals.....	6
Figure 6. The three different models used in the interpretation of resistivity measurements.....	7
Figure 7. A typical 1-D model used in the interpretation of resistivity sounding data for the Wenner array.....	7
Figure 8. A 2-D two-layer model with a low resistivity prism in the upper layer. The calculated apparent resistivity pseudosections for the (a) Wenner and (b) Schlumberger arrays. (c) The 2D model. The mid-point for a conventional sounding survey is also shown.....	9
Figure 9. Apparent resistivity sounding curves for a 2-D model with a lateral inhomogeneity. (a) The apparent resistivity curve extracted from the 2D pseudosection for the Wenner array. The sounding curve for a two-layer model without the low resistivity prism is also shown by the black line curve. (b) The apparent resistivity curves extracted from the 2-D pseudosection for the Schlumberger array with a spacing of 1.0 meter (black crosses) and 3.0 meters (red crosses) between the potential electrodes. The sounding curve for a two-layer model without the low resistivity prism is also shown.....	10
Figure 10. Coupling between neighboring model cells through the roughness filter in a 2-D model. (a) In the horizontal and vertical directions only, and (b) in diagonal directions as well.....	13
Figure 11. (a) Coupling between corresponding model blocks in two time-lapse models using a cross-model time-lapse smoothness constraint. (b) Example Jacobian matrix structure for five time series data sets and models. Each grey rectangle represents the Jacobian matrix associated with a single set of measurements.....	15
Figure 12. The different models for the subsurface used in the interpretation of data from 2-D electrical imaging surveys. (a) A purely cell based model. (b) A purely boundary based model. (c) The laterally constrained model. (d) A combined cell based and boundary based model with rectangular cells, and (e) with boundary conforming trapezoidal cells.....	16
Figure 13. Example of a cell based model with a variable boundary. (a) The test model. (b) The apparent resistivity pseudosection. (c) The inversion model with a variable sharp boundary that is marked by a black line.....	17
Figure 14. The arrangement of electrodes for a 2-D electrical survey and the sequence of measurements used to build up a pseudosection.....	19
Figure 15. The use of the roll-along method to extend the area covered by a 2-D survey.....	20
Figure 16. Sketch outline of the ABEM Lund Imaging System. Each mark on the cables indicates an electrode position (Dahlin, 1996). The cables are placed along a single line (the sideways shift in the figure is only for clarity). This figure also shows the principle of moving cables when using the roll-along technique. The total layout length depends on the spacing between the nodes, but is usually between 160 meters and 800 meters.	22
Figure 17. The Aarhus Pulled Array System. The system shown has two current (C)	

electrodes and six potential electrodes (Christensen and Sørensen 1998, Bernstone and Dahlin 1999).....	23
Figure 18. The Geometrics OhmMapper system using capacitive coupled electrodes. (Courtesy of Geometrics Inc.).....	23
Figure 19. Schematic diagram of a possible mobile underwater survey system. The cable has two fixed current electrodes and a number of potential electrodes so that measurements can be made at different spacings. The above arrangement uses the Wenner-Schlumberger type of configuration. Other configurations, such as the gradient array, can also be used.	24
Figure 20. The apparent resistivity pseudosections from 2-D imaging surveys with different arrays over a rectangular prism.	25
Figure 21. The parameters for the sensitivity function calculation at a point (x,y,z) within a half-space. A pole-pole array with the current electrode at the origin and the potential electrode “ a ” meters away is shown.	26
Figure 22. A plot of the 1-D sensitivity function. (a) The sensitivity function for the pole-pole array. Note that the median depth of investigation (red arrow) is more than twice the depth of maximum sensitivity (blue arrow). (b) The sensitivity function and median depth of investigation for the Wenner array.....	28
Figure 23. 2-D sensitivity sections for the Wenner array. The sensitivity sections for the (a) alpha, (b) beta and (c) gamma configurations.....	32
Figure 24. 2-D sensitivity sections for the dipole-dipole array. The sections with (a) $n=1$, (b) $n=2$, (c) $n=4$ and (d) $n=6$	33
Figure 25. Two possible different arrangements for a dipole-dipole array measurement. The two arrangements have the same array length but different “ a ” and “ n ” factors resulting in very different signal strengths.....	35
Figure 26. 2-D sensitivity sections for the Wenner-Schlumberger array. The sensitivity sections with (a) $n=1$, (b) $n=2$, (c) $n=4$ and (d) $n=6$	36
Figure 27. A comparison of the (i) electrode arrangement and (ii) pseudosection data pattern for the Wenner and Wenner-Schlumberger arrays.....	37
Figure 28. The pole-pole array 2-D sensitivity section.....	38
Figure 29. The forward and reverse pole-dipole arrays.....	39
Figure 30. The pole-dipole array 2-D sensitivity sections. The sensitivity sections with (a) $n=1$, (b) $n=2$, (c) $n=4$ and (d) $n=6$	40
Figure 31. Sensitivity sections for the gradient array. The current electrodes are fixed at $x=0$ and 1.0 meters, and the distance between the potential electrodes is 0.1 m. The position of the P1-P2 potential electrodes at (a) 0.45 and 0.55 m., (b) 0.55 and 0.65 m., (c) 0.65 and 0.75 m, (d) 0.75 and 0.85 m. and (e) 0.80 and 0.90 m.	42
Figure 32. (a) Example of multiple gradient array data set and inversion model. (b) Profile plot using exact pseudodepths. (c) Profile plot using approximate pseudodepths.....	43
Figure 33. The apparent resistivity pseudosection for the dipole-dipole array using overlapping data levels over a rectangular prism. Values of 1 to 3 meters are used for the dipole length ‘ a ’, and the dipole separation factor ‘ n ’ varies from 1 to 5. Compare this with Figure 20c for the same model but with ‘ a ’ fixed at 1 meter, and “ n ” varying from 1 to 10. In practice, a ‘ n ’ value greater than 8 would result in very noisy apparent resistivity values.....	45
Figure 34. Cumulative sensitivity sections for different measurement configurations using (a) a dipole-dipole sequence, (b) a moving gradient array and (c) an expanding Wenner-Schlumberger array.	47
Figure 35. The output from the RES2DMOD software for the SINGLE_BLOCK.MOD 2-D model file. The individual cells in the model are shown in the lower figure, while the	

upper figure shows the pseudosection for the Wenner Beta (dipole-dipole with n=1) array.....	49
Figure 36. An example of a field data set with a few bad data points. The most obvious bad datum points are located below the 300 meters and 470 meters marks. The apparent resistivity data in (a) pseudosection form and in (b) profile form.	53
Figure 37. Selecting the menu option to remove bad data points manually.	54
Figure 38. Error distribution bar chart from a trial inversion of the Grundfor Line 1 data set with five bad data points.	55
Figure 39. Different options to modify the inversion process.	56
Figure 40. Example of inversion results using the l_2 -norm smooth inversion and l_1 -norm blocky inversion model constrains. (a) Apparent resistivity pseudosection (Wenner array) for a synthetic test model with a faulted block ($100 \Omega\cdot m$) in the bottom-left side and a small rectangular block ($2 \Omega\cdot m$) on the right side with a surrounding medium of $10 \Omega\cdot m$. The inversion models produced by (b) the conventional least-squares smoothness-constrained or l_2 -norm inversion method and (c) the robust or l_1 -norm inversion method.	57
Figure 41. Different methods to subdivide the subsurface into rectangular prisms in a 2-D model. Models obtained with (a) the default algorithm, (b) by allowing the number of model cells to exceed the number of data points, (c) a model which extends to the edges of the survey line and (d) using the sensitivity values for a homogeneous earth model....	58
Figure 42. The options to change the thickness of the model layers.	59
Figure 43. The options under the ‘Change Settings’ menu selection.	60
Figure 44. The dialog box to limit the model resistivity values.	61
Figure 45. Landfill survey example (Wenner array). (a) Apparent resistivity pseudosection , (b) model section, (c) model sensitivity section (d) model uncertainty section, (e) minimum and maximum resistivity sections.....	62
Figure 46. Landfill survey depth of investigation determination. (a) Model section with extended depths and (b) the normalized DOI index section.	65
Figure 47. Beach survey example in Denmark. The figure shows the model section with extended depths and the normalized DOI index section.	65
Figure 48. Different methods to incorporate topography into a 2-D inversion model. (a) Schematic diagram of a typical 2-D inversion model with no topography. A finite-element mesh with four nodes in the horizontal direction between adjacent electrodes is normally used. The near surface layers are also subdivided vertically by several mesh lines. Models with a distorted grid to match the actual topography where (b) the subsurface nodes are shifted vertically by the same amount as the surface nodes, (c) the shift in the subsurface nodes are gradually reduced with depth or (d) rapidly reduced with depth, and (e) the model obtained with the inverse Schwartz-Christoffel transformation method.	67
Figure 49. Fixing the resistivity of rectangular and triangular regions of the inversion model.	70
Figure 50. The inversion model cells with fixed regions. The fixed regions are drawn in purple. Note that the triangular region extends beyond the survey line.....	71
Figure 51. Example of an inversion model with specified sharp boundaries. (a) The boundaries in the Clifton survey (Scott <i>et al.</i> , 2000) data set is shown by the blue lines. (b) The measured apparent resistivity pseudosection and the inversion model section....	71
Figure 52. The effect of cell size on the model misfit for near surface inhomogeneities. (a) Model with a cell width of one unit electrode spacing. (b) A finer model with a cell width of half the unit electrode spacing. The near surface inhomogeneities are represented by coloured ovals.	72

Figure 53. Synthetic model (c) used to generate test apparent resistivity data for the pole-dipole (a) and Wenner (b) arrays.....	73
Figure 54. The effect of cell size on the pole-dipole array inversion model. Pole-dipole array. (a) The apparent resistivity pseudosection. The inversion models obtained using cells widths of (b) one, (b) one-half and (c) one-quarter the unit electrode spacing.....	74
Figure 55. Example of the use of narrower model cells with the Wenner-Schlumberger array. (a) The apparent resistivity pseudosection for the PIPESCHL.DAT data set. The inversion models using (b) cells with a width of 1.0 meter that is the same as the actual unit electrode, and (c) using narrower cells with a width of 0.5 meter.....	75
Figure 56. Example of reduction of near-surface 'ripples' in inversion model. (a) Apparent resistivity pseudosection for the BLUERIDGE.DAT data set. (b) Normal inversion using the robust inversion norm and model refinement. (c) Inversion using higher damping factor for first layer to reduce the 'ripple' effect in the top layer.....	75
Figure 57. Inversion models for a long survey line using different settings to reduce the calculation time. (a) The measured apparent resistivity pseudosection for the Redas underwater survey for the first 2600 meters. Inversion models using (b) standard inversion settings with 4 nodes between adjacent electrode positions, (c) standard inversion settings with 2 nodes between adjacent electrode positions, (d) with calculation of Jacobian matrix values for selected model cells, (e) with sparse inversion technique, (f) with 2 meter model cell width and (g) with 3 meter model cell width.....	80
Figure 58. Part of finite-element mesh used to model a survey with submerged electrodes. The resistivity of mesh cells in the water layer are fixed at the known water resistivity.	80
Figure 59. Part of a finite-element mesh for a long survey line. The electrodes used in the same array are 3 meters apart, while the data unit electrode spacing is 1 meter. Using 2 nodes between adjacent electrodes in the mesh will actually result in 6 nodes between electrodes in the same array.....	81
Figure 60. Model resolution sections for the (a) Wenner, (b) Wenner-Schlumberger and (c) simple dipole-dipole array (d) dipole-dipole array with overlapping data levels.....	83
Figure 61. (a) Model resolution section for comprehensive data set. (b) Model resolution section for optimized data set generated by the 'Compare R' method.....	84
Figure 62. Test inversion model for the different arrays. (a) Apparent resistivity pseudosection for the simple dipole-dipole array with a dipole length 'a' of 1.0 meter with the dipole separation factor 'n' of 1 to 6. (b) Apparent resistivity pseudosection for the dipole-dipole array with overlapping data levels. (c) The synthetic model with 4 rectangular blocks of 100 Ωm embedded in a medium of 10 Ωm . as used by Wilkinson <i>et al.</i> (2006b).	85
Figure 63. Inversion results with the (a) Wenner array, (b) Wenner-Schlumberger array, (c) simple dipole-dipole array and (d) dipole-dipole array with overlapping data levels.	86
Figure 64. Inversions models with the (a) optimized data set with 4462 data points and (b) a truncated optimized data set with 413 data points.	86
Figure 65. Comparison between the (a) model resolution, (b) model resolution index and (c) DOI index sections for the Landfill data set.	87
Figure 66. The model resolution plots for the three streamer configurations.....	88
Figure 67. An example of 3-D effects on a 2-D survey. (a) Apparent resistivity pseudosections (Wenner array) along lines at different y-locations over (b) a 3-D structure shown in the form of horizontal slices.	91
Figure 68. The 2-D sensitivity sections for the pole-dipole array with a dipole length of 1 meter and with (a) n=6, (b) n=12 and (c) n=18. Note that as the 'n' factor increases, the zone of high positive sensitive values becomes increasingly concentrated in a shallower zone below the P1-P2 dipole.....	92

Figure 69. Example of apparent resistivity pseudosection with pole-dipole array with large ‘ <i>n</i> ’ values. Note that the anomaly due to a small near-surface high resistivity block becomes greater as the ‘ <i>n</i> ’ factor increases. This means that the sensitivity of the array to the near-surface region between the P1-P2 potential dipole becomes greater as the ‘ <i>n</i> ’ factor increases.....	93
Figure 70. Diagrammatic illustration of differences in objective function shapes for the pole-pole array and dipole-dipole array data sets leading to different models obtained from optimization routine.....	95
Figure 71. The I.P. values for some rocks and minerals.....	97
Figure 72. The Cole-Cole model. (a) Simplified electrical analogue circuit model (after Pelton <i>et al.</i> 1978). ρ = resistivity, m = chargeability, τ = time constant, c = relaxation constant. (b) Amplitude and phase response to sine wave excitation (frequency domain). (c) Transient response to square wave current pulse (time domain). Most I.P. receivers measure the integral of the decay voltage signal over a fixed interval, m_t , as a measure of the I.P. effect.....	97
Figure 73. Magusi River massive sulphide ore body inversion models. (a) Apparent resistivity pseudosection. Resistivity inversion models obtained using the (b) perturbation and (c) complex resistivity methods. (d) Apparent I.P. (metal factor) pseudosection. I.P. models obtained using the (e) perturbation and (f) complex resistivity methods.....	101
Figure 74. Sketch of separated cable spreads setup used (after Dahlin and Loke (2015))....	102
Figure 75. Resistivity and chargeability pseudosection from field demo at 3 rd IP workshop at Ile d’Oleron (after Dahlin and Loke (2015)).....	102
Figure 76. The possible arrangements of the electrodes for the pole-pole array in the cross-borehole survey and the 2-D sensitivity sections. The locations of the two boreholes are shown by the vertical black lines.....	104
Figure 77. A schematic diagram of two electrodes below the surface. The potential measured at P can be considered as the sum of the contribution from the current source C and its image C’ above the ground surface.....	105
Figure 78. The 2-D sensitivity patterns for various arrangements with the pole-bipole array. The arrangement with (a) C1 and P1 in first borehole and P2 in second borehole, (b) C1 in the first borehole and both P1 and P2 in the second borehole, (c) all three electrodes in the first borehole and (d) the current electrode on the ground surface.	106
Figure 79. The 2-D sensitivity patterns for various arrangements of the bipole-bipole array. (a) C1 and P1 are in the first borehole, and C2 and P2 are in second borehole. (b) C1 and C2 are in the first borehole, and P1 and P2 are in second borehole. In both cases, the distance between the electrodes in the same borehole is equal to the separation between the boreholes. The arrangements in (c) and (d) are similar to (a) and (b) except that the distance between the electrodes in the same borehole is half the spacing between the boreholes.	107
Figure 80. Possible measurement sequences using the bipole-bipole array. Other possible measurements sequences are described in the paper by Zhou and Greenhalgh (1997). .	109
Figure 81. Several possible bipole-bipole configurations with a single borehole. (a) The C1 and C2 electrodes at depths of 3 and 2 meters respectively below the 0 meter mark. (b) The C1 and P1 electrodes at depths of 3 and 2 meters respectively below the 0 meter mark. (c). The C1 electrode is at a depth of 3 meters below the 0 meter mark while the C2 electrode is on the surface. (d). The C1 electrode is at a depth of 3 meters below the 0 meter mark while the P1 electrode is on the surface.....	111
Figure 82. A pole-bipole survey with a single borehole. The C1 electrode is at a depth of 3 meters below the 0 meter mark.	111
Figure 83. Test of optimized cross-borehole arrays with a synthetic model. (a) Two-layer test	

model with conductive and resistive anomalies. Inversion models for (b) optimized data set with all arrays, (c) 'standard' data set and (d) the reduced optimized data set that excludes arrays with both current (or potential) electrodes in the same borehole. All the data sets have 1875 data points. The outlines of the rectangular blocks showing their true positions are also shown.....	113
Figure 84. Schematic diagram of the MERIT method with the electrodes are planted along the surface and directly below using the direct push technology (after Harro and Kruse, 2013).....	114
Figure 85. Inversion models for the different data sets for the data collected with electrodes at surface and 7.62 m depth with 4 m horizontal spacing. Models for the (a) standard arrays (405 data points), optimized arrays with (b) 403 and (c) 514 data points.....	115
Figure 86. Landslide field example, Malaysia. (a) The apparent resistivity pseudosection for a survey across a landslide in Cangkat Jering and (b) the interpretation model for the subsurface.....	116
Figure 87. Industrial pollution example, U.K. (a) The apparent resistivity pseudosection from a survey over a derelict industrial site, and the (b) computer model for the subsurface.	117
Figure 88. Mapping of holes in a clay layer, U.S.A. (a) Apparent resistivity pseudosection for the survey to map holes in the lower clay layer. (b) Inversion model and (c) sensitivity values of the model cells used by the inversion program.	118
Figure 89. Water infiltration mapping, U.K. (a) The apparent resistivity and (b) inversion model sections from the survey conducted at the beginning of the Birmingham infiltration study. This shows the results from the initial data set that forms the base model in the joint inversion with the later time data sets. As a comparison, the model obtained from the inversion of the data set collected after 10 hours of irrigation is shown in (c). ..	119
Figure 90. Time-lapse sections from the infiltration study. The sections show the change in the subsurface resistivity values with time obtained from the inversion of the data sets collected during the irrigation and recovery phases of the study.....	120
Figure 91. Hoveringham pumping test, U.K. (a) The apparent resistivity pseudosection at the beginning of the test. The inversion model sections at the (b) beginning and (v) after 220 minutes of pumping.....	121
Figure 92. Percentage relative change in the subsurface resistivity values for the Hoveringham pumping test. To highlight the changes in the subsurface resistivity, the changes in the model resistivity are shown. Note the increase in the model resistivity below the borehole with time.....	121
Figure 93. Use of Archie's Law for the Hoveringham pumping test. Sections showing the relative desaturation values obtained from the inversion models of the data sets collected during the different stages of the Hoveringham pumping test. Archie's Law probably gives a lower limit for the actual change in the aquifer saturation.	122
Figure 94. Groundwater survey, Nigeria. (a). Apparent resistivity pseudosection. (b) The inversion model with topography. Note the location of the borehole at the 175 meters mark.....	123
Figure 95. The inversion model after 4 iterations from an underwater riverbed survey by Sage Engineering, Belgium.....	124
Figure 96. Thames River (CT, USA) survey with floating electrodes. (a) The measured apparent resistivity pseudosection. Inversion models obtained (b) without constraints on the water layer, and (c) with a fixed water layer.....	125
Figure 97. Survey to map oil sands, Alberta, Canada. (a) Location of major tar sands deposits in Alberta, Canada. (b) Example of resistivity log and geologic column of Athabasca oil sands. (c) 2-D resistivity model from imaging survey (Kellett and Bauman, 1999).	126

Figure 98. A simple arrangement of the electrodes for a 3-D survey.....	128
Figure 99. Two possible measurement sequences for a 3-D survey. The location of potential electrodes corresponding to a single current electrode in the arrangement used by (a) a survey to measure the complete data set and (b) a cross-diagonal survey.....	128
Figure 100. 3-D sensitivity plots for the pole-pole array. The plots are in the form of horizontal slices through the earth at different depths.	129
Figure 101. 3-D sensitivity plots for the pole-dipole array with n=1 in the form of horizontal slices through the earth at different depths. The C1 electrode is the leftmost white cross.	131
Figure 102. 3-D sensitivity plots for the pole-dipole array with n=4 in the form of horizontal slices through the earth at different depths.....	131
Figure 103. 3-D sensitivity plots for the dipole-dipole array with n=1 in the form of horizontal slices through the earth at different depths. The C2 electrode is the leftmost white cross.....	133
Figure 104. 3-D sensitivity plots for the dipole-dipole array with n=4 in the form of horizontal slices through the earth at different depths. The C2 electrode is the leftmost white cross.....	133
Figure 105. The 3-D sensitivity plots for the Wenner alpha array at different depths.	134
Figure 106. The 3-D sensitivity plots for the Wenner-Schlumberger array with the n=4 at different depths.....	134
Figure 107. The 3-D sensitivity plots for the Wenner gamma array at different depths.	135
Figure 108. Using the roll-along method to survey a 10 by 10 grid with a multi-electrode system with 50 nodes. (a) Surveys using a 10 by 5 grid with the lines orientated in the x-direction. (b) Surveys with the lines orientated in the y-direction.	136
Figure 109. A 3-D model with 4 rectangular prisms in a 15 by 15 survey grid. (a) The finite-difference grid. (b) Horizontal apparent resistivity pseudosections for the pole-pole array with the electrodes aligned in the x-direction.....	138
Figure 110. The model used in 3-D inversion.	140
Figure 111. Inversion models for the Vetlanda landfill survey data set. (a) Using standard inversion settings. (b) With a higher damping factor for the topmost layer. (c) Using diagonal roughness filter in the horizontal (x-y) directions. (d) Using diagonal roughness filters in the vertical (x-z and y-z) directions as well. (e) Using the roughness filter in all directions.	142
Figure 112. Types of 3-D roughness filters. (a) With components in the x- and y- directions only for the horizontal filter. (b) With components in the diagonal directions in the x-y plane for the horizontal filter. (c) Applying the roughness filter with the corner model cells as well. Only two (out of eight) corner cells are shown.	143
Figure 113. Inversion models for the Vetlanda landfill survey data set using model cells of equal lengths in the x- and y- directions. (a) Using standard inversion settings. (b) With a higher damping factor for the topmost layer. (c) Using diagonal roughness filter in the horizontal (x-y) directions. (d) Using diagonal roughness filters in the vertical (x-z and y-z) directions as well.	144
Figure 114. Synthetic model for long electrodes survey. 3-D model using cells of low resistivity (0.01 $\Omega\cdot m$) that are marked in red to simulate cased wells.	145
Figure 115. Comparison of inversion models using point electrodes with and without long electrodes. (a) Inversion model for pole-pole data set using only surface point electrodes. (b) Inversion model for pole-pole data set using 121 point and 3 long electrodes.	146
Figure 116. 3-D data grid formats.....	147
Figure 117. Methods to model the effect of an electrode using the finite-difference and finite-element methods.....	148

Figure 118. The use of an appropriate mesh spacing to obtain sufficient accuracy for electrodes in the same array that close together.....	148
Figure 119. Map with survey lines and infrastructure at the Hanford site.	149
Figure 120. Types of model grids for the Hanford survey data set. (a) Using a 5 meters spacing model for the entire area. (b) Using a 4 meters spacing model for the entire area. (c) Using a mixture of 4 and 5 meters spacing model grid.	150
Figure 121. Inversion model for Hanford survey site.....	151
Figure 122. Arrangement of survey lines using a 3 cable system with the Abem SAS instrument.....	152
Figure 123. Inversions model for (a) combined Wenner-Schlumberger and dipole-dipole data set, (b) optimized data set. The actual positions of the blocks are marked by black rectangles.....	152
Figure 124. Horizontal sections showing the model resolution for the (a) comprehensive data set, (b) standard arrays and (c) optimized arrays. The electrode positions are marked by small green crosses in the top layer in (a).	153
Figure 125. Vertical cross-sections showing the model resolution for the comprehensive, 'standard', small and large optimized data sets.....	154
Figure 126. The synthetic test model with two 1000 ohm.m rectangular blocks (marked by black rectangles) embedded in a 100 ohm.m background medium.	154
Figure 127. The inversion models for the synthetic model with two 1000 ohm.m rectangular blocks (marked by black rectangles) embedded in a 100 ohm.m background medium.	156
Figure 128. Comprehensive data set point-spread-function plots on a vertical x-z plane located at y=4.5 m for a model cell at different depths with centre at x=4.5m and y=4.5m.	156
Figure 129. Model resolution sections with circular perimeter for (a) comprehensive data set with 180300 arrays, optimized data sets with (b) 946 and (c) 2000 arrays.....	157
Figure 130. Inversion results for survey with a circular perimeter using optimized arrays with (a) 946 and (b) 2000 data points.	157
Figure 131. The (a) initial and (b) perturbed synthetic test models with apparent resistivity pseudosections and inversion models assuming a constant electrode spacing and flat surface. (c) The inversion model obtained with the algorithm that allows the electrodes to shift.....	162
Figure 132. Example of electrode shifts in a 3-D model. (a) Inversion model with fixed electrodes. The shifted electrodes are marked by small black cross in the top layer. (b) Inversion model where electrodes are allowed to shift.	163
Figure 133. (a) Arrangement of electrodes in the Birmingham 3-D field survey. (b) Horizontal and (c) vertical cross-sections of the model obtained from the inversion of the Birmingham field survey data set. The locations of observed tree roots on the ground surface are also shown.....	164
Figure 134. Example L-curve plots. (a) A plot of the model roughness versus the data misfit for the Birmingham survey data set for a number of damping factor values. (b) A plot of the curvature of the curve in (a) for the different damping factor values. The 'optimum' damping factor is at the maximum curvature point.....	164
Figure 135. The 3-D model obtained from the inversion of the Lernacken Sludge deposit survey data set displayed as horizontal slices through the earth.	165
Figure 136. A 3-D view of the model obtained from the inversion of the Lernacken Sludge deposit survey data set displayed with the Slicer/Dicer program. A vertical exaggeration factor of 2 is used in the display to highlight the sludge ponds. Note that the color contour intervals are arranged in a logarithmic manner with respect to the resistivity.....	166
Figure 137. Map of the Panama Canal region with the survey area marked (Noonan and	

Rucker, 2011).....	167
Figure 138. The model grid used for the Panama Canal floating electrodes survey with 20 by 20 meters cells. The location of the electrodes along the surveys lines are shown as colored points.....	167
Figure 139. The inversion model for the Panama Canal floating electrodes survey. The first 4 layers correspond to the water column.....	167
Figure 140. Geological map of the Copper Hill area (White <i>et al.</i> 2001).....	168
Figure 141. Electrodes layout used for the 3-D survey of the Copper Hill area.....	169
Figure 142. The I.P. model obtained from the inversion of the Copper Hill survey data set. Yellow areas have chargeability values of greater than 35 mV/V, while red areas have chargeability values of greater than 45 mV/V (White <i>et al.</i> , 2001).....	169
Figure 143. Location of uranium mines in the Athabasca basin, Saskatchewan (Bingham <i>et al.</i> , 2006)	170
Figure 144. Geological model of uranium deposit (Bingham <i>et al.</i> , 2006).....	171
Figure 145. Example of inversion model from the Midwest deposit area showing the resistivity at a depth of about 200 meters (Bingham <i>et al.</i> , 2006)	171
Figure 146. A complex time-lapse field survey example. (a) Map of Cripple Creek survey site. (b) Overhead view of the inversion model grid with electrodes layout. (c) Iso-surface contours for the -4% resistivity change at different times after the injection of the sodium cyanide solution (that started at 2.8 hours from the first data set in snapshots used). t1= 1.1 hours, t2= 2.4 hours, t3= 3.7 hours, t4= 4.9 hours. (d) Overhead view of iso-surfaces.	172
Figure 147. Geological map of (a) south-west South Australia, (b) the Burra area, and (c) a plot of survey electrodes and model cells layout.	173
Figure 148. Burra survey (a) resistivity and (b) I.P. inversion model layers.....	174
Figure 149. The model (a) resistivity and (b) I.P. resolution index, and (c) VOI values. The red arrows at the left side of (c) shows the position of the vertical slice shown in Figure 150.....	175
Figure 150. Vertical cross-sections of the (a) resistivity model resolution index, (b) I.P. resolution index and (c) VOI in the X-Z plane 0.8 km north of the origin.....	176

List of Tables

Table 1. 1-D inversion examples using the RES1D.EXE program.	11
Table 2. The median depth of investigation (z_e) for the different arrays (Edwards, 1977). L is the total length of the array. Note identical values of z_e/a for the Wenner-Schlumberger and pole-dipole arrays. Please refer to Figure 4 for the arrangement of the electrodes for the different arrays. The geometric factor is for an "a" value of 1.0 meter. For the pole-dipole array, the array length ' L ' only takes into account the active electrodes C1, P1 and P2 (i.e. it does not take into account the remote C2 electrode).....	29
Table 3. Forward modeling examples.....	50
Table 4. Methods to remove bad data points	54
Table 5. Tests with different inversion options	63
Table 6. Tests with different topographic modeling options	68
Table 7. Tests with option to fix the model resistivity	70
Table 8. Inversion times for the long Redas survey data set using different settings.....	79
Table 9. Inversion times for different line lengths.....	79
Table 10. Tests with 2-D I.P. inversion	102
Table 11. A few borehole inversion tests.....	109
Table 12. 3-D forward modeling examples	137
Table 13. 3-D inversion examples	141

1 Introduction to resistivity surveys

1.1 Introduction and basic resistivity theory

The resistivity method is one of the oldest geophysical survey techniques (Loke, 2011). The purpose of electrical surveys is to determine the subsurface resistivity distribution by making measurements on the ground surface. From these measurements, the true resistivity of the subsurface can be estimated. The ground resistivity is related to various geological parameters such as the mineral and fluid content, porosity and degree of water saturation in the rock. Electrical resistivity surveys have been used for many decades in hydrogeological, mining, geotechnical, environmental and even hydrocarbon exploration (Loke *et al.*, 2013a).

The fundamental physical law used in resistivity surveys is Ohm's Law that governs the flow of current in the ground. The equation for Ohm's Law in vector form for current flow in a continuous medium is given by

$$\mathbf{J} = \sigma \mathbf{E} \quad (1.1)$$

where σ is the conductivity of the medium, \mathbf{J} is the current density and \mathbf{E} is the electric field intensity. In practice, what is measured is the electric field potential. We note that in geophysical surveys the medium resistivity ρ , which is equals to the reciprocal of the conductivity ($\rho=1/\sigma$), is more commonly used. The relationship between the electric potential and the field intensity is given by

$$\mathbf{E} = -\nabla\Phi \quad (1.2)$$

Combining equations (1.1) and (1.2), we get

$$\mathbf{J} = -\sigma \nabla\Phi \quad (1.3)$$

In almost all surveys, the current sources are in the form of point sources. In this case, over an elemental volume ΔV surrounding the a current source I , located at (x_s, y_s, z_s) the relationship between the current density and the current (Dey and Morrison, 1979a) is given by

$$\nabla \cdot \mathbf{J} = \left(\frac{I}{\Delta V} \right) \delta(x - x_s) \delta(y - y_s) \delta(z - z_s) \quad (1.4)$$

where δ is the Dirac delta function. Equation (3) can then be rewritten as

$$-\nabla \cdot [\sigma(x, y, z) \nabla\Phi(x, y, z)] = \left(\frac{I}{\Delta V} \right) \delta(x - x_s) \delta(y - y_s) \delta(z - z_s) \quad (1.5)$$

This is the basic equation that gives the potential distribution in the ground due to a point current source. A large number of techniques have been developed to solve this equation. This is the “forward” modeling problem, i.e. to determine the potential that would be observed over a given subsurface structure. Fully analytical methods have been used for simple cases, such as a sphere in a homogenous medium or a vertical fault between two areas each with a constant resistivity. For an arbitrary resistivity distribution, numerical techniques are more commonly used. For the 1-D case, where the subsurface is restricted to a number of horizontal layers, the linear filter method is commonly used (Koefoed, 1979). For 2-D and 3-D cases, the finite-difference and finite-element methods are the most versatile. In Chapter 2, we will look at the use of a forward modeling computer program for 2-D structures.

The more complicated cases will be examined in the later sections. First, we start with the simplest case with a homogeneous subsurface and a single point current source on the ground surface (Figure 1). In this case, the current flows radially away from the source, and the potential varies inversely with distance from the current source. The equipotential surfaces have a hemisphere shape, and the current flow is perpendicular to the equipotential surface. The potential in this case is given by

$$\phi = \frac{\rho I}{2\pi r} \quad (1.6)$$

where r is the distance of a point in the medium (including the ground surface) from the electrode. In practice, all resistivity surveys use at least two current electrodes, a positive current and a negative current source. Figure 2 show the potential distribution caused by a pair of electrodes. The potential values have a symmetrical pattern about the vertical place at the mid-point between the two electrodes. The potential value in the medium from such a pair is given by

$$\phi = \frac{\rho I}{2\pi} \left(\frac{1}{r_{C1}} - \frac{1}{r_{C2}} \right) \quad (1.7)$$

where r_{C1} and r_{C2} are distances of the point from the first and second current electrodes.

In practically all surveys, the potential difference between two points (normally on the ground surface) is measured. A typical arrangement with 4 electrodes is shown in Figure 3. The potential difference is then given by

$$\Delta\phi = \frac{\rho I}{2\pi} \left(\frac{1}{r_{C1P1}} - \frac{1}{r_{C2P1}} - \frac{1}{r_{C1P2}} + \frac{1}{r_{C2P2}} \right) \quad (1.8)$$

The above equation gives the potential that would be measured over a homogenous half space with a 4 electrodes array.

Actual field surveys are conducted over an inhomogenous medium where the subsurface resistivity has a 3-D distribution. The resistivity measurements are still made by injecting current into the ground through the two current electrodes (C1 and C2 in Figure 3), and measuring the resulting voltage difference at two potential electrodes (P1 and P2). From the current (I) and potential ($\Delta\phi$) values, an apparent resistivity (ρ_a) value is calculated.

$$\rho_a = k \frac{\Delta\phi}{I} \quad (1.9)$$

where

$$k = \frac{2\pi}{\left(\frac{1}{r_{C1P1}} - \frac{1}{r_{C2P1}} - \frac{1}{r_{C1P2}} + \frac{1}{r_{C2P2}} \right)}$$

k is a geometric factor that depends on the arrangement of the four electrodes. Resistivity measuring instruments normally give a resistance value, $R = \Delta\phi/I$, so in practice the apparent

resistivity value is calculated by

$$\rho_a = k R \quad (1.10)$$

The calculated resistivity value is not the true resistivity of the subsurface, but an “apparent” value that is the resistivity of a homogeneous ground that will give the same resistance value for the same electrode arrangement. The relationship between the “apparent” resistivity and the “true” resistivity is a complex relationship. To determine the true subsurface resistivity from the apparent resistivity values is the “inversion” problem. Methods to carry out such an inversion will be discussed in more detail at the end of this chapter.

Figure 4 shows the common arrays used in resistivity surveys together with their geometric factors. In a later section, we will examine the advantages and disadvantages of some of these arrays.

There are two more electrical based methods that are closely related to the resistivity method. They are the Induced Polarization (IP) method, and the Spectral Induced Polarization

(SIP) (also known as Complex Resistivity (CR)) method. Both methods require measuring instruments that are more sensitive than the normal resistivity method, and with significantly higher currents. IP surveys are comparatively more common, particularly in mineral exploration surveys. It is able to detect conductive minerals of very low concentrations that might otherwise be missed by resistivity or EM surveys. Commercial SIP surveys are comparatively rare, although it is a popular research subject. Both IP and SIP surveys use alternating currents (in the frequency domain) of much higher frequencies than standard resistivity surveys. Electromagnetic coupling is a serious problem in both methods. To minimize the electromagnetic coupling, the dipole-dipole (or pole-dipole) array is commonly used.

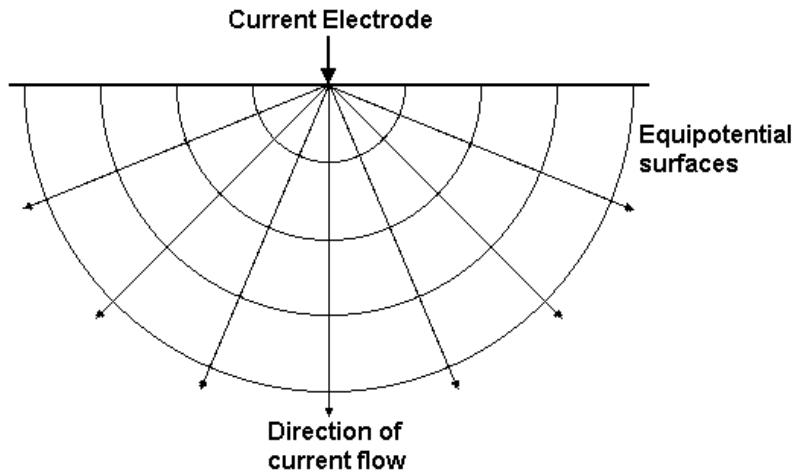


Figure 1. The flow of current from a point current source and the resulting potential distribution.

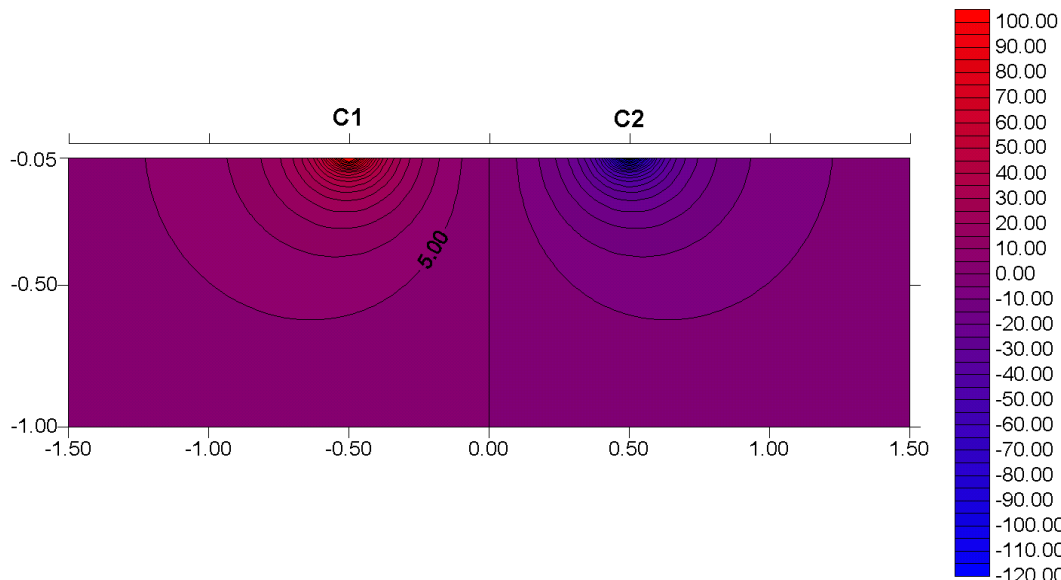


Figure 2. The potential distribution caused by a pair of current electrodes. The electrodes are 1 m apart with a current of 1 ampere and a homogeneous half-space with resistivity of $1 \Omega \cdot \text{m}$.

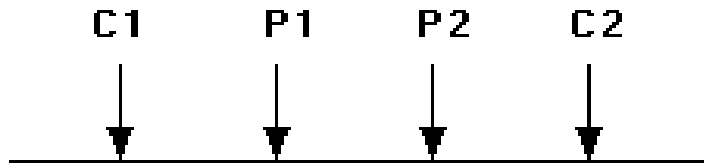


Figure 3. A conventional array with four electrodes to measure the subsurface resistivity.

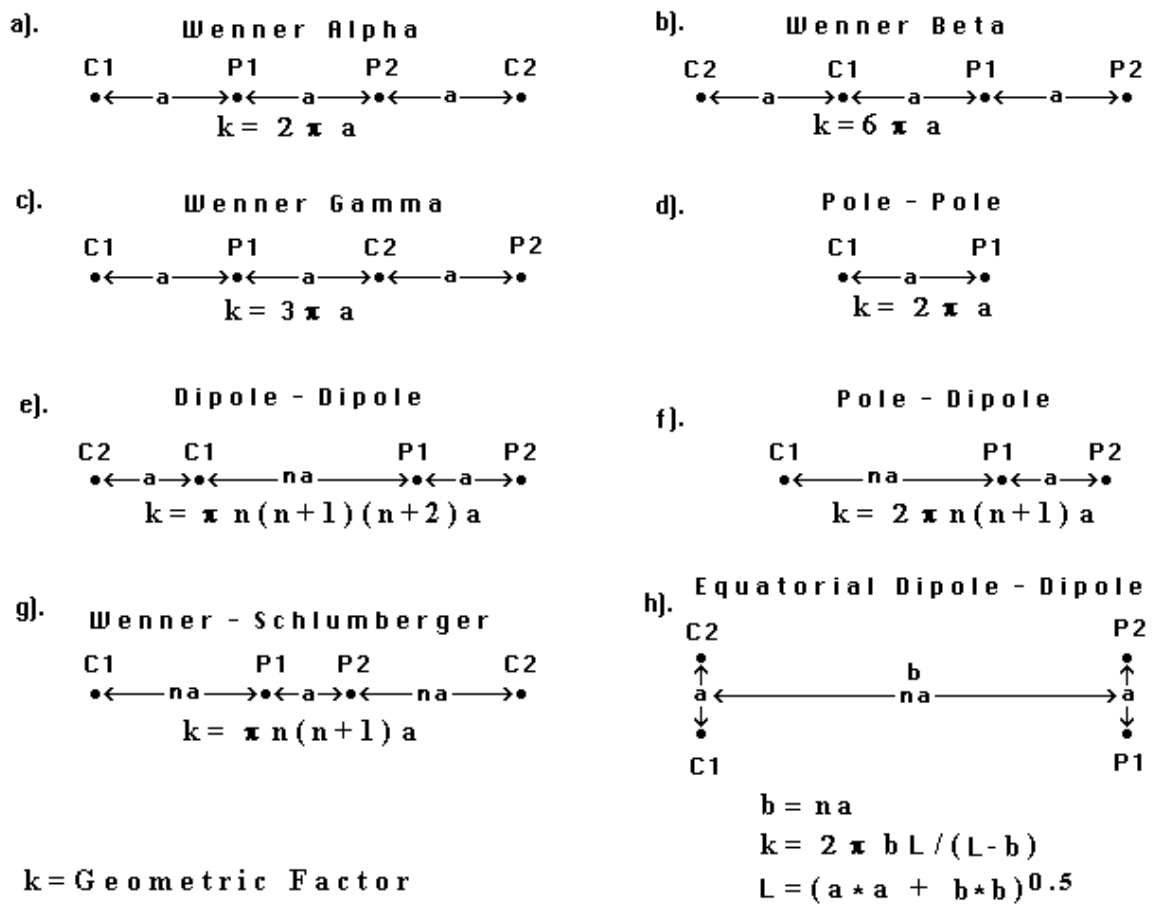


Figure 4. Common arrays used in resistivity surveys and their geometric factors. Note that the dipole-dipole, pole-dipole and Wenner-Schlumberger arrays have two parameters, the dipole length "a" and the dipole separation factor "n". While the "n" factor is commonly an integer value, non-integer values can also be used.

1.2 Electrical properties of earth materials

Electric current flows in earth materials at shallow depths through two main methods. They are electronic conduction and electrolytic conduction. In electronic conduction, the current flow is via free electrons, such as in metals. In electrolytic conduction, the current flow is via the movement of ions in groundwater. In environmental and engineering surveys, electrolytic conduction is probably the more common mechanism. Electronic conduction is important when conductive minerals are present, such metal sulfides and graphite in mineral surveys.

The resistivity of common rocks, soil materials and chemicals (Keller and Frischknecht, 1966; Daniels and Alberty, 1966; Telford *et al.*, 1990) is shown in Figure 5. Igneous and metamorphic rocks typically have high resistivity values. The resistivity of these rocks is greatly dependent on the degree of fracturing, and the percentage of the fractures filled with ground water. Thus a given rock type can have a large range of resistivity, from about 1000 to 10 million $\Omega\cdot\text{m}$, depending on whether it is wet or dry. This characteristic is useful in the detection of fracture zones and other weathering features, such as in engineering and groundwater surveys.

Sedimentary rocks, which are usually more porous and have higher water content, normally have lower resistivity values compared to igneous and metamorphic rocks. The resistivity values range from 10 to about 10000 $\Omega\cdot\text{m}$, with most values below 1000 $\Omega\cdot\text{m}$. The resistivity values are largely dependent on the porosity of the rocks, and the salinity of the contained water.

Unconsolidated sediments generally have even lower resistivity values than sedimentary rocks, with values ranging from about 10 to less than 1000 $\Omega\cdot\text{m}$. The resistivity value is dependent on the porosity (assuming all the pores are saturated) as well as the clay content. Clayey soil normally has a lower resistivity value than sandy soil. However, note the overlap in the resistivity values of the different classes of rocks and soils. This is because the resistivity of a particular rock or soil sample depends on a number of factors such as the porosity, the degree of water saturation and the concentration of dissolved salts.

The resistivity of groundwater varies from 10 to 100 $\Omega\cdot\text{m}$ depending on the concentration of dissolved salts. Note the low resistivity (about 0.2 $\Omega\cdot\text{m}$) of seawater due to the relatively high salt content. This makes the resistivity method an ideal technique for mapping the saline and fresh water interface in coastal areas. One simple equation that gives the relationship between the resistivity of a porous rock and the fluid saturation factor is Archie's Law. It is only applicable for certain types of rocks and sediments, particularly those that have a low clay content. The electrical conduction is assumed to be through the fluids filling the pores of the rock. Archie's Law is given by

$$\rho = a\rho_w\phi^{-m} \quad (1.11)$$

where ρ is the rock resistivity, ρ_w is fluid resistivity, ϕ is the fraction of the rock filled with the fluid, while a and m are two empirical parameters (Keller and Frischknecht, 1966). For most rocks, a is about 1 while m is about 2. For sediments with a significant clay content, other more complex equations have been proposed (Olivar *et al.*, 1990).

The resistivities of several types of ores are also shown. Metallic sulfides (such as pyrrhotite, galena and pyrite) have typically low resistivity values of less than 1 $\Omega\cdot\text{m}$. Note that the resistivity value of a particular ore body can differ greatly from the resistivity of the individual crystals. Other factors, such as the nature of the ore body (massive or disseminated) have a significant effect. Note that graphitic slate has a low resistivity value, similar to the metallic sulfides, which can give rise to problems in mineral surveys. Most oxides, such as hematite, do not have a significantly low resistivity value. One exception is magnetite.

The resistivity values of several industrial contaminants are also given in Figure 5. Metals, such as iron, have extremely low resistivity values. Chemicals that are strong electrolytes, such as potassium chloride and sodium chloride, can greatly reduce the resistivity of ground water to less than $1 \Omega\text{-m}$ even at fairly low concentrations. The effect of weak electrolytes, such as acetic acid, is comparatively smaller. Hydrocarbons, such as xylene ($6.998 \times 10^{16} \Omega\text{-m}$), typically have very high resistivity values. However, in practice the percentage of hydrocarbons in a rock or soil is usually quite small, and might not have a significant effect on the bulk resistivity. However when the concentration of the hydrocarbon is high, such as the commercial oil sands deposits in Canada, the resistivity method has proved to be a useful exploration method for such deposits (see section 7.10 for an example).

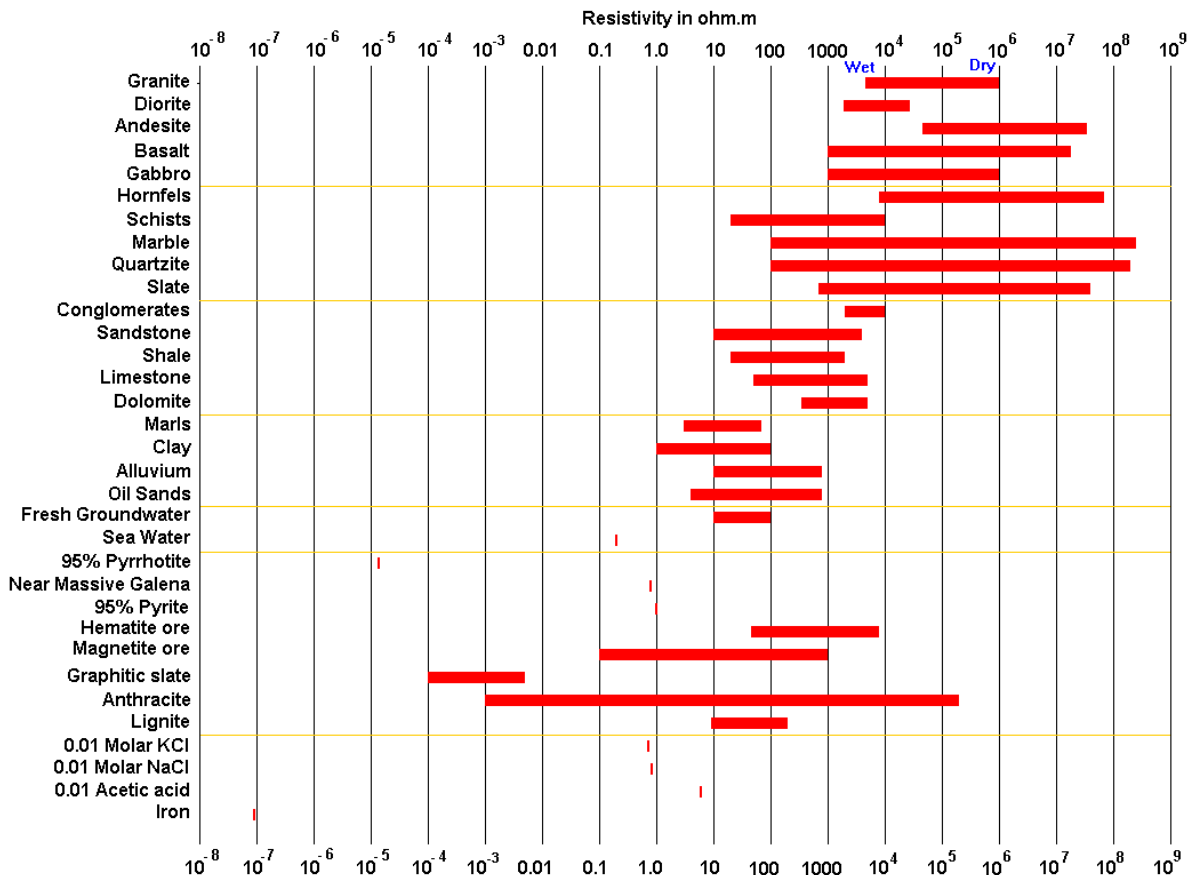


Figure 5. The resistivity of rocks, soils and minerals.

1.3 1-D resistivity surveys and inversions – applications, limitations and pitfalls

The resistivity method has its origin in the 1920's due to the work of the Schlumberger brothers. For approximately the next 60 years, for quantitative interpretation, conventional sounding surveys (Koefoed, 1979) were normally used. In this method, the center point of the electrode array remains fixed, but the spacing between the electrodes is increased to obtain more information about the deeper sections of the subsurface.

The measured apparent resistivity values are normally plotted on a log-log graph paper. To interpret the data from such a survey, it is normally assumed that the subsurface consists of horizontal layers. In this case, the subsurface resistivity changes only with depth, but does not change in the horizontal direction. A one-dimensional model of the subsurface is used to interpret the measurements (Figure 6a). Figure 7 shows an example of the data from a

sounding survey and a possible interpretation model. This method has given useful results for geological situations (such the water-table) where the one-dimensional model is approximately true.

The software provided, RES1D.EXE, is a simple inversion and forward modeling program for 1-D models that consists of horizontal layers. In the software package, several files with extensions of DAT are example data files with resistivity sounding data. Files with the MOD extension are model files that can be used to generate synthetic data for the inversion part of the program. As a first try, read in the file WENNER3.DAT that contains the Wenner array sounding data for a simple 3-layer model.

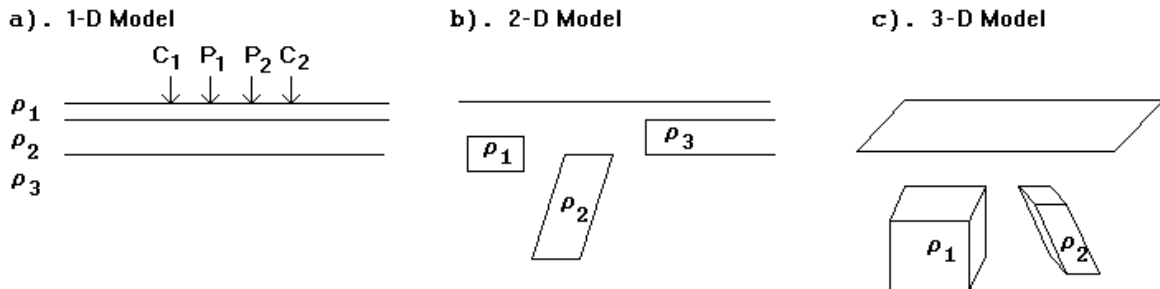


Figure 6. The three different models used in the interpretation of resistivity measurements.

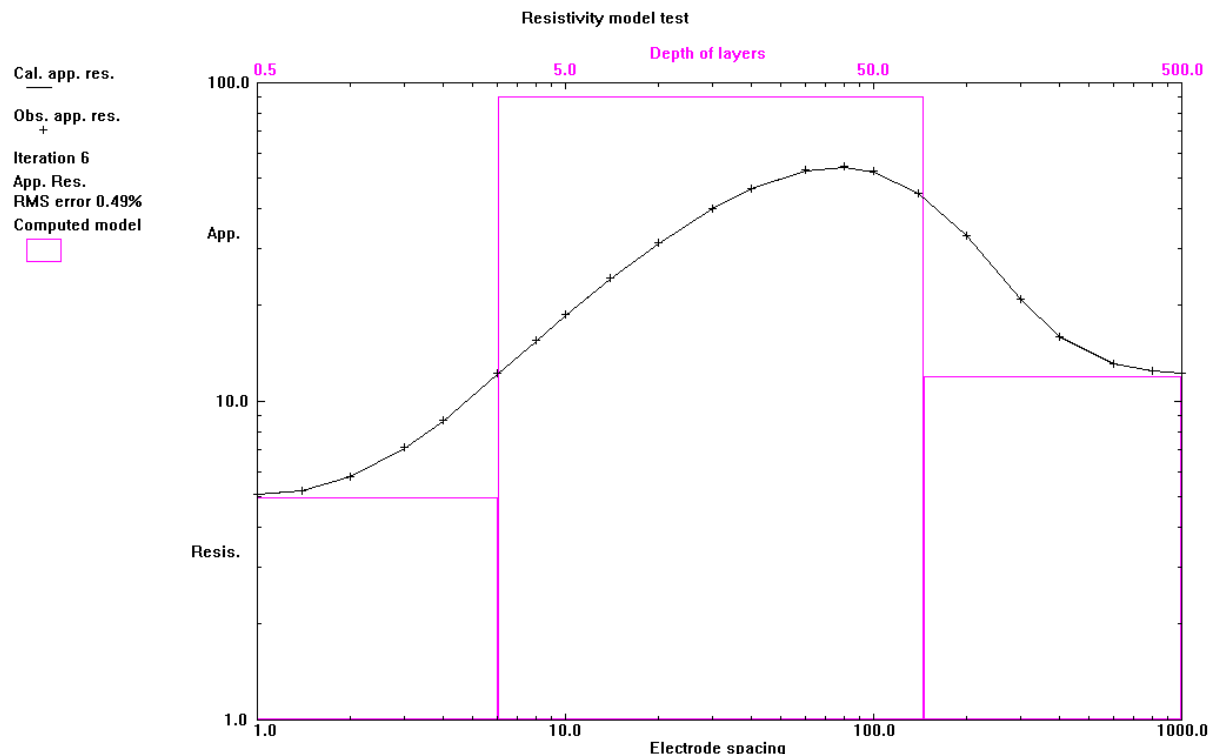


Figure 7. A typical 1-D model used in the interpretation of resistivity sounding data for the Wenner array.

The greatest limitation of the resistivity sounding method is that it does not take into account lateral changes in the layer resistivity. Such changes are probably the rule rather than the exception. The failure to include the effect of such lateral changes can result in errors in the interpreted layer resistivity and/or thickness. As an example, Figure 8 shows a 2-D model

where the main structure is a two-layer model with a resistivity of $10 \Omega\cdot m$ and a thickness of 5 meters for the upper layer, while the lower layer has a resistivity of $100 \Omega\cdot m$. To the left of the center point of the survey line, a low resistivity prism of $1 \Omega\cdot m$ is added in the upper layer to simulate a lateral inhomogeneity. The 2-D model has 144 electrodes that are 1 meter apart. The apparent resistivity pseudosections for the Wenner and Schlumberger array are also shown. For the Schlumberger array, the spacing between the potential electrodes is fixed at 1.0 meter for the apparent resistivity values shown in the pseudosection. The sounding curves that are obtained with conventional Wenner and Schlumberger array sounding surveys with the mid-point at the center of the line are shown in **Figure 9**. In the 2-D model, the low resistivity rectangular prism extends from 5.5 to 18.5 meters to the left of the sounding midpoint. The ideal sounding curves for both arrays for a two-layer model (i.e. without the low resistivity prism) are also shown for comparison. For the Wenner array, the low resistivity prism causes the apparent resistivity values in the sounding curve (**Figure 9a**) to be too low for spacing values of 2 to 9 meters and for spacings larger than 15 meters. At spacings of between 9 to 15 meters, the second potential electrode P2 crosses over the low resistivity prism. This causes the apparent resistivity values to approach the two-layer model sounding curve. If the apparent resistivity values from this model are interpreted using a conventional 1-D model, the resulting model could be misleading. In this case, the sounding data will most likely to be interpreted as a three-layer model.

The effect of the low resistivity prism on the Schlumberger array sounding curve is slightly different. The apparent resistivity values measured with a spacing of 1 meter between the central potential electrodes are shown by black crosses in **Figure 9b**. For electrode spacings (which is defined as half the total length of the array for the Schlumberger array) of less than 15 meters, the apparent resistivity values are less than that of the two-layer sounding curve. For spacings greater than 17 meters, the apparent resistivity values tend to be too high. This is probably because the low resistivity prism lies to the right of the C2 electrode (i.e. outside the array) for spacings of less than 15 meters. For spacings of greater than 17 meters, it lies between the P2 and C2 electrodes. Again, if the data is interpreted using a 1-D model, the results could be misleading. One method that has been frequently recommended to “remove” the effect of lateral variations with the Schlumberger array is by shifting curve segments measured with different spacings between the central potential electrodes. The apparent resistivity values measured with a spacing of 3 meters between the potential electrodes are also shown in **Figure 9b**. The difference in the sounding curves with the spacings of 1 meter and 3 meters between the potential electrodes is small, particularly for large electrode spacings. Thus any shifting in the curve segments would not remove the distortion in the sounding curve due to the low resistivity prism. The method of shifting the curve segments is probably more applicable if the inhomogeneity lies between the central potential electrodes, and probably ineffective if the inhomogeneity is beyond the largest potential electrodes spacing used (which is the case in Figure 8). However, note that the effect of the prism on the Schlumberger array sounding curve is smaller at the larger electrode spacings compared with the Wenner array (**Figure 9**). The main reason is probably the larger distance between the P2 and C2 electrodes in the Schlumberger array.

A more reliable method to reduce the effect of lateral variations on the sounding data is the offset Wenner method (Barker, 1978). It makes use of the property that the effect of an inhomogeneity on the apparent resistivity value is of opposite sign if it lies between the two potential electrodes or if it is between a potential and a current electrode. For the example shown in Figure 8, if the low resistivity body lies in between a current and potential electrode (the P2 and C2 electrodes in this case), the measured apparent resistivity value would be lower. If the low resistivity body lies in between the P1 and P2 electrodes, it will cause the apparent resistivity value to be higher. The reason for this phenomenon can be found in the

sensitivity pattern for the Wenner array (see Figure 23a). By taking measurements with different positions for the mid-point of the array, the effect of the low resistivity body can be reduced.

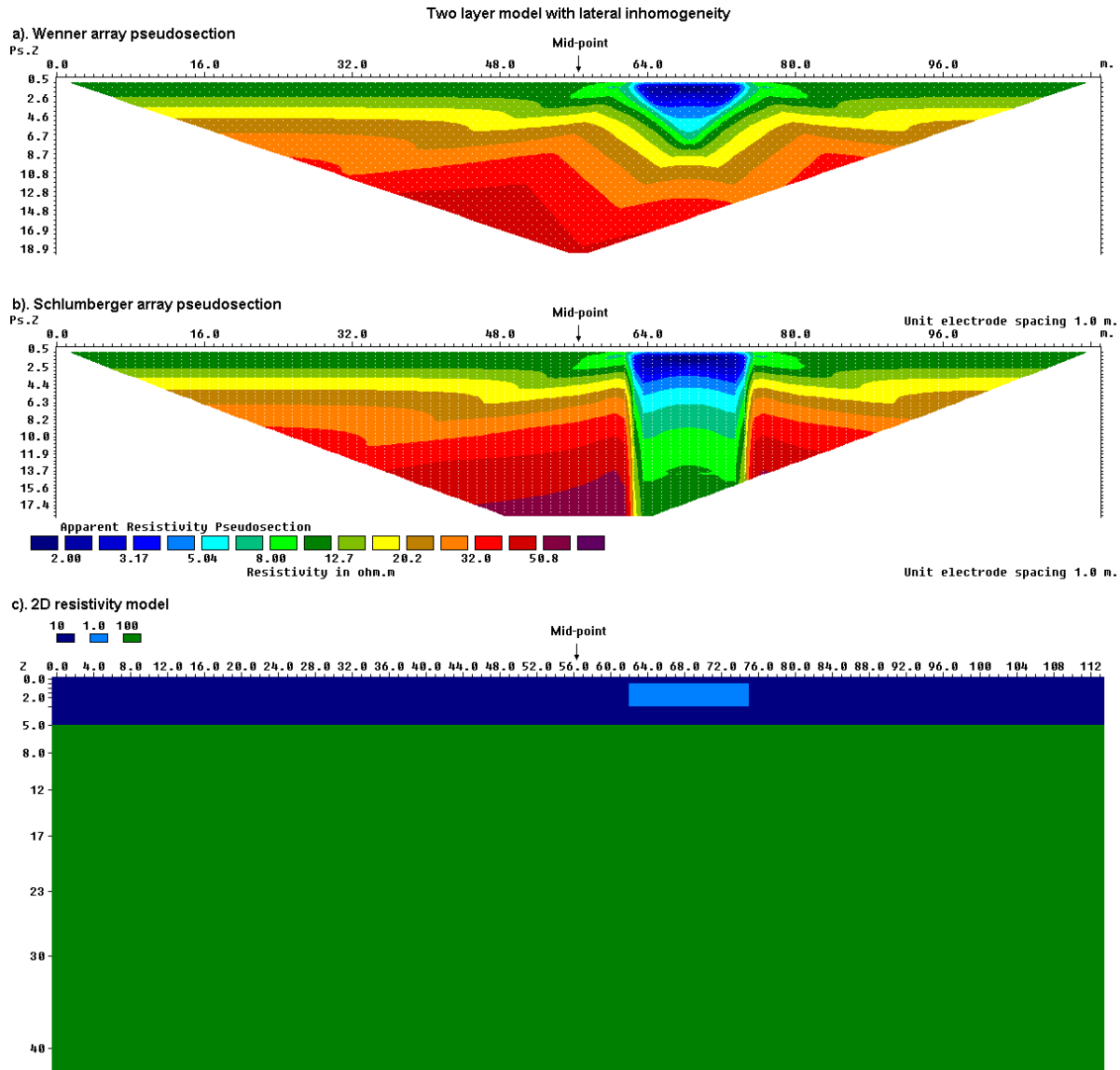


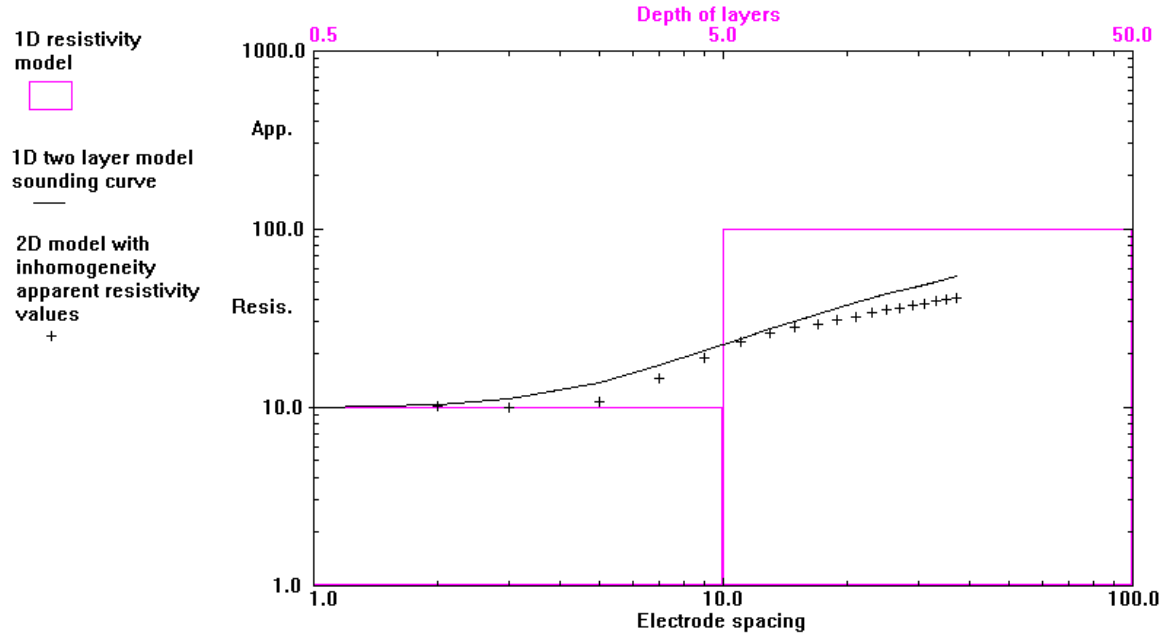
Figure 8. A 2-D two-layer model with a low resistivity prism in the upper layer. The calculated apparent resistivity pseudosections for the (a) Wenner and (b) Schlumberger arrays. (c) The 2D model. The mid-point for a conventional sounding survey is also shown.

Another classical survey technique is the profiling method. In this case, the spacing between the electrodes remains fixed, but the entire array is moved along a straight line. This gives some information about lateral changes in the subsurface resistivity, but it cannot detect vertical changes in the resistivity. Interpretation of data from profiling surveys is mainly qualitative.

The most severe limitation of the resistivity sounding method is that horizontal (or lateral) changes in the subsurface resistivity are commonly found. The ideal situation shown in Figure 6a is rarely found in practice. As shown by the examples in Figure 8 and **Figure 9**, lateral changes in the subsurface resistivity will cause changes in the apparent resistivity

values that might be, and frequently are, misinterpreted as changes with depth in the subsurface resistivity. In many engineering and environmental studies, the subsurface geology is very complex where the resistivity can change rapidly over short distances. The 1-D resistivity sounding method would not be sufficiently accurate for such situations.

a). Wenner array sounding curve



b). Schlumberger array sounding curve

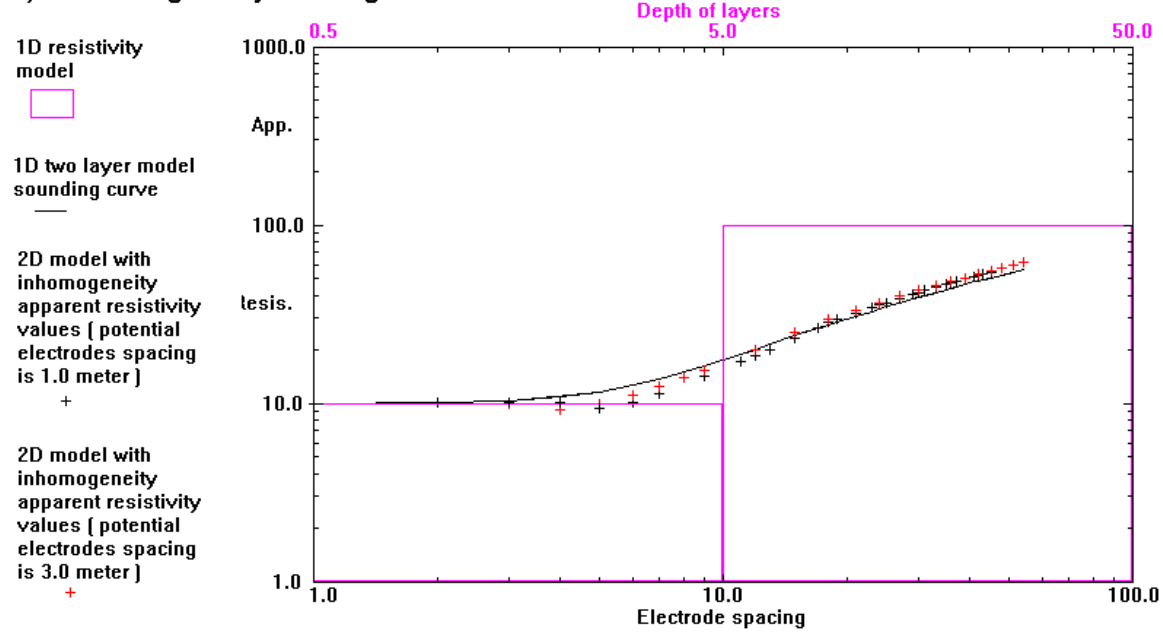


Figure 9. Apparent resistivity sounding curves for a 2-D model with a lateral inhomogeneity. (a) The apparent resistivity curve extracted from the 2D pseudosection for the Wenner array. The sounding curve for a two-layer model without the low resistivity prism is also shown by the black line curve. (b) The apparent resistivity curves extracted from the 2-D pseudosection for the Schlumberger array with a spacing of 1.0 meter (black crosses) and 3.0 meters (red crosses) between the potential electrodes. The sounding curve for a two-layer model without the low resistivity prism is also shown.

To use the RES1D.EXE program for the exercises in the table below, as well as the other programs that we shall use in the later sections, follows the usual sequence used by Windows XP/Vista/7/8/10. Click the ‘Start’ button, followed by ‘Programs’ and the look for the RES1D folder in the list of installed programs. Alternatively, you can create a shortcut icon on the Windows Desktop.

Table 1. 1-D inversion examples using the RES1D.EXE program.

Data set and purpose	Things to try
WENNER3.DAT – A simple synthetic data file for a 3 layer model.	(1). Read in the file, and then run the “Carry out inversion” step.
WENN_LATERAL.DAT and SCHL_LATER.DAT – Wenner and Schlumberger array sounding data shown in Figure 9 that are extracted from the 2-D pseudosections.	(1). Read in the files, and then invert the data sets. (2). Compare the results with the true two-layer model (that has resistivities of $10 \Omega\cdot m$ and $100 \Omega\cdot m$ for the first and second layers, and thickness of 5 meters for the first layer).
WENOFFSET.DAT – A field data set collected using the offset Wenner method.	(1). Read in the files, and then invert the data set.
IPTESTM.DAT – A 1-D sounding data file with IP measurements as well to round things up.	(1). Read in the files, and then invert the data set.

To obtain a more accurate subsurface model than is possible with a simple 1-D model, a more complex model must be used. In a 2-D model (Figure 6b), the resistivity values are allowed to vary in one horizontal direction (usually referred to as the x direction) but assumed to be constant in the other horizontal (the y) direction. This approximation is reasonable for survey lines that are perpendicular to the strike of an elongated structure. The most realistic model would be a fully 3-D model (Figure 6c) where the resistivity values are allowed to change in all 3 directions. The use of 2-D and 3-D surveys and interpretation techniques will be examined in detail in the following chapters.

1.4 Basic Inverse Theory

In geophysical inversion, we seek to find a *model* that gives a response that is similar to the actual measured values. The model is an idealized mathematical representation of a section of the earth. The model has a set of *model parameters* that are the physical quantities we want to estimate from the observed *data*. The *model response* is the synthetic data that can be calculated from the mathematical relationships defining the model for a given set of model parameters. All inversion methods essentially try to determine a model for the subsurface whose response agrees with the measured data subject to certain restrictions and within acceptable limits. In the cell-based method used by the RES2DINV and RES3DINV programs, the model parameters are the resistivity values of the model cells, while the data is the measured apparent resistivity values. The mathematical link between the model parameters and the model response for the 2-D and 3-D resistivity models is provided by the finite-difference (Dey and Morrison, 1979a, 1979b) or finite-element methods (Silvester and Ferrari 1990).

In all optimization methods, an initial model is modified in an iterative manner so that the difference between the model response and the observed data values is reduced. The set of observed data can be written as a column vector \mathbf{y} given by

$$\mathbf{y} = \text{col}(y_1, y_2, \dots, y_m) \quad (1.12)$$

where m is the number of measurements. The model response \mathbf{f} can be written in a similar form.

$$\mathbf{f} = \text{col}(f_1, f_2, \dots, f_m) \quad (1.13)$$

For resistivity problems, it is a common practice to use the logarithm of the apparent resistivity values for the observed data and model response, and the logarithm of the model values as the model parameters. The model parameters can be represented by the following vector

$$\mathbf{q} = \text{col}(q_1, q_2, \dots, q_n) \quad (1.14)$$

where n is the number of model parameters. The difference between the observed data and the model response is given by the discrepancy vector \mathbf{g} that is defined by

$$\mathbf{g} = \mathbf{y} - \mathbf{f} \quad (1.15)$$

In the least-squares optimization method, the initial model is modified such that the sum of squares error E of the difference between the model response and the observed data values is minimized.

$$E = \mathbf{g}^T \mathbf{g} = \sum_{i=1}^n g_i^2 \quad (1.16)$$

To reduce the above error value, the following Gauss-Newton equation is used to determine the change in the model parameters that should reduce the sum of squares error (Lines and Treitel 1984).

$$\mathbf{J}^T \mathbf{J} \Delta \mathbf{q}_i = \mathbf{J}^T \mathbf{g} \quad (1.17)$$

where $\Delta \mathbf{q}$ is the model parameter change vector, and \mathbf{J} is the Jacobian matrix (of size m by n) of partial derivatives. The elements of the Jacobian matrix are given by

$$J_{ij} = \frac{\partial f_i}{\partial q_j} \quad (1.18)$$

that is the change in the i th model response due to a change in the j th model parameter. After calculating the parameter change vector, a new model is obtained by

$$\mathbf{q}_{k+1} = \mathbf{q}_k + \Delta \mathbf{q}_k \quad (1.19)$$

In practice, the simple least-squares equation (1.17) is rarely used by itself in geophysical inversion. In some situations the matrix product $\mathbf{J}^T \mathbf{J}$ might be singular, and thus the least-squares equation does not have a solution for $\Delta \mathbf{q}$. Another common problem is that the matrix product $\mathbf{J}^T \mathbf{J}$ is nearly singular. This can occur if a poor initial model that is very different from the optimum model is used. The parameter change vector calculated using equation (1.17) can have components that are too large such that the new model calculated with (1.19) might have values that are not realistic. One common method to avoid this problem is the Marquardt-Levenberg modification (Lines and Treitel, 1984) to the Gauss-Newton equation that is given by

$$(\mathbf{J}^T \mathbf{J} + \lambda \mathbf{I}) \Delta \mathbf{q}_k = \mathbf{J}^T \mathbf{g} \quad (1.20)$$

where \mathbf{I} is the identity matrix. The factor λ is known as the Marquardt or damping factor, and this method is also known as the ridge regression method (Inman 1975) or damped least-squares method. The damping factor effectively constrains the range of values that the components of parameter change vector can $\Delta \mathbf{q}$ take. While the Gauss-Newton method in equation (1.17) attempts to minimize the sum of squares of the discrepancy vector only, the

Marquardt-Levenberg method also minimizes a combination of the magnitude of the discrepancy vector and the parameter change vector. This method has been successfully used in the inversion of resistivity sounding data where the model consists of a small number of layers. For example, it was used in the inversion of the resistivity sounding example in Figure 7 with three layers (i.e. five model parameters). However when the number of model parameters is large, such as in 2-D and 3-D inversion models that consist of a large number of small cells, the model produced by this method can have an erratic resistivity distribution with spurious high or low resistivity zones (Constable *et al.*, 1987). To overcome this problem, the Gauss-Newton least-squares equation is further modified so as to minimize the spatial variations in the model parameters (i.e. the model resistivity values change in a smooth or gradual manner). This smoothness-constrained least-squares method (Ellis and Oldenburg 1994a, Loke 2011) has the following mathematical form.

$$(\mathbf{J}^T \mathbf{J} + \lambda \mathbf{F}) \Delta \mathbf{q}_k = \mathbf{J}^T \mathbf{g} - \lambda \mathbf{F} \mathbf{q}_k, \quad (1.21)$$

where $\mathbf{F} = \alpha_x \mathbf{C}_x^T \mathbf{C}_x + \alpha_y \mathbf{C}_y^T \mathbf{C}_y + \alpha_z \mathbf{C}_z^T \mathbf{C}_z$

and \mathbf{C}_x , \mathbf{C}_y and \mathbf{C}_z are the roughness filter matrices in the x -, y - and z -directions that couples the model blocks in those directions (Figure 10, Figure 112). α_x , α_y and α_z are the relative weights given to the roughness filters in the x -, y - and z -directions. One common form of the roughness filter matrix is the first-order difference matrix (deGroot-Hedlin and Constable 1990) that is given by

$$\mathbf{C} = \begin{bmatrix} -1 & 1 & 0 & 0 & .. & .. & .. & 0 \\ 0 & -1 & 1 & 0 & .. & .. & .. & 0 \\ 0 & 0 & -1 & 1 & 0 & .. & .. & 0 \\ .. & .. & .. & .. & .. & .. & .. & 0 \\ .. & .. & .. & .. & .. & .. & .. & 0 \\ .. & .. & .. & .. & .. & .. & .. & 0 \end{bmatrix} \quad (1.22)$$

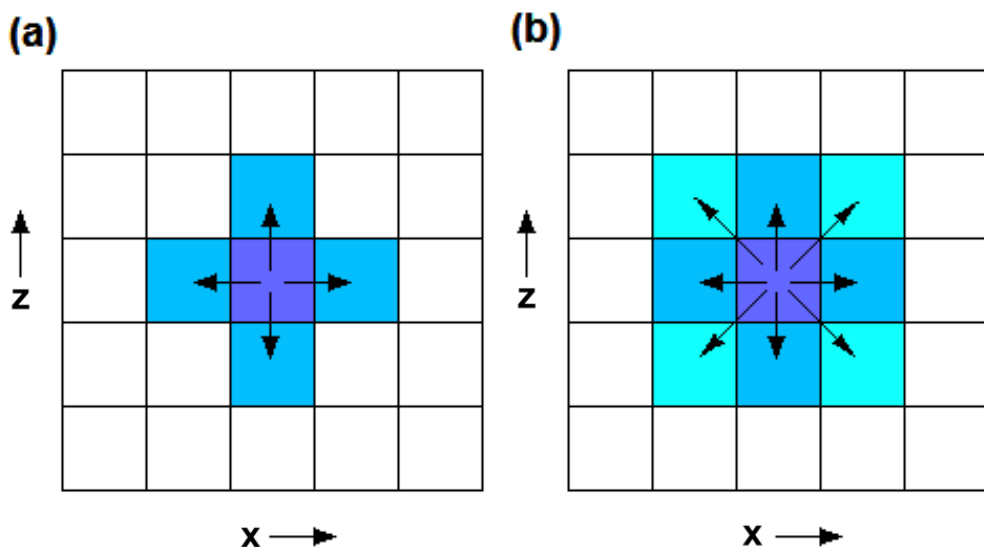


Figure 10. Coupling between neighboring model cells through the roughness filter in a 2-D model. (a) In the horizontal and vertical directions only, and (b) in diagonal directions as

well.

Equation 1.21 also tries to minimize the *square* of the spatial changes, or roughness, of the model resistivity values. It is in fact an l_2 norm smoothness-constrained optimization method. This tends to produce a model with a smooth variation of resistivity values. This approach is acceptable if the actual subsurface resistivity varies in a smooth or gradational manner. In some cases, the subsurface geology consists of a number of regions that are internally almost homogeneous but with sharp boundaries between different regions. For such cases, the inversion formulation in (1.21) can be modified so that it minimizes the *absolute* changes in the model resistivity values (Claerbout and Muir, 1973). This can sometimes give significantly better results. Technically this is referred to as an l_1 norm smoothness-constrained optimization method, or more commonly known as the blocky inversion method. A number of techniques can be used for such a modification. One simple method to implement an l_1 norm based optimization method using the standard least-squares formulation is the iteratively reweighted least-squares method (Wolke and Schwetlick, 1988; Farquharson and Oldenburg, 1998). The optimization equation in (1.21) is modified to

$$(\mathbf{J}^T \mathbf{R}_d \mathbf{J} + \lambda \mathbf{F}_R) \Delta \mathbf{q}_k = \mathbf{J}^T \mathbf{R}_d \mathbf{g} - \lambda \mathbf{F}_R \mathbf{q}_k, \quad (1.23)$$

with $\mathbf{F}_R = \alpha_x \mathbf{C}_x^T \mathbf{R}_m \mathbf{C}_x + \alpha_y \mathbf{C}_y^T \mathbf{R}_m \mathbf{C}_y + \alpha_z \mathbf{C}_z^T \mathbf{R}_m \mathbf{C}_z$

where \mathbf{R}_d and \mathbf{R}_m are weighting matrices introduced so that different elements of the data misfit and model roughness vectors are given equal weights in the inversion process.

Equation (1.23) provides a general method that can be further modified if necessary to include known information about the subsurface geology. As an example, if it is known that the variations in the subsurface resistivity are likely to be confined to a limited zone, the damping factor values can be modified (Ellis and Oldenburg 1994a) such that greater changes are allowed in that zone. If the errors in the data points are known, a diagonal weighting matrix can be used to give greater weights to data points with smaller errors.

One important modification to the least-squares optimization method is in time-lapse inversion using the following equation (Kim et al. 2009, Loke et al. 2014a).

$$[\mathbf{J}_i^T \mathbf{R}_d \mathbf{J}_i + (\lambda_i \mathbf{F}_R + \alpha_i \mathbf{M}^T \mathbf{R}_t \mathbf{M})] \Delta \mathbf{r}_i = \mathbf{J}_i^T \mathbf{R}_d \mathbf{g}_i - (\lambda_i \mathbf{F}_R + \alpha_i \mathbf{M}^T \mathbf{R}_t \mathbf{M}) \mathbf{r}_{i-1} \quad (1.2.4)$$

\mathbf{M} is the difference matrix applied across the time models with only the diagonal and one sub-diagonal elements having values of 1 and -1, respectively. α is the temporal damping factor that gives the weight for minimizing the temporal changes in the resistivity compared to the model roughness and data misfit. Note the smoothness-constraint is not only applied in space through the \mathbf{F} matrix, but also across the different time models through the \mathbf{M} matrix. This is illustrated in Figure 11.

The smoothness-constrained least-squares optimization method involves the damping factor term λ . This term balances the need to reduce the data misfit (so that the calculated apparent resistivity values are as close as possible to the measured values) while producing a model that is ‘reasonably’ smooth and perhaps more geologically realistic. A smaller value of λ term will generally produce a model with a lower data misfit but usually at the expense of larger variations in the model resistivity values. If the error of the measured apparent resistivity values is known, a prudent approach might be to select a model where the data misfit is similar to the known measurement errors. However, for most field data sets, the measurement error is not known. There are generally two methods to automatically select the ‘optimum’ damping factor for such cases, the GCV and L-curve methods (Farquharson and

Oldenburg, 2004). For the inversion of a single data set, either method can be used. However, for time-lapse data sets (Loke et al. 2014a), the L-curve method has a clear advantage due to the sparse block structure of the Jacobian matrix (Figure 11b). The GCV method requires a matrix inversion. However, the inverse of a sparse matrix is usually a full matrix. This makes it impractical to use for time-lapse models with many time-series measurements such that the combined model might have hundreds of thousands of model parameters (i.e. the number of model parameters for a single data set multiplied by the number of time series data sets).

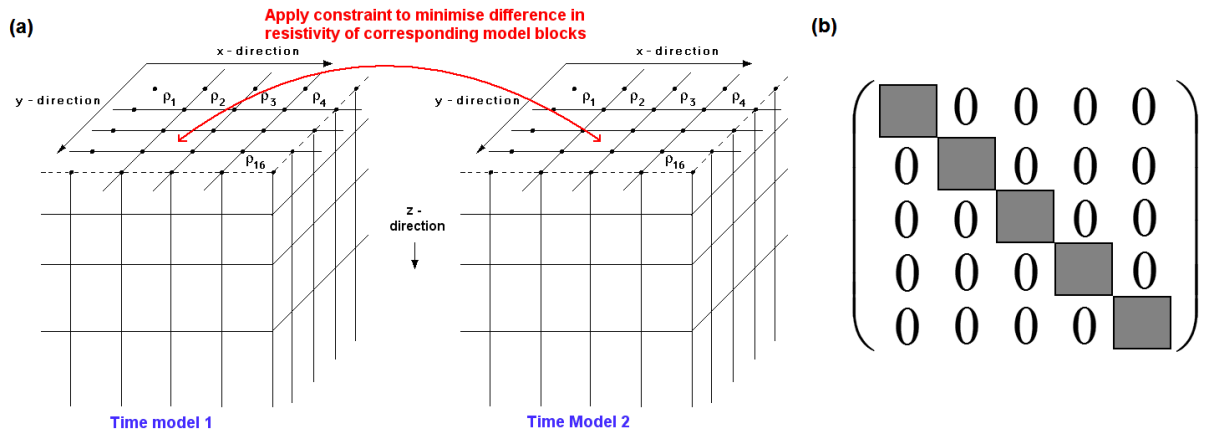


Figure 11. (a) Coupling between corresponding model blocks in two time-lapse models using a cross-model time-lapse smoothness constraint. (b) Example Jacobian matrix structure for five time series data sets and models. Each grey rectangle represents the Jacobian matrix associated with a single set of measurements.

1.5 2-D model discretization methods

In the previous section, we have seen that the least-squares method is used to calculate certain physical characteristics of the subsurface (the “model parameters”) from the apparent resistivity measurements. The “model parameters” are set by the way we slice and dice the subsurface into different regions. Figure 12 shows various possibilities that can be used. The method most commonly used in 2-D (and 3-D) interpretation is a purely cell based model where the subsurface is subdivided into rectangular cells. The positions of the cells are fixed and only the resistivities of cells are allowed to vary during the inversion process. The model parameters are the resistivities the cells. In the example shown in Figure 12, the model parameters are the seventy-two cell resistivity values ρ_1 to ρ_{72} .

A radically different approach is a boundary based inversion method. This method subdivides the subsurface into different regions. The resistivity is assumed to be homogenous within each region. The resistivity is allowed to change in an arbitrary manner across the boundaries, and thus it useful in areas with abrupt transitions in the geology. The resistivity of each region and the depths to the boundaries are changed by the least-squares optimization method so that the calculated apparent resistivity values match the observed values. The “model parameters” for the example shown in Figure 12 are the two resistivity values (ρ_1 and ρ_2) and the depths at five points (z_1 to z_5) along the boundary that gives a total of seven parameters. While this method works well for synthetic data from numerical models, for many field data sets it can lead to unstable results with highly oscillating boundaries (Olayinka and Yaramanci, 2000). Its greatest limitation is probably the assumption of a constant resistivity within each region. In particular, lateral changes in the resistivity near the surface have a very large effect on the measured apparent resistivity values. Since this model

does not take into account such lateral changes, they are often mistakenly modeled as changes in the depths of the boundaries.

More recent efforts have been in combining the cell based and boundary based inversion methods (Smith et al., 1999). One such method is the laterally constrained inversion method (Auken and Christiansen, 2004). In this method, lateral changes (but not vertical changes) are allowed in each region (Figure 12c), and abrupt transitions across the boundaries are also allowed. The “model parameters” for the example in Figure 12 are then the twenty-four resistivity values (ρ_1 and ρ_{24}) and the depths at thirteen points (z_1 to z_{13}) along the boundary giving a total of thirty-seven parameters. Information from other sources, such as borehole or seismic data, can be used to provide an initial estimate of the depth to the boundary. A common situation is when the depth information is available at only one borehole. In this case, the initial boundary is usually set a constant depth. The inversion method then adjusts the depths at a number of points along the boundary during the inversion process. A smoothness-constraint is applied to minimize changes in the depths between adjacent points on the same boundary (Smith et al., 1999). This method works particularly well where the subsurface consists of several sedimentary zones.

A further generalization of this concept is to allow both vertical and lateral changes within each region (as in a pure cell based model) while also allowing sharp changes across the boundaries (Figure 12d). The model shown in Figure 12d has seventy-two resistivity values and five depth values, giving a total of seventy-seven model parameters. This type of discretization is particularly useful where near-surface inhomogeneities that occur at different depths within the top layer have a large effect on the measured apparent resistivity values (Figure 13). The model cells used so far has rectangular shapes (Figure 12). This is partly due to the use of the finite-difference method in calculating the model apparent resistivity values. A slight disadvantage is that the boundary is approximated by a series of rectangular steps. Figure 12e shows a possible variation using the finite-element method with trapezoidal cells where the edges of the cells adjacent to the boundary are adjusted so as to conform to the true shape of the boundary.

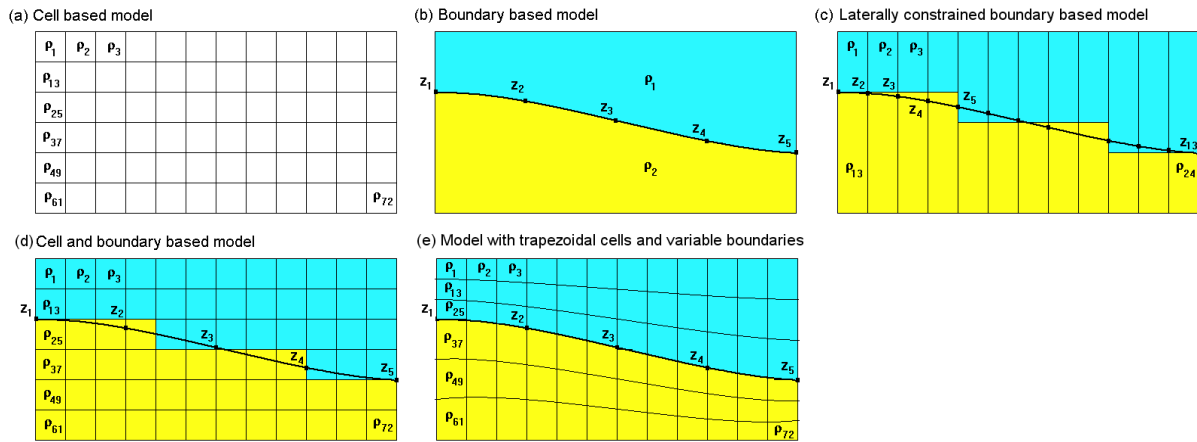


Figure 12. The different models for the subsurface used in the interpretation of data from 2-D electrical imaging surveys. (a) A purely cell based model. (b) A purely boundary based model. (c) The laterally constrained model. (d) A combined cell based and boundary based model with rectangular cells, and (e) with boundary conforming trapezoidal cells.

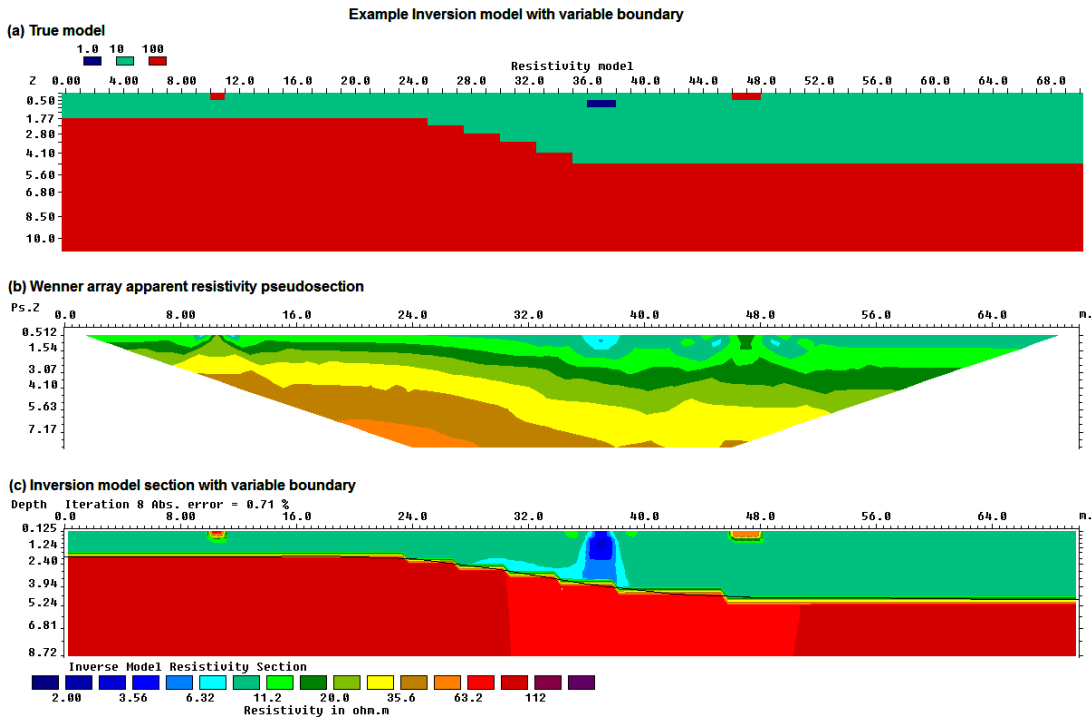


Figure 13. Example of a cell based model with a variable boundary. (a) The test model. (b) The apparent resistivity pseudosection. (c) The inversion model with a variable sharp boundary that is marked by a black line.

2 2-D electrical surveys – Data acquisition, presentation and arrays

2.1 Introduction

We have seen that the greatest limitation of the resistivity sounding method is that it does not take into account horizontal changes in the subsurface resistivity. A more accurate model of the subsurface is a two-dimensional (2-D) model where the resistivity changes in the vertical direction, as well as in the horizontal direction along the survey line. It is assumed that resistivity does not change in the direction that is perpendicular to the survey line. In many situations, particularly for surveys over elongated geological bodies, this is a reasonable assumption. In theory, a 3-D resistivity survey and interpretation model should be even more accurate. However, at the present time, 2-D surveys are the most practical economic compromise between obtaining very accurate results and keeping the survey costs down (Dahlin, 1996). Typical 1-D resistivity sounding surveys usually involve about 10 to 20 readings, while 2-D imaging surveys involve about 100 to 1000 measurements. In comparison, a 3-D survey might involve several thousand measurements.

The cost of a typical 2-D survey could be several times the cost of a 1-D sounding survey, and is probably comparable with a seismic refraction survey. In many geological situations, 2-D electrical imaging surveys can give useful results that are complementary to the information obtained by other geophysical methods. For example, seismic methods can map undulating interfaces well, but will have difficulty (without using advanced data processing techniques) in mapping discrete bodies such as boulders, cavities and pollution plumes. Ground radar surveys can provide more detailed pictures but have very limited depth penetration in areas with conductive unconsolidated sediments, such as clayey soils. Two-dimensional electrical surveys can be used in conjunction with seismic or GPR surveys as they provide complementary information about the subsurface.

2.2 Field survey method - instrumentation and measurement procedure

Two-dimensional electrical imaging/tomography surveys are usually carried out using a large number of electrodes, 25 or more, connected to a multi-core cable (Griffiths and Barker, 1993). A resistivity meter system with an internal microprocessor controlled circuitry together with an electronic switching unit is commonly used to automatically select the relevant four electrodes for each measurement (Figure 14). At present, field techniques and equipment to carry out 2-D resistivity surveys are fairly well developed. The necessary field equipment is commercially available from a number of companies. These systems typically costs from about US\$15,000 upwards. Some institutions have even constructed “home-made” manually operated switching units at a nominal cost by using a seismic cable as the multi-core cable!

Figure 14 shows the typical setup for a 2-D survey with a number of electrodes along a straight line attached to a multi-core cable. Normally a constant spacing between adjacent electrodes is used. The multi-core cable is attached to an integrated resistivity meter system that includes an electronic switching unit. The sequence of measurements to take, the type of array used and other survey parameters (such the current to use) is normally transferred to an internal microprocessor system within the resistivity meter from a personal computer. After reading the control file, the control program then automatically selects the appropriate electrodes for each measurement.

In a typical survey, most of the fieldwork is in laying out the cable and electrodes. After that, the measurements are taken automatically and stored in the resistivity meter system. Most of the survey time is spent waiting for the resistivity meter to complete the set of measurements!

To obtain a good 2-D picture of the subsurface, the coverage of the measurements must be 2-D as well. As an example, Figure 14 shows a possible sequence of measurements for the Wenner electrode array for a system with 20 electrodes. In this example, the spacing between adjacent electrodes is “ a ”. The first step is to make all the possible measurements with the Wenner array with an electrode spacing of “ $1a$ ”. For the first measurement, electrodes number 1, 2, 3 and 4 are used. Notice that electrode 1 is used as the first current electrode C1, electrode 2 as the first potential electrode P1, electrode 3 as the second potential electrode P2 and electrode 4 as the second current electrode C2. For the second measurement, electrodes number 2, 3, 4 and 5 are used for C1, P1, P2 and C2 respectively. This is repeated down the line of electrodes until electrodes 17, 18, 19 and 20 are used for the last measurement with “ $1a$ ” spacing. For a system with 20 electrodes, note that there are 17 ($20 - 3$) possible measurements with “ $1a$ ” spacing for the Wenner array.

After completing the sequence of measurements with “ $1a$ ” spacing, the next sequence of measurements with “ $2a$ ” electrode spacing is made. First electrodes 1, 3, 5 and 7 are used for the first measurement. The electrodes are chosen so that the spacing between adjacent electrodes is “ $2a$ ”. For the second measurement, electrodes 2, 4, 6 and 8 are used. This process is repeated down the line until electrodes 14, 16, 18 and 20 are used for the last measurement with spacing “ $2a$ ”. For a system with 20 electrodes, note that there are 14 ($20 - 2 \times 3$) possible measurements with “ $2a$ ” spacing.

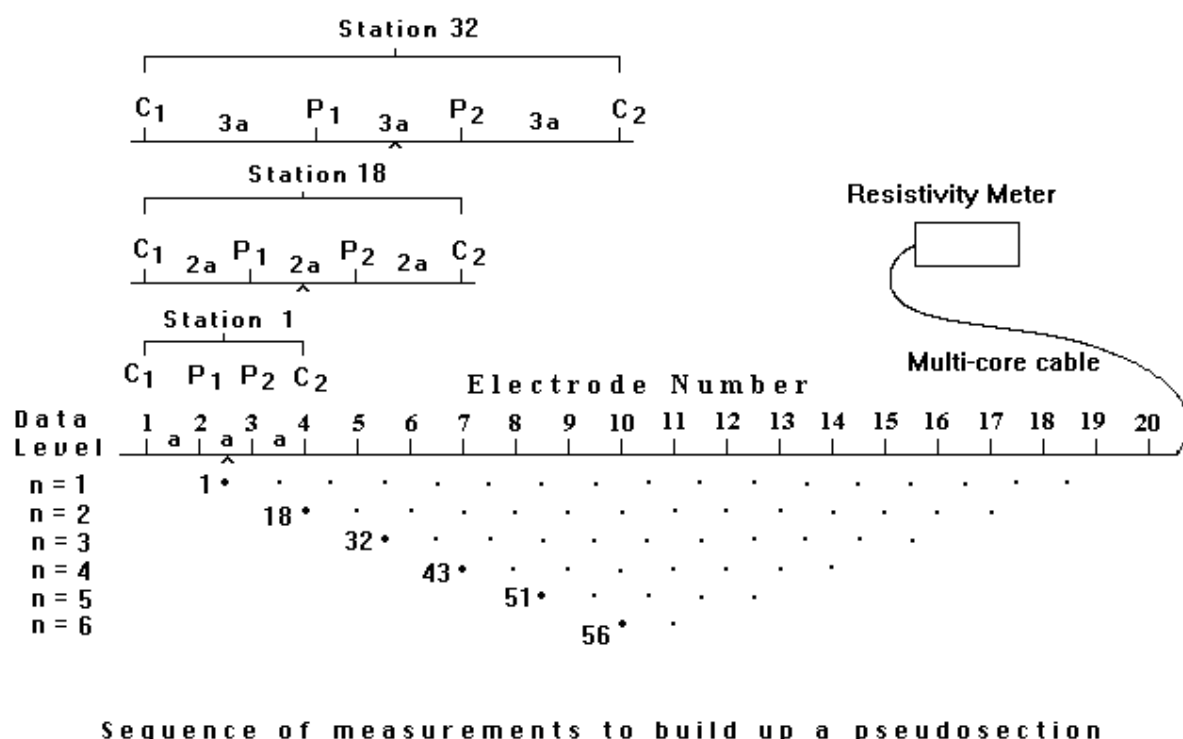


Figure 14. The arrangement of electrodes for a 2-D electrical survey and the sequence of measurements used to build up a pseudosection.

The same process is repeated for measurements with “ $3a$ ”, “ $4a$ ”, “ $5a$ ” and “ $6a$ ” spacings. To get the best results, the measurements in a field survey should be carried out in a systematic manner so that, as far as possible, all the possible measurements are made. This will affect the quality of the interpretation model obtained from the inversion of the apparent resistivity measurements (Dahlin and Loke, 1998).

Note that as the electrode spacing increases, the number of measurements decreases. The number of measurements that can be obtained for each electrode spacing, for a given number of electrodes along the survey line, depends on the type of array used. The Wenner array gives the smallest number of possible measurements compared to the other common arrays that are used in 2-D surveys.

The survey procedure with the pole-pole array is similar to that used for the Wenner array. For a system with 20 electrodes, firstly 19 of measurements with a spacing of “ $1a$ ” are made, followed by 18 measurements with “ $2a$ ” spacing, followed by 17 measurements with “ $3a$ ” spacing, and so on.

For the dipole-dipole, Wenner-Schlumberger and pole-dipole arrays (Figure 1.4), the survey procedure is slightly different. As an example, for the dipole-dipole array, the measurement usually starts with a spacing of “ $1a$ ” between the C1-C2 (and also the P1-P2) electrodes. The first sequence of measurements is made with a value of 1 for the “ n ” factor (which is the ratio of the distance between the C1-P1 electrodes to the C1-C2 dipole length), followed by “ n ” equals to 2 while keeping the C1-C2 dipole pair spacing fixed at “ $1a$ ”. When “ n ” is equals to 2, the distance of the C1 electrode from the P1 electrode is twice the C1-C2 dipole length. For subsequent measurements, the “ n ” spacing factor is usually increased to a maximum value of about 6, after which accurate measurements of the potential are difficult due to very low potential values. To increase the depth of investigation, the spacing between the C1-C2 dipole pair is increased to “ $2a$ ”, and another series of measurements with different values of “ n ” is made. If necessary, this can be repeated with larger values of the spacing of the C1-C2 (and P1-P2) dipole pairs. A similar survey technique can be used for the Wenner-Schlumberger and pole-dipole arrays where different combinations of the “ a ” spacing and “ n ” factor can be used.

It should be noted that in practice the sequence of measurements to take should be arranged so that electrode polarization effects do not occur (Dahlin, 2000). This happens when an electrode that was used as a current electrode is used as potential electrode in a following measurement within a short time.

One technique used to extend horizontally the area covered by the survey, particularly for a system with a limited number of electrodes, is the roll-along method. After completing the sequence of measurements, the cable is moved past one end of the line by several unit electrode spacings. All the measurements that involve the electrodes on part of the cable that do not overlap the original end of the survey line are repeated (Figure 15).

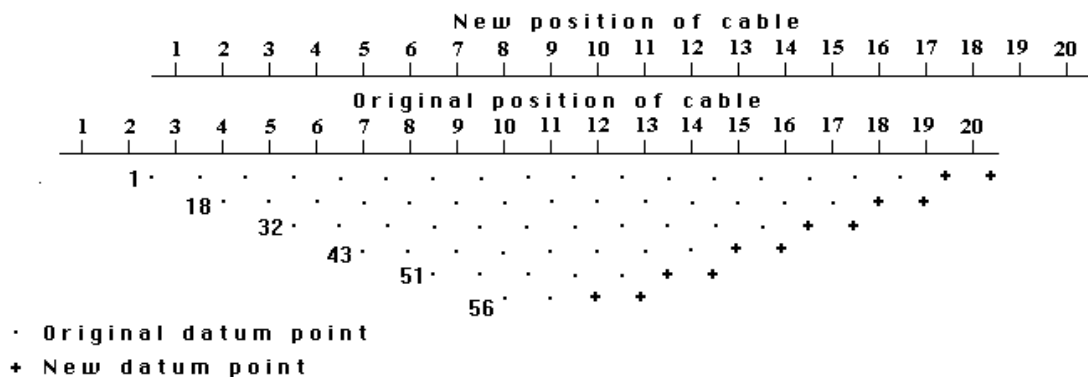


Figure 15. The use of the roll-along method to extend the area covered by a 2-D survey.

2.3 Available field instruments

Over the last 15 years, there has been a steady growth in the number of commercial companies that offer systems for resistivity imaging surveys. The ones that I have come across are listed below in alphabetical order together with the web site address where available.

Manufacturer	Instrument Type		
	Static	Dynamic	IP
Abem Instruments, Sweden (www.abem.se)	x		Y
Advanced Geophysical Instruments, USA (www.agiusa.com)	x		Y
Campus Geophysical Instruments, UK	x		Y
Geofyzika., Czech Republic (www.geofyzika.com)	x		
GF Instruments, Czech Republic (www.gfinstruments.cz)	x		Y
Geometrics, USA (www.geometrics.com)		x	
Geolog, Germany (www.geolog2000.de)	x		
IDS Scintrex, Canada (www.ids-detection.com)	x		Y
Iris Instruments, France (www.iris-instruments.com)	x	x	Y
OYO, Japan	x		
Pasi Geophysics, Italy (www.pasigeophysics.com)	x		Y
MAE srl, Italy (www.mae-srl.it)	x		Y

Most of the above manufacturers have sub-agents in different countries, and there are probably a few others that are not on the list, particularly more recent Russian and Chinese models. A few academic and research institutions have designed their own systems, for example the British Geological Survey has built an electrostatic based mobile system as well as an automatic system for time-lapse surveys.

The instrument type can be divided into two broad categories, static and dynamic systems. Most instruments are of the static type where many electrodes are connected to a multi-electrode cable and planted into the ground during the survey. A typical static system is the Abem Lund system shown in Figure 16. One common configuration is a split spread type of cable connection to the switching unit at the center to reduce the individual cable length and weight. The weight of a cable roll is directly proportional to the number of nodes and the spacing between the nodes! A common spacing used for most engineering and environmental surveys is 5 meters. Most systems come with a minimum of 28 nodes, with some system having up to 128 nodes or more! The Lund system is a little unusual in that there are 4 individual cables. Most systems use a 2 cables arrangement. The static systems can be further divided into two sub-categories depending on the arrangement for the switching of the electrodes. Most of the systems house the switches in a single unit and uses a cable with many individual wires connected to each node. Typical examples are the Abem Lund and Campus systems. Another arrangement is to have a small switching unit at each electrode and a cable with the minimum number of wires. One early example is the Campus MRT system (Griffiths and Turnbull, 1985). More recent examples are the PASI and Iris Syscal systems.

There have been two new and interesting developments in the resistivity meter systems. One is the addition of I.P. capability. However, the usefulness of the I.P. data from most multi-electrode systems is of limited use. Most systems use a battery power source that cannot deliver enough current (usually less than 1 ampere) for reliable I.P. signals, so the I.P.

data is often extremely noisy. However, there have been recent developments to reduce the noise in the I.P. measurements (Dahlin and Leroux, 2012).

The second new development is multi-channel measuring systems. In such a system, a number of potential measurements can be simultaneously made for a single pair of current electrodes. This could significantly reduce the survey time. With certain array configurations, a single 2-D survey line could involve thousands of measurements. The major part of the survey time is waiting for a single channel instrument to complete the measurements that could take more than several hours! The IP and multi-channel capability are relatively new developments, so you will need to check the manufacturer's web site to get the latest information.

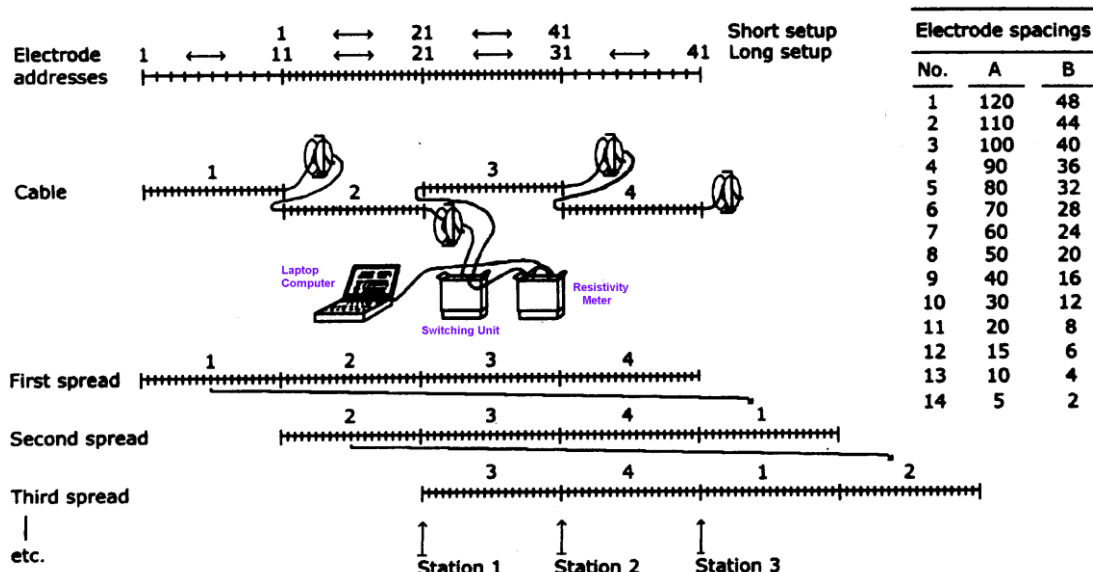


Figure 16. Sketch outline of the ABEM Lund Imaging System. Each mark on the cables indicates an electrode position (Dahlin, 1996). The cables are placed along a single line (the sideways shift in the figure is only for clarity). This figure also shows the principle of moving cables when using the roll-along technique. The total layout length depends on the spacing between the nodes, but is usually between 160 meters and 800 meters.

Static systems use a large number of nodes to get a wide data coverage. In contrast, dynamic systems use a small number of nodes but move the entire system to obtain a wide coverage. An example of such a system designed by Aarhus University in Denmark (Sorenson, 1996) is shown in Figure 17. A 100 meters cable with nine heavy cylindrical electrodes is pulled by a small vehicle. Two of the electrodes are used as current electrodes, while six of them are used for the potential measurements and one is used as a ground electrode. This system relies on the current being injected into the ground by direct contact, so it can only be used in open ground, such as farmlands in Northern Europe. A Wenner-Schlumberger type of arrangement (Figure 4) is used but with non-integer “*n*” values for some of the measurements. Another mobile system that does not require direct contact with the ground but uses capacitive coupling (Gerard and Tabbagh, 1991; Shima *et al.*, 1996, Panissod *et al.*, 1998; Loke *et al.*, 2011a) to induce the flow of current in the ground. This system can be used in areas that are paved, such as roads and city areas. One such system shown in Figure 18 is the Geometrics OhmMapper system where a cable with 4 to 6 electrodes is attached to a measuring unit is pulled by a single operator. The dipole-dipole type of arrangement is used but with non-integer “*n*” values for some measurements.

One of main problems faced by mobile systems on land is to get sufficient current to flow into the ground. Direct contact systems such as the Aarhus Pulled Array System can only be used in areas with open ground. The capacitive coupling type does not require direct ground contact and thus can be used in many areas where normal resistivity surveying systems cannot be used (for example in built-up areas) but has the problem of a more limited depth of penetration due to the limited amount of current that can be induced into the ground compared to direct contact systems. An underwater environment provides an almost ideal situation for a direct contact type of mobile system since there is no problem in obtaining good electrode contact! Figure 19 shows a possible arrangement for an underwater mobile surveying system where a cable with a number of nodes is pulled along the river/lake/sea bottom by a boat. Two of the nodes are used as current electrodes, while the rest are used as potential electrodes. An example of such an underwater survey is described in section 7.9. If this system is coupled with a multi-channel resistivity meter, the survey can be carried out very rapidly. Shallow seismic reflection surveys are frequently used in rivers/lakes/marine environments for engineering site surveys. A mobile resistivity survey might be a useful addition in some situations, such as in seismically opaque areas. In theory, both surveys can be carried out simultaneously to reduce costs.

The arrangement in Figure 19 has the cable dragged along the sea or river bed. This places the electrodes close to the targets of interest but has the disadvantage that the cable can get snagged by obstructions on the bottom. Another system uses a cable floating on the water surface (section 7.9) but this has the disadvantage that most of the current flows within the water layer, and very little goes into the sub-bottom materials which are being mapped. To avoid both problems, some recent surveys use a submerged cable that is suspended about a meter above the water bottom.

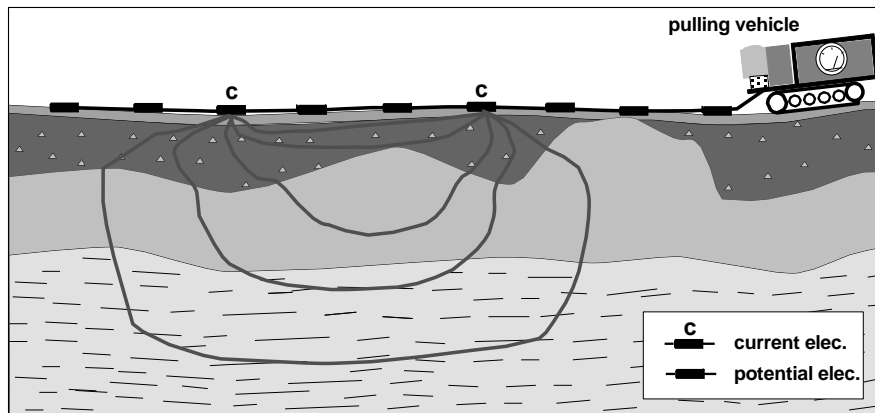


Figure 17. The Aarhus Pulled Array System. The system shown has two current (C) electrodes and six potential electrodes (Christensen and Sørensen 1998, Bernstein and Dahlin 1999).

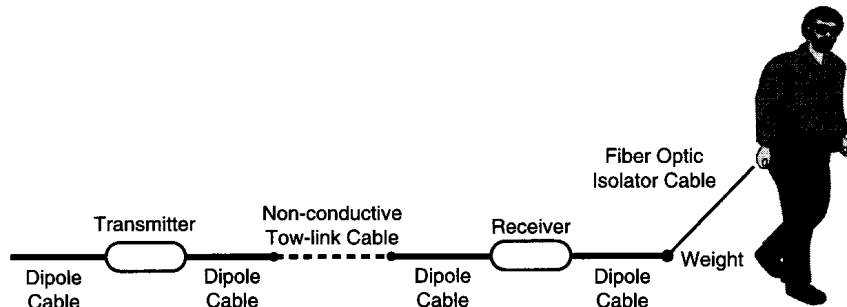


Figure 18. The Geometrics OhmMapper system using capacitive coupled electrodes. (Courtesy of Geometrics Inc.).

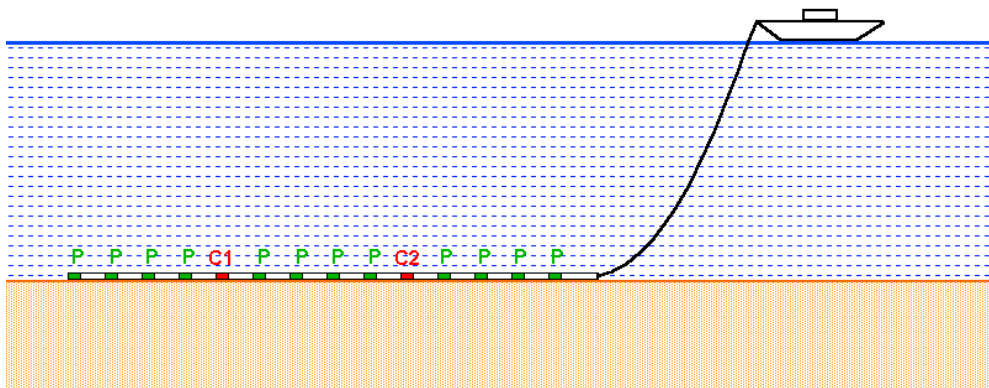


Figure 19. Schematic diagram of a possible mobile underwater survey system. The cable has two fixed current electrodes and a number of potential electrodes so that measurements can be made at different spacings. The above arrangement uses the Wenner-Schlumberger type of configuration. Other configurations, such as the gradient array, can also be used.

2.4 Pseudosection data plotting method

To plot the data from a 2-D imaging survey, the pseudosection contouring method is normally used. In this case, the horizontal location of the data point is placed at the mid-point of the set of electrodes used to make that measurement. The vertical location of the plotting point is placed at a distance that is proportional to the separation between the electrodes. For I.P. surveys using the dipole-dipole array, one common method is to place the plotting point at the intersection of two lines starting from the mid-point of the C1-C2 and P1-P2 dipole pairs with a 45° angle to the horizontal. It is important to emphasize that this is merely a plotting convention, and it does not imply that the depth of investigation is given by the point of intersection of the two 45° angle lines (it certainly does not imply the current flow or isopotential lines have a 45° angle with the surface). Surprisingly, this is still a common misconception, particularly in North America!

Another method is to place the vertical position of the plotting point at the median depth of investigation (Edwards, 1977), or pseudodepth, of the electrode array used. This pseudodepth value is based on the sensitivity values or Frechet derivative for a homogeneous half space. Since it appears to have some mathematical basis, this method that is used in plotting the pseudosections in the later parts of these notes. The pseudosection plot obtained by contouring the apparent resistivity values is a convenient means to display the data.

The pseudosection gives a very approximate picture of the true subsurface resistivity distribution. However the pseudosection gives a distorted picture of the subsurface because the shapes of the contours depend on the type of array used as well as the true subsurface resistivity (Figure 20). The pseudosection is useful as a means to present the measured apparent resistivity values in a pictorial form, and as an initial guide for further quantitative interpretation. One common mistake made is to try to use the pseudosection as a final picture of the true subsurface resistivity. As Figure 20 shows, different arrays used to map the same region can give rise to very different contour shapes in the pseudosection plot. Figure 20 also gives you an idea of the data coverage that can be obtained with different arrays. Note that the pole-pole array gives the widest horizontal coverage, while the coverage obtained by the Wenner array decreases much more rapidly with increasing electrode spacing.

One useful practical application of the pseudosection plot is for picking out bad apparent resistivity measurements. Such bad measurements usually stand out as points with unusually high or low values.

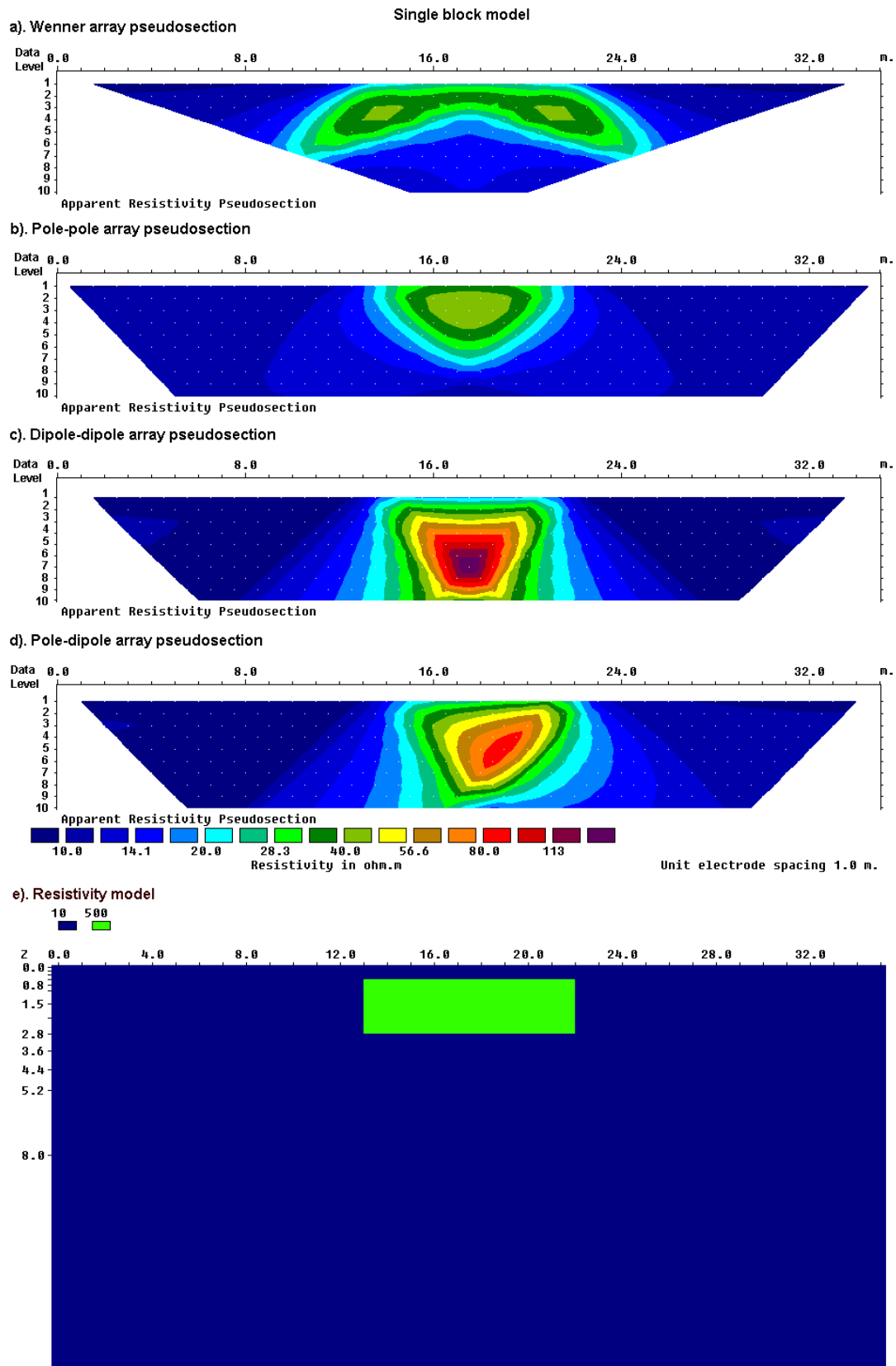


Figure 20. The apparent resistivity pseudosections from 2-D imaging surveys with different arrays over a rectangular prism.

2.5 A comparison of the different electrode arrays

As shown earlier in Figure 20, the shape of the contours in the pseudosection produced by the different arrays over the same structure can be very different. The arrays most commonly used for resistivity surveys were shown in Figure 4. The choice of the “best” array for a field survey depends on the type of structure to be mapped, the sensitivity of the resistivity meter and the background noise level. In practice, the arrays that are most commonly used for 2-D imaging surveys are the (a) Wenner, (b) dipole-dipole (c) Wenner-Schlumberger (d) pole-pole and (d) pole-dipole. Among the characteristics of an array that should be considered are (i) the depth of investigation, (ii) the sensitivity of the array to vertical and horizontal changes in the subsurface resistivity, (iii) the horizontal data coverage and (iv) the signal strength.

2.5.1 The Frechet derivative for a homogeneous half-space

The first two characteristics can be determined from the sensitivity function of the array for a homogeneous earth model. The sensitivity function basically tells us the degree to which a change in the resistivity of a section of the subsurface will influence the potential measured by the array. The higher the value of the sensitivity function, the greater is the influence of the subsurface region on the measurement. Mathematically, the sensitivity function is given by the Frechet derivative (McGillivray and Oldenburg, 1990). Consider the simplest possible array configuration shown in Figure 21 with just one current located at the origin $(0,0,0)$ and one potential electrode located at $(a,0,0)$, i.e. both electrodes are on the ground surface and they are “ a ” meters apart.. We inject 1 ampere of current into the ground through the C1 current electrode that results in a potential ϕ observed at the potential P1 electrode. Suppose we were to change the resistivity within a small volume of the ground located at (x,y,z) by a small amount, say $\delta\rho$. What would be the corresponding change in the potential, $\delta\phi$, measured at P1? It can be shown (Loke and Barker, 1995) that this is given by

$$\delta\phi = \frac{\delta\rho}{\rho^2} \int_V \nabla\phi \cdot \nabla\phi' d\tau \quad (2.1)$$

where the change in the resistivity has a constant value in a small volume element $d\tau$ and zero elsewhere. The parameter ϕ' is the potential resulting from a current electrode located at the position of the P1 potential electrode.

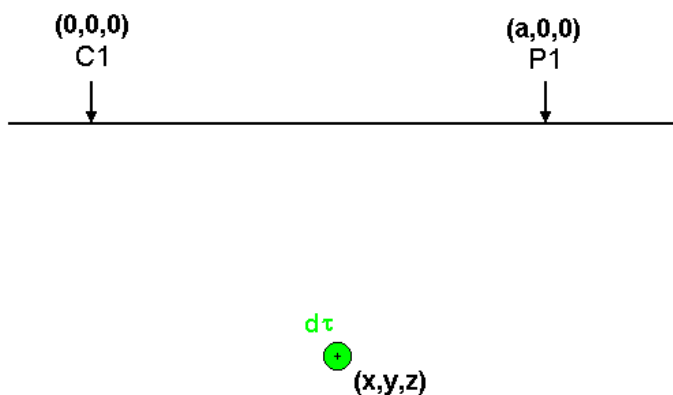


Figure 21. The parameters for the sensitivity function calculation at a point (x,y,z) within a half-space. A pole-pole array with the current electrode at the origin and the potential electrode “ a ” meters away is shown.

For the special case of a homogeneous half-space, the potential ϕ at a point in the half-space due to a unit current source on the surface has a relatively simple form, which is

$$\phi = \frac{\rho}{2\pi(x^2 + y^2 + z^2)^{0.5}} , \text{ and similarly}$$

$$\phi' = \frac{\rho}{2\pi[(x-a)^2 + y^2 + z^2]^{0.5}} \quad (2.2)$$

After differentiating the above equations to obtain the divergence, and substituting into (2.1) we get

$$\frac{\delta\phi}{\delta\rho} = \int_V \frac{1}{4\pi^2} \cdot \frac{x(x-a) + y^2 + z^2}{[x^2 + y^2 + z^2]^{1.5} [(x-a)^2 + y^2 + z^2]^{1.5}} dx dy dz \quad (2.3)$$

The 3-D Frechet derivative is then given by the term within the integral, i.e.

$$F_{3D}(x, y, z) = \frac{1}{4\pi^2} \cdot \frac{x(x-a) + y^2 + z^2}{[x^2 + y^2 + z^2]^{1.5} [(x-a)^2 + y^2 + z^2]^{1.5}} \quad (2.4)$$

This gives the Frechet derivative or sensitivity function for the pole-pole array consisting of just one current and one potential electrode. To obtain the Frechet derivative for a general four electrodes array, we need to just add up the contributions from the four current-potential pairs, just as we have done earlier for the potential in equation (1.8).

2.5.2 A 1-D view of the sensitivity function - depth of investigation

In resistivity sounding surveys, it is well known as the separation between the electrodes is increased, the array senses the resistivity of increasingly deeper layers. One common question is – What is a depth of investigation of an array? One quantitative means to put a numerical value for the depth of investigation is by using the sensitivity function or Frechet derivative of the array. In resistivity sounding surveys, the subsurface is assumed to consist of horizontal layers. What we want to determine is the change in the potential as measured by the array on the surface if the resistivity of a thin horizontal is changed. For a horizontal layer, the x and y limits of the layer extends from $-\infty$ to $+\infty$. Thus the sensitivity function for a thin horizontal layer is obtained by integrating the 3D sensitivity function given in equation (2.4) in the x and y directions, i.e.

$$F_{1D}(z) = \frac{1}{4\pi^2} \int_{-\infty}^{+\infty} \int_{-\infty}^{+\infty} \frac{x(x-a) + y^2 + z^2}{[x^2 + y^2 + z^2]^{1.5} [(x-a)^2 + y^2 + z^2]^{1.5}} dx dy$$

The above equation has a simple analytical solution (Roy and Apparao, 1971), which is given by

$$F_{1D}(z) = \frac{2}{\pi} \cdot \frac{z}{(a^2 + 4z^2)^{1.5}} \quad (2.5)$$

The above function is also known as the depth investigation characteristic and has been used by many authors to determine the properties of various arrays in resistivity sounding surveys (Edwards, 1977; Barker, 1991; Merrick, 1997). Figure 22a shows a plot of this function. Note that it starts from zero and then increases to a maximum value at a depth of about $0.35a$ and then decreases asymptotically to zero. Some authors have used the maximum point as the depth of investigation of the array. However, Edwards (1977) and Barker (1991) have shown that a more robust estimate is the "median depth of investigation". It is the depth above which the area under the curve is equal to half the total area under the curve. In layman's terms, the

upper section of the earth above the "median depth of investigation" has the same influence on the measured potential as the lower section. This tells us roughly how deep we can see with an array. This depth does not depend on the measured apparent resistivity or the resistivity of the homogeneous earth model. It should be noted that the depths are strictly only valid for a homogeneous earth model, but they are probably good enough for planning field surveys. If there are large resistivity contrasts near the surface, the actual depth of investigation could be somewhat different.

The sensitivity function for other arrays can be determined by adding up the contributions from the appropriate four pairs of current-potential electrodes. Figure 22b shows the sensitivity function plot for the Wenner (alpha) array. Note that the curve around the maximum is narrower for the Wenner array compared with the pole-pole array. This implies that the Wenner array has a better vertical resolution than the pole-pole array.

Table 2 gives the median depth of investigation for the different arrays. To determine the maximum depth mapped by a particular survey, multiply the maximum "a" electrode spacing, or maximum array length "L", by the appropriate depth factor given in Table 2. For example, if the maximum electrode "a" spacing used by the Wenner array is 100 meters (or maximum L 300 meters), then the maximum depth mapped is about 51 meters. For the dipole-dipole, pole-dipole and Wenner-Schlumberger arrays, the "n" factor (Figure 4) must also be taken into consideration. For the arrays with four active electrodes (such as the dipole-dipole, Wenner and Wenner-Schlumberger arrays), it is probably easier to use the total array length "L". As an example, if a dipole-dipole survey uses a maximum value of 10 meters for "a" and a corresponding maximum value of 6 for n, then the maximum "L" value is 80 meters. This gives a maximum depth of investigation of 80×0.216 or about 17 meters.

Table 2 also includes the geometric factor for the various arrays for an "a" spacing of 1.0 meter. The inverse of the geometric factor gives an indication of the voltage that would be measured between the P1 and P2 potential electrodes. The ratio of this potential compared to the Wenner alpha array is also given, for example a value of 0.01 means that the potential is 1% of the potential measured by the Wenner alpha array with the same "a" spacing.

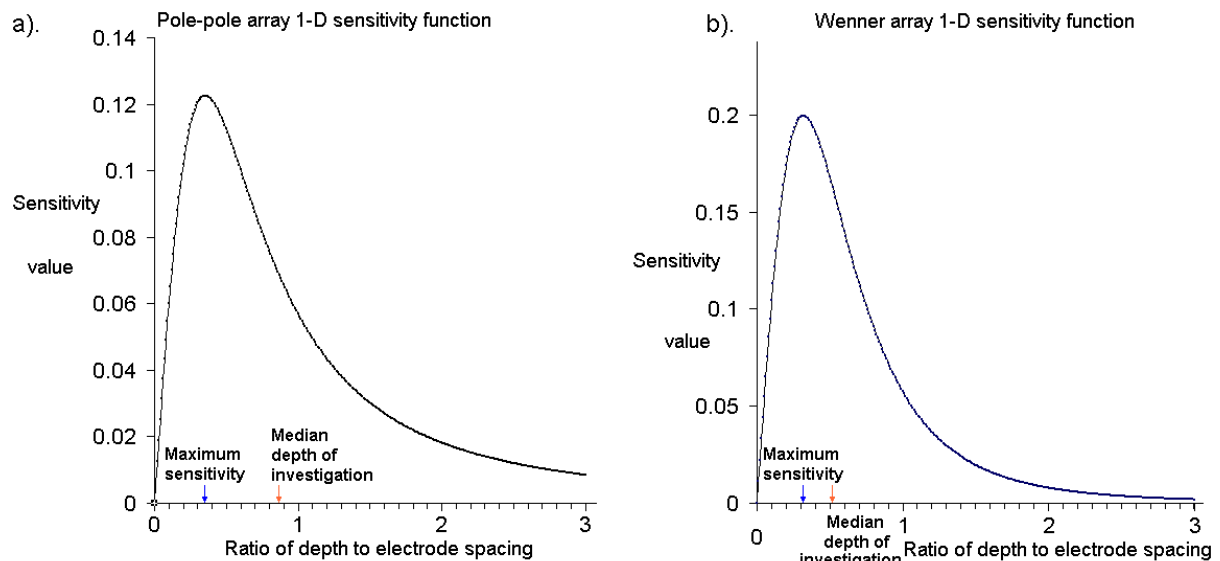


Figure 22. A plot of the 1-D sensitivity function. (a) The sensitivity function for the pole-pole array. Note that the median depth of investigation (red arrow) is more than twice the depth of maximum sensitivity (blue arrow). (b) The sensitivity function and median depth of investigation for the Wenner array.

Table 2. The median depth of investigation (z_e) for the different arrays (Edwards, 1977). L is the total length of the array. Note identical values of z_e/a for the Wenner-Schlumberger and pole-dipole arrays. Please refer to Figure 4 for the arrangement of the electrodes for the different arrays. The geometric factor is for an "a" value of 1.0 meter. For the pole-dipole array, the array length 'L' only takes into account the active electrodes C1, P1 and P2 (i.e. it does not take into account the remote C2 electrode).

	z_e/a	z_e/L	Geometric Factor	Inverse Geometric Factor (Ratio)
Wenner Alpha	0.519	0.173	6.2832	0.15915 (1.0000)
Wenner Beta	0.416	0.139	18.850	0.05305 (0.3333)
Wenner Gamma	0.594	0.198	9.4248	0.10610 (0.6667)
Dipole-dipole	n = 1	0.416	0.139	18.850
	n = 2	0.697	0.174	75.398
	n = 3	0.962	0.192	188.50
	n = 4	1.220	0.203	376.99
	n = 5	1.476	0.211	659.73
	n = 6	1.730	0.216	1055.6
	n = 7	1.983	0.220	1583.4
	n = 8	2.236	0.224	2261.9
Equatorial dipole-dipole				
	n = 1	0.451	0.319	21.452
	n = 2	0.809	0.362	119.03
	n = 3	1.180	0.373	367.31
	n = 4	1.556	0.377	841.75
Wenner - Schlumberger				
	n = 1	0.519	0.173	6.2832
	n = 2	0.925	0.186	18.850
	n = 3	1.318	0.189	37.699
	n = 4	1.706	0.190	62.832
	n = 5	2.093	0.190	94.248
	n = 6	2.478	0.191	131.95
	n = 7	2.863	0.191	175.93
	n = 8	3.247	0.191	226.19
	n = 9	3.632	0.191	282.74
	n = 10	4.015	0.191	345.58
Pole-dipole	n = 1	0.519	0.260	12.566
	n = 2	0.925	0.308	37.699
	n = 3	1.318	0.330	75.398
	n = 4	1.706	0.341	125.66
	n = 5	2.093	0.349	188.50
	n = 6	2.478	0.354	263.89
	n = 7	2.863	0.358	351.86
	n = 8	3.247	0.361	452.39
Pole-Pole		0.867		6.28319
				0.15915 (1.0000)

2.5.3 A 2-D view of the sensitivity function

The plot of the 1-D sensitivity function in Figure 22 suggests that the sensitivity of an array to the topmost layer is very small. The plot actually gives the *net* contribution calculated by summing up the contribution for all x - and y -values at the same depth, and it hides a multitude of effects. The *net* contribution for the topmost strip is small only if the ground is completely homogeneous. If it is not homogeneous, the results can be very different.

To study the suitability of the different arrays for 2-D surveys, we need to go one step beyond the simple 1-D sensitivity function, i.e. the 2-D sensitivity function. In this case, for a particular (x,z) location, we add up the contribution from all points for y -values ranging from $+\infty$ to $-\infty$. This involves the integration of the 3-D sensitivity function in equation (2.4) with respect to y , which is

$$F_{2D}(x,z) = \frac{1}{4\pi^2} \int_{-\infty}^{+\infty} \frac{x(x-a) + y^2 + z^2}{[x^2 + y^2 + z^2]^{1.5} [(x-a)^2 + y^2 + z^2]^{1.5}} dy$$

This integral has an analytic solution (Loke and Barker 1995) that is given in terms of elliptic integrals. The complete solution is

$$F_{2D}(x,z) = \frac{2}{\alpha\beta^2} \left[\frac{\alpha^2 E(k) - \beta^2 K(k)}{(\alpha^2 - \beta^2)} - \frac{\gamma [(\alpha^2 + \beta^2)E(k) - 2\beta^2 K(k)]}{(\alpha^2 - \beta^2)^2} \right] \quad (2.6)$$

where

$$k = \frac{(\alpha^2 - \beta^2)^{0.5}}{\alpha}$$

for $x > 0.5a$,

$$\alpha^2 = x^2 + z^2, \beta^2 = (x-a)^2 + z^2, \gamma = xa$$

and for $x < 0.5a$,

$$\beta^2 = x^2 + z^2, \alpha^2 = (x-a)^2 + z^2, \gamma = a(x-a)$$

and for $x = 0.5a$,

$$F_{2D}(x,z) = \pi \left[\frac{1}{2\alpha^3} - \frac{3a^2}{16\alpha^5} \right], \text{ with } \alpha = 0.25a^2 + z^2$$

As an example, Figure 23a shows the contour pattern for the sensitivity function of the Wenner array. The sensitivity function shows the degree to which a change in the resistivity of a section of the subsurface will influence the potential measured by the array. The higher the value of the sensitivity function, the greater is the influence of the subsurface region on the measurement. Note that for all the three arrays, the highest sensitivity values are found near the electrodes. At larger distances from the electrodes, the contour patterns are different for the different arrays. The difference in the contour pattern of the sensitivity function plot helps to explain the response of the different arrays to different types of structures.

In the following plots of the sensitivity sections, the distance between the first electrode and the last electrode (for example the C1 and C2 in the case of the Wenner alpha array in Figure 23a) is normalized to 1.0 meter. To avoid the singularities at the electrodes, the sensitivity values are shown from a depth of 0.025 meter downwards to 1.0 meter. In all the sensitivity section diagrams, the location of the plotting point used in the pseudosection is marked by a small black cross.

2.5.4 Wenner array

This is a robust array that was popularized by the pioneering work carried by The University of Birmingham research group (Griffiths and Turnbull, 1985; Griffiths, Turnbull and Olayinka, 1990). Many of the early 2-D surveys were carried out with this array. The "normal" Wenner array is technically the Wenner Alpha array. For a four-electrode array, there are three possible permutations of the positions of the electrodes (Carpenter and Habberjam, 1956). In Figure 23a, the sensitivity plot for the Wenner Alpha array has almost horizontal contours beneath the center of the array. Because of this property, the Wenner array is relatively sensitive to vertical changes in the subsurface resistivity below the center of the array. However, it is less sensitive to horizontal changes in the subsurface resistivity. In general, the Wenner array is good in resolving vertical changes (i.e. horizontal structures), but relatively poor in detecting horizontal changes (i.e. narrow vertical structures). In Table 2, the median depth of investigation for the Wenner Alpha array is approximately 0.5 times the " a " spacing used. Compared to other arrays, the Wenner Alpha array has a moderate depth of investigation. The signal strength is inversely proportional to the geometric factor used to calculate the apparent resistivity value for the array (Table 2). The geometric factor for the Wenner array is $2\pi a$. This is smaller than the geometric factor for other arrays. Among the common arrays, the Wenner array has the strongest signal strength. This can be an important factor if the survey is carried in areas with high background noise. One disadvantage of this array for 2-D surveys is the relatively poor horizontal coverage as the electrode spacing is increased (Figure 20). This could be a problem if you use a system with a relatively small number of electrodes.

Note that the sensitivity section shows large negative values near the surface between the C1 and P1 electrodes, as well as between the C2 and P2 electrodes. This means that if a small body with a higher resistivity than the background medium is placed in these negative zones, the measured apparent resistivity value will decrease. This phenomenon is also known as an "anomaly inversion". In comparison, if the high resistivity body is placed between the P1 and P2 electrodes where there are large positive sensitivity values, the measured apparent resistivity will increase. This is the basis of the offset Wenner method by Barker (1992) to reduce the effects of lateral variations in resistivity sounding surveys.

The other two permutations of the Wenner array are the Wenner Beta and the Wenner Gamma arrays. The Wenner Beta array is in fact a special case of the dipole-dipole array where the spacings between the electrodes are the same. Thus this array will be discussed in the following section under the dipole-dipole array. The Wenner Gamma array has a relatively unusual arrangement where the current and potential electrodes are interleaved. The sensitivity section shows that the deepest regions mapped by this array are below the two outer electrodes (C1 and P2 in Figure 23c), and not below the center of the array.

2.5.5 Dipole-dipole array

This array has been, and is still, widely used in I.P. surveys because of the low EM coupling between the current and potential circuits. The arrangement of the electrodes is shown in Figure 4. The spacing between the current electrodes pair, C2-C1, is given as " a " which is the same as the distance between the potential electrodes pair P1-P2. This array has another factor marked as " n " in Figure 4. This is the ratio of the distance between the C1 and P1 electrodes to the C2-C1 (or P1-P2) dipole length " a ". For surveys with this array, the " a " spacing is initially kept fixed at the smallest unit electrode spacing and the " n " factor is increased from 1 to 2 to 3 until up to about 6 in order to increase the depth of investigation.

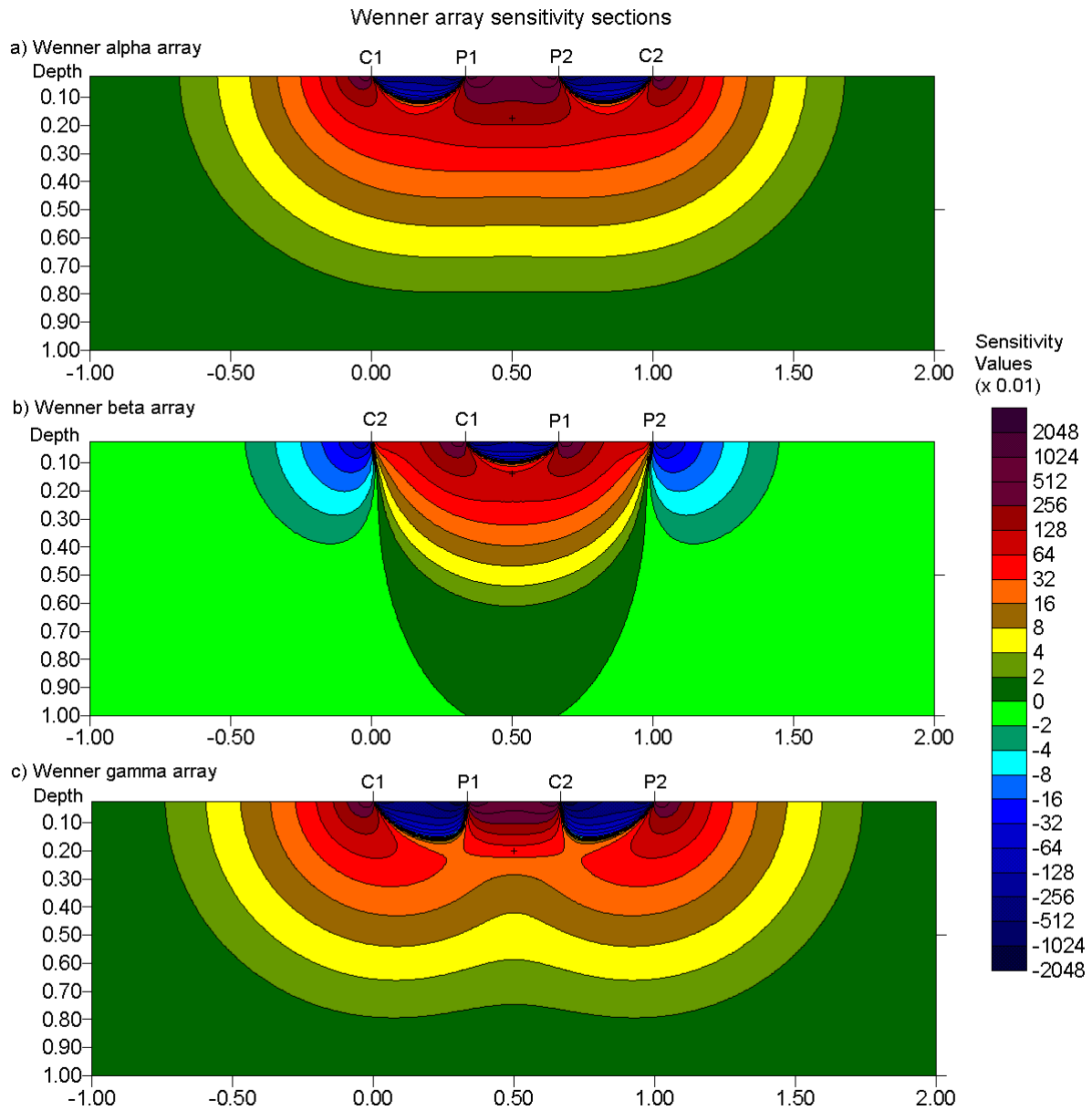


Figure 23. 2-D sensitivity sections for the Wenner array. The sensitivity sections for the (a) alpha, (b) beta and (c) gamma configurations.

Figure 24 shows the sensitivity sections for this array for "n" values ranging from 1 to 6. The largest sensitivity values are generally located between the C2-C1 dipole pair, as well as between the P1-P2 pair. This means that this array is most sensitive to resistivity changes below the electrodes in each dipole pair. As the "n" factor is increased, the high sensitivity values become increasingly more concentrated beneath the C1-C2 and P1-P2 dipoles, while the sensitivity values beneath the center of the array between the C1-P1 electrodes decreases. For "n" values of greater than 2, the sensitivity values at the pseudosection plotting point become negligible. The sensitivity contour pattern becomes almost vertical for "n" values greater than 2. Thus the dipole-dipole array is very sensitive to horizontal changes in resistivity, but relatively insensitive to vertical changes in the resistivity. Thus it is good in mapping vertical structures, such as dykes and cavities, but relatively poor in mapping horizontal structures such as sills or sedimentary layers. The median depth of investigation of this array depends on both the "a" spacing and the "n" factor (Table 2). In general, this array

has a shallower depth of investigation compared to the Wenner array, for example at $n=1$ the depth of investigation is $0.416a$ compared to $0.512a$ for the Wenner Alpha array.

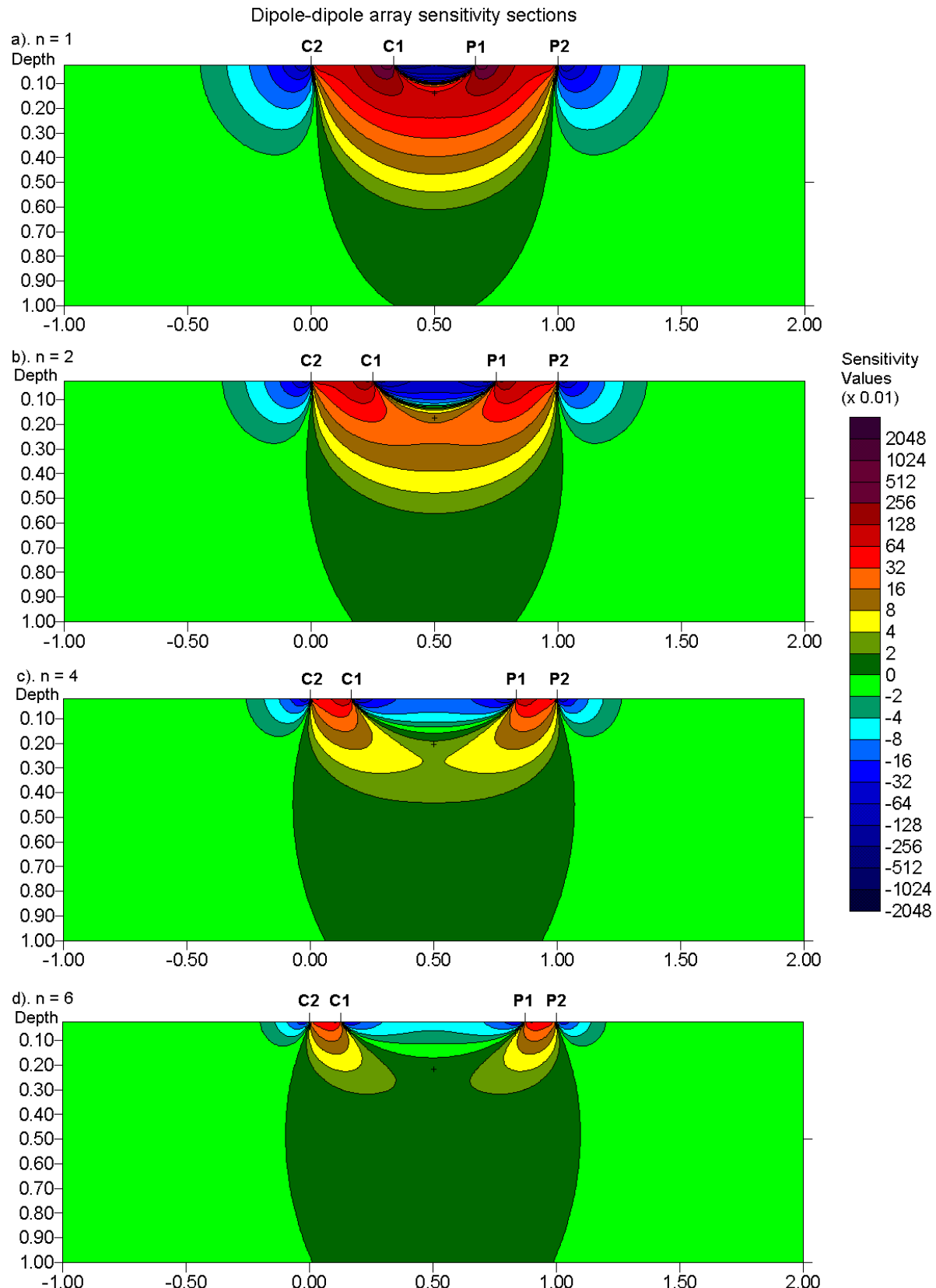


Figure 24. 2-D sensitivity sections for the dipole-dipole array. The sections with (a) $n=1$, (b) $n=2$, (c) $n=4$ and (d) $n=6$.

Due to the almost vertical pattern of the sensitivity contours, the depth of investigation (which a 1-D horizontal average of the sensitivity values) is not particularly meaningful for the dipole-dipole array for "n" values greater than 2. From experience with synthetic modeling and field data, the median depth of investigation might underestimate the depth of structures sensed by this array by about 20% to 30% for the large "n" factors. For 2-D surveys, this array has better horizontal data coverage than the Wenner (Figure 20). This can be an important advantage when the number of nodes available with the multi-electrode system is small.

One possible disadvantage of this array is the very low signal strength for large values of the "n" factor. The voltage is inversely proportional to the *cube* of the "n" factor. For the same current, the voltage measured by the resistivity meter drops by about 56 times when "n" is increased from 1 to 6 (Table 2). One method to overcome this problem is to increase the "a" spacing between the C1-C2 (and P1-P2) dipole pair to reduce the drop in the potential when the overall length of the array is increased to increase the depth of investigation. Figure 25 shows two different arrangements for the dipole-dipole array with the same array length but with different "a" and "n" factors. The signal strength of the array with the smaller "n" factor is about 28 times stronger than the one with the larger "n" factor.

To use this array effectively, the resistivity meter should have comparatively high sensitivity and very good noise rejection circuitry, and there should be good contact between the electrodes and the ground. With the proper field equipment and survey techniques, this array has been successfully used in many areas to detect structures such as cavities where the good horizontal resolution of this array is a major advantage.

The plotting location of the corresponding data point (based on the median depth of investigation) used in drawing the apparent resistivity pseudosection is also shown in Figure 24. Note that the pseudosection plotting point falls in an area with very low sensitivity values for "n" values of 4 and above. For the dipole-dipole array, the regions with the high sensitivity values are concentrated below the C1-C2 electrodes pair and below the P1-P2 electrodes pair. In effect, the dipole-dipole array gives minimal information about the resistivity of the region surrounding the plotting point, and the distribution of the data points in the pseudosection plot does not reflect the subsurface area mapped by the apparent resistivity measurements. Note that if the data point is plotted at the point of intersection of the two 45° angle lines drawn from the center of the two dipoles, it would be located at a depth of 0.7 units in Figure 24d (compared with 0.19 units given by the median depth of investigation method) where the sensitivity values are almost zero!

Loke and Barker (1996a) used an inversion model where the arrangement of the model blocks directly follows the arrangement of the pseudosection plotting points. This approach gives satisfactory results for the Wenner and Wenner-Schlumberger arrays where the pseudosection point falls in an area with high sensitivity values (Figure 23a and Figure 26). However, it is not suitable for arrays such as the dipole-dipole and pole-dipole where the pseudosection point falls in an area with very low sensitivity values. The RES2DINV program uses a more sophisticated method to generate the inversion model where the arrangement the model blocks is not tightly bound to the pseudosection.

A final minor note. In most textbooks, the electrodes for this array are arranged in a C1-C2-P1-P2 order that will in fact give a negative geometric factor. The arrangement assumed in these notes is the C2-C1-P1-P2 arrangement.

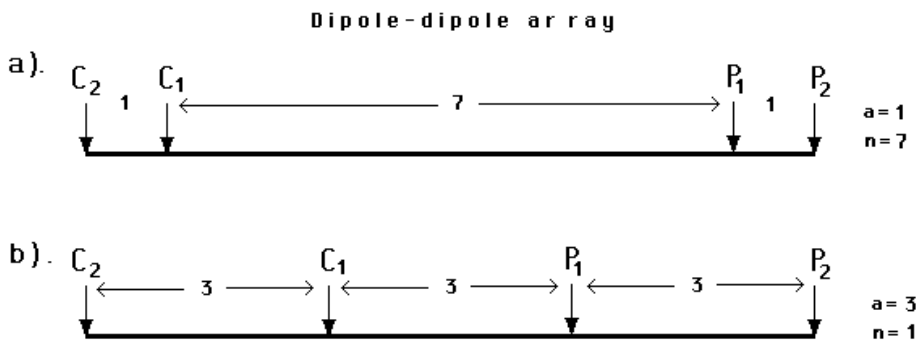


Figure 25. Two possible different arrangements for a dipole-dipole array measurement. The two arrangements have the same array length but different “*a*” and “*n*” factors resulting in very different signal strengths.

2.5.6 Wenner-Schlumberger array

This is a hybrid between the Wenner and Schlumberger arrays (Pazdirek and Blaha 1996) arising out electrical imaging surveys with multi-electrode systems. The classical Schlumberger array is one of the most commonly used arrays for resistivity sounding surveys. A digitized form of this array so that it can be used on a system with the electrodes arranged with a constant spacing is shown in Figure 27b. The “*n*” factor for this array is the ratio of the distance between the C1-P1 (or P2-C2) electrodes to the spacing between the P1-P2 potential pair. Note that the Wenner array is a special case of this array where the “*n*” factor is equals to 1.

Figure 26 shows the sensitivity pattern for this array as the “*n*” factor is increased from 1 (Wenner array) to 6 (the classical Schlumberger array). The area of highest positive sensitivity below the center of the array becomes more concentrated beneath central P1-P2 electrodes as the “*n*” factor is increased. Near the location of the plotting point at the median depth of investigation, the sensitivity contours has a slight vertical curvature below the center of the array. At *n*=6, the high positive sensitivity lobe beneath the P1-P2 electrodes becomes more separated from the high positive sensitivity values near the C1 and C2 electrodes. This means that this array is moderately sensitive to both horizontal (for low “*n*” values) and vertical structures (for high “*n*” values). In areas where both types of geological structures are expected, this array might be a good compromise between the Wenner and the dipole-dipole array. The median depth of investigation for this array is about 10% larger than that for the Wenner array for the same distance between the outer (C1 and C2) electrodes for “*n*” values greater than 3. The signal strength for this array is approximately inversely proportional to the square of the “*n*” value. The signal strength is weaker than that for the Wenner array, but it is higher than the dipole-dipole array and twice that of the pole-dipole.

Figure 27 shows the pattern of the data points in the pseudosections for the Wenner and Wenner-Schlumberger arrays. The Wenner-Schlumberger array has a slightly better horizontal coverage compared with the Wenner array. For the Wenner array each deeper data level has 3 data points less than the previous data level, while for the Wenner-Schlumberger array there is a loss of 2 data points with each deeper data level. The horizontal data coverage is slightly wider than the Wenner array, but narrower than that obtained with the dipole-dipole array.

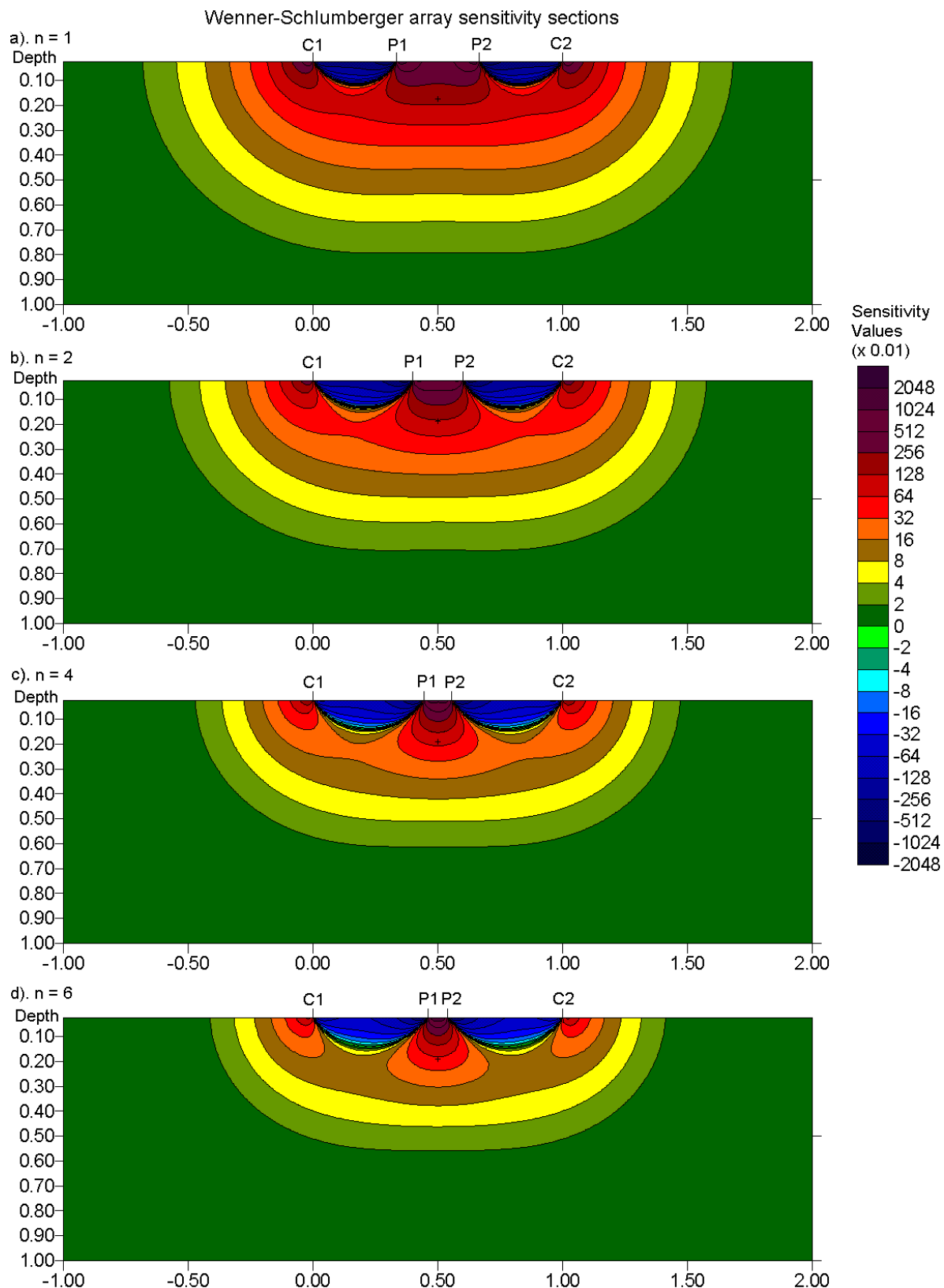


Figure 26. 2-D sensitivity sections for the Wenner-Schlumberger array. The sensitivity sections with (a) $n=1$, (b) $n=2$, (c) $n=4$ and (d) $n=6$.

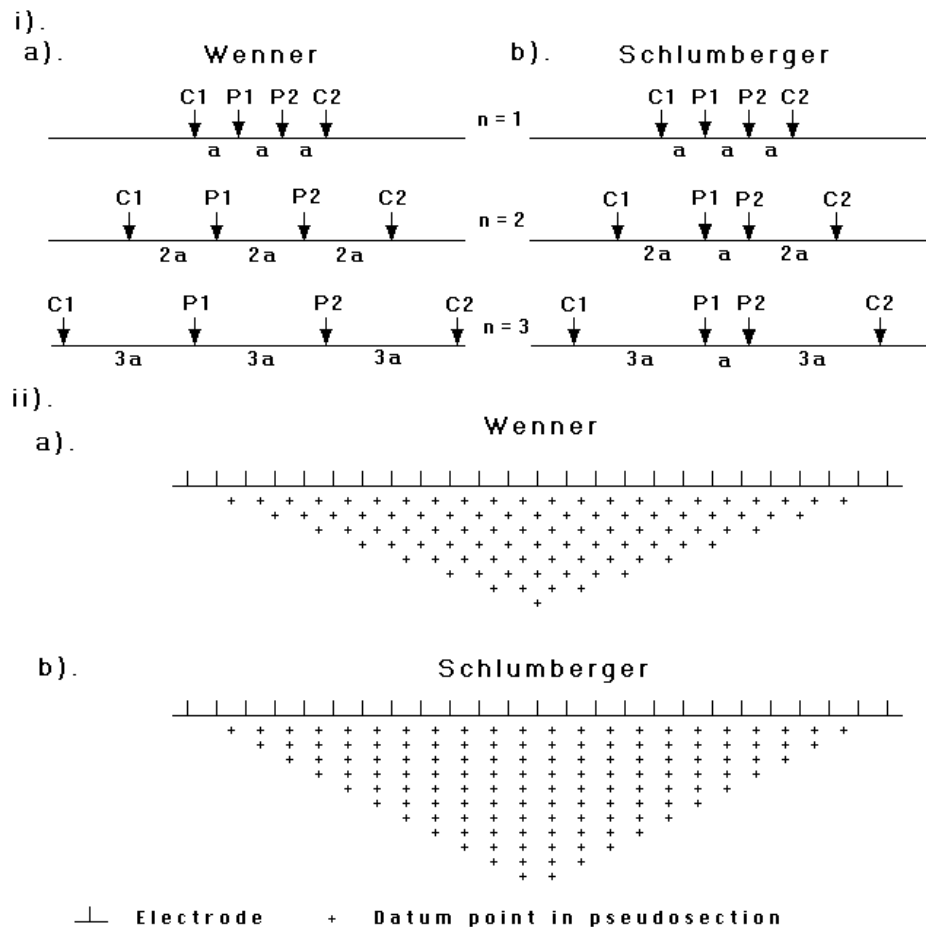


Figure 27. A comparison of the (i) electrode arrangement and (ii) pseudosection data pattern for the Wenner and Wenner-Schlumberger arrays.

2.5.7 Pole-pole array

This array is not as commonly used as the Wenner, dipole-dipole and Schlumberger arrays. In practice the ideal pole-pole array, with only one current and one potential electrode (Figure 4d), does not exist. To approximate the pole-pole array, the second current and potential electrodes (C2 and P2) must be placed at a distance that is more than 20 times the maximum separation between C1 and P1 electrodes used in the survey. The effect of the C2 (and similarly for the P2) electrode is approximately proportional to the ratio of the C1-P1 distance to the C2-P1 distance. If the effects of the C2 and P2 electrodes are not taken into account, the distance of these electrodes from the survey line must be at least 20 times the largest C1-P1 spacing used to ensure that the error is less than 5%. In surveys where the inter-electrode spacing along the survey line is more than a few meters, there might be practical problems in finding suitable locations for the C2 and P2 electrodes to satisfy this requirement. Another disadvantage of this array is that because of the large distance between the P1 and P2 electrodes, it can pick up a large amount of telluric noise that can severely degrade the quality of the measurements. Thus this array is mainly used in surveys where relatively small electrode spacings (less than a few meters) are used. It is popular in some applications such as archaeological surveys where small electrode spacings are used. It has also been used for 3-D surveys (Li and Oldenburg, 1992).

This array has the widest horizontal coverage and the deepest depth of investigation. However, it has the poorest resolution, which is reflected by the comparatively large spacing between the contours in the sensitivity function plot (Figure 28).

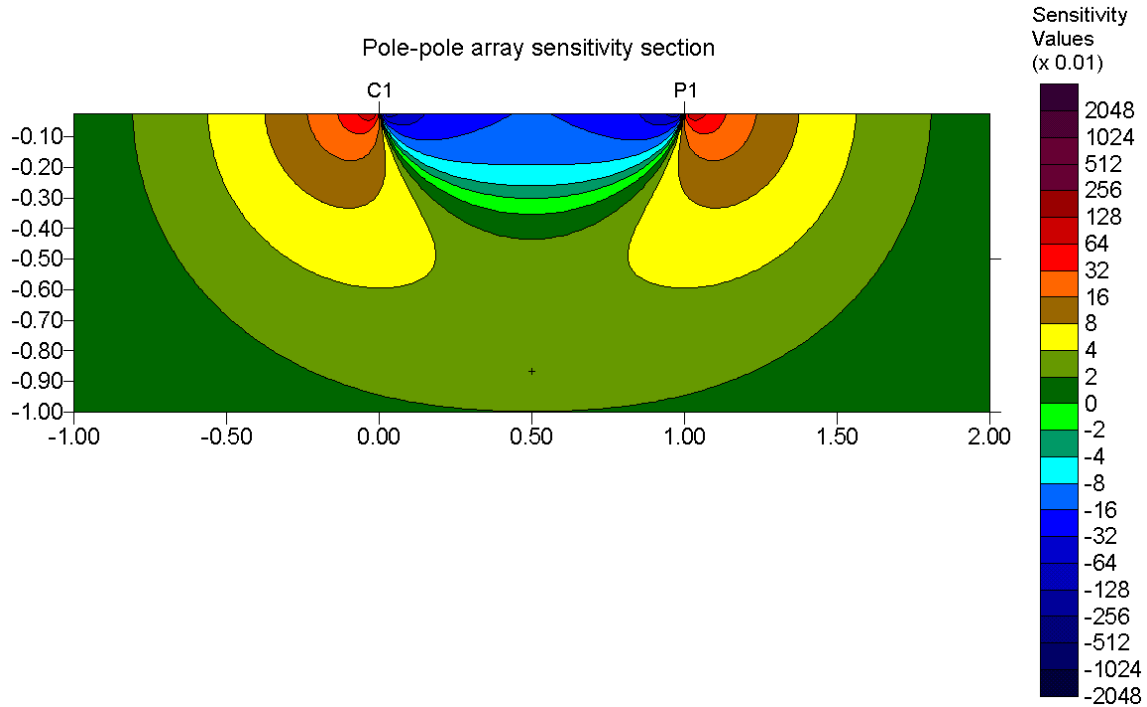


Figure 28. The pole-pole array 2-D sensitivity section.

2.5.8 Pole-dipole array

The pole-dipole array also has relatively good horizontal coverage, but it has a significantly higher signal strength compared with the dipole-dipole array and it is not as sensitive to telluric noise as the pole-pole array. Unlike the other common arrays, the pole-dipole array is an asymmetrical array (Figure 4f). Over symmetrical structures the apparent resistivity anomalies in the pseudosection are asymmetrical (Figure 20d). In some situations, the asymmetry in the measured apparent resistivity values could influence the model obtained after inversion. One method to eliminate the effect of this asymmetry is to repeat the measurements with the electrodes arranged in the reverse manner (Figure 29b). By combining the measurements with the “forward” and “reverse” pole-dipole arrays, any bias in the model due to the asymmetrical nature of this array would be removed. This procedure will double the number of data points and consequently the survey time, but it is not a severe problem with multi-channel systems.

The sensitivity section shows that area with the greatest sensitivity lies beneath P1-P2 dipole pair, particularly for large “ n ” factors. For “ n ” values of 4 and higher, the high positive sensitive lobe beneath the P1-P2 dipole becomes increasingly vertical. Thus, similar to the dipole-dipole array, this array is probably more sensitive to vertical structures. Note also the zone with negative sensitivity values between the C1 and P1 electrodes, as well as the smaller zone of high positive values to the left of the C1 electrode.

The pole-dipole array requires a remote electrode, the C2 electrode, which must be placed sufficiently far from the survey line. We can estimate the effect of the remote electrode by calculating the potential for a simple homogeneous half-space. For the pole-dipole array, the potential due to the C1 electrode is as follows.

$$V_{C1} = \frac{I\rho}{2\pi n(n+1)a}$$

Similarly if the C2 electrode is at ka distance from the P1-P2 dipole, and assuming it is on the same side as the C1 electrode, the potential due to this remote electrode is

$$V_{C2} = \frac{I\rho}{2\pi k(k+1)a}.$$

The ratio of the potentials due to the C2 and the C1 electrodes is then given by

$$\frac{V_{C2}}{V_{C1}} = \frac{n(n+1)}{k(k+1)} \approx \left(\frac{n}{k}\right)^2$$

if n is reasonably large (example 10). Thus the effect of the C2 electrode decreases with *square* of its distance from the survey line. The pole-dipole array measurements are less affected by the C2 remote electrode compared to the pole-pole array. If the distance of the C2 electrode is more than 5 times the largest C1-P1 distance used, the error caused by neglecting the effect of the C2 electrode is less than 5% (the exact error also depends on the location of the P2 electrode for the particular measurement and the subsurface resistivity distribution).

Due to its good horizontal coverage, this is an attractive array for multi-electrode resistivity meter systems with a relatively small number of nodes. The signal strength is lower compared with the Wenner and Wenner-Schlumberger arrays but higher than the dipole-dipole array. For I.P. surveys, the higher signal strength (compared with the dipole-dipole array) combined with the lower EM coupling (compared with the Wenner and Wenner-Schlumberger arrays) due to the separation of the circuitry of the current and potential electrodes makes this array an attractive alternative.

The signal strength for the pole-dipole array decreases with the *square* of the “ n ” factor. While this effect is not as severe as the dipole-dipole array, it is usually not advisable to use “ n ” values of greater than 8 to 10. Beyond this, the “ a ” spacing between the P1-P2 dipole pair should be increased to obtain a stronger signal strength. The ratio of the depth of investigation to the array length does not increase significantly for ‘ n ’ values beyond 4 or 5 (Table 2). Thus to increase the depth of investigation, it is better to increase the ‘ a ’ spacing rather than to keep increasing the ‘ n ’ value when it reaches 5. There is another interesting effect when the ‘ n ’ factor is increased that is frequently not appreciated, and leads to an interesting pitfall in field surveys. This is discussed in section 4.10.

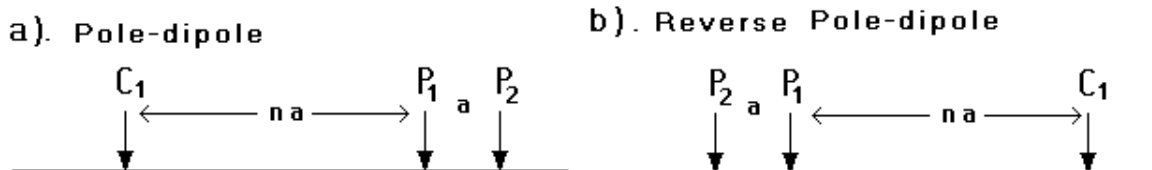


Figure 29. The forward and reverse pole-dipole arrays.

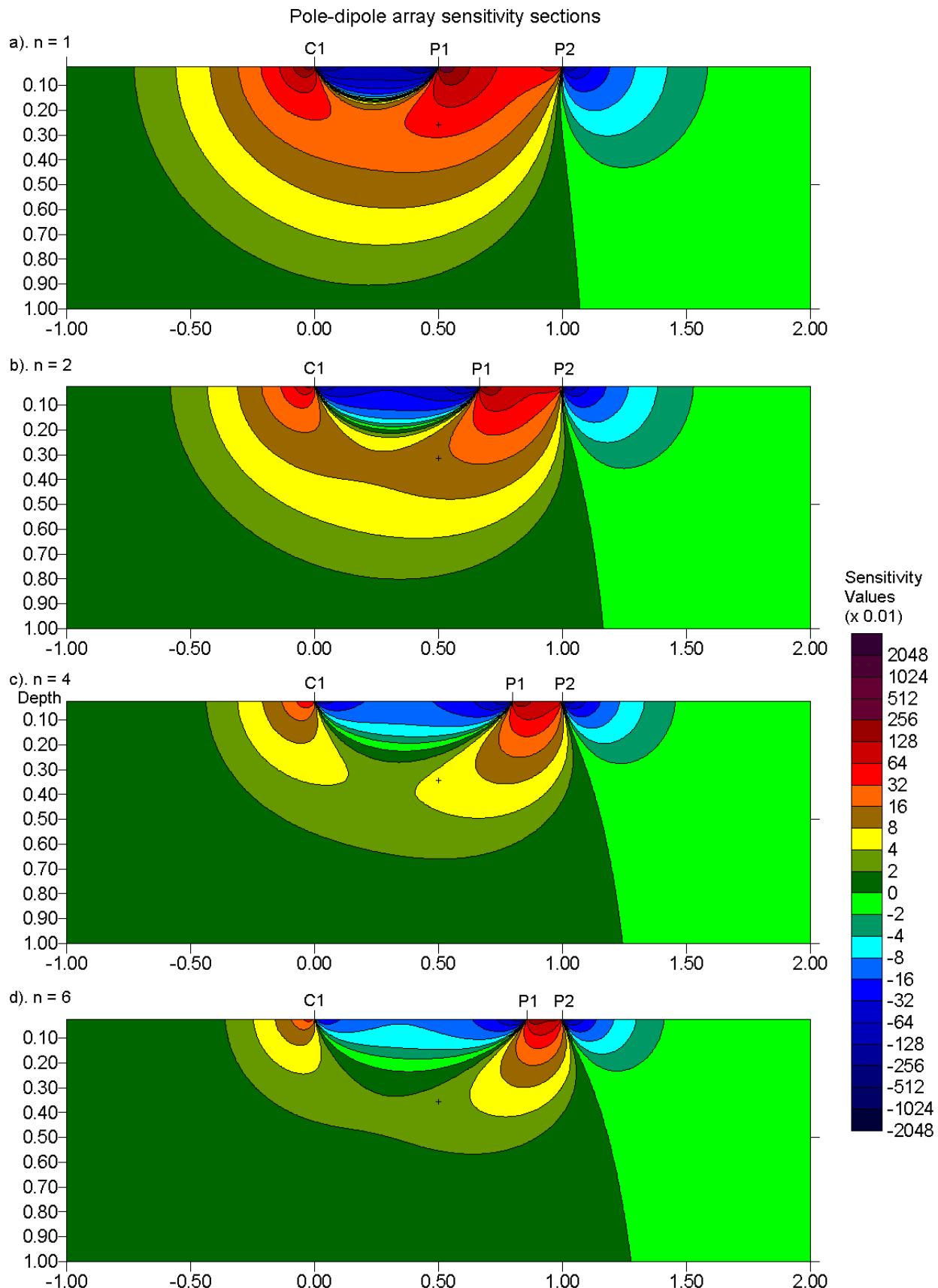


Figure 30. The pole-dipole array 2-D sensitivity sections. The sensitivity sections with (a) $n=1$, (b) $n=2$, (c) $n=4$ and (d) $n=6$.

2.5.9 Multiple gradient array

This is a relatively new array developed primarily for multi-channel resistivity meter systems (Dahlin and Zhou, 2006). A multi-channel system can make several measurements simultaneously with the potential electrode pairs at different locations but with the same positions of the current electrodes. The dipole-dipole and pole-dipole arrays are the obvious arrays that are suitable for such measurements. However, the dipole-dipole array is relatively sensitive to noise while the pole-dipole array requires a remote electrode at a sufficiently large distance from the survey line. For some surveys, an ‘alpha’ type of electrode arrangement with the potential electrodes located between the current electrodes is desirable. One possibility is the ‘reverse’ Schlumberger array with the current electrodes at the centre and the potential electrodes as the outer electrodes. However, this arrangement will be more sensitive to telluric noise due to the large distance between the potential electrodes. The current electrodes in the traditional gradient array are fixed at the end of the line, while measurements are made with the potential electrodes at different positions along the line.

In the multiple gradient array, different sets of measurements are made with the current electrodes at different locations. As an example, for a system with 32 electrodes, one set of measurements can be made with the current electrodes at nodes 1 and 32. Next, another series of measurements are made with the current electrodes at nodes 1 and 16, as well as another with the current electrodes at 16 and 32. A similar set of measurements can be made with the C1-C2 electrodes at 1-8, 8-16, 16-24 and 24-32. This can be repeated using smaller distances between the current electrodes. The sensitivity sections with the same positions of the C1-C2 current electrodes, but with the potential dipole P1-P2 being moved from the center to one end of the array is shown in Figure 31. Not surprisingly, the sensitivity contour pattern slowly changes from a Wenner-Schlumberger pattern (Figure 26) towards the pole-dipole pattern (Figure 30) as the potential dipole moves closer to the current electrode at one end of the array. The results obtained by this array are comparable to those obtained by the Wenner-Schlumberger and pole-dipole arrays (Dahlin and Zhou, 2004) while it has more favourable noise characteristics (Zhou and Dahlin, 2003).

One interesting minor problem associated with this array is the plotting method for the pseudosection and profiles. The vertical position can be easily determined by using the median depth of investigation which can be numerically determined. The main issue is the horizontal position of the plotting point.

Two possibilities are using the average of the locations of all the four electrodes (C1-P1-P2-C2), or just the midpoint of the P1-P2 electrodes (Dahlin and Zhou, 2006). However, for some data sets, both methods might result in a situation where two data points measured with different array configurations end up at the same plotting location. There might be no single method that works satisfactorily in all cases. The RES2DINV program has two options for plotting the data as profiles are shown in Figure 32. The profile plot is commonly used to pick out outliers in the data.

One possible method for selecting the x -location for the pseudosection plotting point for non-symmetrical arrays such as the multiple gradient and pole-dipole is to carry out an integration of the Frechet derivative from $-\infty$ to $+\infty$ in the y and z directions, and from $-\infty$ to x_p in the x direction, such as

$$F_{ID}(x_p) = \frac{1}{4\pi^2} \int_0^{+\infty} \int_{-\infty}^{+\infty} \int_{-\infty}^{x_p} \frac{x(x-a)+y^2+z^2}{[x^2+y^2+z^2]^{1.5} [(x-a)^2+y^2+z^2]^{1.5}} dx dy dz .$$

The value of x_p where this integral reaches half the total value can then be used.

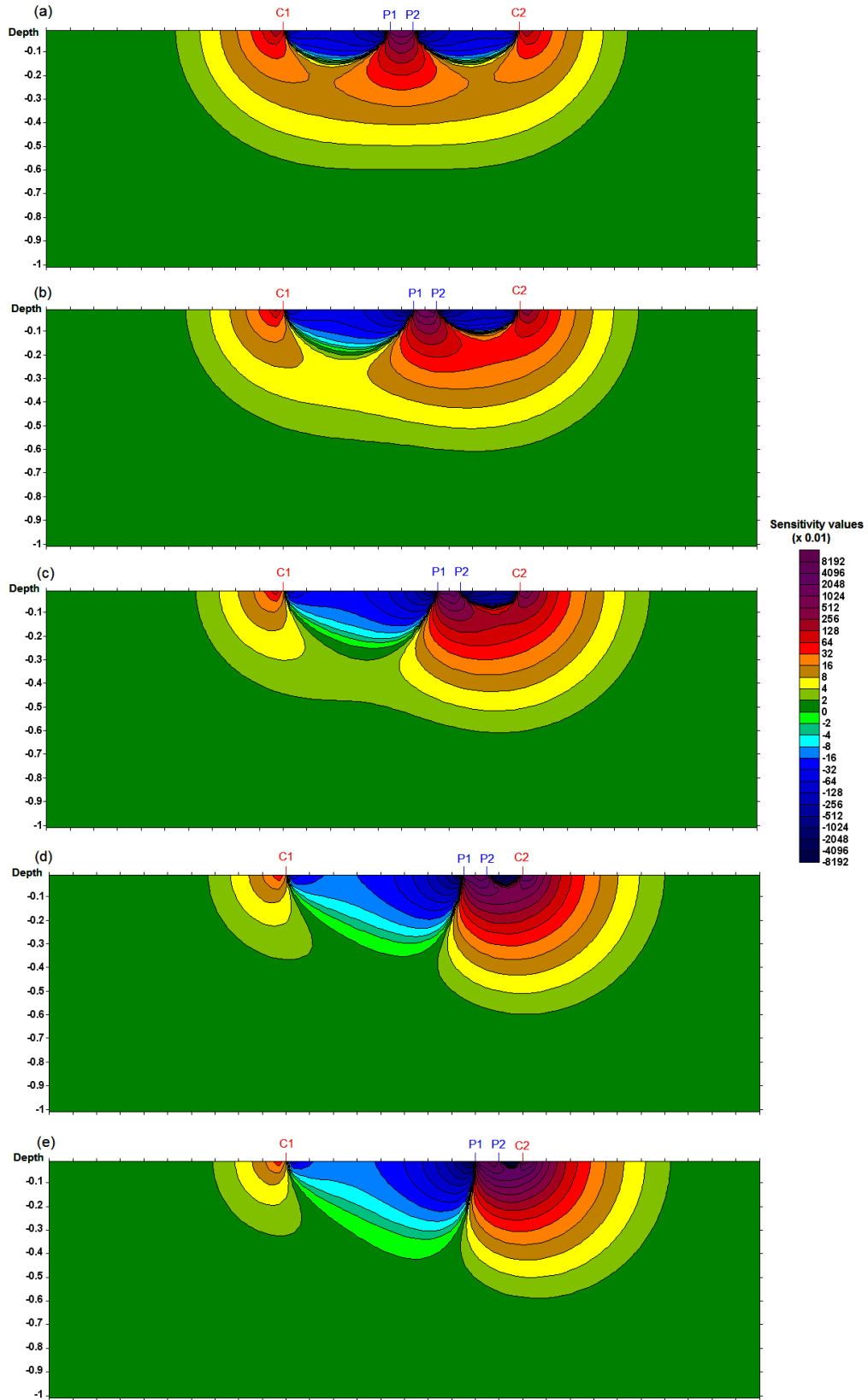


Figure 31. Sensitivity sections for the gradient array. The current electrodes are fixed at $x=0$ and 1.0 meters, and the distance between the potential electrodes is 0.1 m. The position of the P1-P2 potential electrodes at (a) 0.45 and 0.55 m., (b) 0.55 and 0.65 m., (c) 0.65 and 0.75 m, (d) 0.75 and 0.85 m. and (e) 0.80 and 0.90 m.

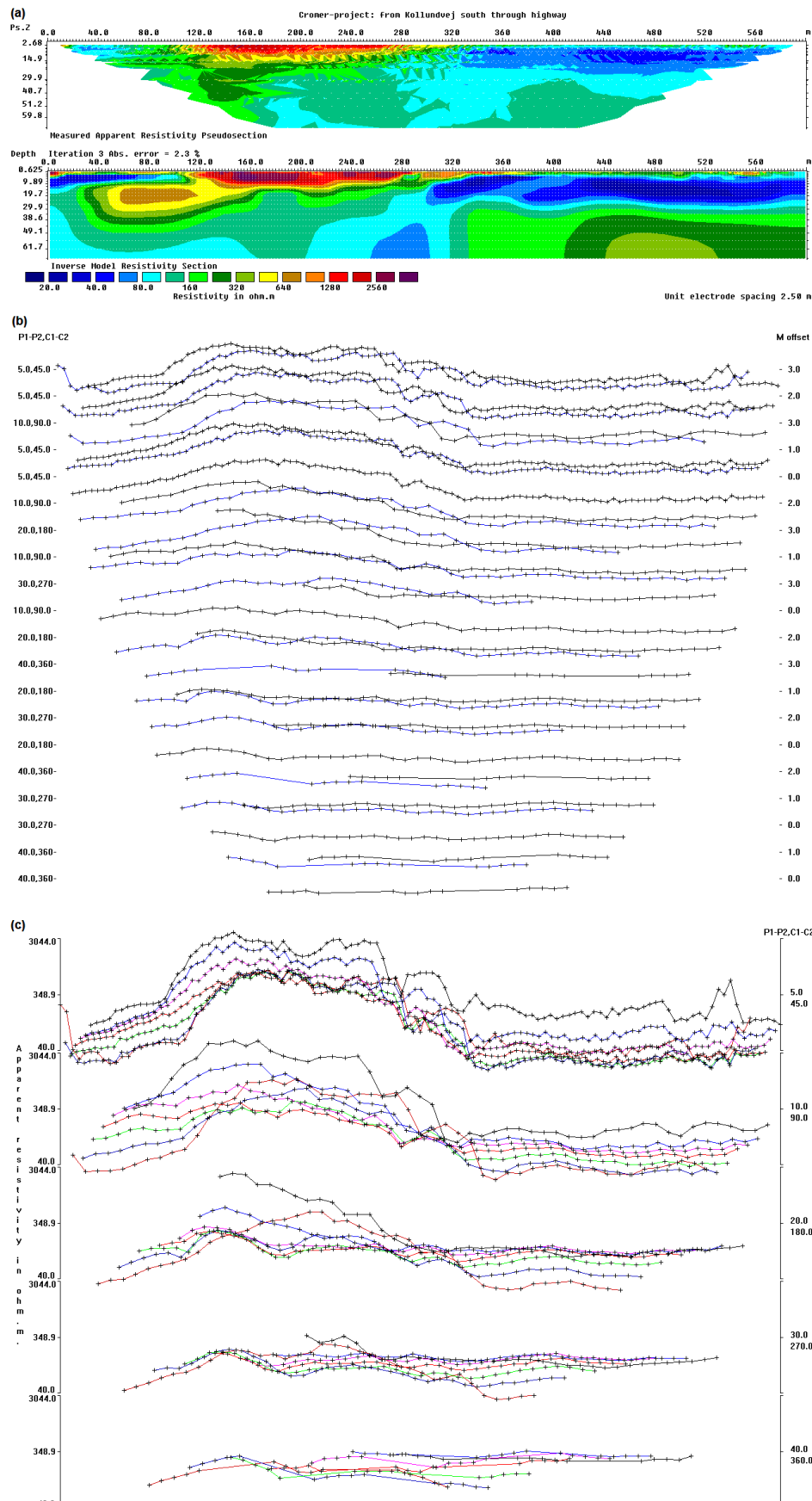


Figure 32. (a) Example of multiple gradient array data set and inversion model. (b) Profile plot using exact pseudodepths. (c) Profile plot using approximate pseudodepths.

2.5.10 High-resolution electrical surveys with overlapping data levels

In seismic reflection surveys, the common depth point method is frequently used to improve the quality of the signals from subsurface reflectors. A similar technique can be used to improve the data quality for resistivity/I.P. surveys, particularly in noisy areas. This is by using overlapping data levels with different combinations of “*a*” and “*n*” values for the Wenner-Schlumberger, dipole-dipole and pole-dipole arrays.

To simplify matters, let us consider the case for the Wenner-Schlumberger array with an inter-electrode spacing of 1 meter along the survey line. A high-resolution Wenner-Schlumberger survey will start with the “*a*” spacing (which is the distance between the P1-P2 potential dipole) equals to 1 meter and repeat the measurements with “*n*” values of 1, 2, 3 and 4. Next the “*a*” spacing is increased to 2 meter, and measurements with “*n*” equals to 1, 2, 3 and 4 are made. This process is repeated for all possible values of the “*a*” spacing. To be on the safe side, the data set should contain all the possible data points for the Wenner array. The number of data points produced by such a survey is more than twice that obtained with a normal Wenner array survey. Thus the price of better horizontal data coverage and resolution is an increase in the field survey time.

A Wenner array with “*a*” equals to 2 meters (Figure 27) will have a total array length of 6 meters and a median depth of investigation of about 1.04 meters. In comparison, a measurement made with “*a*” equals to 1 meter and “*n*” equals to 2 using the Wenner-Schlumberger array will have a total array length of 5 meters and a slightly smaller depth of investigation of 0.93 meter (Figure 27). While the depth of investigation of the two arrangements are similar, the section of the subsurface mapped by the two arrays will be slightly different due to the different sensitivity patterns (Figure 26a,b). So the two measurements will give slightly different information about the subsurface. A measurement with “*a*” equals to 1 meter and “*n*” equals to 3 (Figure 27) will have a depth of investigation of 1.32 meters. If all the 3 combinations are used, the data set will have measurements with pseudodepths of 0.93, 1.02 and 1.32 metres. This results in a pseudosection with overlapping data levels.

A similar “high-resolution” survey technique can also be used with the dipole-dipole and pole-dipole arrays by combining measurements with different “*a*” and “*n*” values to give overlapping data levels. In particular, this technique might be useful for the dipole-dipole array since the signal strength decreases rapidly with increasing “*n*” values (section 2.5.5). A typical high-resolution dipole-dipole survey might use the following arrangement; start with a dipole of “1a” and “*n*” values of 1, 2, 3, 4, 5; followed by a dipole of “2a” and “*n*” values of 1, 2, 3, 4, 5; and if necessary another series of measurements with a dipole of “3a” and “*n*” values of 1, 2, 3, 4, 5. Measurements with the higher “*n*” values of over 4 would have higher noise levels. However, by having such redundant measurements using the overlapping data levels, the effect of the more noisy data points will be reduced. Figure 33 shows the apparent resistivity pseudosection for single prism model using this arrangement. This arrangement has been widely used for I.P. surveys with the dipole-dipole array (Edwards, 1977).

In theory, it should be possible to combine measurements made with different arrays to take advantage of the different properties of the various arrays. Although this is not a common practice, it could conceivably give useful results in some situations. The RES2DINV program supports the use of such mixed data sets.

Besides the standard arrays discussed, there is now interest in automatically computer generated optimized non-standard arrays. This is discussed later in section 4.9.4.

2.5.11 Summary of array types

The Wenner array is an attractive choice for a survey carried out in a noisy area (due to its high signal strength) and also if good vertical resolution is required. The dipole-dipole array might be a more suitable choice if good horizontal resolution and data coverage is important (assuming your resistivity meter is sufficiently sensitive and there is good ground contact). The Wenner-Schlumberger array (with overlapping data levels) is a reasonable all-round alternative if both good and vertical resolutions are needed, particularly if good signal strength is also required. If you have a system with a limited number of electrodes, the pole-dipole array with measurements in both the forward and reverse directions might be a viable choice. For surveys with small electrode spacings and require a good horizontal coverage, the pole-pole array might be a suitable choice. For multi-channel arrays, the possible arrays are the multiple gradient, the dipole-dipole and pole-dipole arrays.

The papers by Dahlin and Zhou (2004) and Zhou and Dahlin (2003) have interesting discussions on the properties of different arrays.

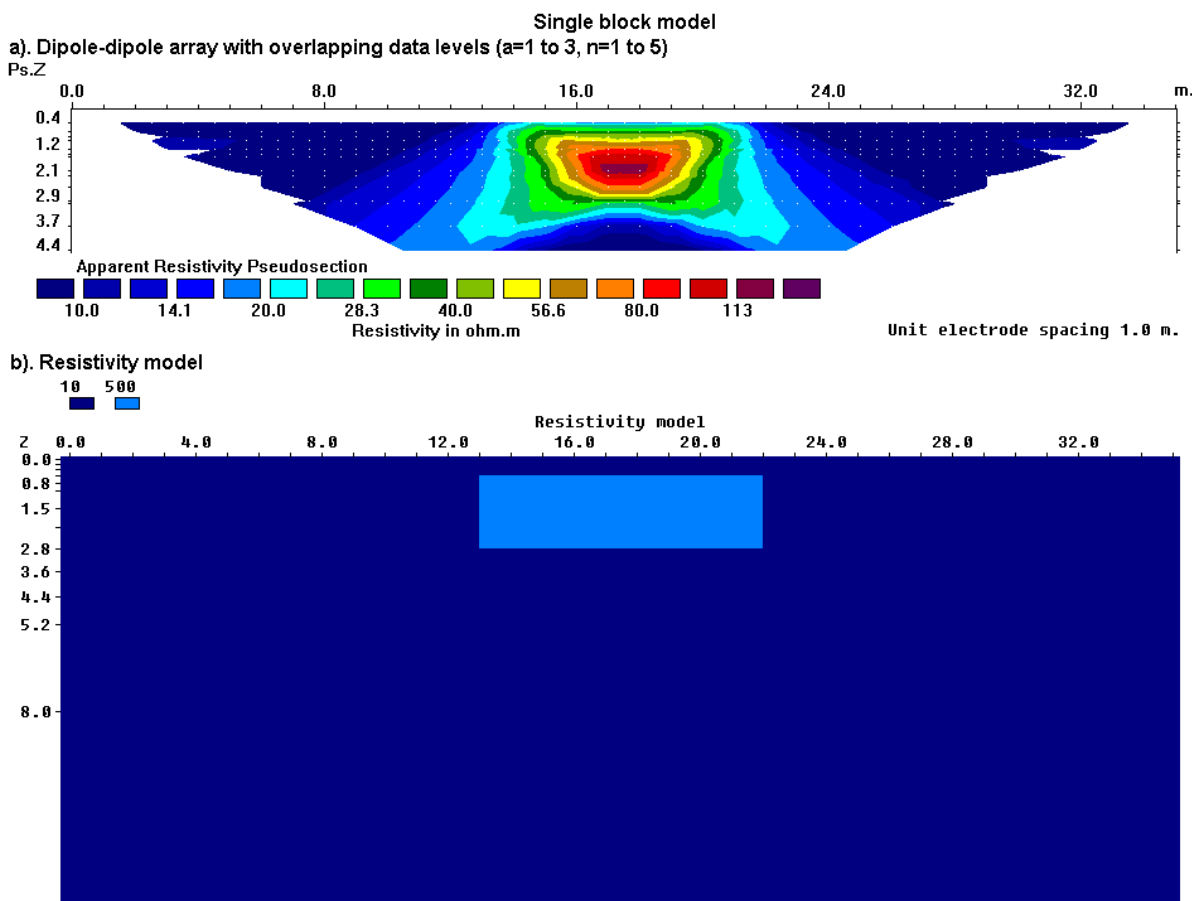


Figure 33. The apparent resistivity pseudosection for the dipole-dipole array using overlapping data levels over a rectangular prism. Values of 1 to 3 meters are used for the dipole length ‘ a ’, and the dipole separation factor ‘ n ’ varies from 1 to 5. Compare this with Figure 20c for the same model but with ‘ a ’ fixed at 1 meter, and “ n ” varying from 1 to 10. In practice, a ‘ n ’ value greater than 8 would result in very noisy apparent resistivity values.

2.5.12 Use of the sensitivity values for multi-channel measurements or streamers

Here we will look at one example of the use of the sensitivity values. The problem faced is as follows.

- We have a multi-channel resistivity meter that can make 8 measurements at a single time.
- The cable used (possibly in the form of a streamer for mobile surveys on land or in water covered areas) has 10 nodes. Two of the nodes are fixed as the current electrodes, while the potential measurements are made using any 2 of the remaining 8 nodes.
- We want to get the most information possible in terms of depth and a uniform horizontal coverage below the streamer for a single set of 8 measurements.

To study the characteristics of the array configurations, we add up the sensitivity values for all the 8 measurements. The formula used for the cumulative absolute sensitivity, F_I , is

$$F_I = \frac{1}{8} \sum_{i=1}^{i=8} |F_{2Di}(x, z)| \quad (2.7)$$

Note that the absolute value of the sensitivity value is used, since negative sensitivity values also give information about the subsurface. This is also to avoid a situation where the negative sensitivity value for one measurement cancels out the positive value for another measurement.

Figure 34a shows a dipole-dipole array based measurement sequence. The two current electrodes are set at one end of the line and the potential measurements are made using successive pairs of the potential nodes. Note the area with the highest cumulative sensitivity is around the first 4 electrodes. The area of deepest penetration is between the second and third electrodes, i.e. between the current dipole and the first potential electrode.

The second configuration places the current electrodes at the ends of the line (Figure 34b). Almost all the measurements are made using a fixed separation of one unit electrode spacing between the potential electrodes. The potential dipole is moved from one end of the survey line to the other end, i.e. a gradient array type of arrangement. One advantage of this configuration over the dipole-dipole arrangement is the larger voltage (i.e. lower noise level) measured by the potential electrodes. The cumulative sensitivity section shows a more uniform pattern compared to that produced by the dipole-dipole configuration. The depth of investigation is slightly deeper below current electrodes, and slightly less below the center of the line.

The third configuration also places the current electrodes at the ends of the lines, but keeps the center of the potential dipoles at or near the center of the line. The first 4 measurements use a symmetrical Wenner-Schlumberger arrangement and increase the separation between the potential electrodes until they reach next to the current electrodes. The second set of 4 measurements uses separations of 2 and 3 times the unit spacing for the potential dipole pair but with a mid-point slightly to one side of the center of the line. The cumulative sensitivity pattern has an even more uniform pattern below the line compared with the gradient array configuration.

To get an idea of the relative depths of investigation for the 3 configurations, we use the light blue contour (with a value of 8 units) as a guide. The expanding Wenner-Schlumberger configuration has the deepest depth with high sensitivity values while the dipole-dipole configuration appears to have the shallowest. Note the current electrodes for dipole-dipole array is limited to the left end of the line, and for this reason the region with the deepest depth of investigation is skewed towards the left.

One problem with using the cumulative sensitivity sections is that it is a rather crude measure of the resolution that the data set has. It probably overestimates the depth of

investigation for the gradient and Wenner-Schlumberger configurations (Figure 34b, c). This is because it does not take into account the orthogonality of data, i.e. the information from two measurements for the same region might not be independent. A better method to evaluate the information content from a group of array configurations is the model resolution (section 4.9.6).

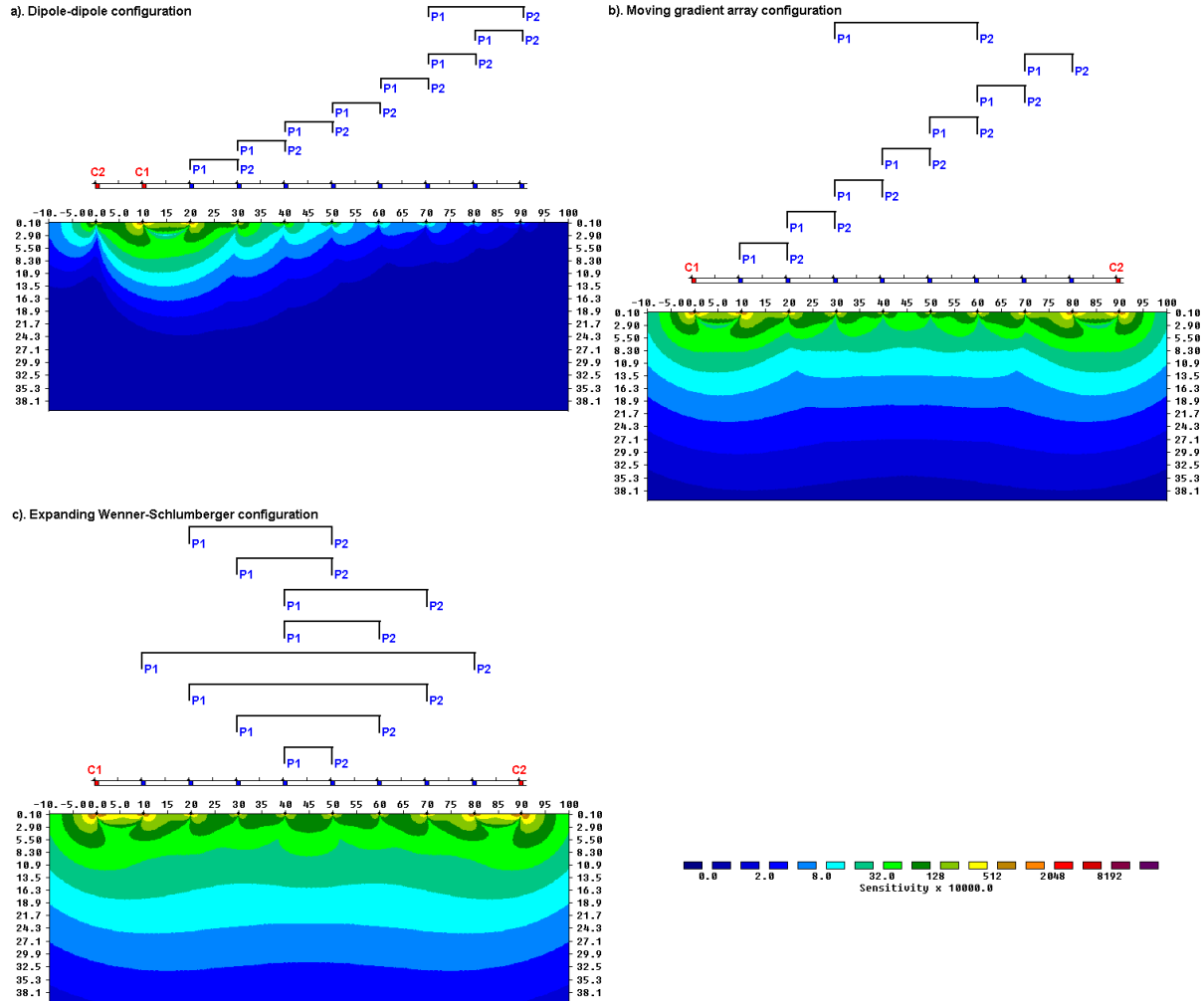


Figure 34. Cumulative sensitivity sections for different measurement configurations using (a) a dipole-dipole sequence, (b) a moving gradient array and (c) an expanding Wenner-Schlumberger array.

3 A 2-D forward modeling program

3.1 Finite-difference and finite-element methods

In the forward modeling problem, the subsurface resistivity distribution is specified and the purpose is to calculate the apparent resistivity that would be measured by a survey over such a structure. A forward modeling subroutine is in fact also an integral part of any inversion program since it is necessary to calculate the theoretical apparent resistivity values for the model produced by the inversion routine to see whether it agrees with the measured values. There are three main methods to calculate the apparent resistivity values for a specified model. They are (i) analytical methods, (ii) boundary element methods and (iii) the finite-difference and finite-element methods. Analytical methods are probably the most accurate methods, but they are restricted to relatively simple geometries (such as a sphere or cylinder). Boundary element methods are more flexible, but the number of regions with different resistivity values that is allowed is somewhat limited (usually less than 10). In engineering and environmental surveys the subsurface can have an arbitrary resistivity distribution, so the finite-difference and finite-element methods are usually the only viable choice. These methods can subdivide the subsurface into thousands of cells with different resistivity values. However, the analytical and boundary element methods are useful independent methods that can be used to check the accuracy of the finite-difference and finite-element methods.

In the RES2DMOD software, the user can choose the finite-difference or the finite-element method. The subsurface is subdivided into a large number of rectangular cells (Figure 35) and the user can specify the resistivity value of each cell. The finite-difference method is based on a method described by Dey and Morrison (1979a) but with a modification by Loke (1994) to correct for a minor inconsistency in the Dey and Morrison discretization by area method. The finite-element method uses the standard first-order triangular elements (Silvester and Ferrari, 1990).

While our main interest is in the inversion of field data, the forward modeling program is also useful, particularly in the planning stage of the survey. In the previous chapter we have seen that different arrays can have sensitivity sections that are radically different. In theory, from the sensitivity sections we can get an idea of the type of array that will give a reasonably good response over a particular class of structures (for example a vertical fracture zone). However, there is no substitute for a hands-on direct calculation of the expected apparent resistivity pseudosection. Before carrying out a field survey, some information about the shape and size of expected targets is frequently known. By trying different arrays digitally on the computer screen, we can avoid using an array that is unsuitable for the detection of the structures of interest. We can also have an idea of a suitable spacing between adjacent electrodes to use, and the maximum electrode separation needed.

In the program, the subsurface is divided into a large number of small rectangular cells. This program is largely intended for teaching about the use of the 2-D electrical imaging method. Hopefully, it will assist the user in choosing the appropriate array for different geological situations or surveys. The arrays supported by this program are the Wenner (Alpha, Beta and Gamma configurations), Wenner-Schlumberger, pole-pole, inline dipole-dipole, pole-dipole and equatorial dipole-dipole (Edwards, 1977). Each type of array has its advantages and disadvantages. This program will hopefully help you in choosing the "best" array for a particular survey area after carefully balancing factors such as the cost, depth of investigation, resolution and practicality.

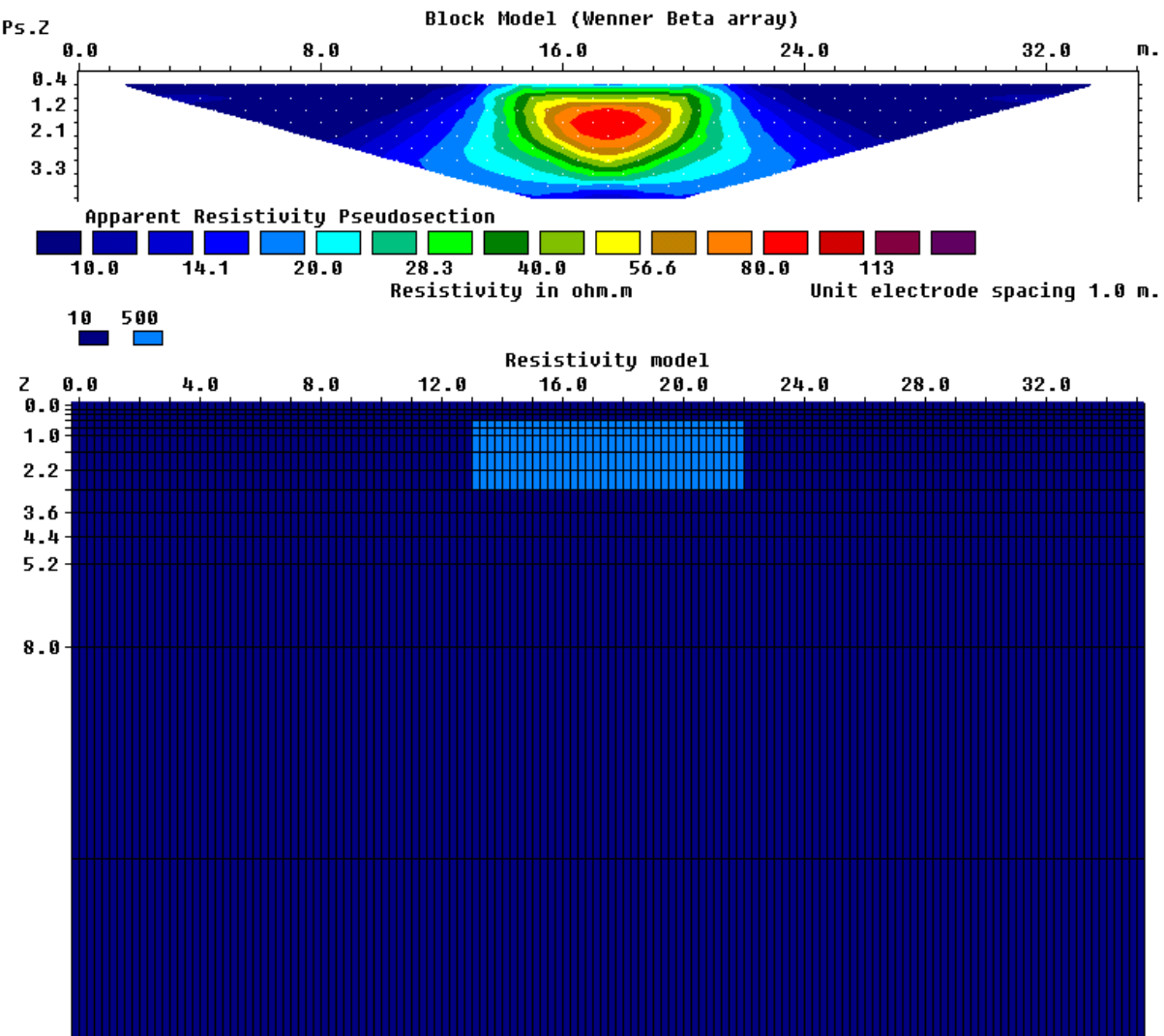


Figure 35. The output from the RES2DMOD software for the SINGLE_BLOCK.MOD 2-D model file. The individual cells in the model are shown in the lower figure, while the upper figure shows the pseudosection for the Wenner Beta (dipole-dipole with $n=1$) array.

3.2 Using the forward modeling program RES2DMOD

The program requires the resistivity model values to be typed in separately in a text file. The model data format, and other details about the use of this program, can be found in the RES2DMOD.PDF manual file. In this course, we will use several model files that are already present in the program package to take a look at the shapes of the contours in the pseudosections for different geological structures. By playing around with this program, you can get a feel of the effects of array type over the amplitude, size and shape of the contours in the pseudosection.

After starting up the RES2DMOD program, click the ‘File’ menu option on the main menu bar. Next select the “Read data file with forward model” suboption to read in one of the example input model files provided. The files with the forward model have a MOD extension. As an example, read in the file SINGLE_BLOCK.MOD that has a simple model with a rectangular prism. After reading in this file, select the “Edit/Display Model” option followed by the “Edit model” suboption to take a look at the model. This will show you the actual cells that make up the model.

The program also allows you to change the model interactively using the left and right

mouse buttons. To change a single cell, click it with the left mouse button. Then move the cursor to one of the color boxes in the legend above the model, and click the resistivity value you want. Press the F1 key to get information about the keys used by the program to edit the model. Note that clicking the cells with the mouse buttons will only change the resistivity of the cells displayed on the screen, but will not change the resistivity of the buffer cells towards the left, right and bottom edges of the mesh. To change the resistivity of the buffer cells, you need to use the “[“, “]” and “D” keys.

Next select the “Model Computation” option to calculate the potential values for this model. The calculations will probably only take a few seconds, after which you should go back to “Edit/Display Model” option. In this option, select the “Edit model” sub-option again to see the apparent resistivity pseudosection for this model. The program will ask you to select the type of contour intervals you wish to use. For most resistivity pseudosections choose the ‘Logarithmic contour intervals’, while for I.P. pseudosections choose the linear contour intervals.

To change the type of array, use the “Change Settings” sub-option. Select another array, such as the pole-pole or dipole-dipole, and see what happens to the shape of the contours in the pseudosection.

3.3 Forward modeling exercises

Here we will try out a few model files that are provided to get a feel of what pseudosections look like, and the effect of different choices on the results. The RES2DMOD program also has an option to save the calculated apparent resistivity values into the format used by the RES2DINV inversion program. You might like to save some of the results from this exercise into this format to use with the RES2DINV program later on. This is useful in studying the model resolution that can be obtained over different structures using various arrays.

Table 3. Forward modeling examples.

Model file and purpose	Things to try
BLOCK_ONE.MOD To see the effect of selecting the array type on the shape of the contours in the pseudosection. The model is a simple rectangular prism.	<ul style="list-style-type: none"> (1). The default array type is the Wenner Alpha. Run the ‘Model computation’ option to get things started. Next use the ‘Edit model’ option to take a look at the pseudosection. Compare the shape of the anomaly in the pseudosection with the actual shape of the prism. What is the maximum apparent resistivity value (compare it with the prism resistivity of $100 \Omega\cdot m$)? (2). Next change the array type to Wenner Beta, and take a look at the shape of the contours. Also, what is the maximum apparent resistivity value? Repeat with the Wenner Gamma array. Among the 3 versions of the Wenner array, which do you think is the ‘best’? (4). Next try the inline dipole-dipole. What is the maximum ‘n’ value you need to use in order to fully map this prism? For a current of 10mA, what would the voltage be for this ‘n’ value when the dipole length is 1 meter? The program also allows you to change the ‘a’ dipole length. Try changing it to 2 and see what happens. (5). To complete things, try out the other arrays, such as the pole-pole, pole-dipole, equatorial dipole-dipole and Wenner-Schlumberger. (6). Edit the model using the ‘Edit Model’ option. Try increasing the thickness and/or width of the prism and see what happens to the anomaly in the pseudosection. Also try changing the resistivity of the prism to $500 \Omega\cdot m$.

BLOCK_TWO2.MOD In this case, we have two prisms at a mean depth of 1 meter, and 2 meters apart. The two prisms are identical and at the same depth. We will try different arrays to which ones are more likely to be able to resolve the prisms in the pseudosection.	(1). The default array type is the Wenner Alpha. Run the 'Model computation' option to get things started. (2). Next, take a look at the pseudosection. Is it possible to separate the highs due to each prism? (3). Try the whole range of arrays, i.e. the 3 different versions of the Wenner, pole-dipole, dipole-dipole, Schlumberger etc. Which arrays are more likely to be able to resolve the two prisms?
BLOCKS_UP.MOD Now we have two prisms, one on top of another. Is it possible to tell them apart?	(1). The default array type is the Wenner Alpha. Run the 'Model computation' option to get things started. (2). Next, take a look at the pseudosection. Is it possible to separate the highs due to each prism? (3). Try the whole range of arrays, i.e. the 3 different versions of the Wenner, pole-dipole, dipole-dipole, Schlumberger etc. Which arrays are more likely to be able to resolve the two prisms?
THICK_DIKE.MOD This model has a wide low resistivity dike in high resistivity bedrock.	(1). The default array type is the Wenner Beta. Calculate the potentials and take a look at the pseudosection. Is it possible to infer the existence of the dike from the pseudosection? (2). Change to the Wenner Alpha, and see what happens. (3). Try other arrays such as the Wenner Gamma, Wenner-Schlumberger and pole-dipole. Which arrays show a significant low resistivity anomaly?
THIN_DIKE.MOD This model has a thin dike in high resistivity bedrock. This is a more difficult target than the thick dike.	(1). The default array type is the Wenner Beta. Calculate the potentials and take a look at the pseudosection. Is it possible to infer the existence of the dike for the pseudosection? (2). Change to the Wenner Alpha, and see what happens. (3). Try other arrays such as the Wenner Gamma, Wenner-Schlumberger and pole-dipole. Which arrays show a significant low resistivity anomaly?
MODEILIP.MOD An I.P. model just to round things up.	(1). The default array type is the dipole-dipole, which is probably the most commonly used array for I.P. surveys. Calculate the potential values, and take a look at the pseudosections. (2). Another array that is sometimes used for I.P. surveys is the pole-dipole that has the advantage of a stronger signal strength. Check the pseudosections obtained with this array.

Now that we had some experience in creating pseudosections, it is time to have a look the inversion program RES2DINV that will do the reverse, i.e. creating a model from the pseudosection.

4 A 2-D inversion program

4.1 Introduction

After the field survey, the resistance measurements are usually reduced to apparent resistivity values. Practically all commercial multi-electrode systems come with the computer software to carry out this conversion. In this section, we will look at the steps involved in converting the apparent resistivity values into a resistivity model section that can be used for geological interpretation. I will assume that the data is already in the RES2DINV format. The conversion program is provided together with many commercial systems. So far, the ones that have the conversion program include Abem, AGI, Campus, Geofysika, Geometrics, Iris, OYO, Pasi and Scintrex. If your equipment manufacturer is not on the list, please contact them about the conversion software. The data format used by the RES2DINV program is described in detail in the RES2DINV.PDF manual provided with the program. Please refer to the manual for the details.

In the next section, we will look at two methods to handle bad data points. Such bad data points should be removed before a final interpretation is made.

Due to the large variety of data sets collected over various geological environments, no single inversion method will give the optimum results in all cases. Thus the RES2DINV program has a number of settings that can be changed by the user to obtain results that are closer to the known geology. The various options are also discussed in the following sections.

4.2 Pre-inversion and post-inversion methods to remove bad data points

To get a good model, the data must be of equally good quality. Bad data points fall into two broad categories, i.e. “systematic” and “random” noise. Systematic noise is usually caused by some sort of failure during the survey such that the reading does not represent a true resistivity measurement. Examples include breaks in the cable, very poor ground contact at an electrode such that sufficient current cannot be injected into the ground, forgetting to attach the clip to the electrode, connecting the cables in the wrong direction etc. Systematic noise is fairly easy to detect in a data set as it is usually present in limited number of readings, and the bad values usually stick out like sore thumbs. Random noise include effects such telluric currents that affects all the readings, and the noise can cause the readings to be lower or higher than the equivalent noise-free readings. This noise is usually more common with arrays such as the dipole-dipole and pole-dipole that have very large geometric factors, and thus very small potentials for the same current compared to other arrays such as the Wenner. It is also common with the pole-pole array due to the large distance between the P1 electrode and the remote (and fixed) P2 electrode. This array tends to pick up a large amount of telluric noise due to the large distance between the two potential electrodes.

As a general rule, before carrying out the inversion of a data set, you should first take a look at the data as a pseudosection plot (Figure 36a) as well as a profile plot (Figure 36b). The bad data points with “systematic” noise show up as spots with unusually low or high values (Figure 36a). In profile form, they stand out from the rest and can be easily removed manually for the data set. In the RES2DINV program, choose the ‘Edit data’ on the top menu bar followed by the ‘Exterminate bad data points’ option (Figure 37). The bad data points can be removed by clicking them with the mouse.

When the noise is of a more random nature, the noisy data points are not as obvious, so it might not be practical to remove them manually. Also, manually picking out the bad data points becomes impractical if there are a large number of bad data points, particularly if the data set contains more than a thousand data points. In some cases, it is not possible to display the data as pseudosections or profiles, such as in 3D data sets. RES2DINV (and RES3DINV) has a general technique to remove the bad data points with minimal input from

the user, and can be used for practically any array and any distribution of the data points. The main disadvantage of the method is the larger amount of computer time needed. In this method, a preliminary inversion of the data set is first carried with all the data points. After carrying out the trial inversion, switch to the 'Display' window in RES2DINV, and read in the INV file containing the inversion results. After that, select the 'RMS error statistics' option that displays the distribution of the percentage difference between the logarithms of the measured and calculated apparent resistivity values. The error distribution is shown in the form of a bar chart, such as in Figure 38. Normally, the highest bar is the one with the smallest errors, and the heights of the bars should decrease gradually with increasing error values. The bad data points, caused by problems such as poor ground contact at a small number of electrodes, should have significantly higher errors than the "good" data points.

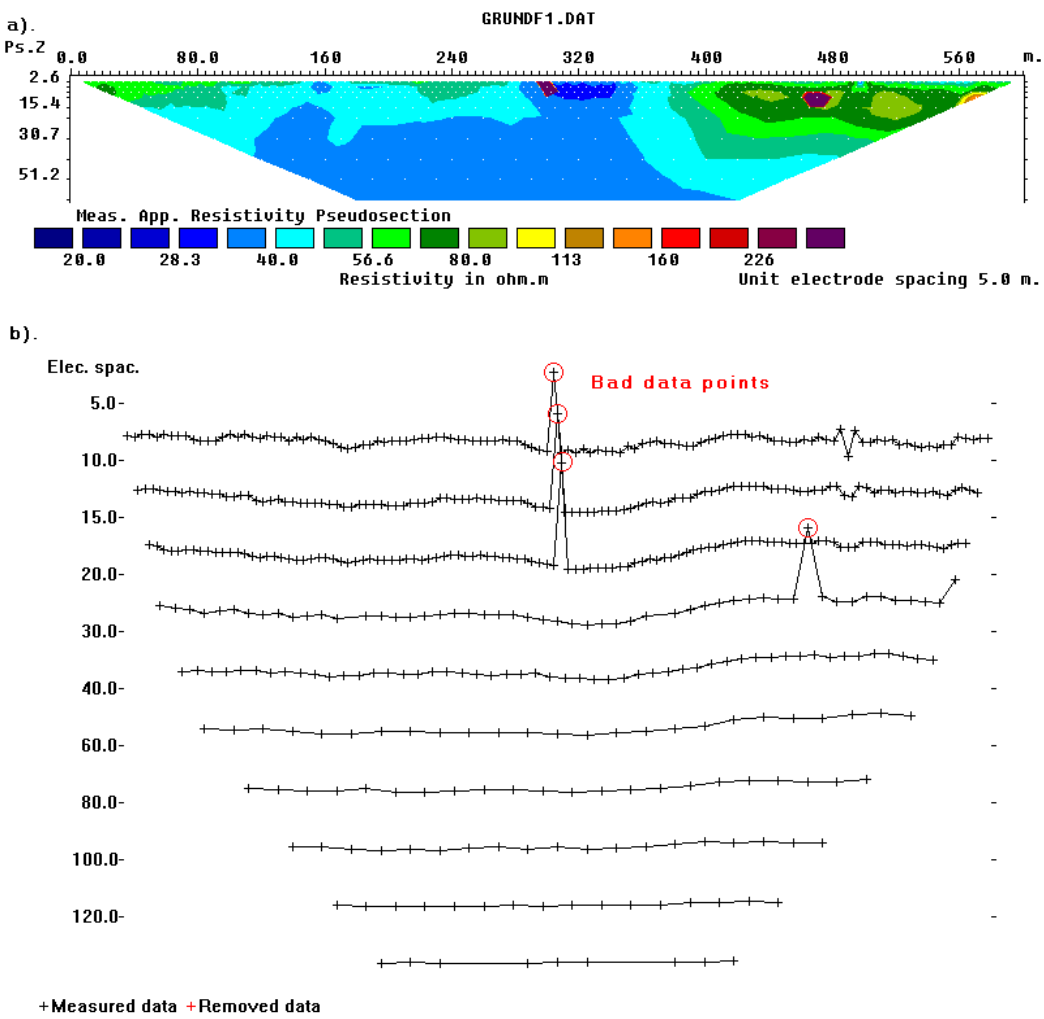


Figure 36. An example of a field data set with a few bad data points. The most obvious bad datum points are located below the 300 meters and 470 meters marks. The apparent resistivity data in (a) pseudosection form and in (b) profile form.

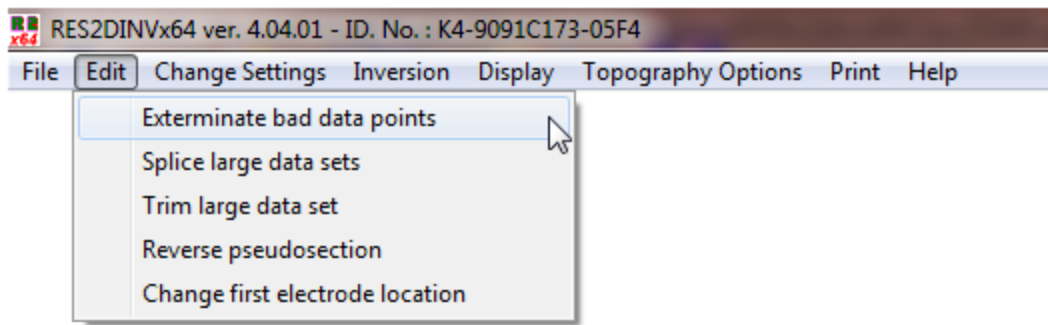


Figure 37. Selecting the menu option to remove bad data points manually.

Figure 38 shows the error distribution bar chart for the data set shown in Figure 36 that has a few bad data points. In the bar chart, almost all the data points have errors of 20 percent or less. The bad data points show up data points with errors of 60 percent and above, which can be easily removed from the data set by moving the green cursor line to the left of the 60% error bar. In this way the 5 bad data points are removed from this data set. For some data sets, the error distribution might show a more complicated pattern. As a general rule, data points with misfits of 100 percent and above can usually be removed.

Table 4. Methods to remove bad data points

Data set and purpose	Things to try
GRUNDF1.DAT – An example of a field data set with bad data points.	<p>(1) Use the ‘File’ and then the ‘Read data file’ options to read in this data file. Go to the ‘Display’ windows, and then the ‘Display data and model sections’ option. The bad data points should be quite obvious.</p> <p>(2) Next, leave the ‘Display’ window, and then choose ‘Edit data’ on the top menu bar followed by the ‘Extermenate bad data points’ option. Pick out the bad data points. After that save the edited data in a file. Read in this edited data file, and then go back to the ‘Display’ window and check the pseudosection again.</p> <p>(3) After that, leave the ‘Display’ window, and then run an inversion of the data set using the ‘Inversion’ and then the ‘Least-squares inversion’ menu options.</p> <p>(4) After the inversion has finished, go the ‘Display’ window to take a look at the model. After that choose the ‘Edit data’ and then the ‘RMS error statistics’ options. Take a look at the bar chart. Is it possible to remove more bad data points?</p> <p>(5). Try running an inversion of the data set without first manually removing the bad data points. Then use the ‘RMS error statistics’ option to remove them. Does this get rid of the bad data points also?</p>

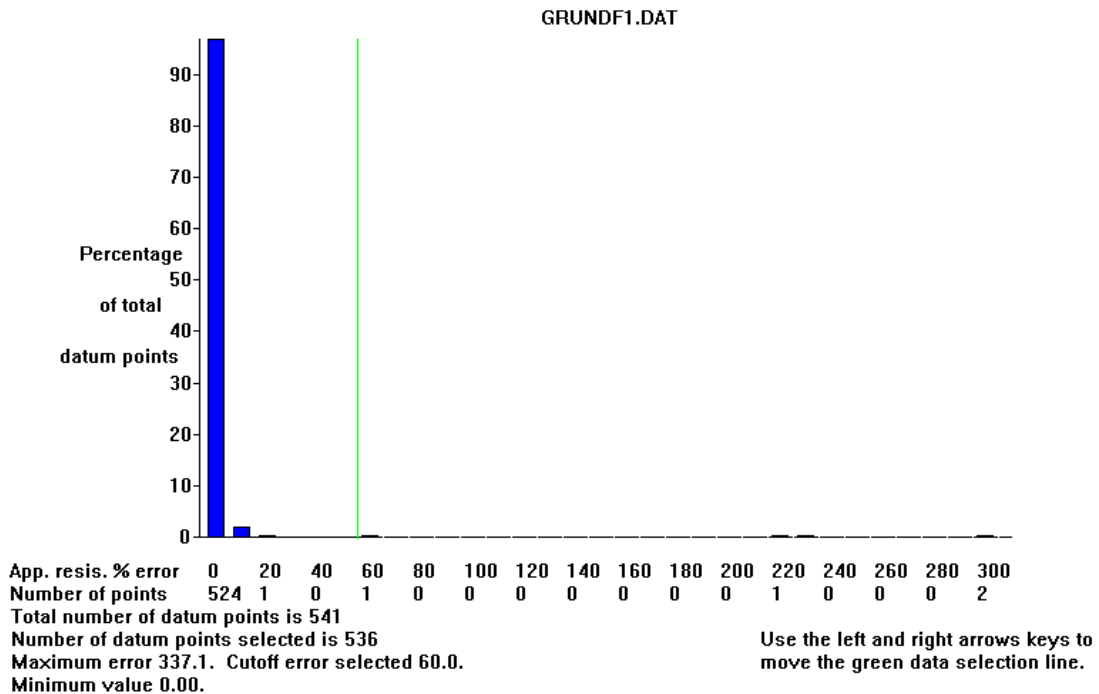


Figure 38. Error distribution bar chart from a trial inversion of the Grundfor Line 1 data set with five bad data points.

4.3 Selecting the proper inversion settings

Many professionals carrying out resistivity imaging surveys will likely to be field engineers, geologists or geophysicists who might not familiar with geophysical inversion theory. The RES2DINV program is designed to operate, as far as possible, in an automatic and robust manner with minimal input from the user. It has a set of default parameters that guides the inversion process. In most cases the default parameters give reasonable results. This section describes some of the parameters the user can modify to fine-tune the inversion process. In the program, the different options are divided into six major groups. The groups are placed under the ‘Change Settings’ or ‘Inversion’ choices on the main menu bar. Here, we will look at a few of the more important settings that can be changed.

a). Inversion methods

The problem of non-uniqueness is well known in the inversion of resistivity sounding and other geophysical data. For the same measured data set, there is wide range of models that can give rise to the same calculated apparent resistivity values. To narrow down the range of possible models, normally some assumptions are made concerning the nature of the subsurface that can be incorporated into the inversion subroutine. In almost all surveys, something is known about the geology of the subsurface, for example whether the subsurface bodies are expected to have gradational or sharp boundaries.

The default smoothness-constrained inversion formulation used by the RES2DINV program is given by (please refer to section 1.4 for the details)

$$(\mathbf{J}^T \mathbf{J} + \lambda \mathbf{F}) \Delta \mathbf{q} = \mathbf{J}^T \mathbf{g}. \quad (4.1)$$

This formulation constrains the *change* in the model resistivity values, $\Delta \mathbf{q}$, to be smooth but does not guarantee that the resistivity values change in a smooth manner. However, this formulation has been quite popular and used by a number of researchers (deGroot-Hedlin and Constable, 1990; Sasaki, 1992).

The first option ‘Include smoothing of model resistivity’ uses a formulation that will apply the smoothness constrain directly on the model resistivity values. This formulation is

given by

$$(\mathbf{J}^T \mathbf{J} + \lambda \mathbf{W}^T \mathbf{W}) \Delta \mathbf{q} = \mathbf{J}^T \mathbf{g} - \lambda \mathbf{W}^T \mathbf{W} \mathbf{q}, \quad (4.2)$$

so that the model resistivity values, \mathbf{q} , changes in a smooth manner. The next option ‘Use combined inversion method’ attempts to combine the smoothness-constrained method as given in (4.1) with the Marquardt-Levenberg as given in (1.20). However, the result obtained by this combination has not been very impressive and will not be examined.

The ‘Select robust inversion’ option has proved to be much more useful. It modifies the formulation in (4.2) so that different elements of the model parameter change and data misfit vectors have the same magnitudes. It is given by

$$(\mathbf{J}^T \mathbf{R}_d \mathbf{J} + \lambda \mathbf{W}^T \mathbf{R}_m \mathbf{W}) \Delta \mathbf{q}_k = \mathbf{J}^T \mathbf{R}_d \mathbf{g} - \lambda \mathbf{W}^T \mathbf{R}_m \mathbf{W} \mathbf{q}_k. \quad (4.3)$$

The details are described in section 1.4. This method is also known as an l_1 -norm or robust or blocky inversion method (Loke et al. 2003), whereas the conventional smoothness-constrained least-squares method as given in equation (4.2) is an l_2 -norm inversion method. The l_2 -norm inversion method gives optimal results where the subsurface geology exhibits a smooth variation, such as the diffusion boundary of a chemical plume. However, in cases where the subsurface consists of bodies that internally homogeneous with sharp boundaries (such as an igneous dyke), this method tends to smear out the boundaries. The l_1 -norm or blocky optimization method tends to produce models that are piecewise constant (Ellis and Oldenburg, 1994a). This might be more consistent with the known geology in some situations.

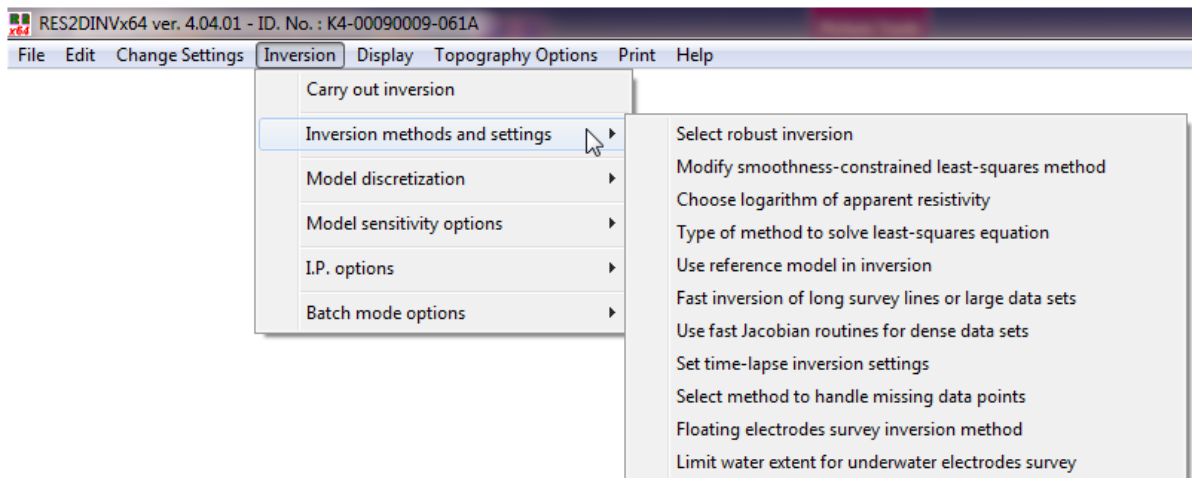


Figure 39. Different options to modify the inversion process.

Figure 40 shows the inversion results for data from a synthetic model with sharp boundaries. In this case, the robust inversion method gives significantly better results since the true model consists of three homogenous regions with sharp boundaries. Many synthetic test models are of a similar nature with sharp boundaries, so not surprisingly, results obtained with the l_2 -norm smooth inversion method are not optimal for such data sets (Olayinka and Yaramanci, 2000).

Resistivity values have a logarithmic range, possibly ranging from less than 1 to over 1000 $\Omega\cdot\text{m}$ in a single data set. By using the logarithm of the resistivity values as the parameters in the inversion process, the numerical range of the parameters can be reduced to a linear range. However, in some situations, it is not possible to make use of the logarithm if there are negative or zero values. This does not usually occur for normal surface surveys with the standard arrays, but could occur in borehole surveys or if non-standard arrays are used.

The program also allows the use to use the apparent resistivity value directly as the inversion parameter in the “Choose logarithm of apparent resistivity” option.

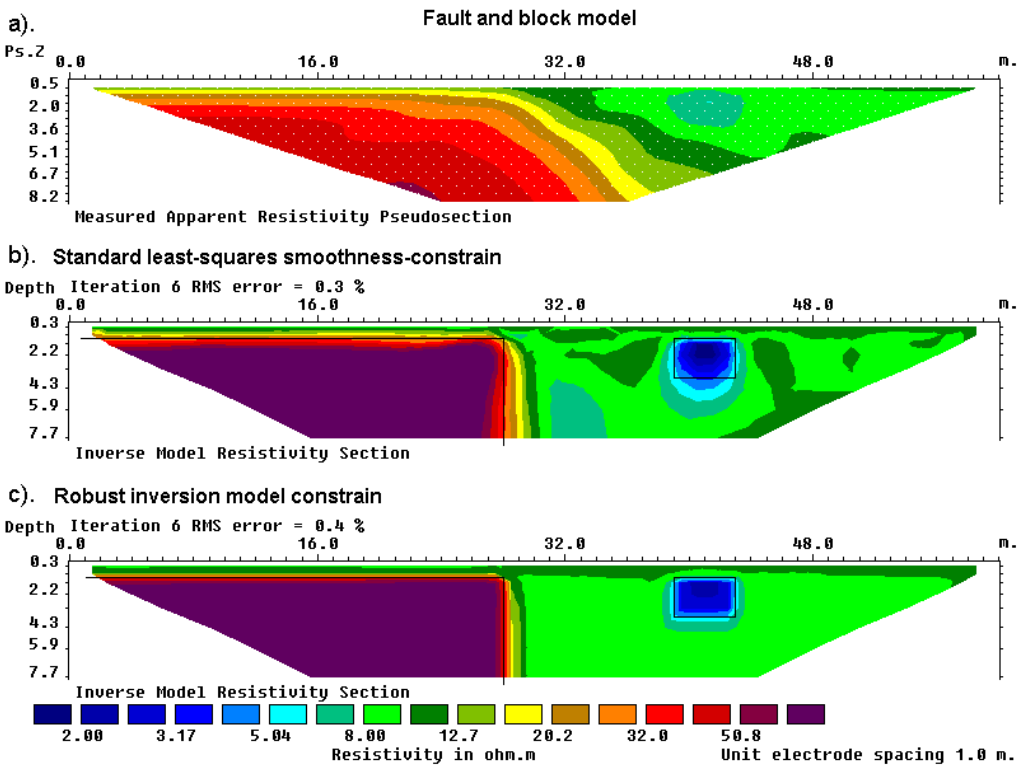


Figure 40. Example of inversion results using the l_2 -norm smooth inversion and l_1 -norm blocky inversion model constrains. (a) Apparent resistivity pseudosection (Wenner array) for a synthetic test model with a faulted block ($100 \Omega\cdot\text{m}$) in the bottom-left side and a small rectangular block ($2 \Omega\cdot\text{m}$) on the right side with a surrounding medium of $10 \Omega\cdot\text{m}$. The inversion models produced by (b) the conventional least-squares smoothness-constrained or l_2 -norm inversion method and (c) the robust or l_1 -norm inversion method.

The setting ‘Type of method to solve least-squares equation’ provides two numerical methods to solve the least-squares equation (as in equations 4.1 to 4.3). The default method, particularly when the number of model parameters n is small, is the standard (or complete) Gauss-Newton method where a direct method (Golub and van Loan, 1989) is used to solve the equation. This method produces an exact solution but as the time taken is proportional to n^3 , it could take a very long time for large data set with over 5000 model cells. An alternative method, the incomplete Gauss-Newton method, can be used for such cases. In the incomplete Gauss-Newton method, an approximate solution of the least method is determined by using an iterative method (Golub and van Loan, 1989). The final solution obtained with this method has a difference of about 1 to 2 percent compared to the complete Gauss-Newton method solution. By sacrificing a small amount of accuracy in the solution to the least-squares equation, the computer time required could be reduced by a factor of 5 to 10 times for very large models.

b). Model discretization

This set of options control the way the program subdivides the subsurface into rectangular cells. By default, the program uses a heuristic algorithm partly based on the position of the data points to generate the size and position of the model blocks. In the default

algorithm used, the depth to the deepest layer in the model is set to be about the same as the largest depth of investigation of the data points, and the number of model cells does not exceed the number of data points. The thickness of each deeper layer is increased to reflect the decreasing resolution of the resistivity method with increasing depth. In general, this produces a model where the thickness of the layers increases with depth, and with thicker cells at the sides and in the deeper layers (Figure 41a). For most cases, this gives an acceptable compromise. The distribution of the data points in the pseudosection is used as a rough guide in allocating the model cells, but the model section does not rigidly follow the pseudosection. However, the user can change the width and thickness of the cells using a variety of options.

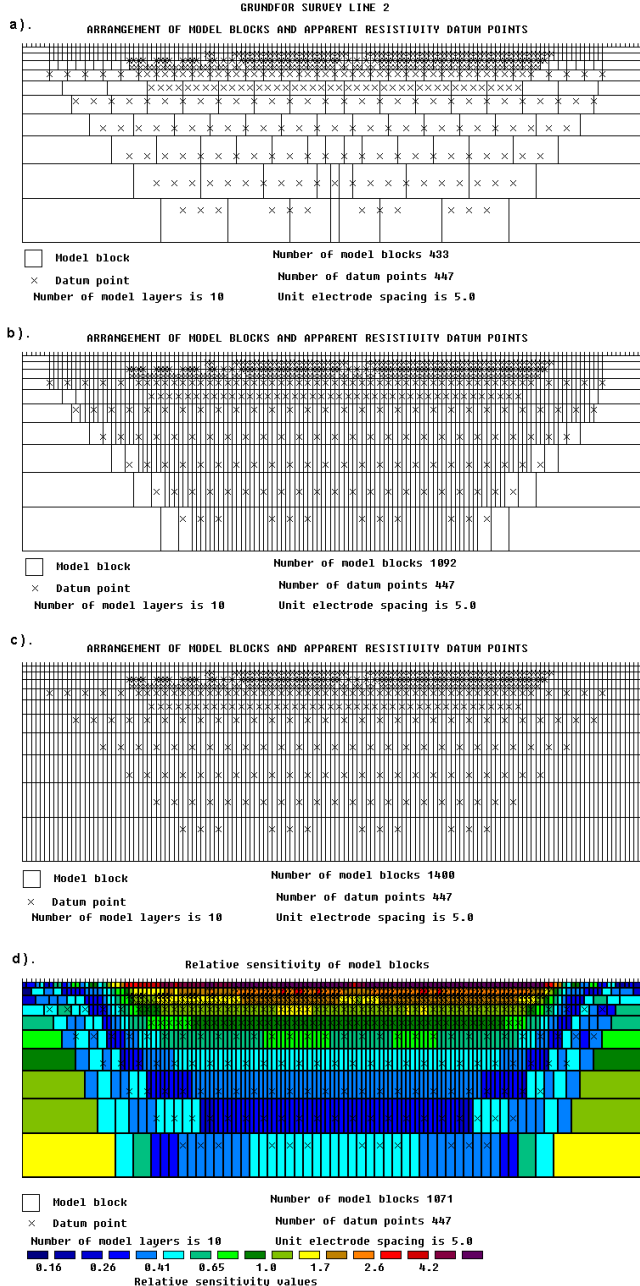


Figure 41. Different methods to subdivide the subsurface into rectangular prisms in a 2-D model. Models obtained with (a) the default algorithm, (b) by allowing the number of model cells to exceed the number of data points, (c) a model which extends to the edges of the survey line and (d) using the sensitivity values for a homogeneous earth model.

After reading a data file, clicking the ‘Display model blocks’ option will show the distribution of the model cells currently used by the program, such as in Figure 41. Clicking the ‘Change thickness of layers’ option will bring up the following dialog box.

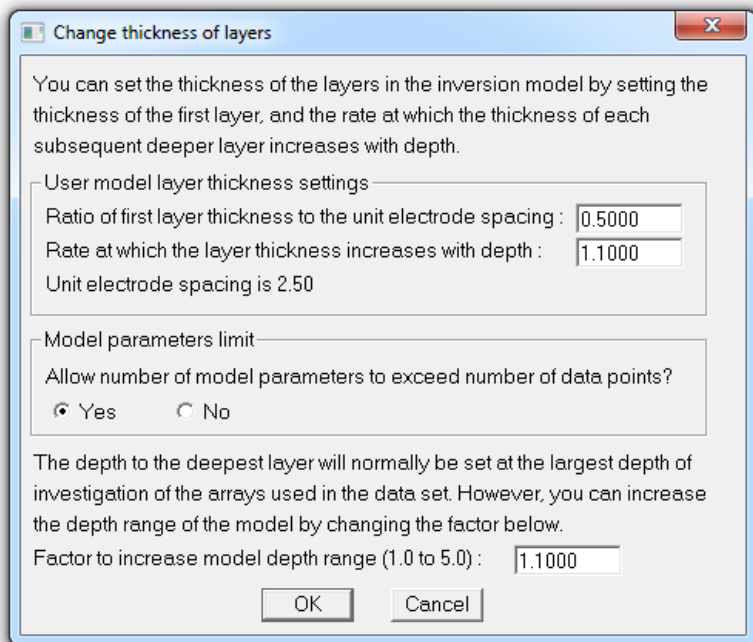


Figure 42. The options to change the thickness of the model layers.

When the program reads in a data file, it will normally set the first layer thickness using the minimum pseudodepth of the data points. For surface surveys, since the resolution decreases with depth, the thickness of the layers is normally increased by between 5 to 15 % with each deeper layer. The program normally uses a model where the depth to the deepest layer does not exceed the maximum pseudodepth in the data set. To use a model that spans a deeper depth range, you can change the factor to increase model depth range, for example from 1.0 to 1.30 to increase the model depth range by 30%. In this dialog box, you can also allow the program to use a model where the number of model cells exceeds the number of data points. This is useful to avoid having a model with very wide cells near the bottom for data sets with very sparse data sets. Figure 41b shows such an example with this option enabled.

The ‘Modify depth to layers’ option allows you to set the depth to each layer individually. This is useful if you want a layer boundary to coincide exactly with a known geological boundary.

In ‘Use extended model’ option, model cells of uniform thickness right up to the left and right edges of the survey line are used (Figure 41c). This is probably an extreme case. As the number of model parameters increase, the computer time needed to carry out the inversion also increases. This can be an important consideration for very large data sets with several hundred electrodes. The ‘Make sure model blocks have same widths’ option is probably more useful. It uses a base model such as in Figure 41b, but avoids thicker cells at the sides. It ensures that the cells at the sides to have the equal widths.

The ‘Reduce effect of side blocks’ option affects the calculation of the Jacobian matrix values for the model cells located at the sides and bottom of the model section. Normally, for a cell located at the side, the contributions by all the mesh elements associated with the model cell are added up right to the edge of the mesh. This gives a greater weight to the side cell compared to the interior cells. In some cases, particularly when the robust

inversion option is used, this can result in unusually a high or low resistivity value for the side cell. This option leaves out the contribution of the mesh elements outside the limits of the survey line to the Jacobian matrix values for the side cells.

The last two options, 'Change width of blocks' and 'Type of cross-borehole model', are only used for certain special cases, and will not be described here. Please refer to the RES2DINV.PDF manual for the details.

c). Model sensitivity options

This set of options relate to the model sensitivity (Jacobian matrix) values. The 'Display model blocks sensitivity' option will display the sum of the absolute values of the sensitivity values associated with the model cell. Figure 41d shows an example. Note the blocks at the sides and bottom has greater sensitivity values due to the larger sizes. To avoid this effect, the 'Display subsurface sensitivity' option divides the subsurface into cells of equal size and shows the sensitivity values. This is useful to get an idea of the regions of the subsurface "scanned" by the survey configuration used.

All the techniques used to subdivide the subsurface described in the earlier section are based on heuristic algorithms. Figure 41d shows the block distribution generated by a more quantitative approach based the sensitivity values of the model cells. This method is selected by the 'Generate model block' option. This technique takes into account the information contained in the data set concerning the resistivity of the subsurface for a homogeneous earth model. It tries to ensure that the data sensitivity of any cell does not become too small (in which case the data set does not have much information about the resistivity of the cell).

The next set of inversion options are grouped below the 'Change Settings' choice on the main menu bar. Clicking this will bring up the list of options shown in **Error! Reference source not found..**

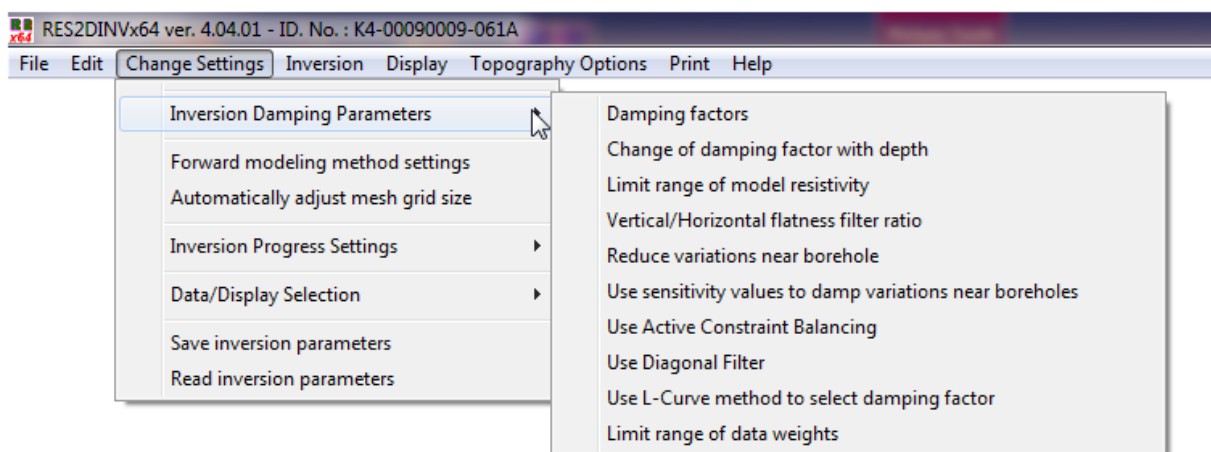


Figure 43. The options under the 'Change Settings' menu selection.

d). INVERSION DAMPING PARAMETERS

This set of options is related to the damping factor λ used in the least-squares equations (4.1) to (4.3). By default, the program uses a value of 0.16 for the initial damping factor value for the first iteration. The damping factor is decreased by about half after each iteration. However, to avoid instability in the model values due to a damping factor value that is too small, a minimum limit of 0.015 is used by the program.

The 'Damping factors' option allows you to set the initial damping factor and the minimum limit. If the data set appears to be very noisy, and unusually high or low model

resistivity values are obtained with the default values, try using larger values for the damping factors.

Since the model resolution decreases with depth, the program increases the damping factor value by about 5% for each deeper layer. You can change this factor using the ‘Change damping factor with depth’ option. Instead of automatically decreasing the damping factor by half after each iteration, the ‘Optimize damping factor’ option allows the program to look for an optimum damping factor. The time taken per iteration will be more, but fewer iterations might be needed for the program to converge.

The ‘Limit range of model resistivity values’ option is intended for cases where the default settings (without limits) produces a model with resistivity values that are too high or too low. Selecting this option will bring up the dialog box shown in Figure 44. In this example, the upper limit for is 20 times the average model resistivity value for the previous iteration while the lower limit is 0.05 times (i.e. 1/20 times). The program uses “soft” limits that allow the actual resistivity model values to exceed the limits to a certain degree. However, this option will avoid extremely small or large model resistivity values that are physically unrealistic.

The ‘Vertical/Horizontal flatness filter ratio’ option allows the user to fine-tune the smoothness-constrain to emphasize vertical or horizontal structures in the inversion model. Some geological bodies have a predominantly horizontal orientation (for example sedimentary layers and sills) while others might have a vertical orientation (such as dykes and faults). This information can be incorporated into the inversion process by setting the relative weights given to the horizontal and vertical flatness filters. If for example the structure has a predominantly vertical orientation, such as a dyke, the vertical flatness filter is given a greater weight than the horizontal filter.

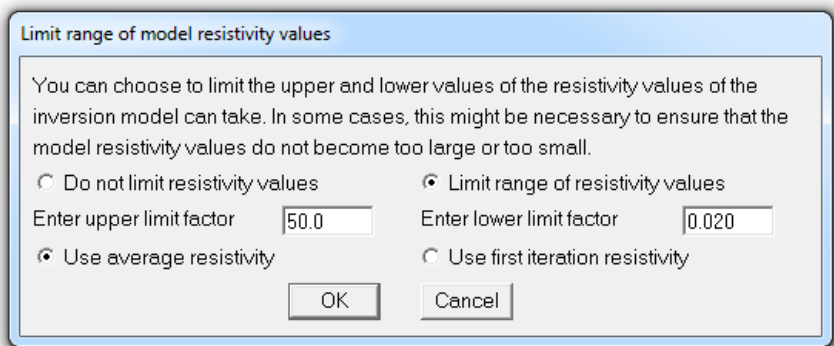


Figure 44. The dialog box to limit the model resistivity values.

e). Forward modeling method settings

This set of options controls the finite-element or finite-difference mesh used by the forward modeling subroutine. The ‘Finite mesh grid size’ option changes the mesh size in the *horizontal* direction, while the ‘Mesh refinement’ option changes the mesh settings in the *vertical* direction. Using a finer mesh normally increases the accuracy of the forward modeling subroutine, particularly if very large resistivity contrasts are present.

4.4 Using the model sensitivity and uncertainty values

The depth of investigation and sensitivity sections described in section 2.5 gives an idea of the depth of the regions sensed by a single electrode configuration. A 2-D survey typically has hundreds of data points collected with electrodes at different locations and spacings. A question that frequently arises in 2-D interpretation is as follows. What are the regions of the subsurface sensed by the survey, and what is the reliability of the results? The

first question can be easily determined, but at present there is no simple answer to the second.

The “Display blocks sensitivity” option under the “Inversion” menu will show a plot of the sensitivity of the cells used in the inversion model. The cumulative sensitivity value (see equation 2.17 in section 2.5.12) is a measure of the amount of information about the resistivity of a model block cell in the measured data set. The higher the sensitivity value, the more reliable is the model resistivity value. In general, the cells near the surface usually have higher sensitivity values because the sensitivity function has very large values near the electrodes. The cells at the sides and bottom can also have high sensitivity values due to the much larger size of these cells that are extended to the edges of the finite-difference or finite-element mesh (the program has an option to reduce this effect which might produce artifacts at the edges of the model). If you had carried out an inversion of the data set before calling this option, the program will make use of the Jacobian matrix of the last iteration. Otherwise, it will calculate the Jacobian matrix for a homogenous earth model. Figure 41d shows an example of a plot of the sensitivity section for a model.

Figure 45b shows the model section obtained from the inversion of a data set for a survey to map leakage of pollutants from a landfill site (Niederleithinger, 1994). The model sensitivity section in Figure 45c shows high sensitivity values near the surface with decreasing values with depth. This is to be expected as the near surface materials have a larger influence on the measured apparent resistivity values.

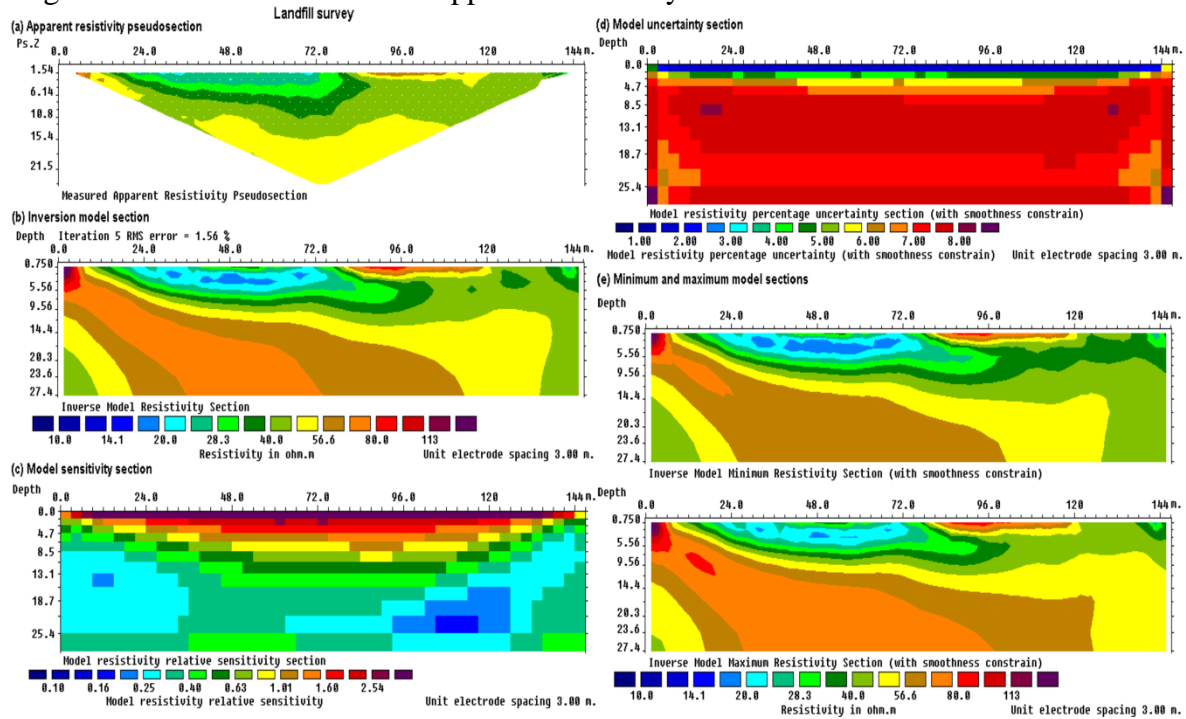


Figure 45. Landfill survey example (Wenner array). (a) Apparent resistivity pseudosection , (b) model section, (c) model sensitivity section (d) model uncertainty section, (e) minimum and maximum resistivity sections.

In order to assess the accuracy of the inversion model, an estimate of the reliability of the model values is required. One possible approach is by using the model covariance matrix (Menke, 1984). This is commonly used for models that consist of a small number of parameters (such as the 1-D model in Figure 7). Figure 45d shows the model uncertainty values obtained from the covariance matrix method as described by Alumbaugh and Newman (2000) where the smoothness constraint is included in the model uncertainty estimate. In this way, the model uncertainty values are less sensitive to size of the model cells. However, the uncertainty values are only meaningful if the subsurface resistivity varies in a smooth

manner, as assumed by the smoothness constraint. If the subsurface resistivity does not vary in a smooth manner, this method is likely to underestimate the actual uncertainty. Figure 45e shows the maximum and minimum resistivity values of each cell at the limits of the model uncertainty range. Features that are common to both model sections can be considered more reliable.

Table 5. Tests with different inversion options

Data set and purpose	Things to try
GRUNDFOR.DAT – An example of a field data with smooth variation of the resistivity values. The purpose is to see the effect of the different model discretizations. The purpose of this field survey was to map the soil lithology (Christensen and Sorenson 1994).	<p>(1). Read in the data set using the ‘File’ and then carry out the inversion with the default model discretization. You can take a look at the way the subsurface is divided into cells by selecting the ‘Display model blocks’ option.</p> <p>(2). Now choose the option to ‘Allow number of model blocks to exceed data points’, and run the inversion again. Make sure to use a different name for the inversion results file, for example GRUNFOR2.INV. Check out the arrangement of the cells again using the ‘Display model blocks’ option.</p> <p>(3). Now we will reduce the width of the side cells as well. Select the ‘Make sure model blocks have same widths’ option, and check out the arrangement of the cells. Next run the inversion again.</p> <p>(4). Finally we will use an arrangement with even more model cells. Select the ‘Use extended model’ option, and then run the inversion.</p> <p>As the number of model cells increase, the computer time increases. Which do you think is the best compromise between getting a finer model and reducing the computer time?</p>
BLOCK_ONE.DAT – A synthetic test model. To show advantage of robust l_1 norm inversion for models with sharp boundaries.	<p>(1). After reading in the data file, choose the ‘Include smoothing of model resistivity’ option to ensure inversion model is smooth. Run the inversion and see what you get. You might like to display the inversion model in the form of blocks rather than contours. This shows up the smearing out of the boundaries better. Compare the maximum and minimum model resistivity values with the true values.</p> <p>(2). Next select the ‘Select robust inversion’ option, and enable both the robust model and data constraints. Check out the resulting inversion model.</p>
ODARSLOV.DAT – A field data set with a vertical dike.	<p>(1). To get the best results, enable both the option to “Allow number of model blocks to exceed datum points”. Make sure the option ‘Include smoothing of model resistivity’ is on to get a maximally smooth model.</p> <p>(2). Next use the robust inversion method. You should see a dramatic change in the model.</p> <p>(3). One of the undesirable side effects of the robust inversion option is the model resistivity values at the bottom-left and bottom-right corners can take extreme values. To reduce this effect, select the ‘Reduce effect of side blocks’ option, and then run the inversion again.</p>

A different approach is to empirically determine the depth of investigation of the data set by carrying out at least two inversions of the data set using different constraints. Oldenburg and Li (1999) used the following least-squares formulation to carry out the 2-D inversion.

$$(\mathbf{J}^T \mathbf{J} + \lambda \mathbf{F}_R) \Delta \mathbf{q}_k = \mathbf{J}^T \mathbf{R}_d \mathbf{g} - \lambda \mathbf{F}_R (\mathbf{q}_k - \mathbf{q}_o), \quad (4.4)$$

with $\mathbf{F}_R = \alpha_s + \alpha_x \mathbf{C}_x^T \mathbf{R}_m \mathbf{C}_x + \alpha_z \mathbf{C}_z^T \mathbf{R}_m \mathbf{C}_z$.

\mathbf{q}_o is a homogeneous half-space reference model and α_s is an additional “self” damping factor that has a value of about 0.0001 to 0.01 times the α_x and α_z damping factors. In the proposed method, two inversions are carried out using different resistivity values for the reference model. Typically, the second reference model has a resistivity of 10 to 100 times the first reference model. From the model resistivity values, the following depth of investigation (DOI) index is calculated.

$$R(x, z) = \frac{m_1(x, z) - m_2(x, z)}{m_{1r} - m_{2r}} \quad (4.5)$$

m_{1r} and m_{2r} are the resistivity of first and second reference models, $m_1(x, z)$ and $m_2(x, z)$ are model cell resistivity obtained from the first and second inversions. R will approach a value of zero where the inversion will produce the same cell resistivity regardless of the reference model resistivity. In such areas, the cell resistivity is well constrained by the data. In areas where the data do not have much information about the cell resistivity, R will approach a value of one as the cell resistivity will be similar to the reference resistivity. Thus the model resistivity in areas where R has small values is considered to be “reliable”, while in areas with high R values are not reliable.

The model used to calculate the DOI index use cells that extend to the ends of the survey line, and a depth range of about three to five times the median depth of investigation of the largest array spacing used. This ensures that data has minimal information about the resistivity of the cells near the bottom of the model, i.e. in theory the bottom cells have DOI values of almost 1.0.

Figure 46a shows the inversion model of the landfill survey data set with a depth range of about 3.5 times the maximum pseudodepth in the apparent resistivity pseudosection in Figure 45a. The resistivity of the reference model used is obtained from the average of the logarithms of the apparent resistivity values. Figure 46b shows the DOI plot calculated after carrying out a second inversion using a reference model with 100 times the resistivity of the first reference model. Oldenburg and Li (1999) recommended using a value of 0.1 as the cut-off limit for the effective depth of investigation of the data set. The depth to the contour with a DOI value of 0.1 is about 28 m. along most of the survey line. This is close to the maximum median depth of investigation of about 25 m. for this data set. There are shallower regions with high DOI value, particularly below the 50 m. mark. This is probably partly due to the low resistivity plume that limits the amount of current flowing into the deeper sections below it. The resistivity method uses the electrical current as a probing tool, and where the current flow is limited, the amount of information provided is less. Note the regions with high DOI values at the sides of the section. This is to be expected as the sides of the survey line have less data points compared to the center.

Figure 47 shows the DOI plot from a survey to map the boundary between the salt and fresh water zones across a beach in Denmark (Marescot and Loke, 2003). The profile is perpendicular to the seashore and the electrodes 1 to 16 are under the seawater, while the rest of the profile is above the water. Note the strong increase in DOI values on the left part of the profile that is covered with seawater. As this section is covered with seawater, most of the current actually flows within the seawater and does not penetrate into the subsurface. Thus the depth of investigation there is much shallower.

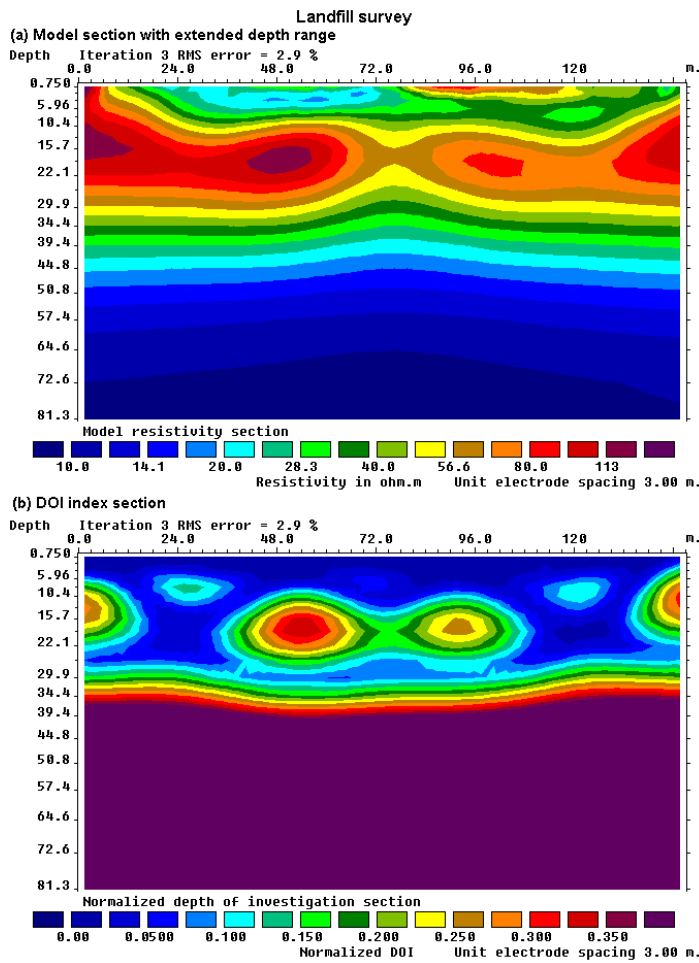


Figure 46. Landfill survey depth of investigation determination. (a) Model section with extended depths and (b) the normalized DOI index section.

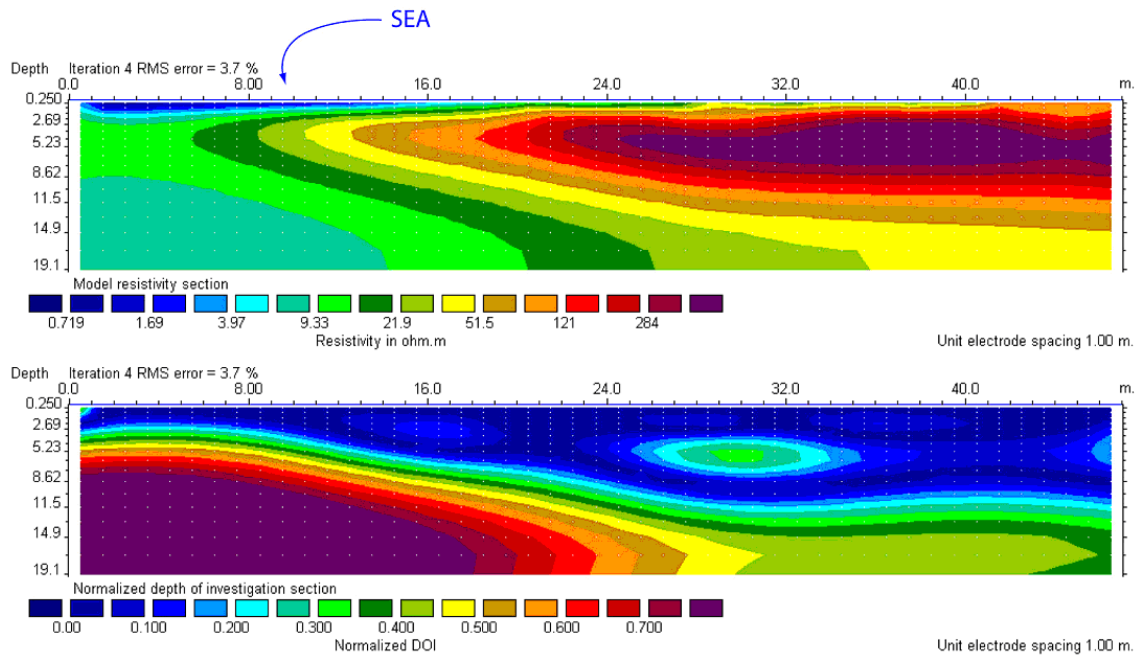


Figure 47. Beach survey example in Denmark. The figure shows the model section with extended depths and the normalized DOI index section.

The DOI method is useful in marking the regions where the model values are well constrained by the data set, and thus greater confidence can be placed on the model resistivity values at such regions. The DOI method may be considered an empirical method to determine the regions where we can reasonably resolve the subsurface. Another method based on the model resolution values is discussed in section 4.9.

4.5 Methods to handle topography

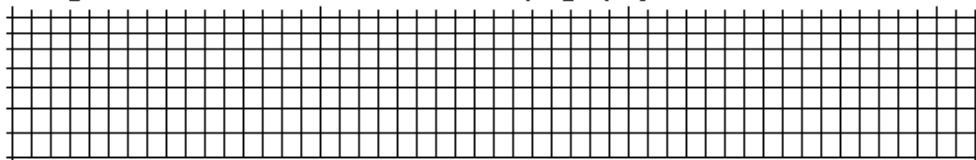
In surveys over areas with significant changes in the elevation of the ground surface, the effect of the topography must be taken into account when carrying out an inversion of the data set. It is now generally recognized that the traditional method of using the “correction factors” for a homogeneous earth model (Fox *et al.*, 1980) does not give sufficiently accurate results if there are large resistivity variations near the surface (Tong and Yang, 1990). Instead of trying to “correct” for the effect of the topography on the measurements, the preferred method now is to incorporate the topography into the inversion model. The RES2DINV program has three different methods that can be used to incorporate the topography into the inversion model (Loke, 2000).

The three methods are similar in that they use a distorted finite-element mesh. In all these methods, the surface nodes of the mesh are shifted up or down so that they match the actual topography. In this case, the topography becomes part of the mesh and is automatically incorporated into the inversion model. The difference between these three methods is the way the subsurface nodes are shifted. The simplest approach, used by the first finite-element method, is to shift all the subsurface nodes by the same amount as the surface node along the same vertical mesh line. This is probably acceptable for cases with a small to moderate topographic variation (Figure 48b).

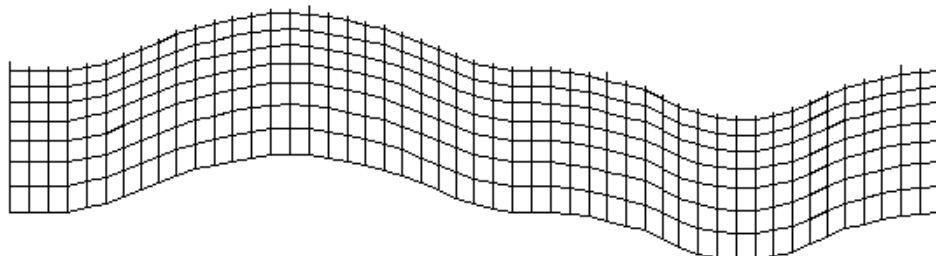
In the second approach, the amount the subsurface nodes are shifted is reduced in an exponential manner with depth (Figure 48c) such that at a sufficiently great depth the nodes are not shifted. This comes from the expectation that the effect of the topography is reduced or damped with depth. This produces a more pleasing section than the first finite-element method in that every kink in the surface topography is not reproduced in all the layers. For data sets where the topography has moderate curvature, this is probably a good and simple method. One possible disadvantage of this method is that it sometimes produces a model with unusually thick layers below sections where the topography curves upwards. Thus in Figure 48d, the model is probably slightly too thick near the middle of the line where the topography curves upwards and too thin towards the right end of the line where the topography curves downwards. The resulting model is partly dependent on the degree of damping chosen by the user. A value of 0.5 to 1.0 is usually used for the topography damping factor in the RES2DINV program. One main advantage of this method is that it can be easily implemented, particularly for 3-D models (Holcombe and Jirack, 1984).

In the third method, the inverse Schwartz-Christoffel transformation method (Spiegel *et al.*, 1980) is used to calculate the amount to shift the subsurface nodes (Loke, 2000). Since this method takes into account the curvature of the surface topography it can, for certain cases, avoid some of the pitfalls of the second finite-element method and produces a more “natural” looking model section (Figure 48e). For this data set, this method avoids the bulge near the middle of the line produced by the second finite-element method with a damped distorted mesh. However, in the middle part of the line, the model produced by this method is slightly thicker than that produced by the first finite-element method with a uniform distorted mesh.

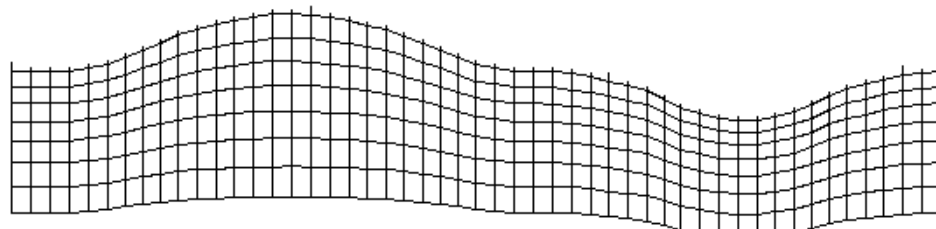
a). Arrangement of model blocks without topography



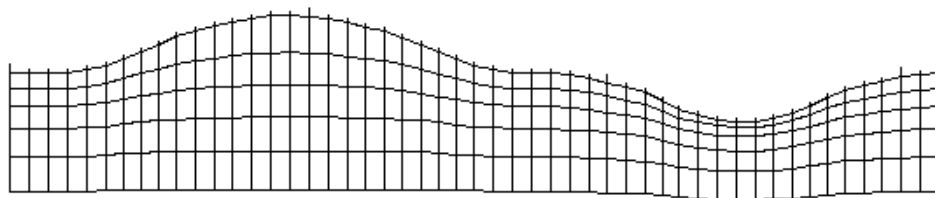
b). Arrangement of model blocks with a uniformly distorted grid



c). Arrangement of model blocks with a moderately damped distorted grid



d). Arrangement of model blocks with a highly damped distorted grid



e). Arrangement of model blocks with the inverse Schwartz-Christoffel transformation

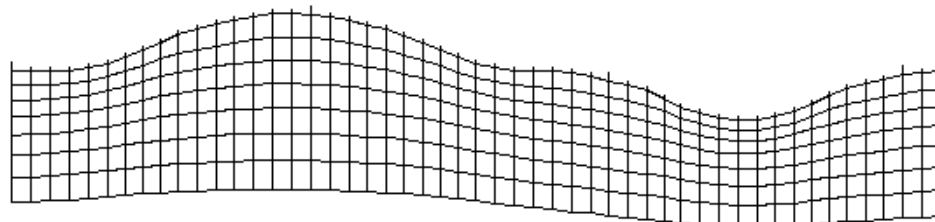


Figure 48. Different methods to incorporate topography into a 2-D inversion model. (a) Schematic diagram of a typical 2-D inversion model with no topography. A finite-element mesh with four nodes in the horizontal direction between adjacent electrodes is normally used. The near surface layers are also subdivided vertically by several mesh lines. Models with a distorted grid to match the actual topography where (b) the subsurface nodes are shifted vertically by the same amount as the surface nodes, (c) the shift in the subsurface nodes are gradually reduced with depth or (d) rapidly reduced with depth, and (e) the model obtained with the inverse Schwartz-Christoffel transformation method.

Table 6. Tests with different topographic modeling options

Data set and purpose	Things to try
RATCHRO.DAT – An example field data with significant topography. This survey was conducted over a possible ancient burial mound in Ireland (Waddell and Barton 1995).	<p>(1). After reading the data file, select the robust inversion option as the burial chamber probably has a sharp contrast with the soil. After that, click the ‘Display topography’ option under the ‘Topography Options’ in the Main Menu bar.</p> <p>(2). Next click the ‘Type of topographic modeling’ option. Select the uniformly distorted grid method. Run the inversion, and then switch to the ‘Display’ window to take a look at the results. In the ‘Display’ window, choose the ‘Display sections’ followed by ‘Include topography in model display’ options.</p> <p>(3). Now, select the damped distorted grid option in the ‘Type of topographic modeling’ dialog box. Run the inversion again, and then take a look at the model section with the topography. Now we will reduce the width of the side cells as well. Select the ‘Make sure model blocks have same widths’ option, and check out the arrangement of the cells. Next run the inversion again.</p> <p>(4). Next select the inverse Schwartz-Christoffel transformation method in the ‘Type of topographic modeling’ dialog box. Run the inversion again, and take a look at the model with the topography.</p> <p>Which topographic modeling method do you prefer?</p>
GLADOE2.DAT – A data set taken to check for leakage from a dam (Dahlin pers. comm.). The survey area has topography.	<p>(1). If you have the time, run the same tests as you did earlier for the RATHCRO.DAT data set.</p> <p>This is another example where the option to reduce the effect of the side cells makes a significant difference when the robust inversion option is used.</p>

4.6 Incorporating information from borehole logs and seismic surveys

In some areas, information from borehole logs is available concerning the resistivity of part of the subsurface. This program allows you to fix the resistivity of up to 1000 sections of the subsurface. The shape of the section to be fixed must be rectangular or triangular. Borehole logs give the resistivity of the formations along the borehole. However, some caution must be used when incorporating the borehole log information into an inversion model for surface measurements. Borehole measurements usually only give the resistivity of a very limited zone near the borehole. Depending on the type of instrument used, the borehole log generally samples the subsurface within about 1 meter from the borehole. In contrast, the inversion model gives the average resistivity of a much larger region of the subsurface. Thus the RES2DINV program uses a flexible method to incorporate the borehole log information.

The format used by the input data file for RES2DINV to fix the model resistivity values is described in detail in the RES2DINV manual. Here, we will only look at a fragment of it to illustrate the general ideas involved. As an example, part of the example data file

MODELFIX.DAT with the resistivity fixing option is listed below.

2	Number if regions to fix, put 0 if none
R	Type of first region, R for rectangular
24,0.7	X and Z coordinates of top-left corner of rectangle
28,2.3	X and Z coordinates of bottom-right corner of rectangle
2.0	Resistivity value of rectangular region
2.0	Damping factor weight
T	Type of second region, T for triangular
30,0.0	X and Z coordinates of first corner of triangle
30,3.0	X and Z coordinates of second corner of triangle
45,3.0	Coordinates of third corner of triangle
10.0	Resistivity value of triangular region
2.0	Damping factor weight

The first item is the number of regions where the resistivity is to be specified. In the example above, 2 regions are specified. If a value of 0 is given (default value), then there is no region where the resistivity is specified by the user. Next, the shape of the region is given, R for rectangular or T for triangular. If a rectangular region is specified, then the X and Z coordinates of the top-left and bottom-right corners of the rectangle are given, as shown in the Figure 49. If a triangular region is chosen, the X and Z coordinates of the 3 vertices of the triangle must be given in an anti-clockwise order. After the coordinates of the region to be fixed are given, the next data item is the resistivity of the region. After that, the damping factor weight for the resistivity of the region is needed. This parameter allows you control the degree in which the inversion subroutine can change the resistivity of the region. There is usually some degree of uncertainty in resistivity of the region. Thus, it is advisable that the program should be allowed (within limits) to change the resistivity of the region. If a damping factor weight of 1.0 is used, the resistivity of the region is allowed to change to the same extent as other regions of the subsurface model. The larger the damping factor weight is used, the smaller is the change that is allowed in the resistivity of the "fixed" region. Normally, a value of about 1.5 to 2.5 is used. If a relatively large value is used, for example 10.0, the change in the resistivity of the region would be very small during the inversion process. Such a large value should only be used if the resistivity and shape of the region is accurately known. Figure 50 shows the allocation of the cells in the subsurface model together with the fixed regions for the MODELFIX.DAT data set.

Seismic refraction and seismic reflection surveys are commonly used in engineering surveys. Both methods can give accurate and detailed profiles of the subsurface interfaces. In some cases, a distinct and sharp transition between two layers can be mapped by the seismic survey. This information can be used to improve the results from the inversion of a 2-D resistivity imaging survey along the same line. The subsurface in the inversion model can be divided into two zones, one above and one below the interface calculated from the seismic survey. The resistivity values are constrained to vary in a smooth manner within each zone, but an abrupt transition across the zone boundary is allowed by removing any constraint between the resistivity values below and above the zone boundary (Smith *et al.* 1999).

Figure 51 shows an example where the boundaries of a clay and a gravel layer were known from a seismic refraction survey (Scott *et al.*, 2000). The known boundaries were then incorporated into the resistivity inversion model (Figure 51a) that allows the model resistivity to change abruptly across the boundaries. Note the sharp contrast across the gravel layer and the underlying low resistivity clay layer (marked by the bottom blue region in lower section in Figure 51b).

Fixing model resistivities

Data format	Rectangular regions
R x ₁ , z ₁ x ₂ , z ₂ ρ 2.0	(x_1, z_1) (x_2, z_2)
Data format	Triangular regions
T x ₁ , z ₁ x ₂ , z ₂ x ₃ , z ₃ ρ 2.0	(x_1, z_1) (x_2, z_2)

Figure 49. Fixing the resistivity of rectangular and triangular regions of the inversion model.

Table 7. Tests with option to fix the model resistivity

Data set and purpose	Things to try
MODELFIX.DAT – A synthetic data file with two fixed regions.	(1). After reading the data file, select the robust inversion option as the synthetic model has sharp boundaries. Next choose the ‘Display model blocks’ option to take a look at the locations of the fixed regions. Run the inversion of the data set.
CLIF4_NORMAL.DAT – A data set from the Clifton, Birmingham area (Scott <i>et al.</i> 2000) to map layers within the unconsolidated sediments. CLIF4_LAYERS.DAT – The same data set but with the layers specified. The depths to the layers were determined from a seismic refraction survey.	(1). After reading in the CLIF4_NORMAL.DAT data file, select the robust inversion option, and then run an inversion of the data set. In this case, we have not included additional constraints on the inversion. You might have to use the option to “Reduce effect of the side blocks” to avoid distortions at the bottom-left and bottom-right corners of the inversion model. (2). Do the same for the CLIF4_LAYERS.DAT data file. In this file, the depths to two layers determined from a seismic refraction survey have been included. Take a look the distribution of the model cells, as well as the layers specified, using the ‘Display model blocks’ option. Run the inversion again, and compare the results with that obtained earlier without the layers.

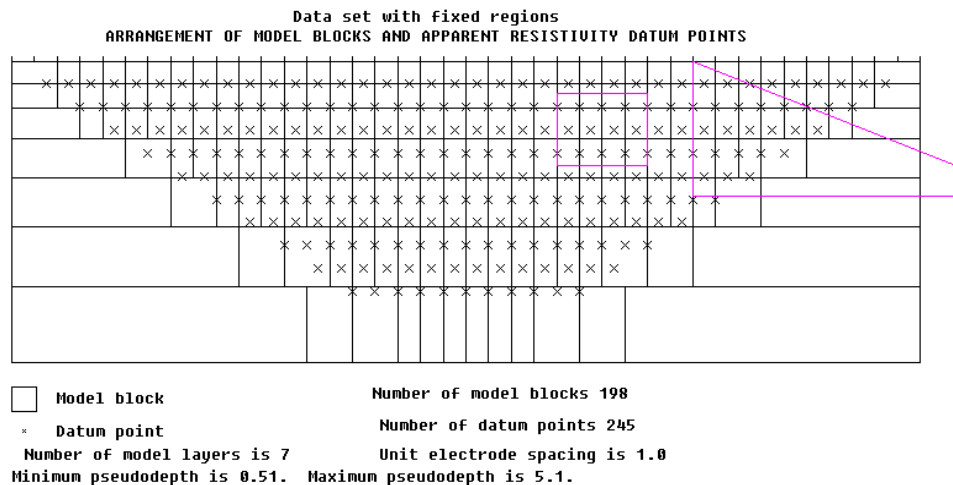


Figure 50. The inversion model cells with fixed regions. The fixed regions are drawn in purple. Note that the triangular region extends beyond the survey line.

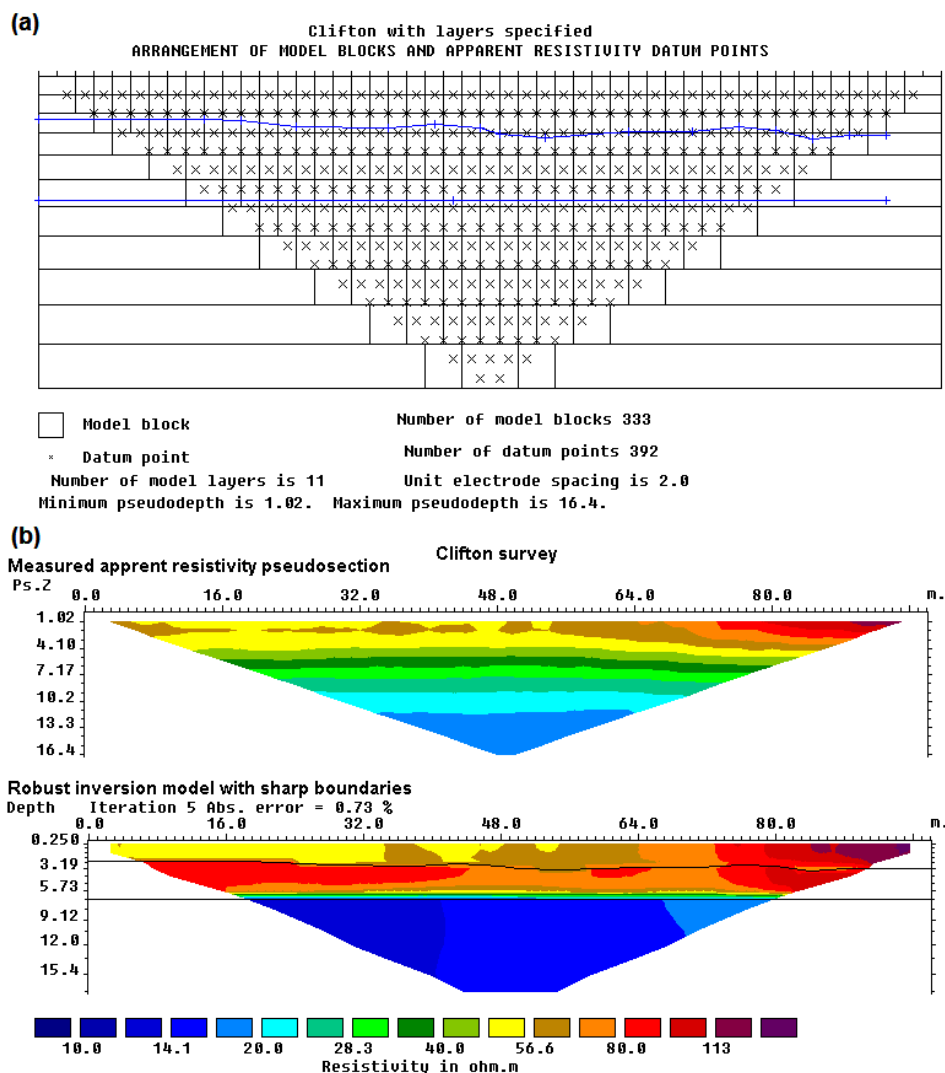


Figure 51. Example of an inversion model with specified sharp boundaries. (a) The boundaries in the Clifton survey (Scott *et al.*, 2000) data set is shown by the blue lines. (b) The measured apparent resistivity pseudosection and the inversion model section.

4.7 Model refinement

Normally RES2DINV uses a model where the width of the interior model cells is the same as the unit electrode spacing (for example as in Figure 51a). In some situations with large resistivity variations near the ground surface, this might not be sufficiently accurate. The model with a cell width of one unit electrode spacing has a maximum possible misfit of one-half the electrode spacing for a near-surface inhomogeneity (Figure 52a). In some cases, this misfit can cause significant distortions in the lower sections of the inversion model. The cell size is too coarse to accurately model the anomalies due to the small near-surface inhomogeneities. This forces the inversion program to distort the lower sections of the model in an attempt to reduce the data misfit.

A finer model with a cell width of half the electrode spacing has a maximum misfit of one-quarter the unit electrode spacing (Figure 52b), so the effect of the model cell boundary misfit should be much less. In theory, it is possible to reduce the cell width further, but the error due to the misfit becomes increasingly less significant. Reducing the cell increases the number of model parameters, thus increasing the computer time and memory required.

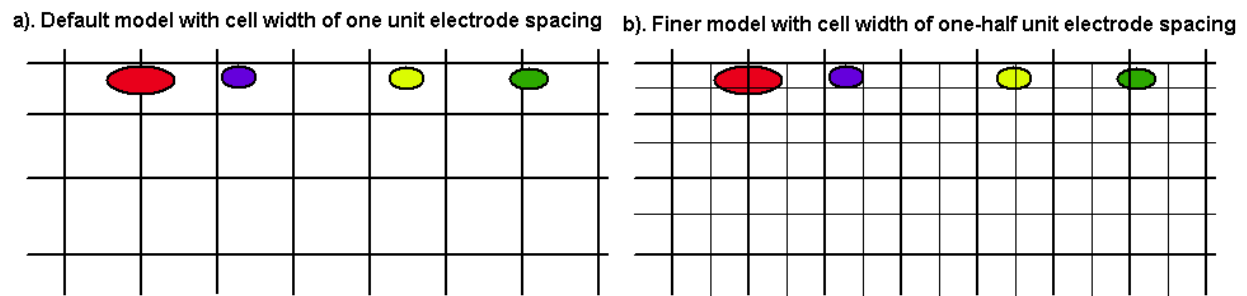


Figure 52. The effect of cell size on the model misfit for near surface inhomogeneities. (a) Model with a cell width of one unit electrode spacing. (b) A finer model with a cell width of half the unit electrode spacing. The near surface inhomogeneities are represented by coloured ovals.

Figure 53 shows a synthetic model used to illustrate the effect of the model cell misfit. The main structure is a faulted block of $100 \Omega\cdot m$ and a rectangular prism of $1 \Omega\cdot m$ in a medium of $10 \Omega\cdot m$. A series of small near-surface high resistivity blocks with widths of 1.0, 0.75, 0.50 and 0.25 m. and resistivity of $300 \Omega\cdot m$ are placed above the faulted block. A similar series of low resistivity blocks of $1.0 \Omega\cdot m$ are located to the left. The pole-dipole array has the P1-P2 dipole length ("a") fixed at 1.0 m., but with "n" factor ranging from 1 to 16. Note the strong anomalies produced by the near-surface inhomogeneities. Note also that the Wenner array is much less affected by the near-surface inhomogeneities. The reason lies in the sensitivity patterns of the two arrays (compare Figure 23 and Figure 30). For the pole-dipole array with large "n" values, the region with the highest positive sensitivity values is concentrated below the P1-P2 dipole pair.

Figure 54 shows the inversion results for the pole-dipole data set with different cell widths. The model with a cell width of 1.0 m. (i.e. one unit electrode spacing) shows significant distortions near the top of the faulted block as well as in the low resistivity rectangular block (Figure 54b). Most of the distortions are removed in the model with a cell width of half the unit electrode spacing (Figure 54c). This means the residual misfits with widths of up to one-quarter the unit electrode spacing does not have a significant effect on the calculated apparent resistivity values. The model with a cell width of one-quarter the unit electrode spacing (Figure 54d) does not show any major improvement over the half-cell width model although in theory it should more accurately model the near surface inhomogeneities. In fact, there is a poorer agreement with the true model in the lower part of

the faulted block (Figure 54d). Experiments with a number of data sets show that using a cell width of one-quarter the unit electrode spacing can sometimes lead to oscillating model resistivity values. This is probably because the data does not have sufficient information to accurately resolve such small cells.

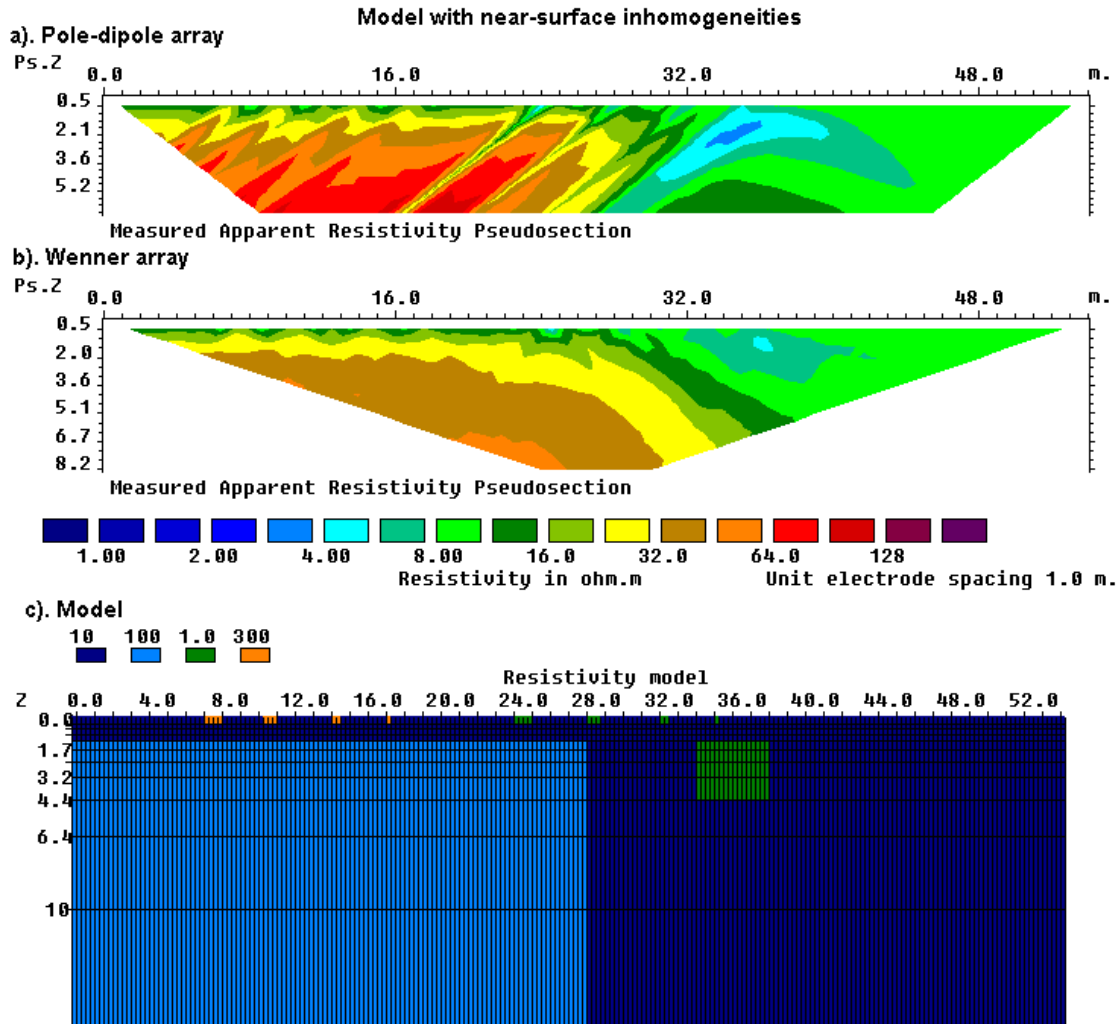


Figure 53. Synthetic model (c) used to generate test apparent resistivity data for the pole-dipole (a) and Wenner (b) arrays.

Figure 55 shows an example from a survey over an underground pipe using the Wenner-Schlumberger array. There are large resistivity variations near the surface, probably due to stones in the topmost layer of the soil. If the effect of the near surface variations are not accurately accounted for by the inversion model, it can lead to distortions in the lower portions of the model as the programs attempts to reduce the data misfit by distorting the lower part of the model. The model with a cell width of half the unit electrode spacing in Figure 55c shows a slightly better fit with the measured data (i.e. lower RMS error) and a more circular shape for the low resistivity anomaly below the 12 meters mark.

In conclusion, for most cases, using a cell width of half the unit electrode spacing seems to give the optimum results. Using a cell width of one-third the unit spacing seems to be beneficial only in certain cases with the pole-dipole and dipole-dipole arrays with very large 'n' values (see section 4.10). A cell width of one-quarter the unit spacing sometimes

leads to instability with oscillating model values, particularly in the first few layers. Thus the use of a cell width of less than one-quarter the true unit electrode spacing is not advisable.

Note that using finer cells will lead to longer inversion times, so using a width of the half the unit electrode spacing seems to provide the best trade-off. These examples present a strong case for using a model with a cell width of half the unit electrode spacing as the default choice in the inversion of most data sets. It avoids the problem caused by model cells boundary misfits if the cell is too coarse, and the increase in computer time is tolerable.

One effect of using finer model cells for some data set is the emergence of 'ripples' in the first couple of layers in the inversion model. Figure 56a shows the pseudosection from a survey in the Blue Ridge region in north-east USA (Seaton and Burbey, 2000). The inversion model using the blocky model inversion norm in Figure 56b show some rapid near-surface alternating resistivity values between the 160 and 240 meter marks. These artifacts can be significantly reduced by using a higher damping factor for the top layer as shown in Figure 56c.

As a final note, it appears that the effect of using narrower model cells is less dramatic in 3-D inversion. This is probably because in the 2-D model each cell extends to infinity in the y -direction, whereas in the 3-D model the same cell is divided into a large number of much smaller cells. Thus the effect of a single near-surface cell in the 3-D model on the calculated apparent resistivity values is much smaller than in the equivalent 2-D model.

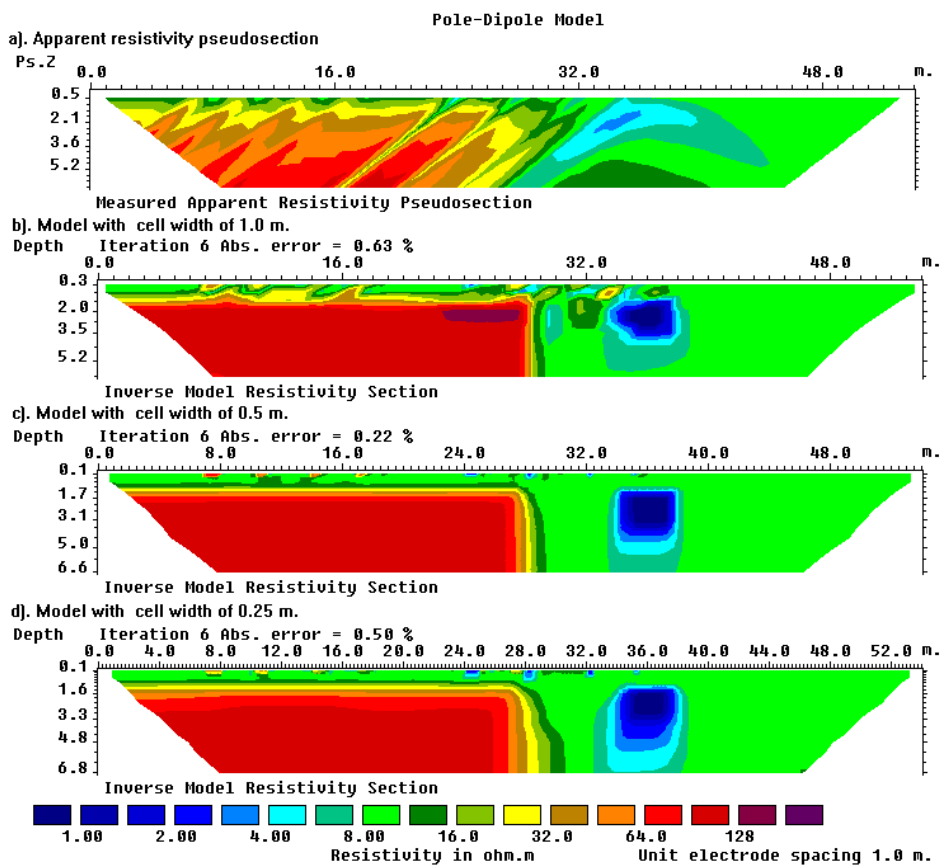


Figure 54. The effect of cell size on the pole-dipole array inversion model. Pole-dipole array. (a) The apparent resistivity pseudosection. The inversion models obtained using cells widths of (b) one, (b) one-half and (c) one-quarter the unit electrode spacing.

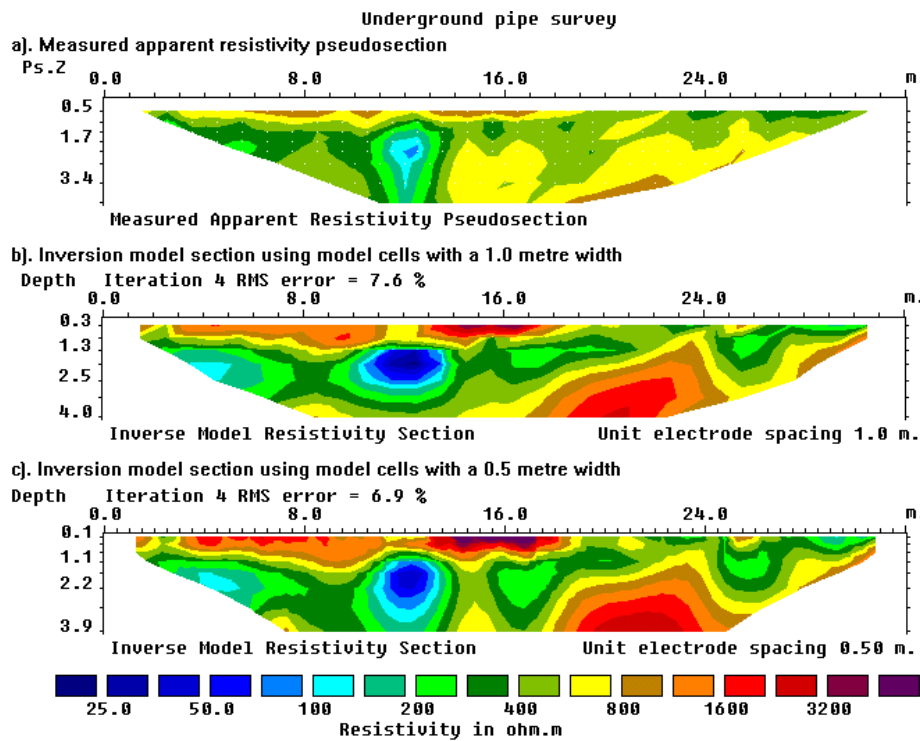


Figure 55. Example of the use of narrower model cells with the Wenner-Schlumberger array. (a) The apparent resistivity pseudosection for the PIPECHL.DAT data set. The inversion models using (b) cells with a width of 1.0 meter that is the same as the actual unit electrode, and (c) using narrower cells with a width of 0.5 meter.

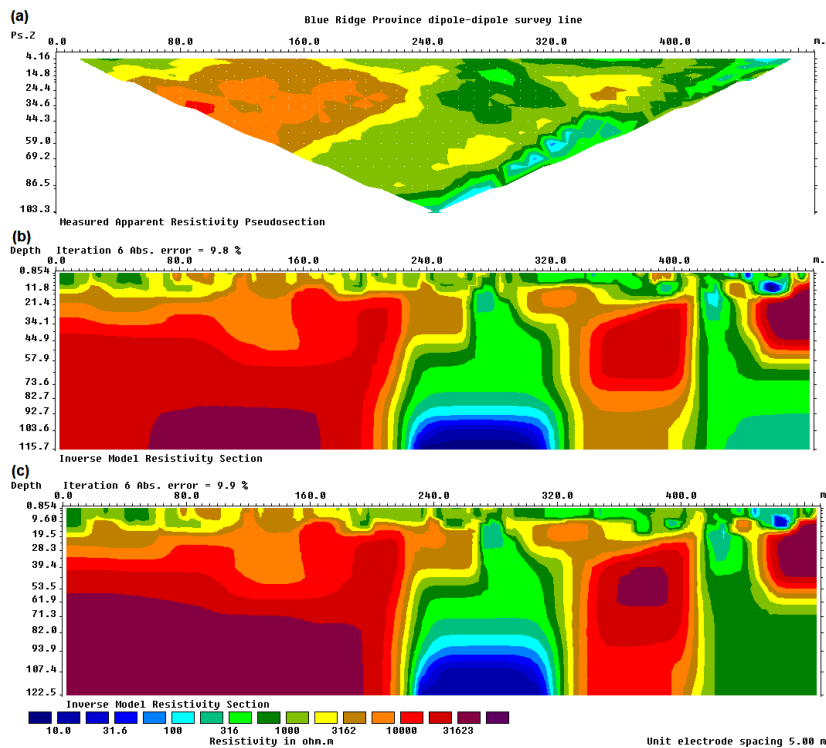


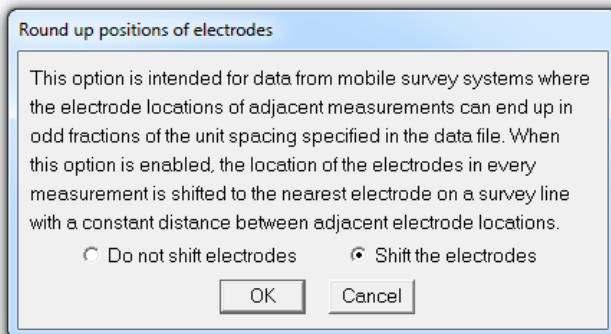
Figure 56. Example of reduction of near-surface 'ripples' in inversion model. (a) Apparent resistivity pseudosection for the BLUERIDGE.DAT data set. (b) Normal inversion using the robust inversion norm and model refinement. (c) Inversion using higher damping factor for first layer to reduce the 'ripple' effect in the top layer.

4.8 Fast inversion of long 2-D survey lines

Mobile resistivity systems such as the capacitive coupled systems or aquatic surveys (section 2.3) can produce very long survey lines. For example, a line can easily cover 10 kilometers with readings made at every 1 meter. Frequently only a very limited number of different array configurations are used, so the data density and maximum depth of investigation tends to be low compared with conventional systems. There are a number of techniques that can be used to greatly reduce the inversion time required for such data sets.

4.8.1 Preprocessing steps

While data measured using a standard multi-core cable system have electrode positions that are equally spaced, measurements made with a mobile system normally have the electrode positions that are not regularly spaced. Data collected with a multi-core cable system will have electrode positions with a minimum spacing equal to the spacing between adjacent takeouts on the cable. In contrast, data measured with a mobile system can have measurement positions that are much less than the minimum spacing between electrodes positions in the towed cable. To overcome the problem of measurement positions that are not equally spaced, the true electrode positions are rounded up to the nearest convenient chosen unit electrode spacing. A guide to an appropriate value to select for the 'unit electrode spacing' is the minimum takeout spacing in the cable. As shown in the previous section, the measured data is unlikely to resolve structures that are much less than the half the minimum spacing between electrodes in the cable. Thus a value of between half to one-quarter the minimum cable takeout spacing is usually used. As an example, if the minimum takeout spacing is 3 meters, a convenient value might be 1 meter. The program can automatically shift the positions of the electrodes for the data points using the 'File - Round up positions of electrode' option shown below.



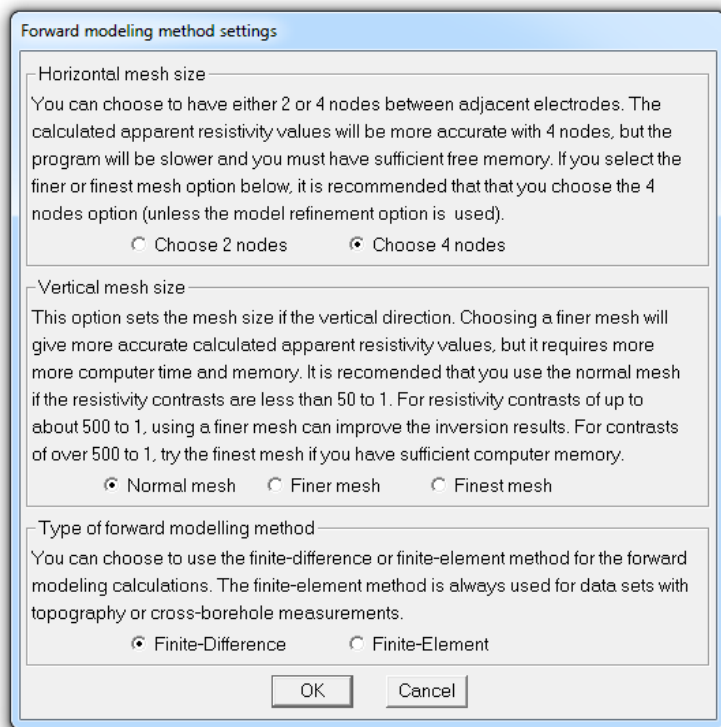
This will round up the positions of the electrodes for all the data points to the nearest unit electrode spacing specified in the data file. Once the data is in the correct format, we next look at ways to reduce the computer time needed to invert the data set.

4.8.2 Data set and computer system used for tests

The data set from an underwater survey where the cable was dragged along the bottom of a river will be used as an example. A section of the data set with a line length of nearly 2600 meters with a nominal unit electrode spacing of 1 meter is used (Figure 57a). The Res2dinvx64 program is used for the data inversion on a PC with a hex-core Intel i7 970 CPU.

4.8.3 Finite-element mesh size

For the underwater survey data set, the Res2dinv program will automatically use the finite-element method. Figure 58 shows part of the finite-element mesh used in calculating the potential values. The first setting we will look at is the horizontal mesh size. This setting is accessed via the 'Change Settings - Forward modeling methods settings' option that brings up the following dialog box.

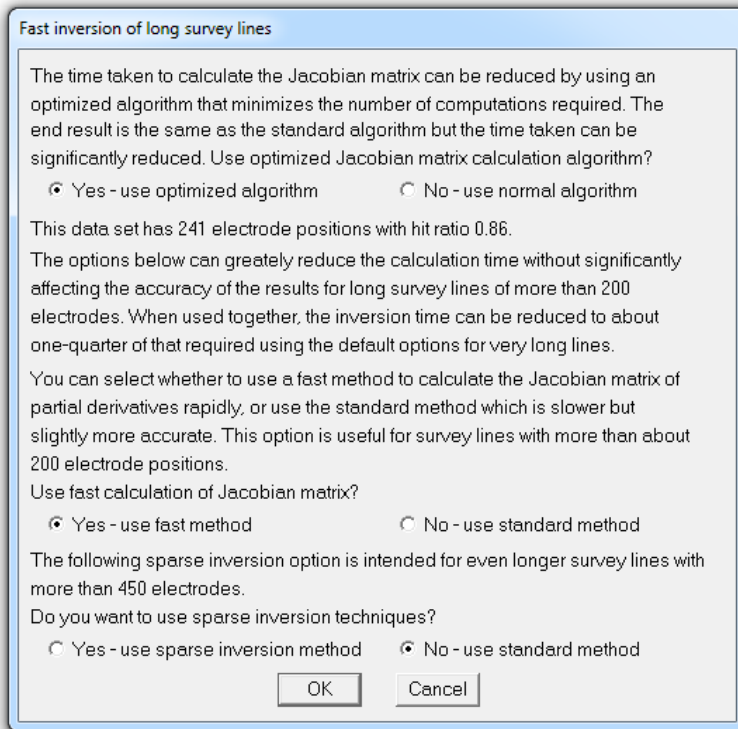


The program has options to use 2 or 4 nodes between adjacent electrodes. For a long survey line, the program automatically selects the 2 nodes option. Here we will examine the effect of using 2 or 4 nodes on the resulting inversion model. Normally selecting the 4 nodes option increases the accuracy of the finite element routine used. However, due to the nature of the data from a mobile survey, the effect might be minimal. There should be at least 4 horizontal nodes between two electrodes in an array used in a measurement. In mobile surveys, the distance between adjacent electrode positions is frequently much smaller than the electrode spacing in an array. The example in Figure 59 has a spacing of 1 meter between adjacent electrode positions but has an electrode spacing of 3 meter in an array. Thus there are 6 nodes between two electrodes in the same array although a 2 nodes spacing is used between adjacent electrode positions. As shown in Table 8, using 2 nodes instead of 4 nodes reduces the inversion time by almost half (from 2093 to 1074 seconds) for the test data set. The effect on the resulting inversion model is minimal as shown by Figure 57b,c. The difference in the data misfit is only about 0.1% and there are no obvious differences in the model sections.

4.8.4 Limit calculation of Jacobian matrix values

The program normally calculates the Jacobian matrix values for all the model cells for every data point. The data set in Figure 57 has 2293 data points while the inversion model has 11673 cells. The Jacobian matrix value at a model cell far from the electrodes used in a measurement is likely to be very small, and can be neglected without significantly affecting the resulting inversion model. This option is accessed via the 'Inversion - Inversion methods and settings - Fast inversion of long survey lines'. Selecting the 'Fast calculation of Jacobian matrix' option will limit the calculation for model cells that are 'close' to the electrodes in the

array. This further reduces the calculation time by about 14% (Table 8), while the inversion model (Figure 57d) is essentially identical to the one obtained with the full Jacobian matrix (Figure 57c).



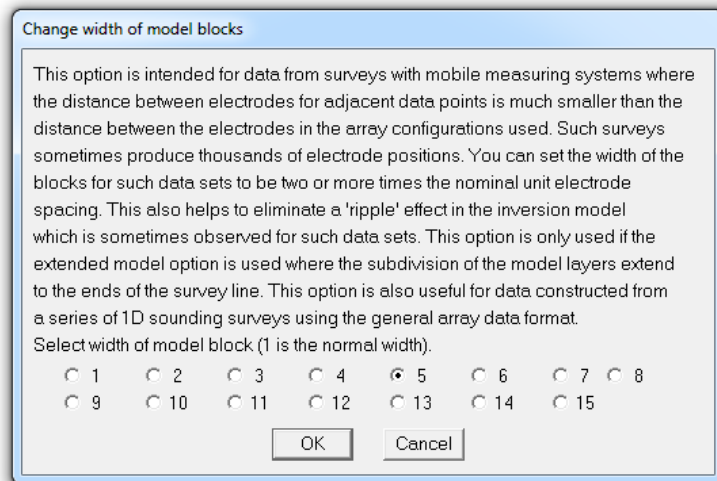
4.8.5 Use sparse inversion techniques

Mobile electrical resistivity imaging surveys can have thousands of electrode positions, data points, and model cells. Because long survey lines results in a finite-element grid where the number of nodes in the horizontal direction is very much greater than the number of nodes in the vertical direction, the calculation time can be greatly reduced by splitting up the finite-element grid into a number of overlapping sub-grids. This also automatically reduces the size of the Jacobian matrix as well. This method is enabled using the 'sparse inversion techniques' option in the above dialog box. This method will still produce a contiguous model along the entire survey line, but takes advantage of the segmented finite-element grid and sparse nature of the Jacobian matrix to reduce the number of calculations needed. Using this option makes a major reduction in the calculation time (by nearly a factor of 5 times) to 210 seconds, while the resulting inversion model (Figure 57e) does not show significant differences from previous models.

4.8.6 Use wider cells

The smallest spacing between two electrodes used in the same array for the data set is 3 meters while the width of the model cells is 1 meter. Since we have seen that most arrays are unlikely to resolve structures less than half the minimum array electrode spacing, we next examine the use of coarser model cells. This is accessed via the 'Inversion - Model discretization - Change width of model blocks' option that brings up the following dialog box. Selecting a value of '2' will create a model where the cells have widths of twice the nominal unit electrode spacing (1 meter in this example). The resulting models with cells widths of 2 and 3 meters are shown in Figure 57f,g. Using a model cell width of 2 meters gives a significant reduction in the calculation time of about 15% with very small changes in the resulting inversion model. This probably provides the best compromise for this data set. As a general guide, using a slight smaller cells width of about one-third to two-thirds the smallest

electrode spacing in the arrays used seems to provide the best results.



4.8.7 Overview of methods to reduce the calculation time

The methods described have reduced the calculation time for the example data set by more than a factor of 10, from 2093 to 181 seconds. Table 9 shows the inversion times for data sets from the same survey with different line lengths. Note the largest data set with nearly 7500 electrode positions takes less than 17 minutes on an inexpensive desktop PC. The inversion of a 10 kilometers survey line with a nominal unit electrode spacing of 1 meter will take less than 30 minutes. The field survey time will certainly be much longer than the data inversion time.

Table 8. Inversion times for the long Redas survey data set using different settings.

Trial	Setting used	Time (s)
1	Standard settings with 4 nodes between adjacent electrodes.	2093
2	Standard settings with 2 nodes between adjacent electrodes.	1074
3	Use fast calculation of Jacobian matrix values	934
4	Use sparse inversion techniques	210
5	Use 2 meter model cells	181
6	Use 3 meter model cells	171

Table 9. Inversion times for different line lengths.

Length (m.)	No. of electrodes	No. of data points	No. of model cells	Time (s)
1589	1413	1244	6354	78
2912	2595	2293	11673	181
4099	3672	3252	16524	290
8329	7479	6636	33651	995

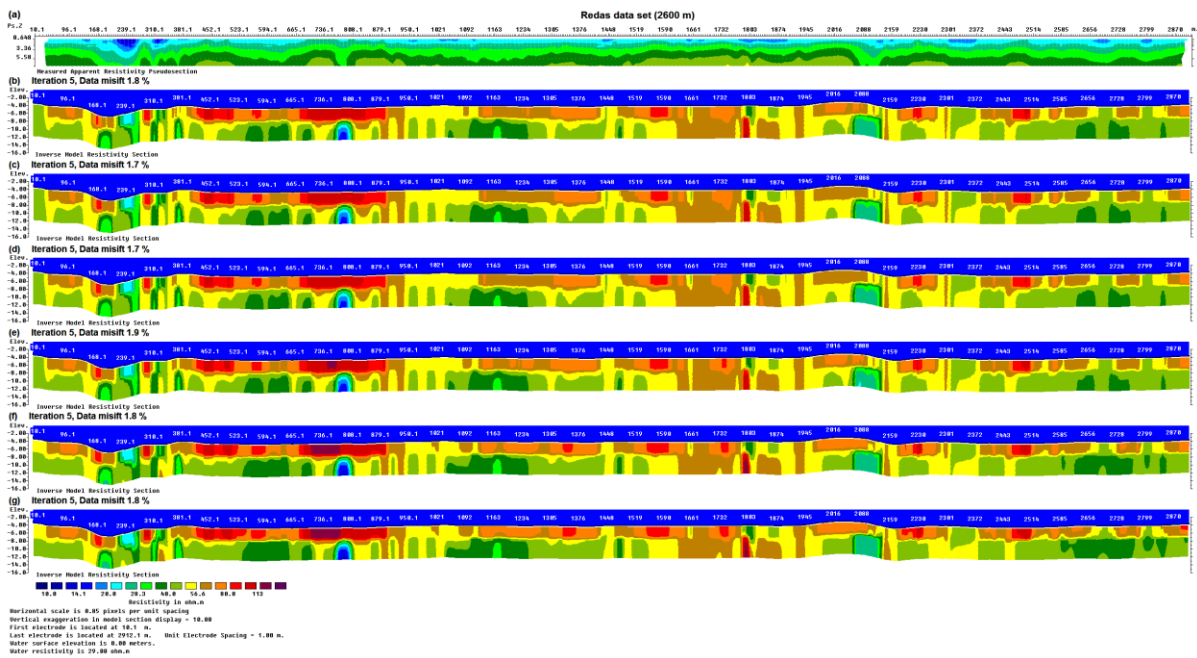


Figure 57. Inversion models for a long survey line using different settings to reduce the calculation time. (a) The measured apparent resistivity pseudosection for the Redas underwater survey for the first 2600 meters. Inversion models using (b) standard inversion settings with 4 nodes between adjacent electrode positions, (c) standard inversion settings with 2 nodes between adjacent electrode positions, (d) with calculation of Jacobian matrix values for selected model cells, (e) with sparse inversion technique, (f) with 2 meter model cell width and (g) with 3 meter model cell width.

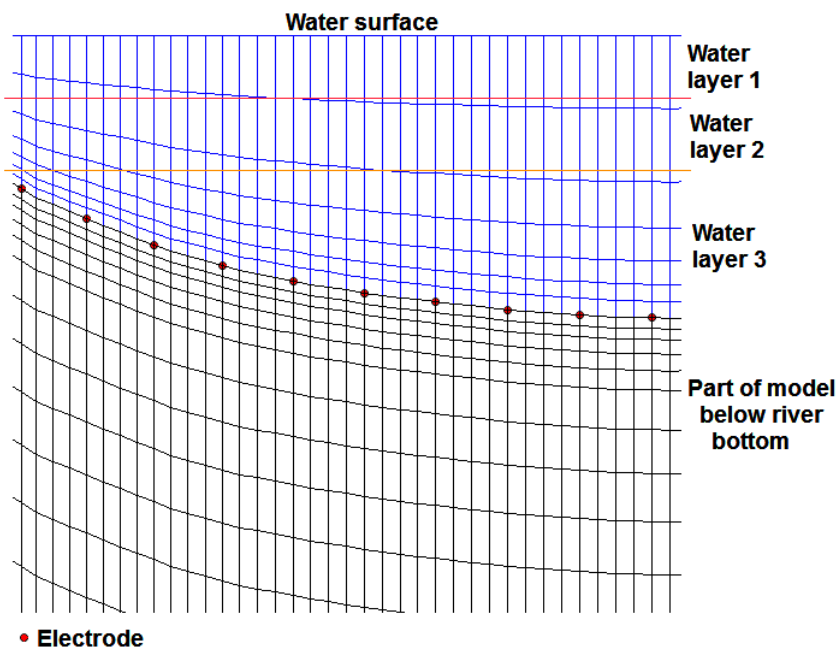


Figure 58. Part of finite-element mesh used to model a survey with submerged electrodes. The resistivity of mesh cells in the water layer are fixed at the known water resistivity.

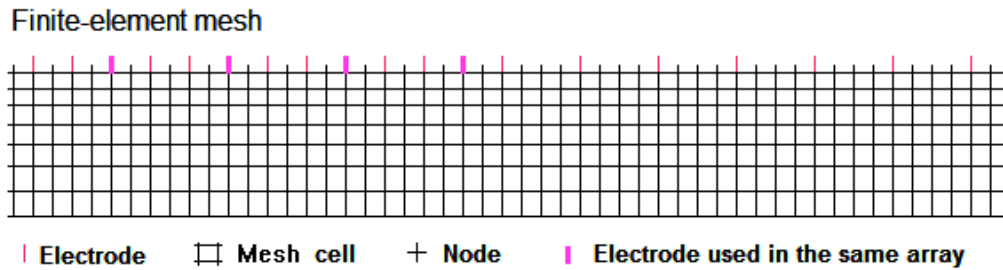


Figure 59. Part of a finite-element mesh for a long survey line. The electrodes used in the same array are 3 meters apart, while the data unit electrode spacing is 1 meter. Using 2 nodes between adjacent electrodes in the mesh will actually result in 6 nodes between electrodes in the same array.

4.9 Model resolution and automatic array optimization methods

4.9.1 Concept of model resolution

The sensitivity functions plots are useful explaining the behavior of common arrays, but they only tell us the characteristics of each individual array. This will help in selecting an array for certain structures, eg. for predominantly horizontal or vertical structures. However, a survey consists of many measurements with different spacings and horizontal positions along the line. The cumulative sensitivity values described in the previous section is a simple method to combine the sensitivity values from different measurements. It can be calculated rapidly but it is not mathematically rigorous. Our purpose in carrying out the survey is to detect or resolve structures below the survey line. How do we quantify the model ‘resolution’?

The model resolution equation (Day-Lewis *et al.*, 2005) is related to the least-squares equation used for the inversion for resistivity data described earlier in section 1.4.

$$(\mathbf{J}^T \mathbf{J} + \lambda \mathbf{F}) \Delta \mathbf{q}_k = \mathbf{J}^T \mathbf{g} - \lambda \mathbf{F} \mathbf{q}_k, \quad (4.6)$$

Using linear approximations, it can be shown that the relation between the calculated model resistivity and the true resistivity is approximately given by

$$\mathbf{q}_{\text{Model}} \approx \mathbf{R} \mathbf{q}_{\text{True}},$$

where

$$\mathbf{R} = (\mathbf{J}^T \mathbf{J} + \lambda \mathbf{F})^{-1} \mathbf{J}^T \mathbf{J} \quad (4.7)$$

The model resolution matrix \mathbf{R} may be viewed as a filter through which the inversion method attempts to resolve the subsurface resistivity. In the ideal case with perfect resolution, the elements of the main diagonal (R_{jj}) are 1 while the off-diagonal elements are 0.

4.9.2 A heuristic explanation of model resolution – through a glass darkly

This section attempts to give an illustration of model resolution in a less mathematical manner. The effect of the model resolution matrix can be shown diagrammatically below. Consider an original optical image used in testing eyesight, such as

A B C

A person with less than perfect eyesight might see it as

A B C

Someone with very poor eyesight might see it as

ABC

The matrix \mathbf{R} might be considered as a ‘blurring’ matrix which contaminates the calculated value with values from nearby cells. To illustrate it in terms of the model used in resistivity inversion, consider a simple model with only 4 cells.

Model with 4 cells

q_1	q_2
q_3	q_4

This can be written in matrix form as

$$\begin{pmatrix} q_{M1} \\ q_{M2} \\ q_{M3} \\ q_{M4} \end{pmatrix} = \begin{pmatrix} R_{11} & R_{12} & R_{13} & R_{14} \\ R_{21} & R_{22} & R_{23} & R_{24} \\ R_{31} & R_{32} & R_{33} & R_{34} \\ R_{41} & R_{42} & R_{43} & R_{44} \end{pmatrix} \begin{pmatrix} q_{A1} \\ q_{A2} \\ q_{A3} \\ q_{A4} \end{pmatrix}$$

$\mathbf{q}_{\text{Model}} = \mathbf{R} \mathbf{q}_{\text{Actual}}$ (4.8)

If the cells are perfectly resolved, the model resolution matrix will have the form below where the diagonal elements are 1.0 and elsewhere it is 0, so the model resolution matrix can be written as

$$\begin{pmatrix} q_{M1} \\ q_{M2} \\ q_{M3} \\ q_{M4} \end{pmatrix} = \begin{pmatrix} 1.0 & 0.0 & 0.0 & 0.0 \\ 0.0 & 1.0 & 0.0 & 0.0 \\ 0.0 & 0.0 & 1.0 & 0.0 \\ 0.0 & 0.0 & 0.0 & 1.0 \end{pmatrix} \begin{pmatrix} q_{A1} \\ q_{A2} \\ q_{A3} \\ q_{A4} \end{pmatrix}$$

This means the calculated value for each cell only depends on the true value. In the case with imperfect resolution, we might have something like

$$\begin{pmatrix} q_{M1} \\ q_{M2} \\ q_{M3} \\ q_{M4} \end{pmatrix} = \begin{pmatrix} 0.7 & 0.1 & 0.1 & 0.1 \\ 0.1 & 0.7 & 0.1 & 0.1 \\ 0.1 & 0.1 & 0.5 & 0.3 \\ 0.1 & 0.1 & 0.3 & 0.5 \end{pmatrix} \begin{pmatrix} q_{A1} \\ q_{A2} \\ q_{A3} \\ q_{A4} \end{pmatrix}$$

$\mathbf{q}_{\text{Model}} = \mathbf{R} \mathbf{q}_{\text{Actual}}$

The diagonal elements give the ‘degree’ of resolution, while the off diagonal elements give the degree of ‘contamination’ or cross-correlation with the neighboring model cells. One way to illustrate the resolution is to plot the values of the diagonal elements of the \mathbf{R} matrix. This shows the degree at which the calculated model value depends on the true value. Some authors choose a value of about 0.05 (5%) as the ‘cutoff’ value.

4.9.3 Examples of model resolution with standard arrays

The diagonal elements of the resolution matrix give a quantitative means to compare the resolving power of different arrays. In this section, plots of the model resolution values of three common arrays are shown. As a simple example, we consider the case for a multi-

electrode system with 30 independent nodes and a spacing of 1.0 meter between adjacent electrodes. First we look at the resolution for the widely used Wenner array. Assume we make all the possible measurements, with the ‘ a ’ spacing ranging from 1.0 to 9.0 meters giving a total of 135 data points. The model resolution section (Figure 60a) shows that the resolution is greatest near the surface, decreases rapidly with depth, and is very small below a depth of about 2.0 meters. Next we look at the Wenner-Schlumberger array with the ‘ a ’ spacing ranging from 1.0 to 3.0 m. and the ‘ n ’ factor ranging from 1 to 8 giving a total of 292 data points. It performs significantly better than the Wenner array (Figure 60b) with significant resolution values up to about 3.0 m. The third array we will look at is the dipole-dipole array with the dipole length ‘ a ’ fixed at 1.0 m. and the ‘ n ’ factor ranging from 1 to 6, giving a total of 147 data points. Its performance is surprisingly good and comparable to the Wenner-Schlumberger array with significant model resolution values to about 3.5 meters, although it only has about half the number of data points (Figure 60c). It is much better than the Wenner array although it only has 12 more data points.

In an attempt to improve the resolution for the dipole-dipole array, we next attempt to use overlapping data levels with it. The ‘ a ’ dipole length ranges from 1.0 to 3.0 m. while the ‘ n ’ factor ranges from 1 to 6. The region with significant resolution values increases to about 5 meters (Figure 60d), an improvement from the 3.5 meters limit with a single ‘ a ’ dipole length (although it is mainly concentrated near the center). It only has about 50 data points more than the Wenner-Schlumberger (342 compared to 292), but it is a significant improvement.

It is possible to further improve the resolution we can get for a limited number of independent nodes and data points?

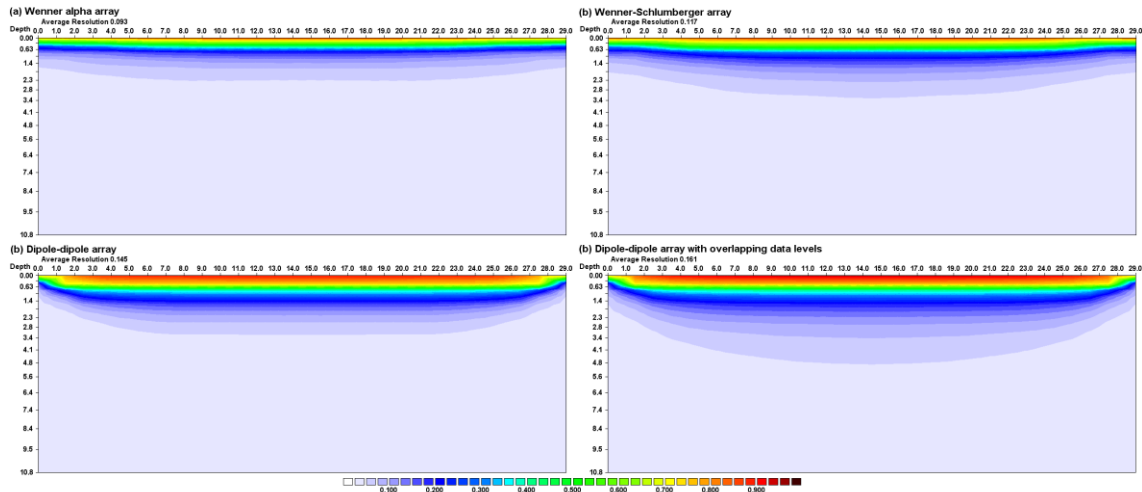


Figure 60. Model resolution sections for the (a) Wenner, (b) Wenner-Schlumberger and (c) simple dipole-dipole array (d) dipole-dipole array with overlapping data levels.

4.9.4 Array optimization methods

The model resolution section gives an insight on the section of the subsurface we can resolve. Is there a way to automatically select the arrays that will give the maximum resolution for a given number of electrodes? In recent years, there have been some significant developments in this effort (Stummer *et al.*, 2004; Wilkinson *et al.*, 2006b; Loke *et al.*, 2010a, 2010b, 2015a). Consider a survey system with N independent electrodes. The number of possible array combinations (M) with 4 electrodes is

$$M = N(N-1)(N-2)(N-3)/8$$

As an example, for a system with 30 electrodes, there are 82215 possible configurations. We can reduce the number by rejecting all configurations with the Gamma arrangement (with interleaved current and potential electrodes), and those with very high geometric factors (i.e. low potentials) of greater than the dipole-dipole with $a=1$ and $n=6$. This reduces the total number of possible array configurations to 51283, which is called the ‘comprehensive’ data set (Stummer *et al.*, 2004; Wilkinson *et al.*, 2006b). If we make measurements with all these possible array configurations, we should get the best possible resolution. The model resolution section for this ‘comprehensive’ data set is shown in Figure 61a. The region with significant resolution values extends to about 8 meters, significantly more than the dipole-dipole (5 meters) array.

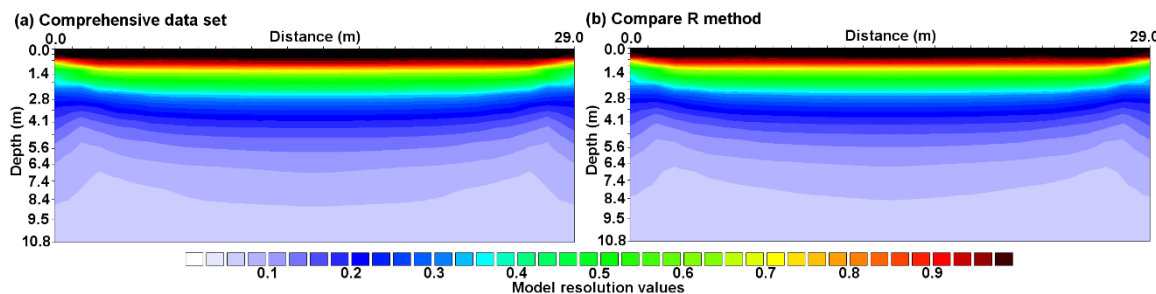


Figure 61. (a) Model resolution section for comprehensive data set. (b) Model resolution section for optimized data set generated by the ‘Compare R’ method.

Although taking all the 51283 possible readings will give the maximum possible resolution, this is not practical in an actual field survey. We want to take a small subset of the possible readings that gives almost the same resolution. The main steps taken by the array optimization routine is as follows.

1. Start with a small set, the ‘base’ data set, such as the dipole-dipole readings with $a=1$ and $n=1$ to 6 (147 readings).
2. Calculate the increase in the model resolution as each new array is added to the ‘base’ set (there are several alternatives for this step with differences in speed and accuracy). Add the arrays that give the highest increase to the model resolution (and are sufficiently independent of each other) to the base set. After each iteration, increase the base set by a set percentage (usually about 1% to 5%).
3. Use the new set (base plus new arrays) as the base set, and repeat the procedure. Stop when the desired maximum number of arrays (eg. 5000) is reached.

Different Methods have been proposed to carry out step (2) in selecting the arrays that will give the maximum increase in the model resolution (Wilkinson *et al.*, 2006b). Here, only the results of one method, the ‘Compare R’ method, will be shown. It gives the most accurate results in terms of optimized arrays, but it also takes the longest computer time to generate the arrays (Wilkinson *et al.*, 2006b). However the time needed has been reduced by more than three orders of magnitude using optimized computer code and parallel programming techniques (Loke *et al.*, 2010a, 2010b, 2015a). The model resolution section for optimized data set (Figure 61b) is almost identical with that for the ‘comprehensive’ data set (Figure 61a). The optimized data set has only 4462 array configurations, which is about 9% of the ‘comprehensive’ data set.

To illustrate the performance of the different array configurations in detecting subsurface structures, a test model with four rectangular blocks at different depths (Wilkinson *et al.*, 2006b) is used (Figure 62). Synthetic data sets were generated for the Wenner, Wenner-Schlumberger, dipole-dipole and optimized arrays. The data sets were then inverted to recover back the subsurface resistivity.

Figure 63a shows the resulting inversion model for the Wenner array data set. The two topmost blocks are well resolved while the third block is poorly resolved. The deepest block is completely unresolved. The Wenner-Schlumberger array data set (Figure 63b) performs slight better in resolving the third block but still cannot resolve the deepest block. The simple dipole-dipole array data set with a single dipole length ($a=1.0\text{m}$) performs significantly better than even the Wenner-Schlumberger array data set where the third block is well resolved (Figure 63a), even though it has fewer data points (147 compared with 292). However, it still cannot resolve the deepest block. The dipole-dipole array data set with multiple dipole lengths (all possible data points with $a=1.0$ to 3.0 meters and $n=1$ to 6, with the restriction that the geometric factor cannot exceed that for $a=1.0$ meter and $n=6$) shows higher resistivity values at the location of the deepest block but it is not able to resolve the block (Figure 63d).

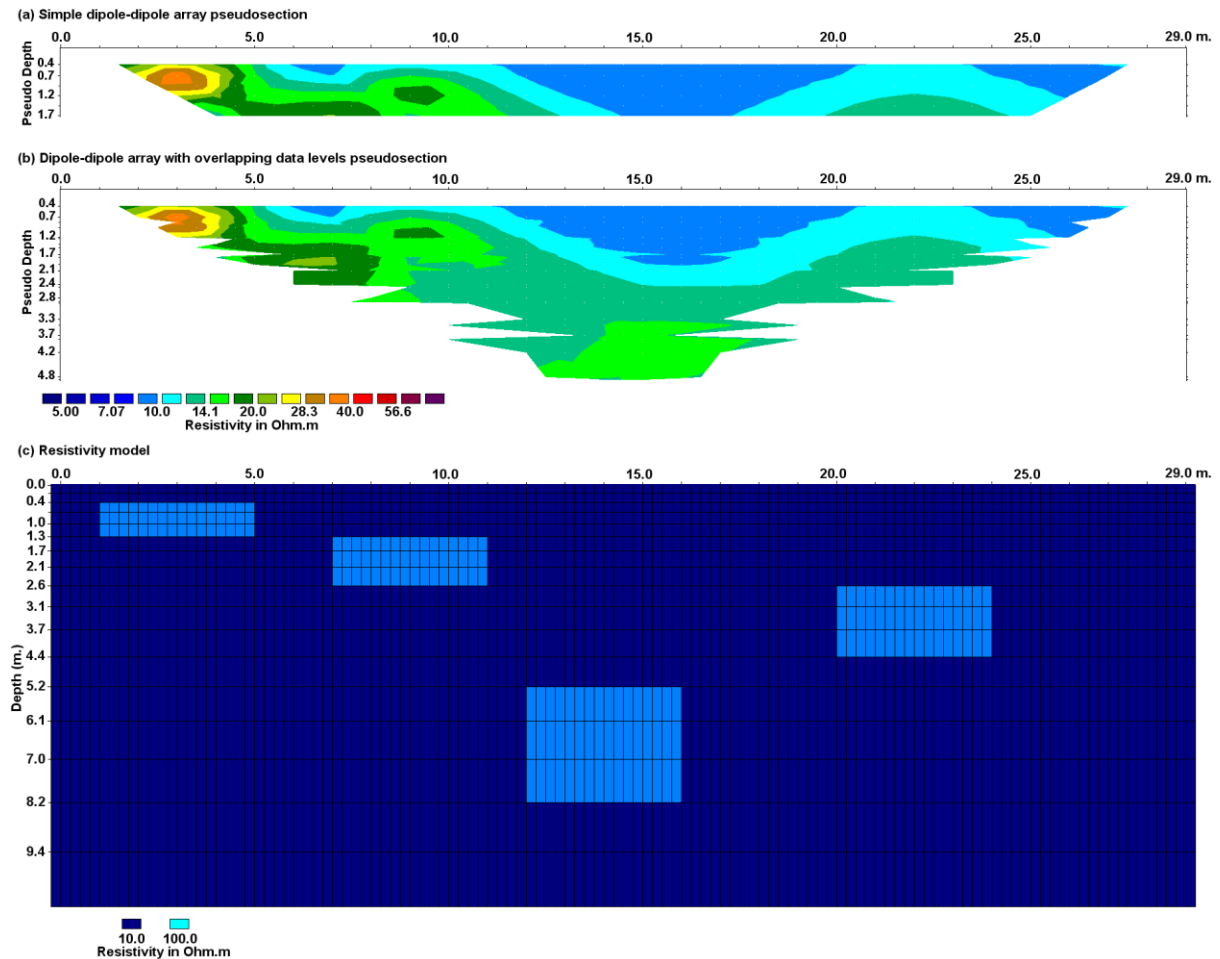


Figure 62. Test inversion model for the different arrays. (a) Apparent resistivity pseudosection for the simple dipole-dipole array with a dipole length ‘ a ’ of 1.0 meter with the dipole separation factor ‘ n ’ of 1 to 6. (b) Apparent resistivity pseudosection for the dipole-dipole array with overlapping data levels. (c) The synthetic model with 4 rectangular blocks of $100 \Omega\text{.m}$ embedded in a medium of $10 \Omega\text{.m}$. as used by Wilkinson *et al.* (2006b).

The deepest block is fairly well resolved in the inversion model for the optimized data set with 4462 data points (Figure 64a) where the shape and dimensions are close to the true structure. It might be argued that the better performance of the optimized data set compared to the dipole-dipole array with multiple dipole lengths is due to the much larger number of data points (4462 compared to 342). Next we use a truncated subset of the optimized data set

with only 413 data points that is comparable to the dipole-dipole array data set. The inversion model with the truncated optimized data set (Figure 64b) still shows significant better resolution for the deepest block compared to the dipole-dipole array model (Figure 63d). While the shape of the deepest block is significantly less sharp compared to the large optimized data set, it still is better defined compared to the dipole-dipole array model. The third deepest block is also much better resolved by both optimized data sets with resistivity values of over 50 Ohm.m at the center compared to less than 30 Ohm.m for the dipole-dipole array model.

This simple example shows that there can be significant improvements in the depth resolution by using an optimized data set. An old rule of thumb in resistivity sounding is that the maximum depth of investigation is about one-sixth (17%) the line length, i.e. slightly less than 6 meters near the center of the line in the above examples. However, using an optimized data set has pushed this limit close to 8 meters or slightly more than one-fifth (about 28%) the line length.

The array optimization problem for 2-D surveys has been quite well studied (Wilkinson *et al.*, 2012). Loke *et al.* (2014) describes the use of array optimization for cross-borehole surveys. With recent advances in computer software and hardware, it can be used for long 2-D survey lines (Loke *et al.*, 2015a) and even 3-D surveys (Loke *et al.*, 2014c). It is interesting to note since the initial work by Wilkinson *et al.* (2006b), the calculation time required by the ‘Compare R’ method to generate the optimized arrays for a survey line with 30 electrodes has been reduced from about 6 hours to 3 seconds, an improvement of about 7,000 times (Loke *et al.*, 2015a) over 9 years!

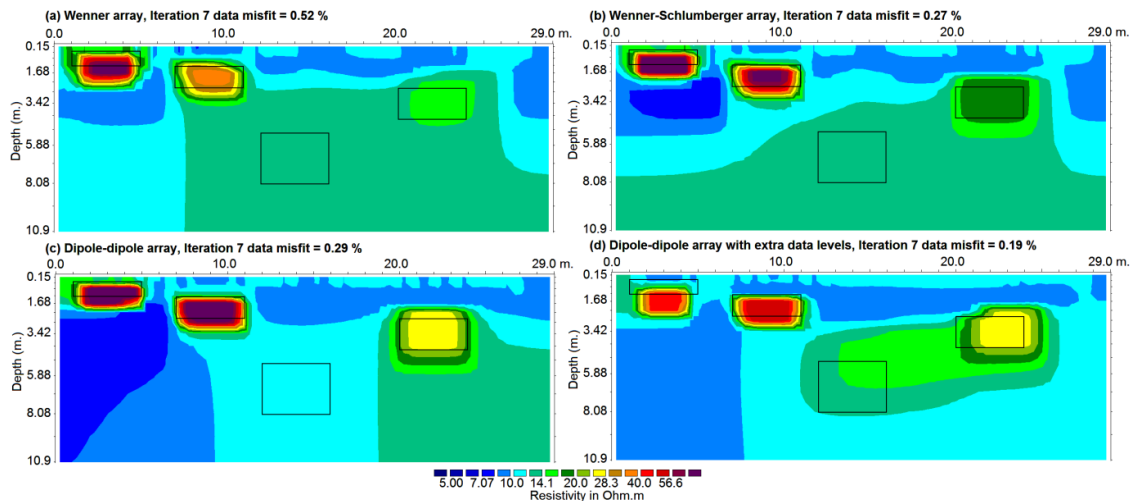


Figure 63. Inversion results with the (a) Wenner array, (b) Wenner-Schlumberger array, (c) simple dipole-dipole array and (d) dipole-dipole array with overlapping data levels.

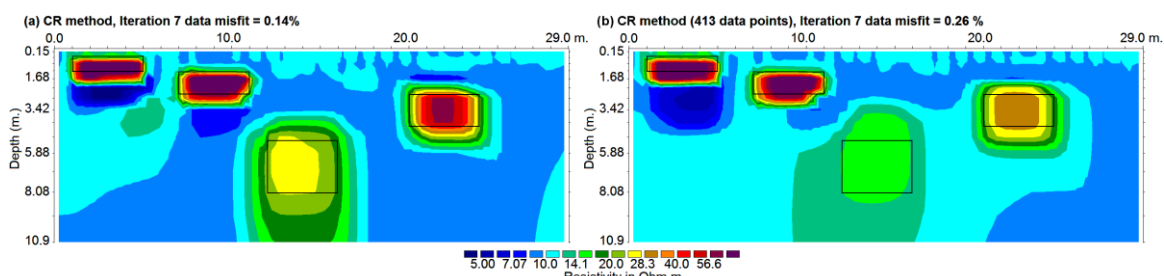


Figure 64. Inversions models with the (a) optimized data set with 4462 data points and (b) a truncated optimized data set with 413 data points.

4.9.5 DOI versus model resolution?

In section 4.4 we have looked at the Depth of Investigation (DOI) method to estimate the practical depth of investigation of field data sets. How does the model resolution section compare with the DOI? The model sections and DOI section for the Landfill survey data set were shown in Figure 45 and Figure 46. Figure 65 shows a comparison between the model resolution and DOI sections for this data set. Using a value of 0.05 as the cutoff point for the model resolution values might be arbitrary as it does not take into account the model discretization used. If a finer model discretization (with more model cells) is used, we would expect on the average the model resolution for a cell at the same location will be reduced since the cell size is smaller. Theoretically the sum of the elements in a column of the model resolution matrix (equation 4.8) is equals to 1.0. The average value of the array elements in the column would then be equals to $1.0/m$, where m is the number of model cells. A more useful measure to judge whether a model cell is resolved is the ratio the cell resolution value (i.e. the diagonal element of the resolution matrix) to this average value. If a value of about 10 is used for this ratio (model resolution index), then the average maximum depth of survey is probably about 12 to 14 meters. It is slight deeper between the 72 and 120 meters marks and slightly shallower between the 24 and 72 meters marks (Figure 65b). This is similar to that shown by the DOI index section using the 0.1 contour as the cut-off value (Figure 65c) The model resolution sections shows a more gradual change with depth (and also laterally) in the resolution values, compared to the DOI index section that has localized regions with high DOI index values.

One advantage of the model resolution section is that it avoids the localized regions with high DOI index values (that is sometimes caused by local high resistivity regions, or noise in the data). It has a theoretical appeal in that it is less empirical in nature compared to the DOI index method. One disadvantage of the model resolution method is that it requires an inversion of a matrix with a computer time that is proportional to n^3 (where n is the number of model cells). This makes it impractical for models with more than about 100000 cells that could be a significant limit for very large 3-D models with present PC technology. Research is being carried out to extend the practical limit to beyond about 100000 cells. One possible solution is to use GPU technology (Loke *et al.*, 2010b).

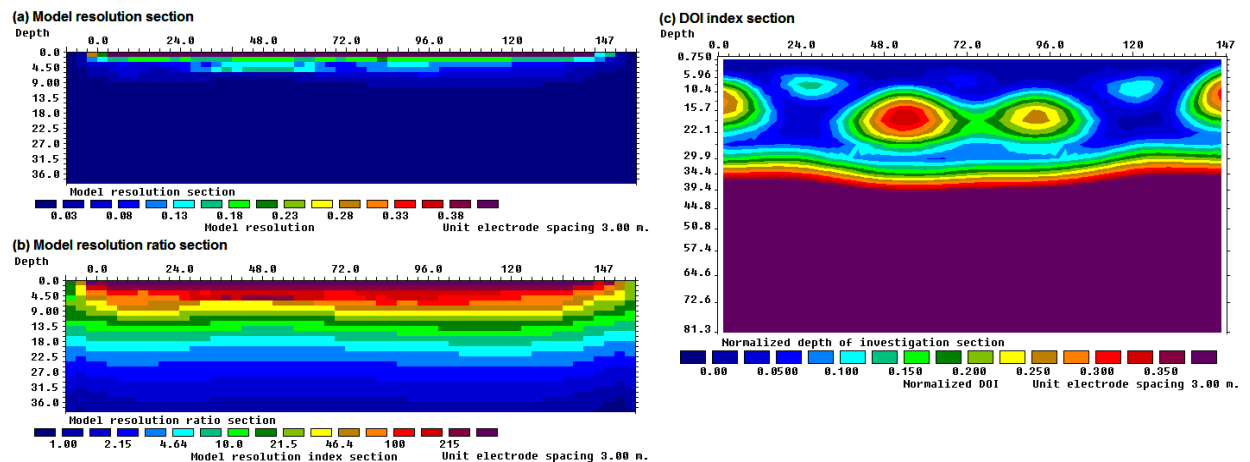


Figure 65. Comparison between the (a) model resolution, (b) model resolution index and (c) DOI index sections for the Landfill data set.

4.9.6 The streamer design problem using a model resolution approach.

In section 2.5.12 we compared the sensitivity values for several possible streamer configurations. Here we revisit the streamer design problem using a model resolution

approach. To reduce the edge effects, we plot the resolution sections for 26 consecutive sets of measurements for the three streamer configurations. This gives 208 (26 x 8) measurements for each streamer. Figure 66 shows the resulting model resolution sections for the dipole-dipole, gradient and Wenner-Schlumberger array streamers.

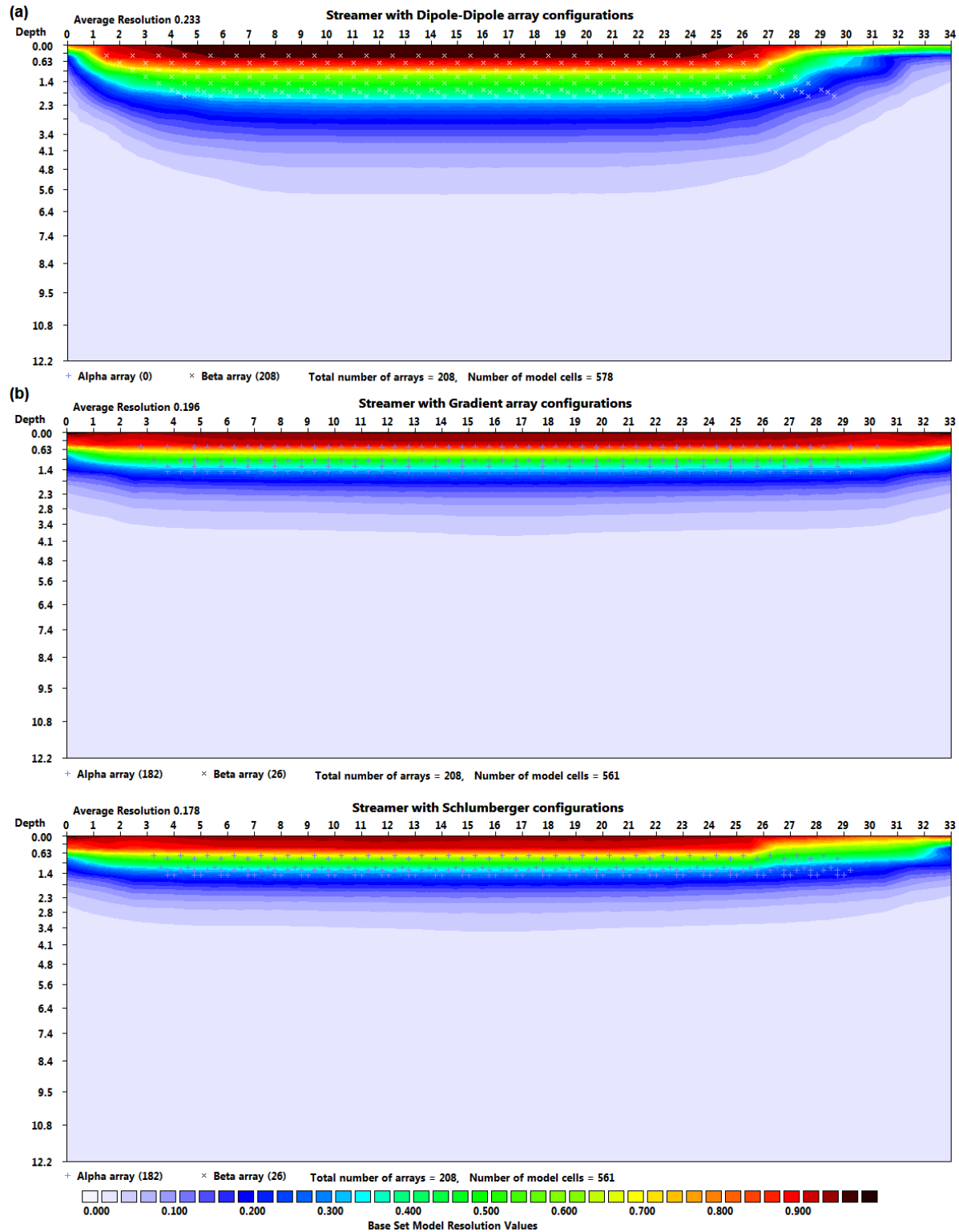


Figure 66. The model resolution plots for the three streamer configurations.

The resolution plot for the dipole-dipole array streamer (Figure 66a) shows the maximum depth of investigation is about 4.5 meters. For long survey lines that consists of hundreds of measurements the end effects are negligible so the resolution values with almost flat contours near the center of the section gives an estimate of the maximum depth with significant resolution values. The performance of gradient array streamer (Figure 66b) is much poorer. The resolution plot shows the maximum depth of investigation is about 3 meters that is significantly less than the dipole-dipole array streamer. The maximum depth of investigation of the Wenner-Schlumberger array streamer (Figure 66c) is slightly less than the gradient array streamer, between 2.5 and 3 meters, and much less than the dipole-dipole array streamer. Overall, the dipole-dipole streamer has the best depth penetration but it has the lowest signal strength that has to be compensated for in a practical design. The results from the model resolution plots are significantly different from the cumulative sensitivity plots (Figure 34), so some care must be exercised in using the results from the sensitivity plots.

4.10 Pitfalls in 2-D resistivity surveys and inversion

While 2-D resistivity surveys have made the mapping of many complex structures possible, caution must still be exercised in interpreting the results from the data. Below are some of the common pitfalls.

(a). Incorrect use of the dipole-dipole array. This is still a surprisingly common problem. There are two common mistakes in the use of this array. The first is to assume that the depth of investigation is at the point of intersection of the two 45° diagonals projected from the dipoles. This greatly overestimates the depth of investigation. For example, for the case where the dipole separation factor “ n ” is equals to 6, the point of intersection is about 3 times the median depth of investigation (see Table 2). The second common mistake is to monotonically increase the “ n ” factor, while keeping the dipole length “ a ” fixed, in an effort to increase the depth of investigation. This usually results in very noisy and unusable data, with negative apparent resistivity values in some cases, for “ n ” values of greater than 8. To solve this problem the “ n ” value should not exceed 6, and the method of overlapping data levels (section 2.5.6) with different “ a ” dipole lengths can be used.

(b). Poor electrode ground contact. This problem arises in stony or dry soils where it is not possible to plant the electrodes to a sufficient depth, and/or the soil is too dry such that it is not possible to pass enough current into the ground. In the pseudosection, this is seen as an inverted “V” shaped pattern of bad data points with the two legs originating from an electrode. This problem is more severe when the electrode is used as a current electrode. The potential electrode is less sensitive to poor ground contact, so this problem in certain situations can be overcome by swapping the current and potential electrodes.

(c). Poor current penetration. The success of the resistivity method depends on a current flowing through the areas to be mapped. If the top layer has a very high resistivity, it might be very difficult to get enough current to flow through the ground at all. The opposite problem occurs if the top layer has an extremely low resistivity. The current might be trapped in the top layer, so not much information is expected from the lower layers.

(d). Not letting the current charge decay. When an electrode is used as a current electrode, charges tend to build up around the electrode. When the current is no longer flowing through the electrode, it still takes a finite amount of time for the charges to disperse. If the same electrode is used as a potential electrode immediately after it has been used as a current electrode, this could result in an erroneous reading (Dahlin, 2000).

(e). Mistakes in the field. This can arise from a variety of sources. It could be caused by instrumentation errors during the field survey, poor electrode contact in dry, sandy or stony ground, shorting of electrodes due to very wet conditions or metal objects (such as fences,

pipes etc.) or mistakes such as attaching electrodes to the wrong connectors. Fortunately, it is usually very easy to pick out such bad data points by viewing the pseudosection or the data in the form of profiles. Before inverting a data set, take a look at it!

(f). 3-D geology. It is assumed that the subsurface is 2-D when interpreting the data from a single line. This assumption is valid if the survey is carried out across the strike of an elongated structure. If there are significant variations in the subsurface resistivity in a direction perpendicular to the survey line (i.e. the geology is 3-D), this could cause distortions in the lower sections of the model obtained. Measurements made with the larger electrode spacings are not only affected by the deeper sections of the subsurface, they are also affected by structures at a larger horizontal distance from the survey line. This effect is most pronounced when the survey line is placed near a steep contact with the line parallel to the contact. Figure 67 shows the apparent resistivity pseudosection for the Wenner array over a 3-D model that has two structures of $100 \Omega\cdot m$ that have the same widths within a $10 \Omega\cdot m$ medium. One structure is truly 2-D while the second is truncated near the middle of the area at the y-axis coordinate of 3 meters. At a large distance from the edge of the second structure, for example at the y-axis coordinate of 8 meters, the anomaly due to the right structure is almost as high as that due to the left structure. However, close to the edge, for example at y-axis coordinate of 5 meters, the anomaly due to the right structure is significantly weaker. If a survey was carried out along this line, and the subsurface was assumed to be 2-D, then the dimensions of the right structure obtained from an inversion of the data set would be wrong. Dahlin and Loke (1997) did a comparison of the sensitivity of different arrays to structures off the axis of a 2-D survey line. In general, it was found that the dipole-dipole array was the most sensitive (i.e. suffered the greatest distortion) due to off-axis structures. The best way to handle 3-D structures would be a full 3-D survey and data inversion. We will look at 3-D surveys in the later part of these notes.

It must be emphasized that a 2-D survey with very good quality data and very dense data coverage, and inverted with a good inversion algorithm, can still give the wrong results if the assumption of a 2-D geology on which the model is based is seriously wrong. This is a particularly a problem in mineral surveys (which commonly also involve I.P. measurements) where very complex geological structures and mineralization patterns are usually encountered. In such situations, the results from a 2-D resistivity and I.P. model should be treated with some reservations unless it is confirmed by a 3-D survey and model. There have been many cases where expensive drill-holes have passed through barren zones in areas where the 2-D model shows a strong IP anomaly.

(g). Limits of the physics of the resistivity method. While 2-D and 3-D surveys and data inversion has greatly extended the range of field problems that can be solved using the resistivity method, there are still basic laws of physics that place certain limitations on these techniques. The resolution of the resistivity method decreases exponentially with depth. We see the subsurface “as through a glass darkly” and the image becomes increasingly fuzzier with depth. It is unlikely to be able to map a structure with a size of 1 meter at a depth of 10 meters using the resistivity method. The resistivity phenomenon is based on the diffusion equations, so its resolution is inherently poorer than the seismic or ground radar method at depths greater than one wavelength.

(h). Non-uniqueness. It is well known that more than one model can produce the same response that agrees with the observed data within the limits of the data accuracy. In 1-D resistivity sounding modeling, the problems of equivalence and suppression are well known. The problems, in different forms, also occur in 2-D and 3-D modeling. A good example was shown in the paper by Oldenburg and Li (1999). In 2-D and 3-D modeling, constraints are used so that a stable solution can be obtained. The use of a smooth or blocky constraint results in the production of models that look more reasonable, but it is no guarantee that they

are indeed correct. The accuracy of the result is only as good as the accuracy of the assumptions made. The resulting model thus depends to a significant extent on the constraint used, and will closely approximate the true subsurface resistivity only if the constraints correspond to the real situation.

(i). Optimization versus inversion. The RES2DINV program, like most non-linear inversion programs, actually carries out an optimization (i.e. not a direct one-to-one inversion in the sense it must have only one solution) in that it tries to reduce the difference between the calculated and measured apparent resistivity values. If there is infinite data and a perfect fit between the calculated and measured values, how the data is measured should not have an effect on the results. However with real, noisy and limited data, how the data is measured does have an effect. A model with 5% RMS error in the fit between the measured and calculated apparent resistivity values with one data set might not give the same model as a 5% RMS error with another data set although both might be from the same place. For this reason, the dipole-dipole array gives an inversion model with much better resolution than the pole-pole array although in theory the dipole-dipole values can be extracted from the pole-pole values.

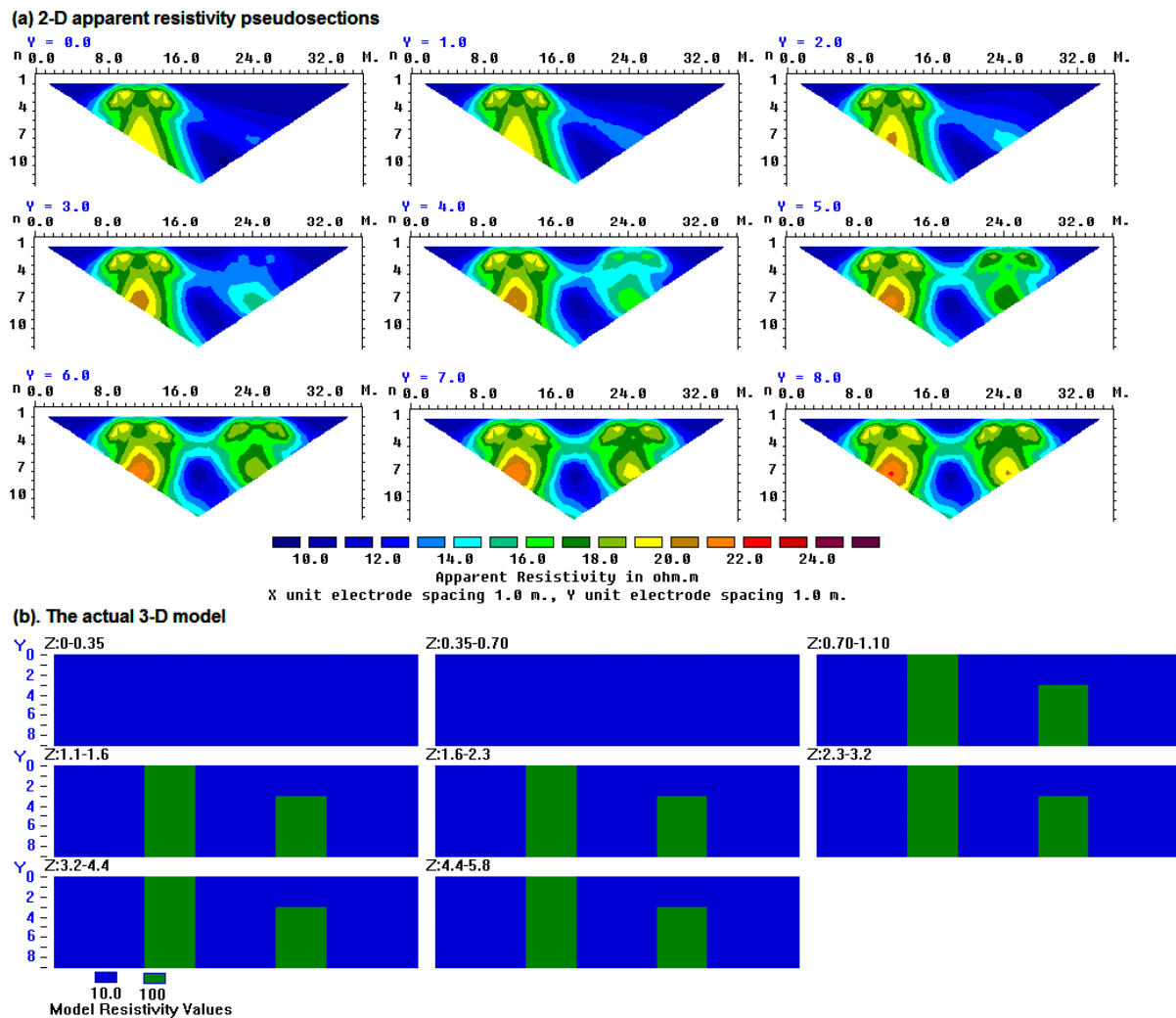


Figure 67. An example of 3-D effects on a 2-D survey. (a) Apparent resistivity pseudosections (Wenner array) along lines at different y-locations over (b) a 3-D structure shown in the form of horizontal slices.

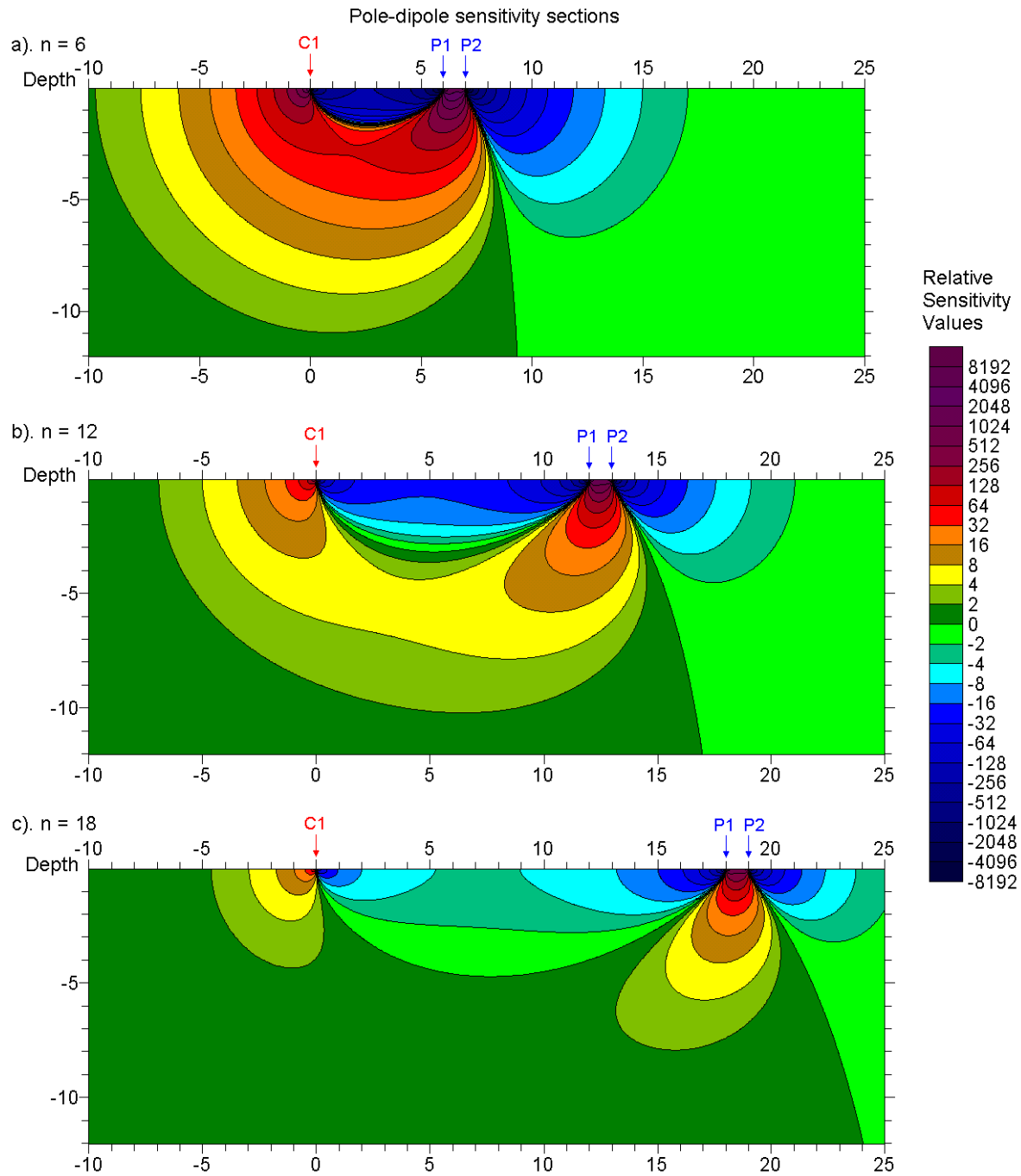


Figure 68. The 2-D sensitivity sections for the pole-dipole array with a dipole length of 1 meter and with (a) $n=6$, (b) $n=12$ and (c) $n=18$. Note that as the ‘ n ’ factor increases, the zone of high positive sensitive values becomes increasingly concentrated in a shallower zone below the P1-P2 dipole.

(j). Increasing the electrode separation does not always increase the survey depth. It is generally assumed that as the separation between the electrodes is increased, the region of the subsurface that is ‘sensed’ by the array also increases. While this is true of most arrays, there are certain important exceptions. In particular, this is not true of the pole-dipole array under certain circumstances. In some surveys with the pole-dipole array, the separation between the C1 current electrode and the P1-P2 dipole is increased in an effort to increase the depth of survey by the array. However, if this is done with the P1-P2 dipole length (the ‘ a ’ factor in

Figure 4) kept at a constant spacing, certain interesting effects come into play. In section 2.5.8 this practice was strongly discouraged on the basis that the potential will decrease with the square of the ‘ n ’ factor. This problem can be overcome by a combination of using higher currents and more sensitive receivers. However, the problem caused by the change in the array sensitivity pattern as the ‘ n ’ factor is monotonically increased is usually not taken into account. The change in the sensitivity pattern when the ‘ n ’ factor changes from 1 to 6 was shown earlier in Figure 30. Figure 68 shows what happens when the ‘ n ’ factor jumps from 6 to 12 to 18. Here, the dipole length is kept constant at 1 meter. When ‘ n ’ is equal to 6 there are reasonably high sensitivity values to a depth of about 3 to 4 meters between the C1 current and the P1 potential electrode. When ‘ n ’ is increased to 12, the zone of high sensitivity values becomes increasingly more concentrated below the P1-P2 dipole in an even shallower region. This means that the array with ‘ n ’ equals to 12 is in fact less sensitive to deeper structures than the array with ‘ n ’ equals to 6. This effect is even more pronounced when ‘ n ’ is increased to 18.

Thus increasing the separation between the current electrode and the potential dipole, while keeping the dipole length fixed, does not increase the survey depth of the array. It, in fact, effectively decreases the depth of the region sensed by the array!

Figure 69 shows the apparent resistivity anomaly due to a small near-surface high resistivity block for the pole-dipole array for ‘ n ’ values of up to 28. Note that the amplitude of the high resistivity anomaly due to the near-surface block increases with the ‘ n ’ value, i.e. the array becomes increasingly more sensitive to the near-surface block as the separation between the electrodes increase. In field surveys with the pole-dipole array where the ‘ n ’ factor is monotonically increased in the belief that this increases the survey depth, the pseudosection is frequently dominated by a series of parallel slanting high-amplitude anomalies due to near-surface inhomogeneities. The anomalies due to the near-surface structures frequently mask the anomalies due to deeper structures that are of interest.

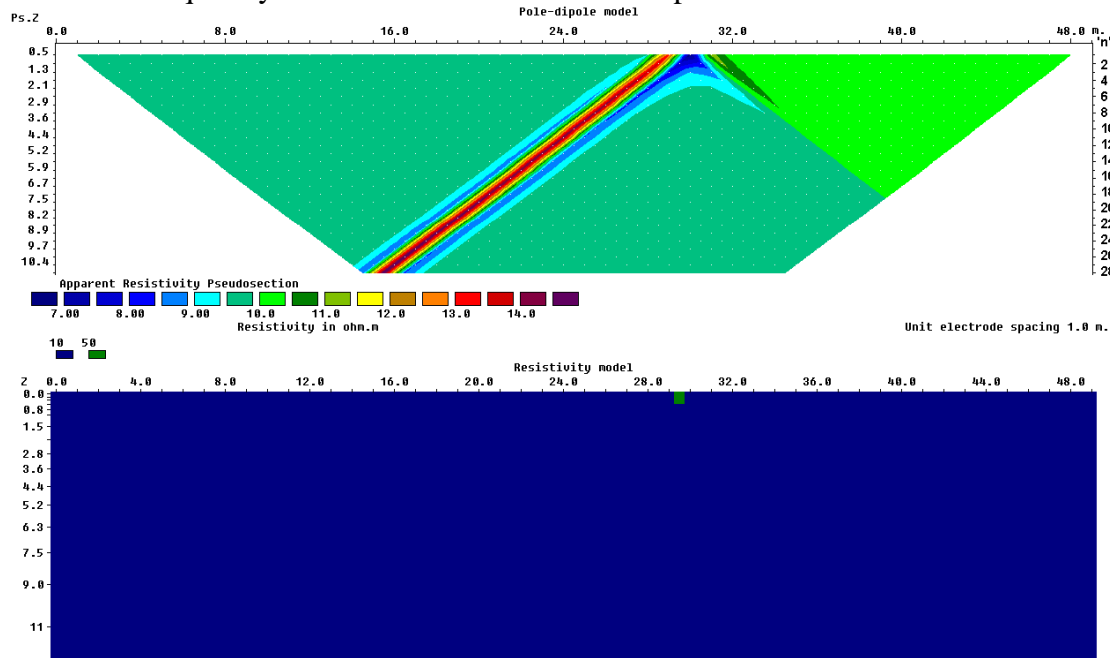


Figure 69. Example of apparent resistivity pseudosection with pole-dipole array with large ‘ n ’ values. Note that the anomaly due to a small near-surface high resistivity block becomes greater as the ‘ n ’ factor increases. This means that the sensitivity of the array to the near-surface region between the P1-P2 potential dipole becomes greater as the ‘ n ’ factor increases.

To increase the depth of penetration with the pole-dipole array, the ‘ a ’ dipole length should be increased when the ‘ n ’ factor exceeds 6 to 8. This method was discussed in detail in section 2.5.9. For example, instead of fixing the ‘ a ’ dipole length to 1 meter and increasing the ‘ n ’ factor to 28 in Figure 69, a more prudent approach is increase the ‘ a ’ spacing from 1 to 4 meters while ensuring the ‘ n ’ factor does not exceed 8.

4.11 The pole-pole inversion paradox

In theory, if we were to take all the possible pole-pole measurements, we can reconstruct the measurements for any array such as the dipole-dipole array. The maximum number of possible measurements (complete data set) for a survey line with N electrodes for the pole-pole array is only $N(N-1)/2$, compared to $N(N-1)(N-2)(N-3)/8$ for four-electrode arrays. Since the measurements for any four-electrodes arrays can be reconstructed from the pole-pole measurements, the pole-pole complete data set should have all information that can be obtained from a resistivity survey. However, we have seen that the data for some arrays such as the dipole-dipole has much higher resolution compared to the pole-pole array, which seems inconsistent if the complete pole-pole array data set has the same information. This is an interesting paradox that has come up occasionally, for example there is a mention of it in Blome *et al.* (2011) concerning the reconstruction of 4-electrodes arrays data from pole-dipole measurements.

My own personal opinion is that when we carry out an ‘inversion’, it is not a direct inversion where we go from the data to a unique in one step but rather a non-linear optimization is carried out where we try to find the minimum of an objective function by using the slope or gradient of the function. A pole-pole measurement is relatively insensitive to changes in the resistivity of a model cell, i.e. the Jacobian matrix values have smaller amplitudes compared to a 4-electrodes array such as the dipole-dipole where the apparent resistivity changes by a larger amount for the same change in the cell resistivity. The objective function for the pole-pole data set has a relatively broad minimum with gentle slopes, and within the limits of the measurement error (eg. 1%) it cannot distinguish between the different models in the vicinity of the global minimum. The inversion method tries to minimize the model roughness as well, so it ends up with the model with the minimum structure possibly in a local minimum. The objective function for a dipole-dipole data set has steeper slopes, so for the same data misfit it ends up closer to the global minimum. The situation is shown diagrammatically in Figure 70.

A similar principle applies in cases where four-electrode arrays measurements are reconstructed from pole-bipole measurements (Blome et al., 2011).

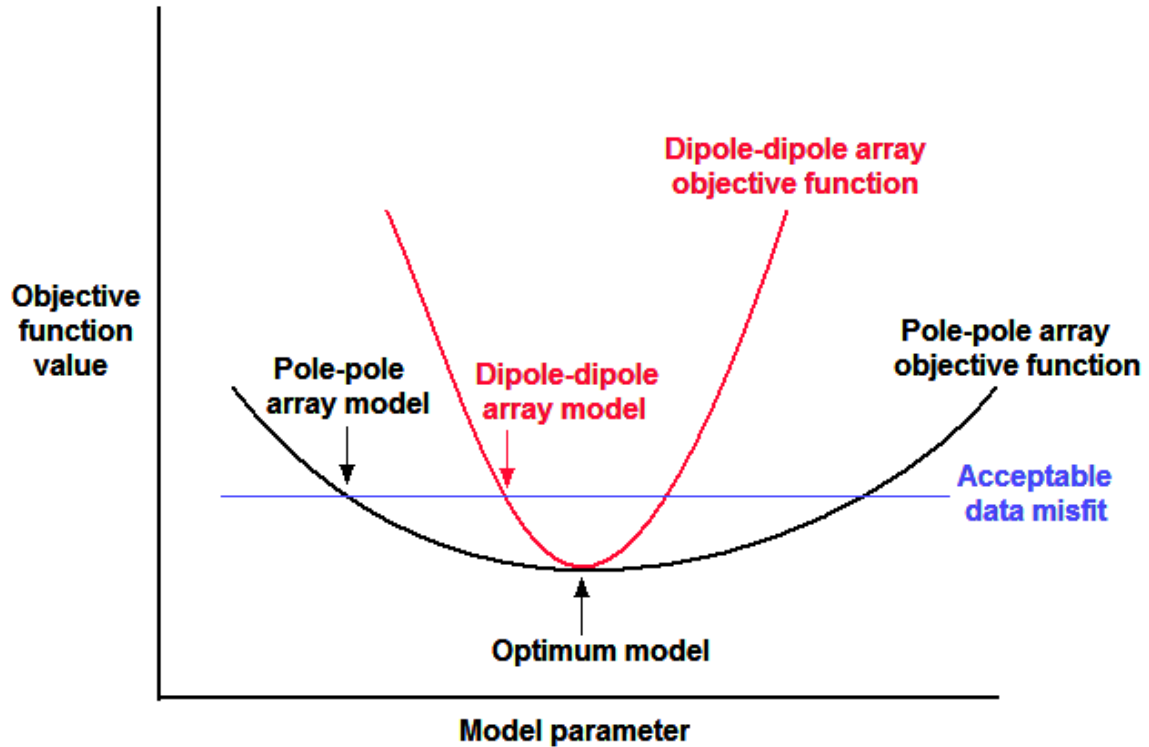


Figure 70. Diagrammatic illustration of differences in objective function shapes for the pole-pole array and dipole-dipole array data sets leading to different models obtained from optimization routine.

5 I.P. inversion

5.1 Introduction

One of the more recent developments in the instrumentation for electrical imaging surveys has been the addition of Induced Polarization (I.P.) capability in the multi-electrode resistivity meter system. Many of the early 2-D surveys were resistivity and I.P. surveys carried out using conventional 4-electrode systems in the 1950's onwards for mineral exploration, particularly for conductive sulfide ore bodies. Quantitative interpretation of such historical data was rather limited due to the limited computing facilities available at that time. Such historical data provides an interesting source of data for testing modern 2-D and 3-D inversion software. Re-interpretation of such old data to produce quantitative models sometimes has shed new light on the geological structures.

One of the distinctive characteristics of the I.P. method has been the different parameters in the time and frequency domains used to represent the I.P. effect. The following section briefly discusses the I.P. phenomena and the different I.P. parameters. This is followed by a few exercises in the inversion of IP data with the RES2DINV program. The data format used by the RES2DINV and RES3DINV programs is described in their respective manuals. As such, we will not cover it here.

5.2 The IP effect

A very brief description of the IP effect will be given here. Further details can be found in many fine textbooks, such as by Keller and Frischknecht (1966), Summer (1976), Telford *et al.* (1990) and Zhdanov and Keller (1994).

The I.P. effect is caused by two main mechanisms, the membrane polarization and the electrode polarization effects. The membrane polarization effect is largely caused by clay minerals present in the rock or sediment. This is particularly relevant in engineering and environmental surveys. The chargeability of clays are in the 10 to 50 mV/V range (Sumi, 1965) is much smaller than that due to conductive minerals. Interestingly, negative I.P. effects have been reported for certain types of clays (Brandes and Acworth, 2003). Another application of I.P. in environmental surveys in detecting decomposing organic matter (Weller *et al.*, 2000). The electrode polarization effect is caused by conductive minerals in rocks such that the current flow is partly electrolytic (through groundwater) and partly electronic (through the conductive mineral). This effect is of particular interest in surveys for metallic minerals, such as disseminated sulfides.

I.P. measurements are made in the time-domain or frequency domain. In the time-domain, the I.P. effect is measured by the residual decay voltage after the current is switched off (Figure 72c). The time domain I.P. unit (chargeability) is usually given in millivolt per volt (mV/V) or in milliseconds. Figure 71 shows the I.P. values (in terms of mV/V) for several mineralized rocks and common rocks. Note that the I.P. effect due to sulfide mineralization (the electrode polarization effect with values in the 100 to 200 mV/V range) is much larger than that due to clay minerals (membrane polarization) in sandstone and siltstones. The high I.P. effect for disseminated metallic sulfides makes I.P. surveys a standard tool for exploration of such minerals. The resistivity contrast for such deposits is frequently low due to its disseminated nature which makes detection by standard resistivity and EM surveys difficult.

In the frequency domain (Figure 72b), the I.P. effect is measured by the change in apparent resistivity value from low to high frequencies (typically 1 to 10 Hz) where the unit used is the percent frequency effect. Another measure of the I.P. effect in the frequency domain is the phase shift between the potential signal and the input current, where the unit used is in milli- radians.

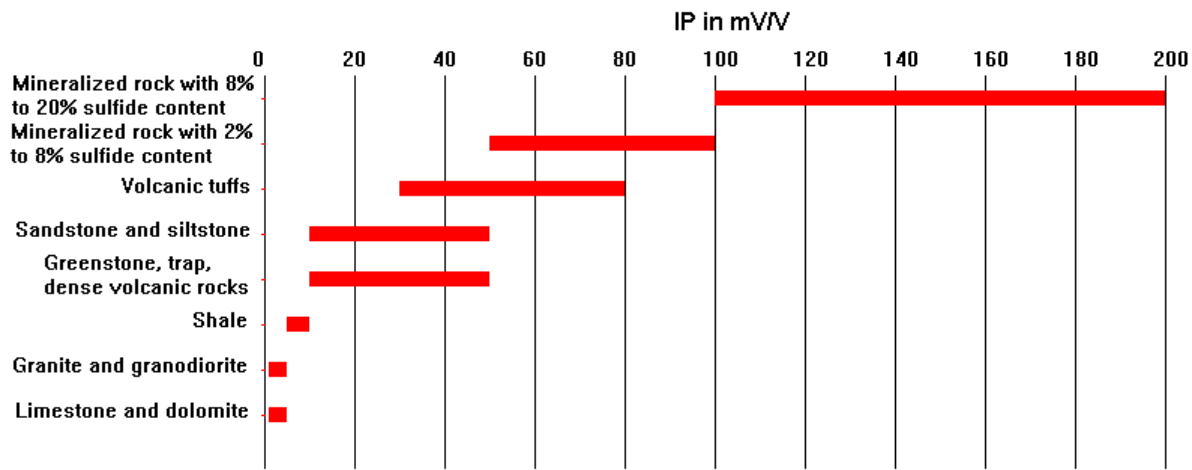
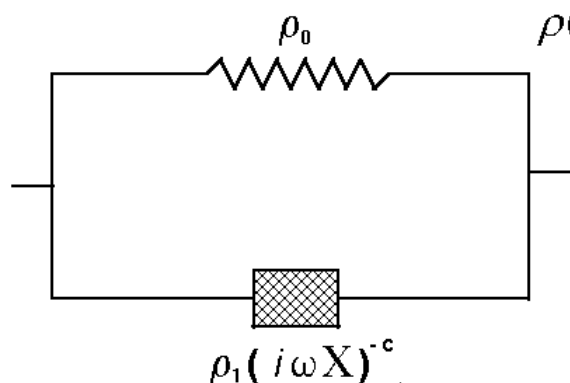


Figure 71. The I.P. values for some rocks and minerals.

a). Equivalent circuit

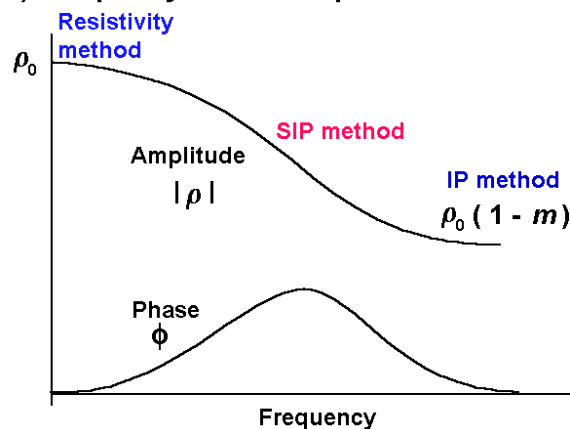


$$\rho(\omega) = \rho_0 \left[1 - m \left(1 - \frac{1}{1 + (i\omega\tau)^c} \right) \right]$$

$$m = \rho_0 / (\rho_0 + \rho_1)$$

$$\tau = X (\rho_0 + \rho_1)^{1/c}$$

b). Frequency-domain response



c). Time-domain response

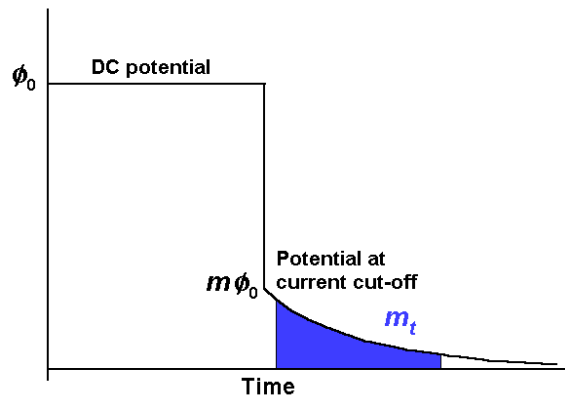


Figure 72. The Cole-Cole model. (a) Simplified electrical analogue circuit model (after Pelton *et al.* 1978). ρ = resistivity, m = chargeability, τ = time constant, c = relaxation constant. (b) Amplitude and phase response to sine wave excitation (frequency domain). (c) Transient response to square wave current pulse (time domain). Most I.P. receivers measure the integral of the decay voltage signal over a fixed interval, m_t , as a measure of the I.P. effect.

One mathematical model that attempts to explain variation of resistivity with frequency observed in the IP method is the Cole-Cole mode (Pelton *et al.*, 1978), which is defined by

$$\rho(\omega) = \rho_0 \left[1 - m \left(1 - \frac{1}{1 + (i\omega\tau)^c} \right) \right] \quad (5.1)$$

where ρ_0 is the DC resistivity, m is the chargeability, ω is the angular frequency ($2\pi f$), τ is a time constant and c is the exponent or relaxation constant. While the DC resistivity and chargeability determine the behavior of the material at very low and very high frequencies, the variation of the amplitude and phase curves at intermediate frequencies are also affected by the time and relaxation constants.

The time constant factor τ has a large range, from 0.01 second to several thousand seconds. The relaxation constant factor c is bounded by 0.0 to 1.0, with values frequently between 0.2 and 0.7. Much of the earlier work was on the use of spectral I.P. (SIP) measurements to differentiate between different types of conductive minerals for mining purposes (Van Voorhis *et al.*, 1973; Zonge and Wynn, 1975; Pelton *et al.*, 1978; Vanhalla and Peltoniemi, 1992). More recently, attempts have been made to use the SIP method for environmental surveys, such as in the detection contaminants (Vanhala *et al.*, 1992). Figure 72 shows a simplified electrical analogue circuit for the Cole-Cole model, together with typical response curves in the frequency and time domain.

5.3 IP data types

Although the chargeability is defined as the ratio of amplitude of the residual voltage to the DC potential (Figure 72c) immediately after the current cut-off, this is not used in actual field measurements. Field measurements of the I.P. effect may be divided into two main groups, the time-domain and frequency domain methods.

(a) Time domain IP measurements

In the time-domain method, the residual voltage after the current cut-off is measured. Some instruments measure the amplitude of the residual voltage at discrete time intervals after the current cut-off. A common method is to integrate the voltage electronically for a standard time interval. In the Newmont M₍₃₃₁₎ standard (Van Voorhis *et al.*, 1973), the chargeability, m_t , is defined as

$$m_t = 1870 \frac{\int_{0.15}^{1.1} V_s dt}{V_{DC}}, \quad (5.2)$$

where the integration is carried out from 0.15 to 1.1 seconds after the current cut-off. The chargeability value is given in milliseconds. The chargeability value obtained by this method is calibrated (Summer 1976) so that the chargeability value in msec. has the same numerical value as the chargeability given in mV/V. In theory, the chargeability in mV/V has a maximum possible value of 1000.

I.P. surveys have traditionally been used in the mineral exploration industry, particularly for metal sulfides, where heavy electrical generators producing high currents of the order of 10 Amperes are used. The apparent I.P. values from such surveys are usually less than 100 msec. (or mV/V). One recent development is the addition of I.P. capability to battery based systems used in engineering and environmental surveys where currents of 1 Ampere or less are normally used. An accompanying phenomenon is the observation of I.P. values of over 1000 msec. (or less than -1000 msec.) in some data sets. Such values are almost certainly caused by noise due to a very weak IP signal. To check whether such high I.P. values are real, first check the apparent resistivity pseudosection. If it shows unusually high and low values that vary in an erratic manner, the data is noisy. If the apparent resistivity values are noisy, then the apparent I.P. values are almost certainly unreliable. Next check the

apparent I.P. pseudosection. If the apparent I.P. values show an erratic pattern (frequently with anomalous values lined up diagonally with an apex at a doubtful electrode), then the I.P. values are too noisy to be interpretable. There has been some recent work on improving the reliability of I.P. measurements made with the multi-electrode type of systems (Dahlin and Leroux, 2012).

(b) Frequency domain I.P. measurements

In the frequency-domain methods, the apparent resistivity is measured at least two frequencies, for example at 1 Hz. and 10 Hz. The higher frequency is usually set at 10 times time the lower frequency. One commonly used frequency domain IP unit is the percent frequency effect, PFE, which is defined by

$$PFE = \frac{\rho(\omega_L) - \rho(\omega_H)}{\rho(\omega_H)} \cdot 100 \quad (5.3)$$

Another closely related unit that is also commonly used is the metal factor *MF* which is defined by

$$MF = \frac{\rho(\omega_L) - \rho(\omega_H)}{\rho(\omega_L) \cdot \rho(\omega_H)} \cdot 2\pi \cdot 10^5 \quad (5.4)$$

Another common frequency domain IP unit is the phase angle, ϕ . It is the phase shift between the transmitter current and the measured voltage, and the unit commonly used is milliradians. This has the advantage that only measurement at a single frequency is need, but the current circuit must be coupled with the potential measuring circuit in some way so that the phase shift between the measured potential and the input current can be determined. This is not a problem in the multi-electrode type of system, such as the Pasi Polares system, where both circuits are in the same unit.

(c) Relationship between the time and frequency domain IP units

From the measurement of the amplitude and phase spectrum of porphyry copper mineralization, Van Voorhis et al. (1973) proposed the following equation to describe the observed spectra.

$$\rho(\omega) = K(j\omega)^{-b} \quad (5.5)$$

K is constant and *b* is a measure of the IP effect. It is a positive number of more than 0 and less than 0.1. This is also known as the constant phase model (Weller et al., 1996). By using the above model, the following relationship between the different IP units and the *b* parameter were derived.

$$\begin{aligned} PFE &= (10^b - 1)100 \\ \phi &= 1571 b \\ m_t &= 1320b \end{aligned} \quad (5.6)$$

These relationships provide a numerical link between the different IP units (Van Voorhis et al., 1973; Nelson and Van Voorhis, 1973). An alternative relationship is given in the paper by Kemna et al. (1997).

There have been a large number of 2-D I.P. surveys published over the years, so there is certainly no lack of data to test the IP inversion with the RES2DINV program. Most of the newer multi-electrode systems now come with an IP option. However, the data from many of these systems is rather noisy due to the limited current that can be injected into the ground. For reasonable IP data quality, a current of at least 0.5 Amperes is probably necessary. For environmental and engineering surveys, the most useful application of the IP data is probably in differentiating between sand and clay sediments.

5.4 IP mathematical models

There are generally two methods to calculate I.P. effects in a forward modeling program, the perturbation and the complex resistivity methods. The first approach considers the I.P. model as a small perturbation of the base resistivity model. Consider a base model that has a conductivity σ_{DC} that is measured by a normal resistivity survey. The effect of the chargeability m is to decrease the effective conductivity to $\sigma_{IP} = (1 - m) \sigma_{DC}$. The apparent I.P. is then calculated by two forward models using the original and perturbed conductivities, such as

$$m_a = [\phi(\sigma_{IP}) - \phi(\sigma_{DC})] / \phi(\sigma_{DC}) \quad (5.7)$$

Where ϕ is the calculated potential. This approach works well in most cases. The inversion of I.P. data is a two step process (Oldenburg and Li, 1994).

- (1). A resistivity inversion step using the apparent resistivity data alone is first carried out. This produces a resistivity model (ρ_{DC}) that is independent of the measured IP data.
- (2). Using the resistivity model as a base, the apparent I.P. values are calculated using equation 5.7. An inversion of the apparent I.P. data is then carried out to obtain a chargeability model (m_{IP}). The resistivity model (ρ_{DC}) is kept fixed during this inversion step.

There are two main problems with the perturbation approach. The apparent chargeability is calculated from the difference of two DC potentials. The difference is usually less than 1% of the DC potential values, so this tends to magnify numerical errors in the finite-difference or finite-element methods used to calculate the DC potentials. For most traditional arrays, this is usually not a serious problem. However, the increasing popularity of the offset pole-dipole and dipole-dipole arrays (White *et al.*, 2001) can produce array configurations with extreme geometrical factors. In some situations, with rugged topography and large resistivity contrasts, this can sometimes lead to negative apparent resistivity values (Jung *et al.*, 2009). In such situations, it is found that the apparent chargeability values calculated using equation (5.7) is not reliable, particularly for 3-D models. The second problem is that it does not take into consideration the apparent chargeability values when calculating the resistivity model, although for a non-homogeneous model the resistivity values have a significant effect on the calculated apparent chargeability values. The resistivity model is optimal for the apparent resistivity data but it might not be optimal for the apparent chargeability data. This can lead to some distortions in the I.P. inversion model as it is also based on the resistivity model.

The second approach for I.P. model calculation is to treat the conductivity as a complex quantity with real and imaginary components (Kenma *et al.*, 2000). The complex conductivity is given by

$$\sigma = \sigma_{DC} - i m \sigma_{DC} \quad (5.8)$$

The DC conductivity σ_{DC} forms real part, while $m \sigma_{DC}$ forms the imaginary part. A complex potential is then calculated for this complex model.

$$\phi = \phi_r + i \phi_i \quad (5.9)$$

The complex potential has two components, ϕ_r and ϕ_i . The apparent chargeability is calculated using the ratio of the imaginary component to the real component, $m_a = \phi_i / \phi_r$. The inversion process using a complex resistivity approach is as follows.

- (1). A joint inversion where both the apparent resistivity and apparent I.P. data (ρ_a, m_a) are used together to generate a resistivity and chargeability model (ρ_{DC}, m_{IP}) is carried out.
- (2). The first inversion tends to reduce the apparent resistivity data misfit at the expense of the apparent I.P. misfit, i.e. it tends to produce a more accurate resistivity model at the expense of the I.P. model. A second inversion is commonly carried out to refine the I.P. model. The resistivity model (ρ_{DC}) is kept fixed, and only the I.P. model (m_{IP}) is changed to

further reduce the apparent IP (m_a) data misfit.

Figure 73 below shows the inversion results from both I.P. inversion methods for the data from the Magusi River ore body (Edwards, 1977) survey. The models obtained by both methods are generally similar. The ore body shows up as a low resistivity body with high IP values near the middle of the survey line in the model sections. The blocky inversion method was used to sharpen the boundary between the ore body and the surrounding country rocks in the model. The massive sulfide ore body shows as a prominent low resistivity and high I.P. structure. The complex resistivity method gives a model with slightly higher I.P. values.

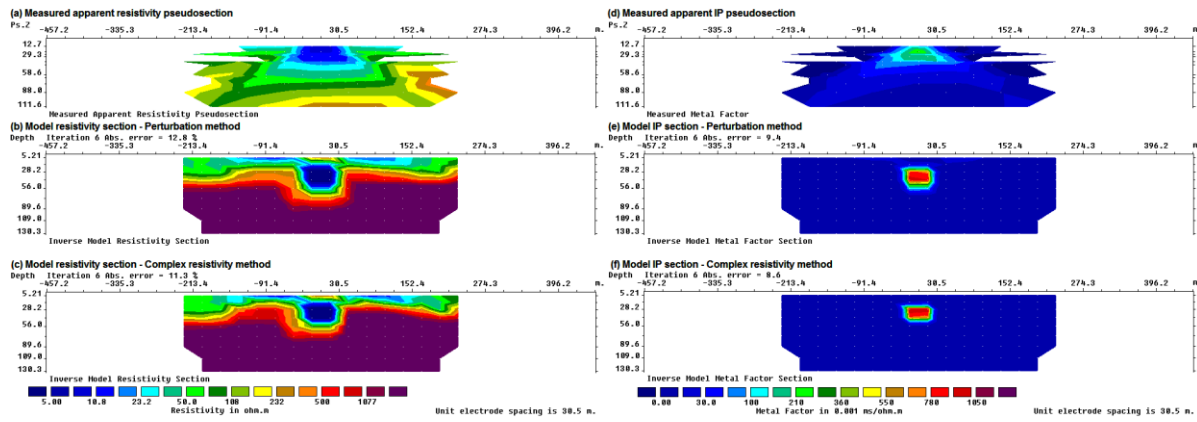
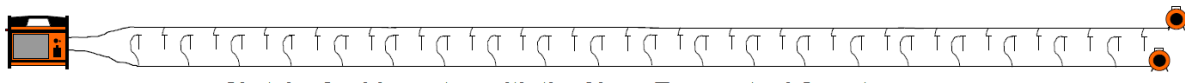


Figure 73. Magusi River massive sulphide ore body inversion models. (a) Apparent resistivity pseudosection. Resistivity inversion models obtained using the (b) perturbation and (c) complex resistivity methods. (d) Apparent I.P. (metal factor) pseudosection. I.P. models obtained using the (e) perturbation and (f) complex resistivity methods.

5.5 I.P. surveys with multi-electrode systems

Many multi-electrode systems now offer an I.P. measurement option. The maximum current from battery-based systems is usually 1 Amp or less. This is usually too low to give reliable I.P. data when the electrode spacing is more than a few meters. However there have been recent improvements in the electronic circuitry and field survey procedure (Dahlin and Leroux, 2012.) to improve the data quality. One method that can be used with conventional multi-electrode systems that has two separate cables is by using different cables for the current and potential electrodes (Figure 74). This reduces the EM coupling between the current and potential cables. The possible current and potential electrodes positions are reduced and special control files are needed for this configuration. However, this method can be used with any multi-electrode system that uses a two cable arrangement. The two cables are separated at a distance that is twice the electrode to cable jumper distance, which is about as far as apart as possible. The results from a multi gradient array survey are shown in Figure 75. A demonstration of the data acquisition method with separated parallel cable spreads for current transmission and potential measurement (Dahlin and Leroux, 2012) was made at the 3rd International Workshop on Induced Polarization held on Ile d'Oleron on 7-9 April 2014. The site is geologically characterized by sedimentary deposits including marine clay, locally known as “bri”, and river alluvium (Gouet, 2007). The resistivity section (Figure 75a) shows an upper 3 to 4 meters sandy layer underlain by lower resistivity saline mud sediments (Dahlin and Loke, 2015). The I.P. section (Figure 75b) shows a top 1 to 2 meters layer with chargeability values of 4 to 8 mV/V which is probably sandy sediments with some organic content. The low I.P. values below this layer is probably due to high salinity that tends to reduce the I.P. effect (Weller *et al.*, 2011). Note the apparent resistivity pseudosection shows fairly regular contour patterns, whereas the bottom part of the I.P. pseudosection has noisier data due to larger electrode spacings and weaker signals.



Sketch of cables setup with the Abem Terrameter LS system.

Figure 74. Sketch of separated cable spreads setup used (after Dahlin and Loke, 2015).

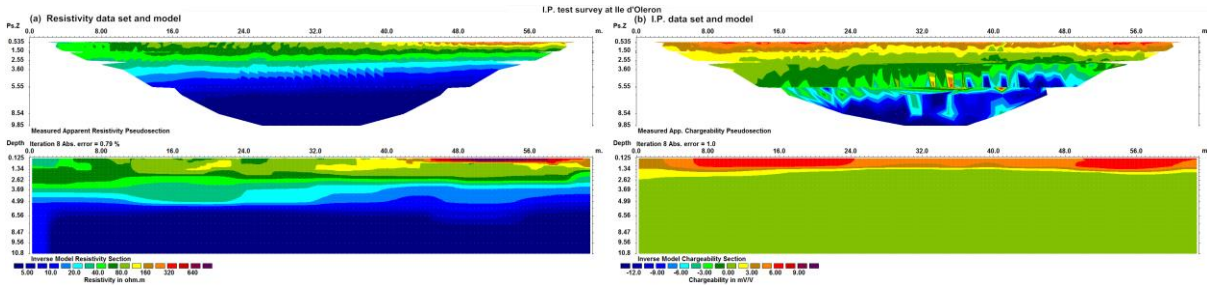


Figure 75. Resistivity and chargeability pseudosection from field demo at 3rd IP workshop at Ile d'Oleron (after Dahlin and Loke, 2015).

Table 10. Tests with 2-D I.P. inversion

Data set and purpose	Things to try
IPMODEL.DAT – A time-domain synthetic data set.	(1). After reading the data file, run the inversion with the default inversion options. (2). Next try with the robust inversion option. (3). The program also has an option to carry out the IP inversion sequentially after the resistivity inversion (under the “Type of IP inversion method” option in the “Inversion” menu). Try this and see if there are any differences in the results.
IPSHAN_PFE.DAT – A field data set from Burma (Edwards, 1977) with measurements in PFE.	(1). After reading the data file, carry out the inversion with the default inversion options. Try again using the option to ‘Limit the range of model resistivity’ option. (2). Try reducing the unit electrode spacing in the data file with a text editor to half the given value. Does it improve the inversion results?
IPMAGUSI_MF.DAT – A field data set from Canada (Edwards, 1977) with measurements in metal factor values.	(1). After reading the data file, carry out the inversion with the default inversion options. Try again using the option to ‘Limit the range of model resistivity’ option. (2). Run the inversion again with the ‘Select robust inversion’ option. This should make a significant difference in the results. (3). Try reducing the unit electrode spacing in the data file with a text editor to half the given value. Does it improve the inversion results?
IPKENN_PA.DAT – A field data set with the IP values in phase angles (Hallop, 1990).	(1). After reading the data file, carry out the inversion with the default inversion options.

6 Cross-borehole imaging

6.1 Introduction

One of the most severe limitations of 2-D imaging surveys carried out along the ground surface is the reduction in the resolution with depth. This is a fundamental physical limitation that no amount of reconfiguration of the surface arrays or computer modeling can overcome. In theory, the only way to improve the resolution at depth is to place the sensors (i.e. the electrodes) closer to the structures of interest. This is not always possible, but when such boreholes are present, cross-borehole surveys can give more accurate results than is possible with surface surveys alone.

That has been many fine publications on such surveys; such as by Zhao *et al.* (1986), Daily and Owen (1991), Sasaki (1992), LaBrecque *et al.* (1996), Slater *et al.* (1997, 2000), Zhou and Greenhalgh (1997, 2000) and Wilkinson *et al.* (2006a, 2008). In the following section, I will attempt to summarize the main results with regards to the choice of array configurations for cross-borehole surveys. However, please refer to the original papers for the details.

6.2 Electrode configurations for cross-borehole surveys

In theory, any array that is used for normal surface surveys can be adapted for cross-borehole surveys. We can have arrays with two electrodes, three electrodes and four electrodes.

6.2.1 Two electrodes array – the pole-pole

There are two possible configurations, both electrodes can be in the same borehole (Figure 76a), or the electrodes can be in different boreholes (Figure 76b). Figure 76c considers a third possibility that is sometimes not considered, with one electrode on the surface. In all cases, the areas of highest sensitivities are concentrated near the electrodes, particularly if the two electrodes are far apart in different boreholes as in Figure 76c. Note that the electrodes do not actually scan the area between them, as would be expected for a seismic survey with the source and receiver in different boreholes. Note that the region between the two electrodes generally has negative sensitivity values.

If there are n electrodes (including surface electrodes, if any), there are a total of $n(n-1)/2$ possible independent measurements. Most authors recommend measuring all the possible readings at the other electrodes for a current electrode, i.e. measure all the possible combinations. One problem with this array is the physical location of the two remote electrodes, C2 and P2. They must be sufficiently far so that the pole-pole approximation is sufficiently accurate. This means they must be located at a distance of at least 20 times the maximum separation used by the active C1 and P1 electrodes in the boreholes. The large distance between the P1 and P2 electrodes leads to the problem of contamination by telluric noise. These problems are exactly the same as that faced with the pole-pole array for normal surface arrays.

While many earlier researchers have used this array for cross-borehole surveys (Dailey and Owen, 1991; Shima, 1992; Spies and Ellis, 1995), more recent work tends to be less enthusiastic about it. Sasaki (1992) and Zhou and Greenhalgh (2000) found that this array has a significantly poorer resolution than the bipole-bipole and pole-bipole arrays.

The subsurface pole-pole array gives a useful illustration of the change in the geometric factor for subsurface arrays. We have seen that for a pole-pole array with both electrodes located on the surface of a half-space, the geometric factor k is given by

$$k = 2\pi a$$

where a is the spacing between the electrodes. For the case where both electrodes are within an infinite medium, the geometric factor is given by

$$k = 4\pi a$$

where r is the distance between the current and potential electrodes. For the case where both electrodes are below the surface of a half-space, the geometric factor is given by

$$k = 4\pi \left(\frac{rr'}{r+r'} \right)$$

where r' is the distance of the reflected image of the current (Figure 77) from the potential electrode.

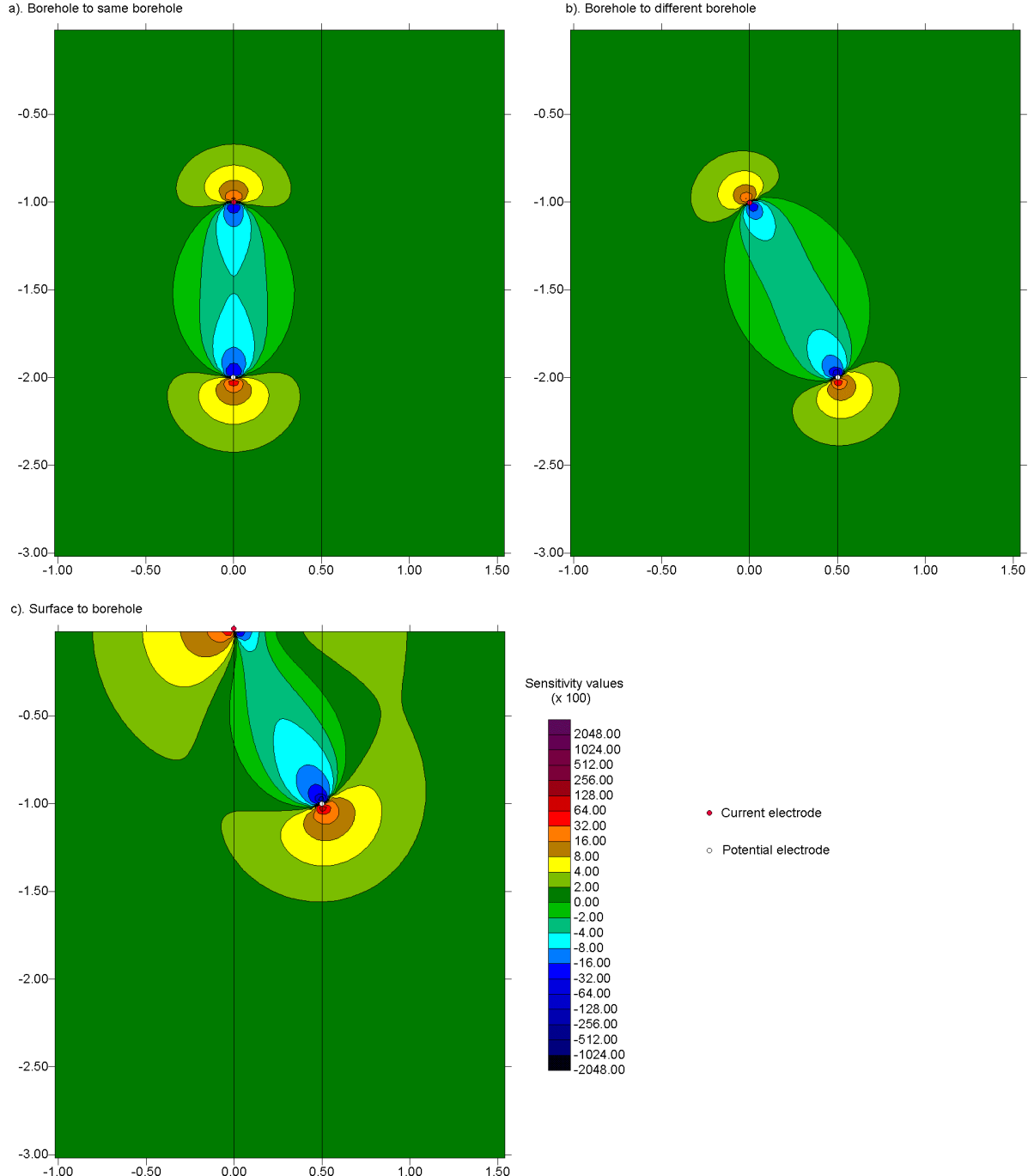


Figure 76. The possible arrangements of the electrodes for the pole-pole array in the cross-borehole survey and the 2-D sensitivity sections. The locations of the two boreholes are shown by the vertical black lines.

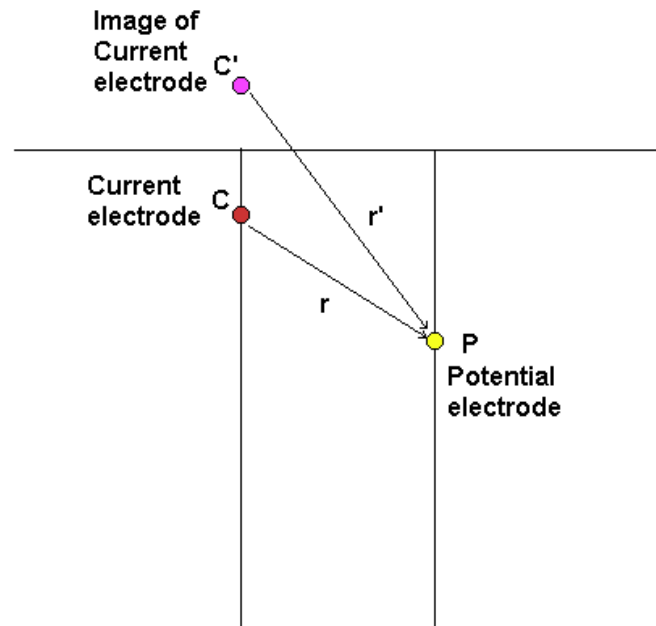


Figure 77. A schematic diagram of two electrodes below the surface. The potential measured at **P** can be considered as the sum of the contribution from the current source **C** and its image **C'** above the ground surface.

6.2.2 Three electrodes array – the pole-bipole

According to Zhou and Greenhalgh (1997), there are six possible independent configurations for the pole-bipole type of array (ignoring the surface electrodes). Of these six configurations there are two basic combinations, with the current electrode and one potential electrode in one borehole and the other potential electrode in the second borehole (Figure 78a), and with the current electrode in one borehole and both potential electrodes in the other borehole (Figure 78b). Zhou and Greenhalgh (1997) recommend the configuration with one current and potential electrode in the same borehole, and the second potential electrode in the other borehole (the C1P1-P2 or AM-N configuration). In Figure 78a, it can be seen that this configuration has high positive sensitivity values in between the two boreholes. This means that it provides significant information about the resistivity of the material between the two boreholes. The zones with the negative sensitivity values are confined to between the C1 and P1 electrodes in the first borehole and to the left of the P2 electrode in the second borehole.

The second configuration, with the current electrode in one borehole and both potential electrodes in the other borehole, has large negative sensitivity values between the C1 and P1 electrode and large positive values between the C1 and P2 electrodes. In between these two bands, there is a zone with small sensitivity values, i.e. the array does not give significant information about the resistivity in this zone. Another possible disadvantage of this array is that for some positions of the P1-P2 bipole, the potential value measured is very small or zero. This causes the signal to noise ratio to be small.

Figure 78c shows the sensitivity pattern when all three electrodes are in the same borehole. There are very high negative and positive sensitivity values in the vicinity of the borehole. Sugimoto (1999) recommends that such measurements also be made as they give valuable information about the dip of structures between the boreholes. Figure 78d shows the sensitivity pattern when the current electrode is on the surface. The sensitivity values between the C1 and P1 electrodes are relatively small (probably due to the large distance between these two electrodes), while the sensitivity values between the P1 and P2 electrodes have

moderate positive values.

Overall, many authors have positive remarks about this array. It provides better resolution and is less sensitive to telluric noise (since the two potential electrodes are kept within the survey area) compared to the pole-pole array. While in theory the resolution of the array is slightly poorer than the bipole-bipole array, the potential values measured are significantly higher.

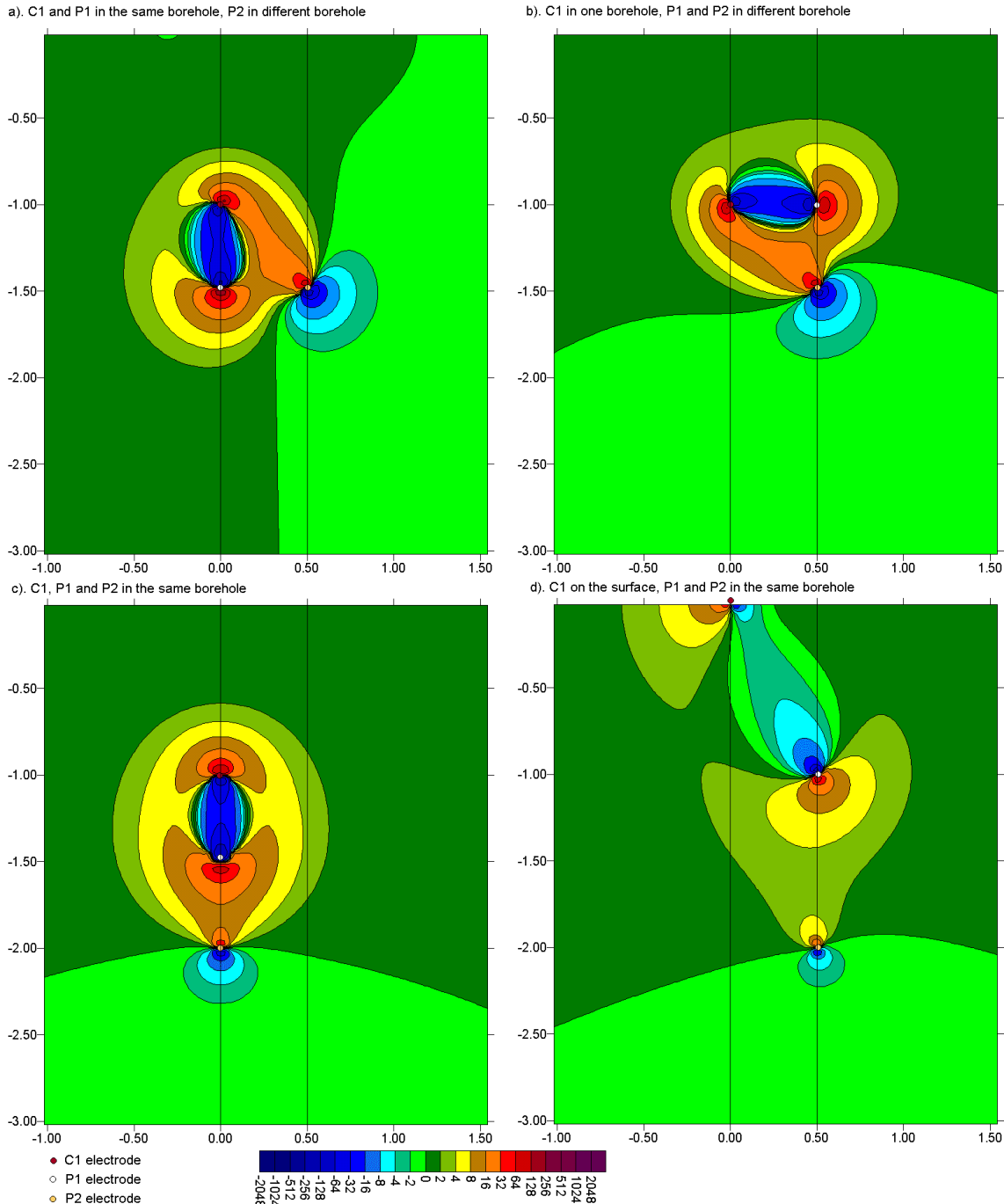


Figure 78. The 2-D sensitivity patterns for various arrangements with the pole-bipole array. The arrangement with (a) C1 and P1 in first borehole and P2 in second borehole, (b) C1 in the first borehole and both P1 and P2 in the second borehole, (c) all three electrodes in the first borehole and (d) the current electrode on the ground surface.

6.2.3 Four electrodes array – the bipole-bipole

Zhou and Greenhalgh (1997) list four possible independent configurations for this array, of which there two basic combinations. In the first arrangement, the positive current and potential electrodes C1 and P1 are located in one borehole, while the negative current and potential electrodes C2 and P2 are located in the second borehole (Figure 79a).

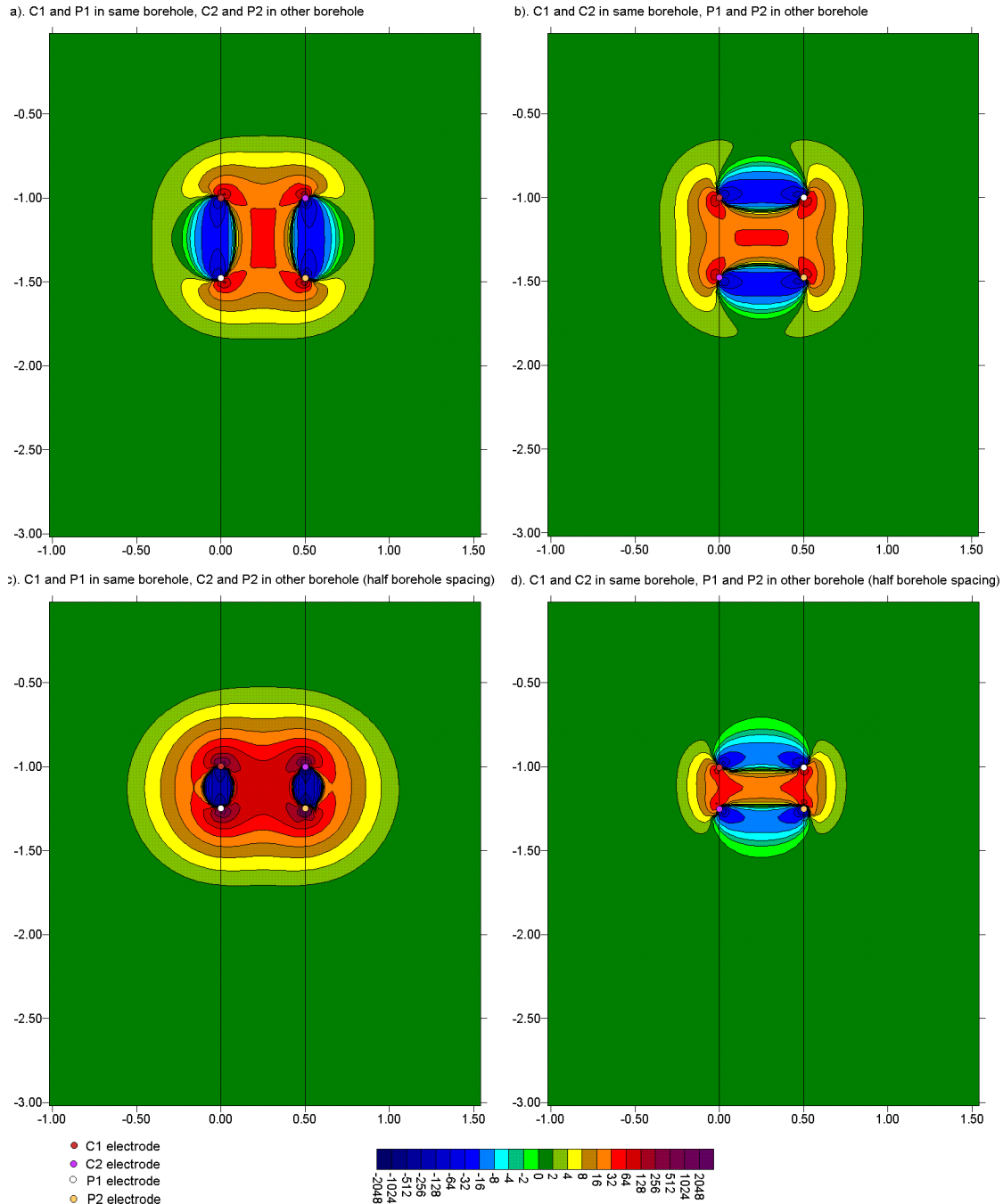


Figure 79. The 2-D sensitivity patterns for various arrangements of the bipole-bipole array. (a) C1 and P1 are in the first borehole, and C2 and P2 are in second borehole. (b) C1 and C2 are in the first borehole, and P1 and P2 are in second borehole. In both cases, the distance between the electrodes in the same borehole is equal to the separation between the boreholes. The arrangements in (c) and (d) are similar to (a) and (b) except that the distance between the electrodes in the same borehole is half the spacing between the boreholes.

In this arrangement, the C1P1-C2P2 configuration (i.e. the AM-BN arrangement of Zhou and Greenhalgh (1997), there are large positive sensitivity values in the area between the two boreholes. This is a desirable property for a cross-borehole array since the intention is to map the material between the two boreholes. The large negative sensitivity values are confined to the region along the boreholes between the C1 and P1 (and C2 and P2 electrodes). Figure 79c shows a similar arrangement, but with the spacing between the electrodes in the same borehole reduced to half the spacing between the boreholes. Note again the large positive sensitivity values between the two boreholes.

In the second basic configuration (Figure 79b), the C1C2 current bipole is located in one borehole while the P1P2 potential bipole is located in the other borehole. There is also a large region with positive sensitivity values between the two boreholes. However it is flanked by two zones with large negative sensitivity values. Thus the response of this C1C2-P1P2 arrangement to inhomogeneities between the boreholes is more complicated than the first arrangement. When the bipole length is reduced, the positive region is significantly reduced. These features make this arrangement less desirable for cross-borehole surveys. Another disadvantage is that the potential signal strength is weaker in the C1C2-P1P2 arrangement compared to C1P1-C2P2 configuration.

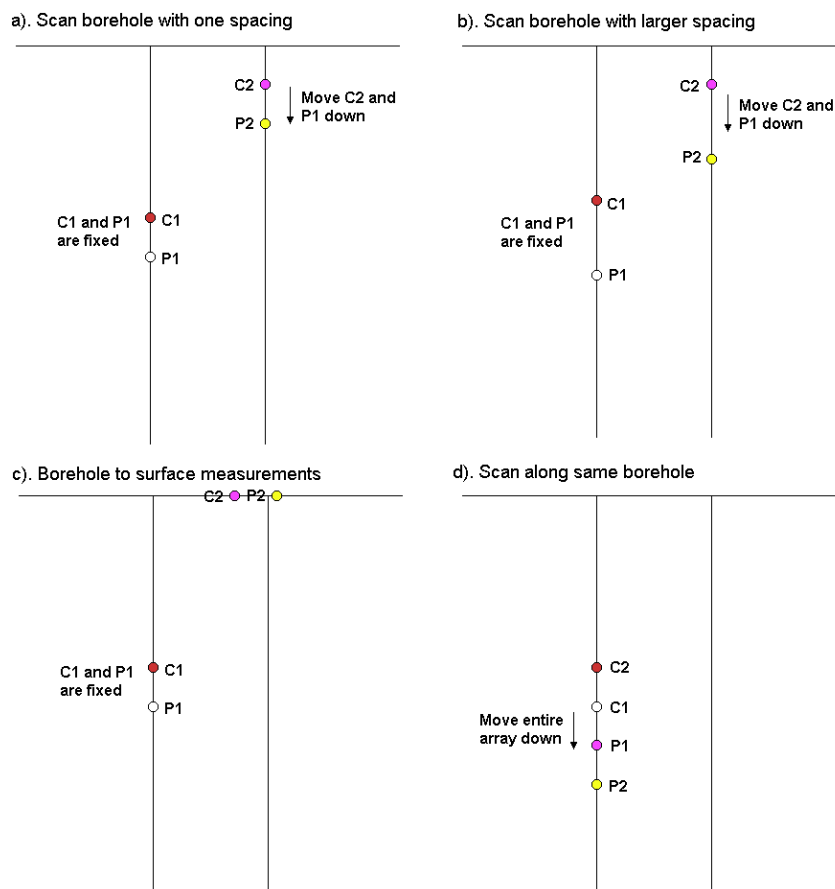
Overall, Zhou and Greenhalgh (1997, 2000) recommended the C1P1-C2P2 configuration. Sasaki (1992) has found the bipole-bipole array to have better resolution compared to the pole-pole and pole-dipole arrays. Figure 80 shows one possible field survey measurement sequence. A series of measurements is first made with a short spacing (for example half the distance between the boreholes) starting from the top. Next, measurements are repeated with a larger spacing between the electrodes. Due to the symmetry in the arrangements shown in Figure 80a,b measurements should also be made with other less symmetrical arrangements. Figure 80c,d show two other possible measurement sequences.

Note that the length of the boreholes must be comparable to the distance between the boreholes. Otherwise, if the spacing between the electrodes in the same borehole is much smaller than the distance between the boreholes, the readings are likely to be more influenced by the materials in the immediate vicinity of the boreholes, rather than the material in between the boreholes. In such a situation, the only alternative is probably to include the surface-surface and surface-borehole measurements.

Some more recent research in cross-borehole imaging may be found in the papers by Oldenborger et al. (2005), Chambers et al (2007), Wilkinson et al (2008) and Nimmer et al (2008).

Table 11. A few borehole inversion tests.

Data set and purpose	Things to try
BOREHOLE.DAT – A synthetic data set with the pole-bipole array.	(1). Read in the file, and try an inversion with the default inversion parameters. (2). Next you can try with the robust inversion option.
BORELUND.DAT – A pole-pole array field data set from Lund University, Sweden. The survey was conducted to map fractures in a limestone-marl formation (Dahlin pers. comm.).	(1). Read in the file, and try an inversion with the default inversion parameters. (2). Next you can try different settings, such as the robust inversion option. (3). The program also has an option to reduce the size of the model cells by half, which you might like to try.
BORELANC.DAT – A bipole-bipole array field data set from Lancaster University, U.K (Slater et al. 1997). The survey was conducted to map the flow of a saline tracer from the ground surface through the unsaturated zone.	(1). Read in the file, and run the inversion. The path of the saline tracer is represented by regions with low resistivity values. Can you identify the tracer in the model sections?

**Figure 80.** Possible measurement sequences using the bipole-bipole array. Other possible measurements sequences are described in the paper by Zhou and Greenhalgh (1997).

6.3 Single borehole surveys

When only a single borehole is available, only the borehole to surface measurements are possible. Figure 81a and Figure 81b shows two possible arrangements with two electrodes in the borehole and two electrodes on the surface. The first arrangement (Figure 81a) has the C1-C2 current bipole in the borehole while the P1-P2 bipole is on the surface. This arrangement has large positive sensitivity values between the C1-C2 bipole, and also between the P1-P2 bipole. The region of the subsurface between the two bipoles have moderate positive sensitivity values, while an approximately parallel zone stretching from the C2 current electrode (which is higher in the borehole) to the left of the P2 potential electrode has moderate negative sensitivity values. Figure 81b shows the alternative arrangement with the C1 and P1 electrodes in the borehole and the C2 and P2 pair on the surface. There is a small region of large negative sensitivity values along the borehole between the C1 and P1 electrodes. There is also a small near-surface zone between the C2 and P2 electrodes with large negative sensitivity values. However, note that most of the region between the two pairs of electrodes has relatively high positive sensitivity values. Since the intention of the survey is to map the subsurface between the two pairs of electrodes, this might be a better arrangement than the one given in Figure 81a.

In some situations, it might only be possible to have only one subsurface electrode, for example at the end of a drill bit or penetrometer (Sorensen, 1994). Figure 81c and Figure 81d shows the arrangements where the upper electrode that was formerly in the borehole (in Figure 81a and Figure 81b) is now placed on the surface near the borehole. The arrangement with the C1 electrode in the borehole and the C2 electrode on the surface (Figure 81c) has a near-surface zone of large negative sensitive values between the C2 electrode and the P2 electrode. However, there are moderately high positive sensitivity values in the region between the C1 electrode in the borehole and the P1-P2 bipole on the surface. The alternative arrangement with the C1 electrode in the borehole and the P1 electrode near the top of the borehole has a zone of large negative sensitivity values along the borehole. The region between the borehole and the C2-P2 electrodes has generally high positive sensitivity values, so this arrangement again might be better.

Figure 82 shows a pole-bipole configuration with the C1 current electrode in the borehole and the P1-P2 potential bipole on the surface. The sensitivity pattern is fairly similar to that obtained in Figure 81a. There is a region with moderate positive sensitivity values between the C1 electrode and the P1-P2 bipole, together with an approximately parallel zone of moderate negative sensitivity values between the C1 electrode and the region to the left of the P1 electrode. Overall, the arrangement shown in Figure 81d appears to be best due to the large zone of high positive sensitivity values between the borehole and the surface electrode pair. For all the possible arrangements, it is assumed that the normal surface-to-surface measurements are also made to fill in the gaps not covered by the borehole to surface measurements. The surface-to-surface measurements are particularly important to accurately map the resistivity distribution in the near-surface zone.

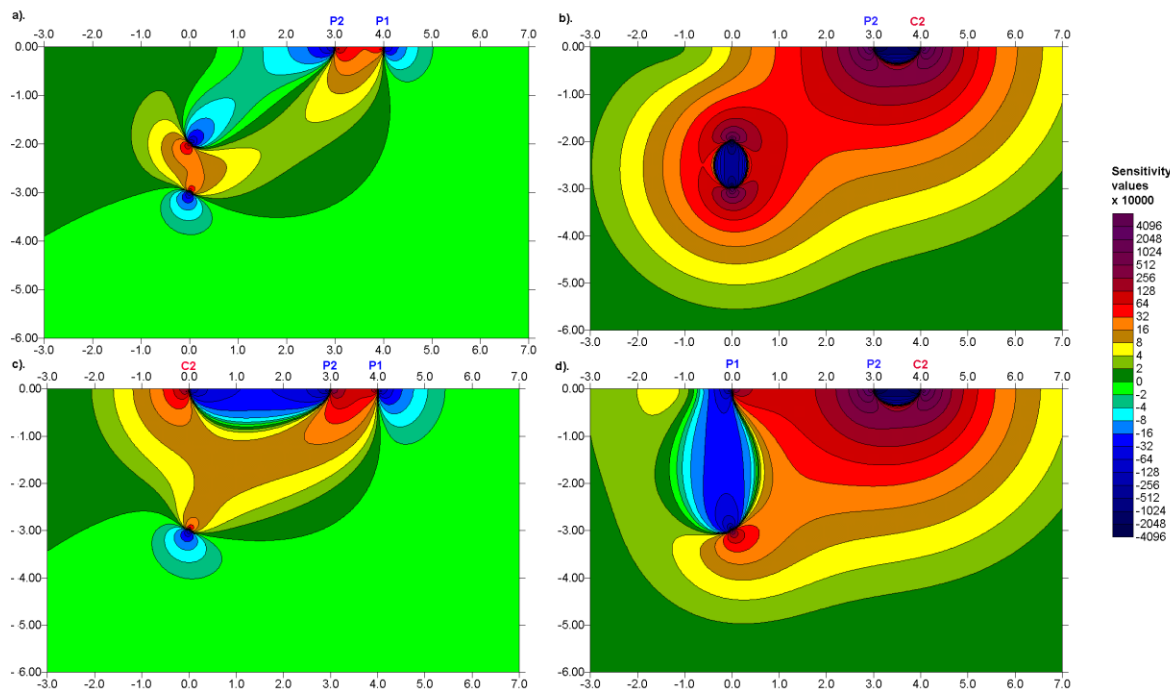


Figure 81. Several possible bipole-bipole configurations with a single borehole. (a) The C1 and C2 electrodes at depths of 3 and 2 meters respectively below the 0 meter mark. (b) The C1 and P1 electrodes at depths of 3 and 2 meters respectively below the 0 meter mark. (c). The C1 electrode is at a depth of 3 meters below the 0 meter mark while the C2 electrode is on the surface. (d). The C1 electrode is at a depth of 3 meters below the 0 meter mark while the P1 electrode is on the surface.

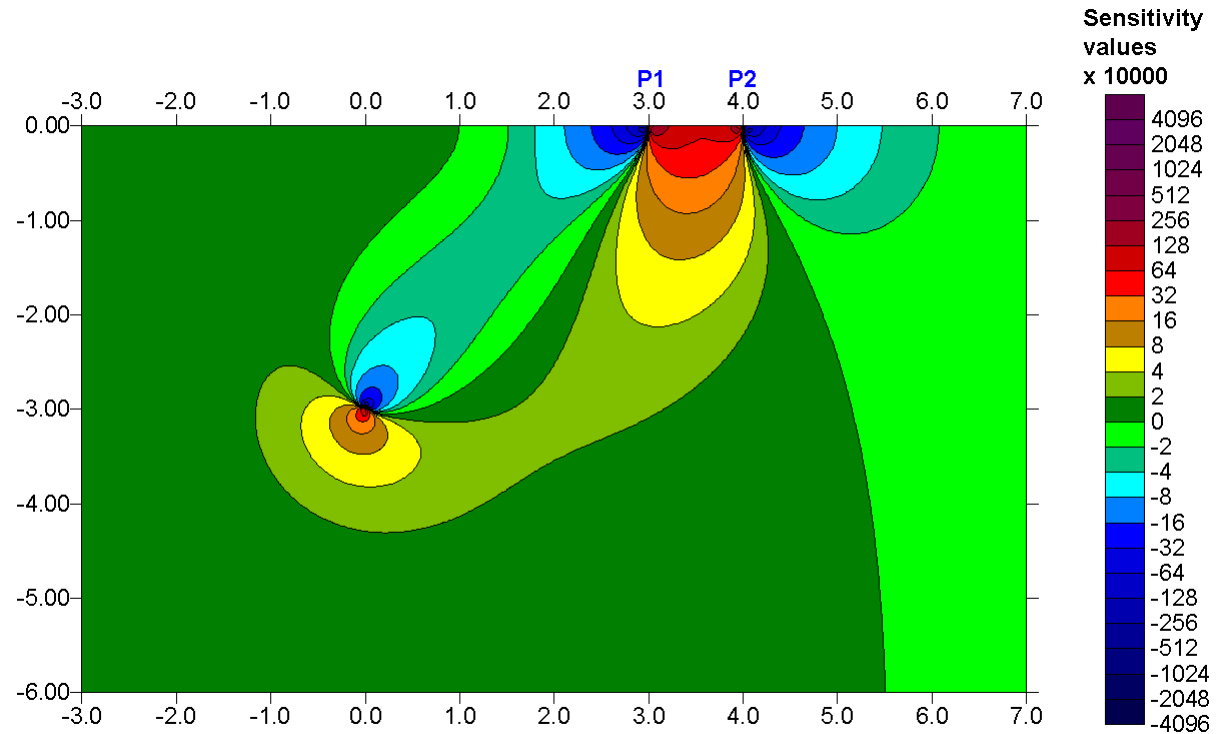


Figure 82. A pole-bipole survey with a single borehole. The C1 electrode is at a depth of 3 meters below the 0 meter mark.

6.4 Cross-borehole optimized arrays

Generating possible measurement sequences such as that described in section 6.2.3 involves some degree of subjective guesswork. A possibly more objective approach is to use the automatic array optimization method described earlier in section 4.9.4, which is described in detail in Loke *et al.* (2014b). As the details can be found in this paper, one of the results is shown here to illustrate the improvements that can be obtained. The test model consists of conductive and resistive blocks in a two-layer medium (Figure 83a). A block is also placed beyond the right column of borehole electrodes to assess the resolution of the different arrays for structures outside the borehole region. Three test arrays are used, (i) a 'standard' cross-borehole measurement sequence with 1875 data points that was used by Wilkinson *et. al.* (2006a) (ii) an optimized data set generated using the 'Compare R' method and (iii) a 'reduced' optimized data sets that excludes arrays with both current or both potential electrodes in the same borehole to avoid 'current channelling effects' in cases where the resistivity of the fluid filling the boreholes is much lower than the surrounding subsurface materials (Wilkinson *et al.*, 2006a). Measurements are made using 20 electrodes in each borehole together with 9 electrodes on the surface that are 1 meter apart. Gaussian random noise with a maximum amplitude of 1.0 milliohm was added to the resistance values before they were converted to apparent resistivity values. This resulted in average noise levels of 2.6%, 0.1% and 1.0% in the final apparent resistivity values for the full optimized, 'standard' and reduced optimized data sets. The higher noise levels of the optimized data sets are due to the higher average geometric factor of the arrays used.

The inversion models (Figure 83) show that the boundary between the two layers is well resolved by all the data sets. The background resistivity values, away from the embedded rectangular blocks, in the models are also generally within a few percent of the true values of 100 and 30 ohm-m in the two layers. The topmost high resistivity block is well resolved by all three data sets. The models with the full and reduced optimized data sets give maximum values of 888 and 980 ohm-m respectively (that are closer to the true value of 1000 ohm-m), while the 'standard' data set achieved a maximum value of only 653 ohm-m. The second (low resistivity) block within the borehole region is also detected by the three data sets. The full optimized data set model gives a minimum resistivity value of 50 ohm-m (true value 30 ohm-m), while the reduced optimized and 'standard' data sets give values of 56 and 65 ohm-m respectively. The third deepest block between the boreholes is well resolved by all the three data sets, with lowest model values of 15, 16 and 22 ohm-m (true value 10 ohm-m) respectively for the full optimized, reduced optimized and 'standard' data sets. The deepest block is resolved only in the full optimized data set (Figure 83b). The high resistivity block to the right of the borehole region is resolved by the full and reduced optimized data sets giving values of about 138 and 135 ohm-m (true value 1000 ohm-m) that are well above the background value of 100 ohm-m, while the 'standard' data set model fails to detect it. Overall, the optimized data sets perform better than the standard measurement sequence. One advantage of using the array optimization method that it is completely automatic taking just minutes on modern PCs.

6.5 Optimized arrays with subsurface electrodes

The cost involved in drilling conventional vertical boreholes and placement of the subsurface electrodes is much higher compared to conventional surveys with electrodes only on the ground surface. This in practice the number of cross-borehole field surveys is relatively small compared to conventional surface only surveys. An inexpensive and innovative method to overcome the high costs of drilling conventional boreholes is the MERIT (Multi-Electrode Resistivity Implant Technique) system using a direct-push installation technique (Harro and Kruse, 2013) where a matching set of subsurface electrodes

is installed directly below a line of surface electrodes (Figure 84). The cost to install the subsurface electrodes is about half that of a conventional vertical borehole. This system is useful when it is necessary to image a region of a long horizontal extent over a limited depth range. In a typical survey, the length of the line is about 5 times the depth of the subsurface electrodes.

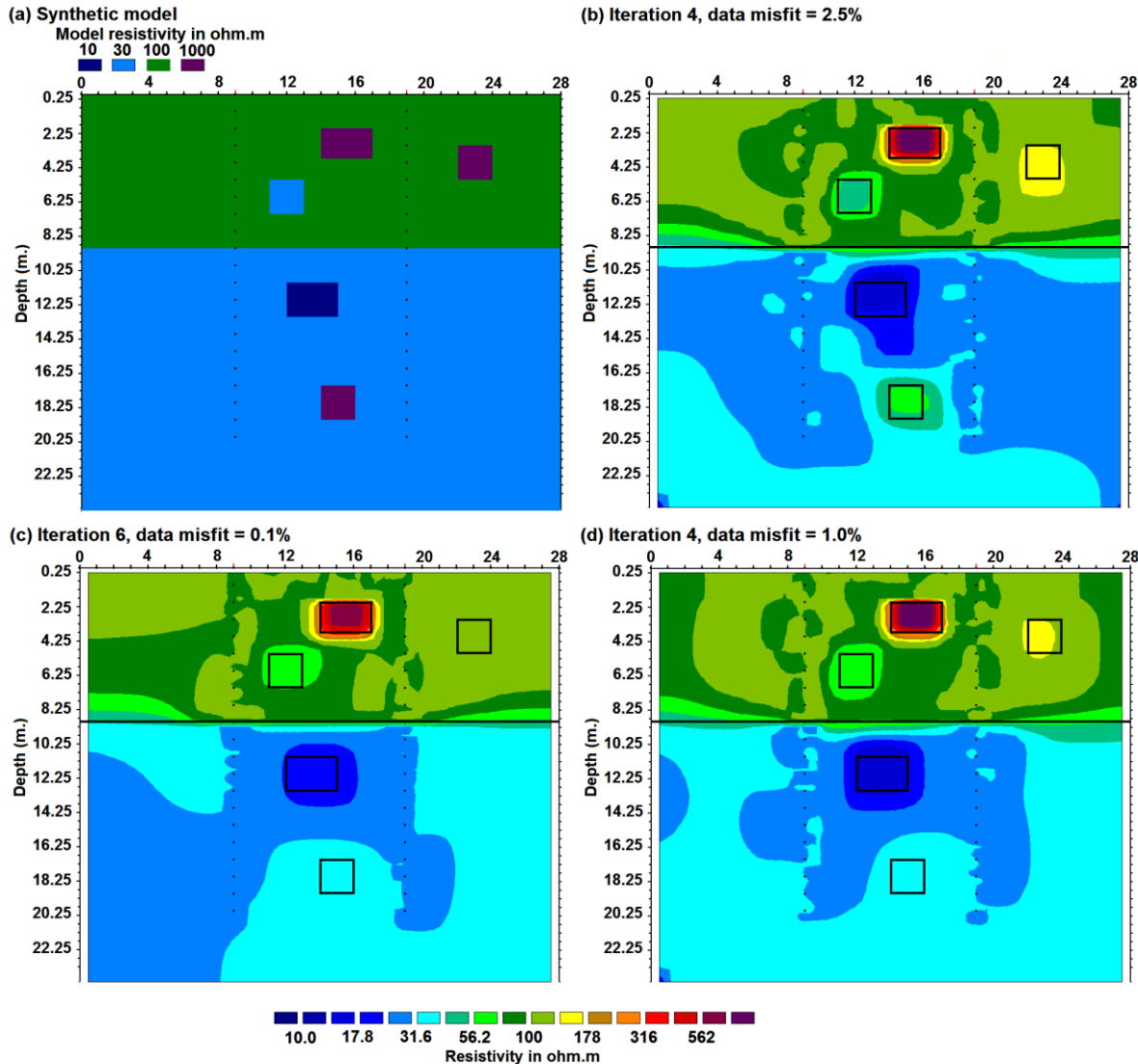


Figure 83. Test of optimized cross-borehole arrays with a synthetic model. (a) Two-layer test model with conductive and resistive anomalies. Inversion models for (b) optimized data set with all arrays, (c) 'standard' data set and (d) the reduced optimized data set that excludes arrays with both current (or potential) electrodes in the same borehole. All the data sets have 1875 data points. The outlines of the rectangular blocks showing their true positions are also shown.

A method to generate optimized arrays for this type of survey configuration is described in Loke *et al.* (2015b). An example of the improvement that can be obtained compared to 'standard' arrays generated manually using heuristic rules (Harro and Kruse, 2013) is shown in Figure 85. The survey was carried out at the Geopark research site on University of South Florida campus in west-central Florida, United States. The site is characterized by karstified limestone bedrock overlain by about 5 meters of overburden soils consisting of granular

sands over more cohesive sandy clay and clay soil with clay content generally increasing with depth (Loke *et al.*, 2015b). Depths to contacts were available for standard penetration tests (SPTs), cone penetration tests (CPTs) and GPR data (Stewart and Parker, 1992). A deep array of 14 electrodes was implanted at 7.62 m below ground surface with an electrode spacing of 4 m with a matching set of 14 electrodes on the surface directly above the implanted electrodes. The models for the optimized data sets (Figure 85b and c) shows better agreement with the known geology from the geotechnical and GPR data, in terms of the lower boundary of the top sandy layer and the positions of the cavities, compared to the ‘standard’ arrays model (Figure 85a).

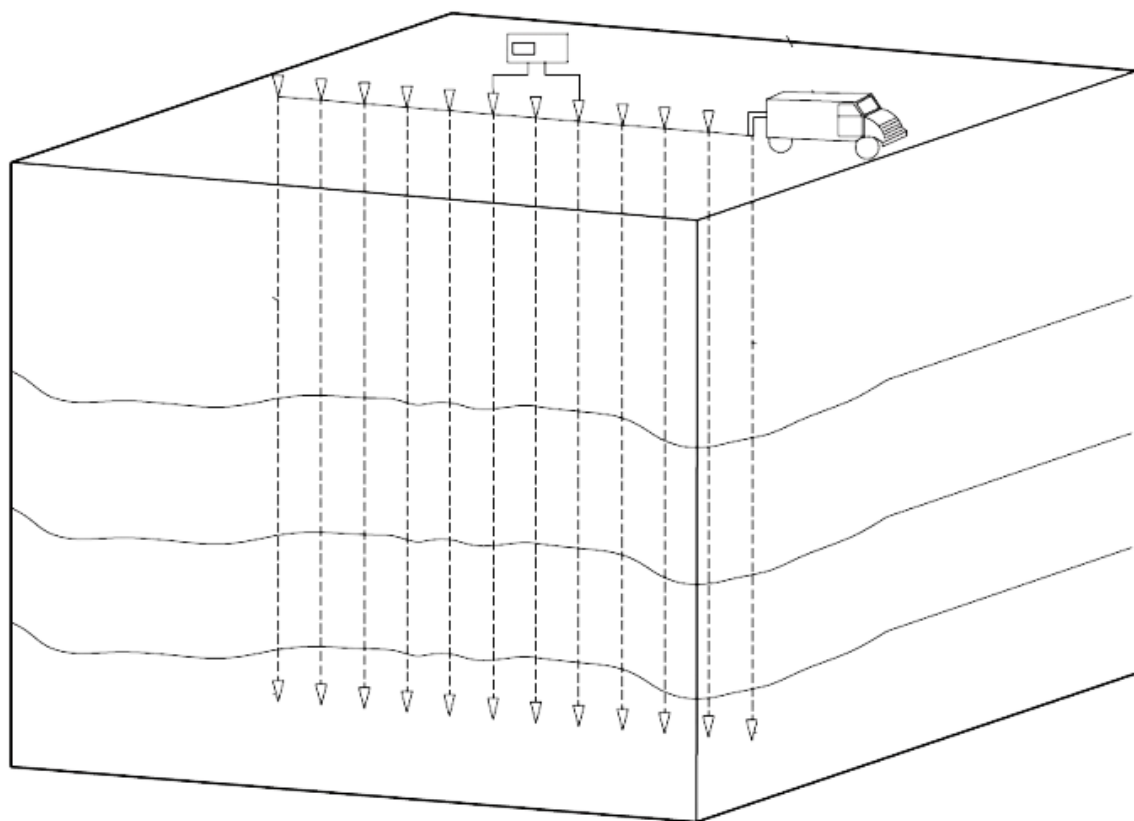


Figure 84. Schematic diagram of the MERIT method with the electrodes are planted along the surface and directly below using the direct push technology (after Harro and Kruse, 2013).

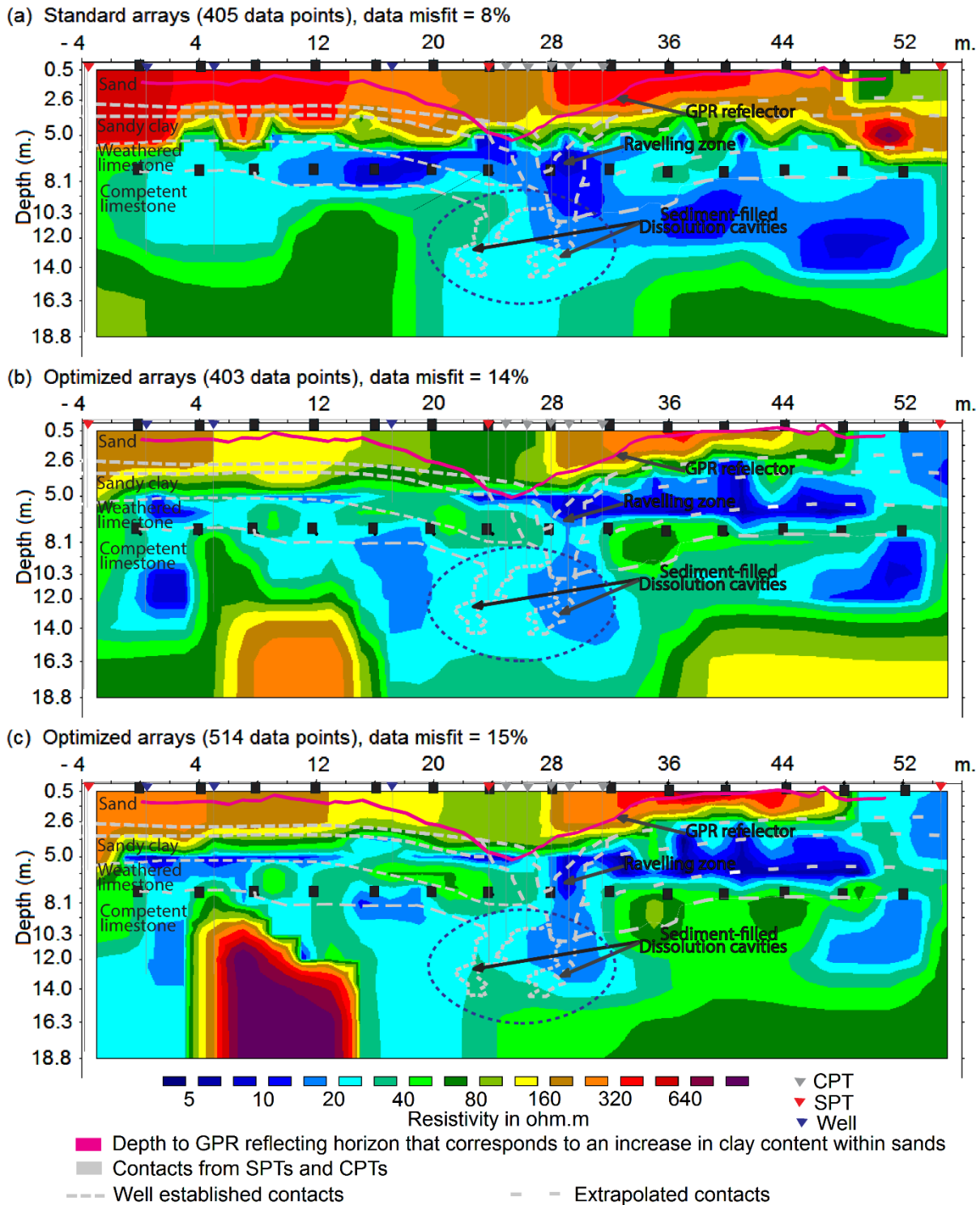


Figure 85. Inversion models for the different data sets for the data collected with electrodes at surface and 7.62 m depth with 4 m horizontal spacing. Models for the (a) standard arrays (405 data points), optimized arrays with (b) 403 and (c) 514 data points.

7 2-D field examples

7.1 Introduction

Here we will look at a number of examples from various parts of the world to give you an idea of the range of practical survey problems in which the electrical imaging method has been successfully used.

7.2 Landslide - Cangkat Jering, Malaysia

A common problem faced in Malaysia is landslides on hill slopes. The landslides are often triggered by water accumulation within part of the slope that leads to weakening of a section of the slope. Figure 86 shows the results from a survey conducted on the upper part of a slope where a landslide had occurred in the lower section. Weathering of the granite bedrock produces a clayey sandy soil mixed with core boulders and other partially weathered material. The image obtained from this survey shows a prominent low resistivity zone below the center of the survey line. This is probably caused by water accumulation in this region that reduces the resistivity to less than 600 $\Omega\cdot\text{m}$. To stabilize the slope, it would be necessary to pump the excess water from this zone. Thus, it is important to accurately map the zone of ground water accumulation. This data set also shows an example with topography in the model section.

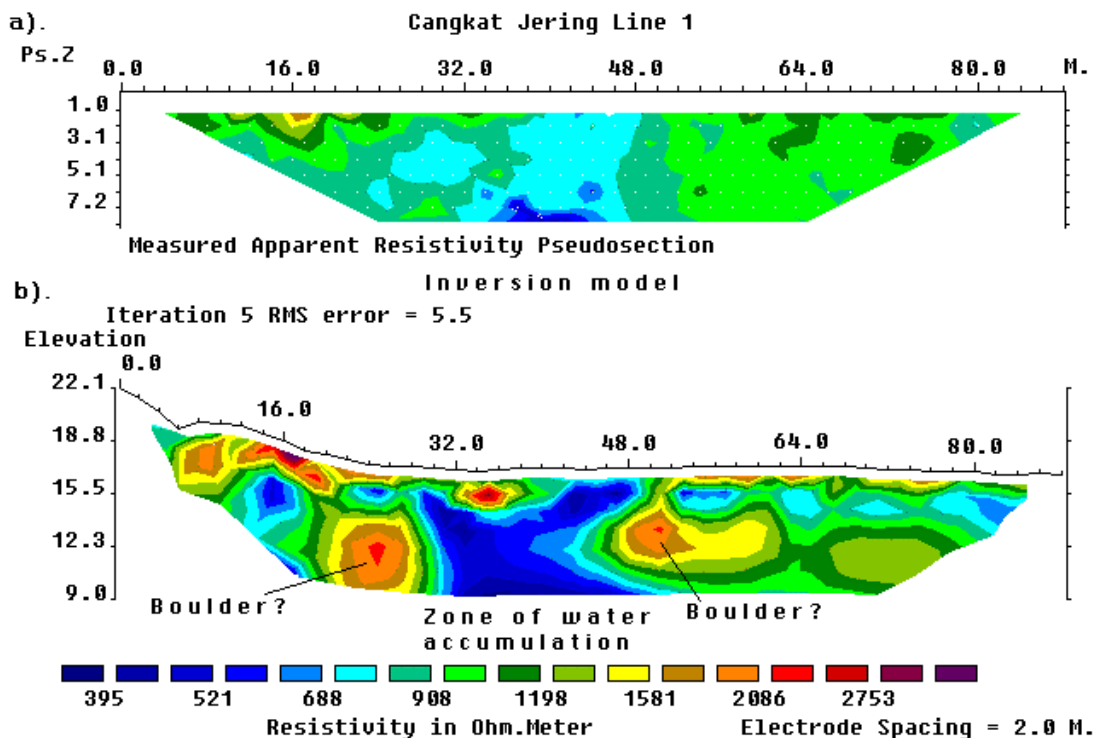


Figure 86. Landslide field example, Malaysia. (a) The apparent resistivity pseudosection for a survey across a landslide in Cangkat Jering and (b) the interpretation model for the subsurface.

7.3 Old Tar Works - U.K.

A common environmental problem in industrial countries is derelict industrial land. Before such land can be rehabilitated, it is necessary to map old industrial materials (such as metals, concrete blocks and chemical pollutants) that are left buried in the ground. Another problem in such areas is chemical wastes that had been stored within the factory grounds.

Due to the nature of such sites, the subsurface is often very complex and is a challenging target for most geophysical methods. The survey for this example was carried out on a derelict industrial site where leachate was known, from a small number of exploratory wells, to be moving from a surface waste lagoon into the underlying sandstones (Barker, 1996). Eventually the leachate was seen seeping into a nearby stream. However, the extent of the subsurface contamination was not known.

An electrical imaging survey was carried out along an old railway bed between the lagoon and the stream. The metal railway lines had been removed except for short lengths embedded in asphalt below a large metal loading bay. In the apparent resistivity pseudosection (Figure 87a), the area with contaminated ground water shows up as a low resistivity zone to the right of the 140 meters mark. The metal loading bay causes a prominent inverted V shaped low resistivity anomaly at about the 90 meters mark. In the inversion model (Figure 87b), the computer program has managed to reconstruct the correct shape of the metal loading bay near the ground surface. There is an area of low resistivity at the right half of the section that agrees with what is known from wells about the occurrence of the contaminated ground water. The plume is clearly defined with a sharp boundary at 140 meters along the profile. The contaminated zone appears to extend to a depth of about 30 meters.

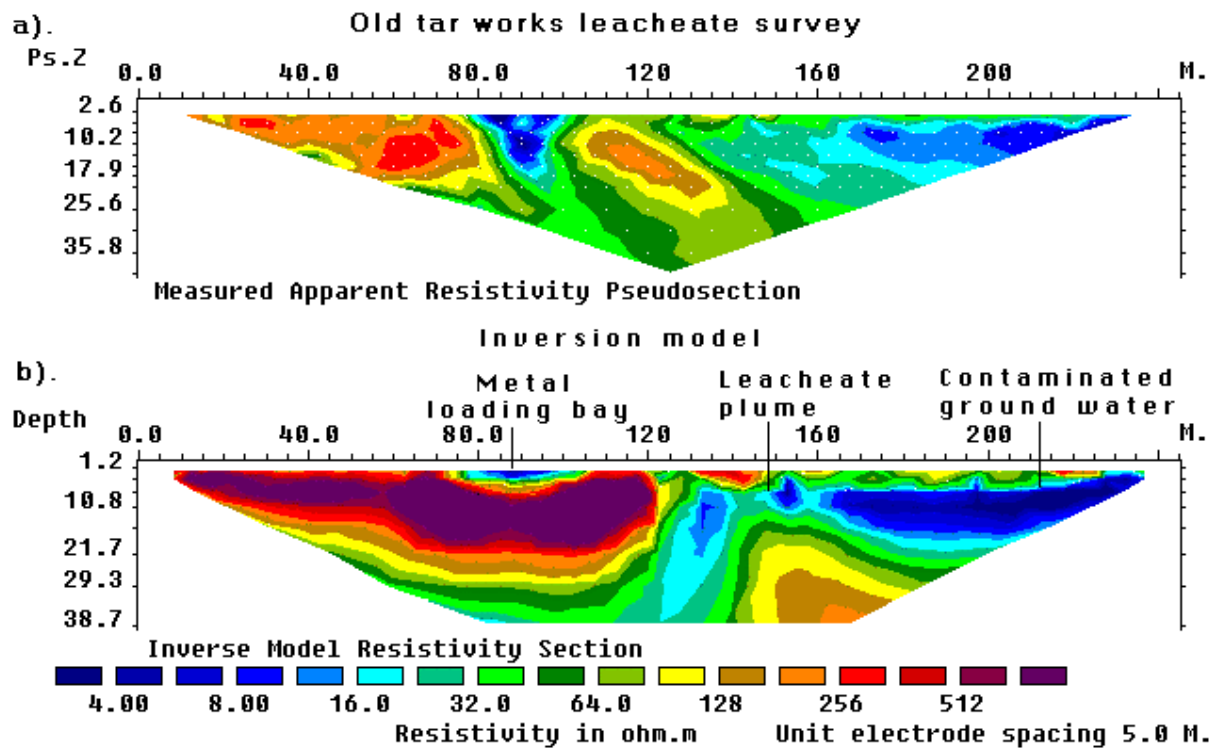


Figure 87. Industrial pollution example, U.K. (a) The apparent resistivity pseudosection from a survey over a derelict industrial site, and the (b) computer model for the subsurface.

7.4 Holes in clay layer - U.S.A.

This survey was carried out for the purpose of mapping holes in a clay layer that underlies 8 to 20 feet (2.5 to 6.2 meters) of clean sand (Cromwell pers. comm.). The results from the electrical imaging survey were subsequently confirmed by boreholes.

The pseudosection from one line from this survey is shown in Figure 88a. The data in the pseudosection was built up using data from horizontally overlapping survey lines. One interesting feature of this survey is that it demonstrates the misleading nature of the

pseudosection, particularly for the dipole-dipole array. In the inversion model, a high resistivity anomaly is detected below the 200 ft. mark, which is probably a hole in the lower clay layer (Figure 88b). This feature falls in an area in the pseudosection where there is an apparent gap in the data.

However, a plot of the sensitivity value of the cells used in the inversion model shows that the model cells in the area of the high resistivity body have higher sensitivity values (i.e. more reliable model resistivity values) than adjacent areas at the same depth with more data points in the pseudosection plot (Figure 88c). This phenomenon is due to the shape of the contours in the sensitivity function of the dipole-dipole array (Figure 24), where the areas with the highest sensitivity values are beneath the C1C2 and P1P2 dipoles, and not at the plotting point below the center of the array. This example illustrates the danger of only using the distribution of the data points in the pseudosection to constrain the position of the model cells (Barker, 1992; Loke and Barker, 1996a). If the model cells are placed only at the location of the data points, the high resistivity body will be missing from the inversion model, and an important subsurface feature would not be detected!

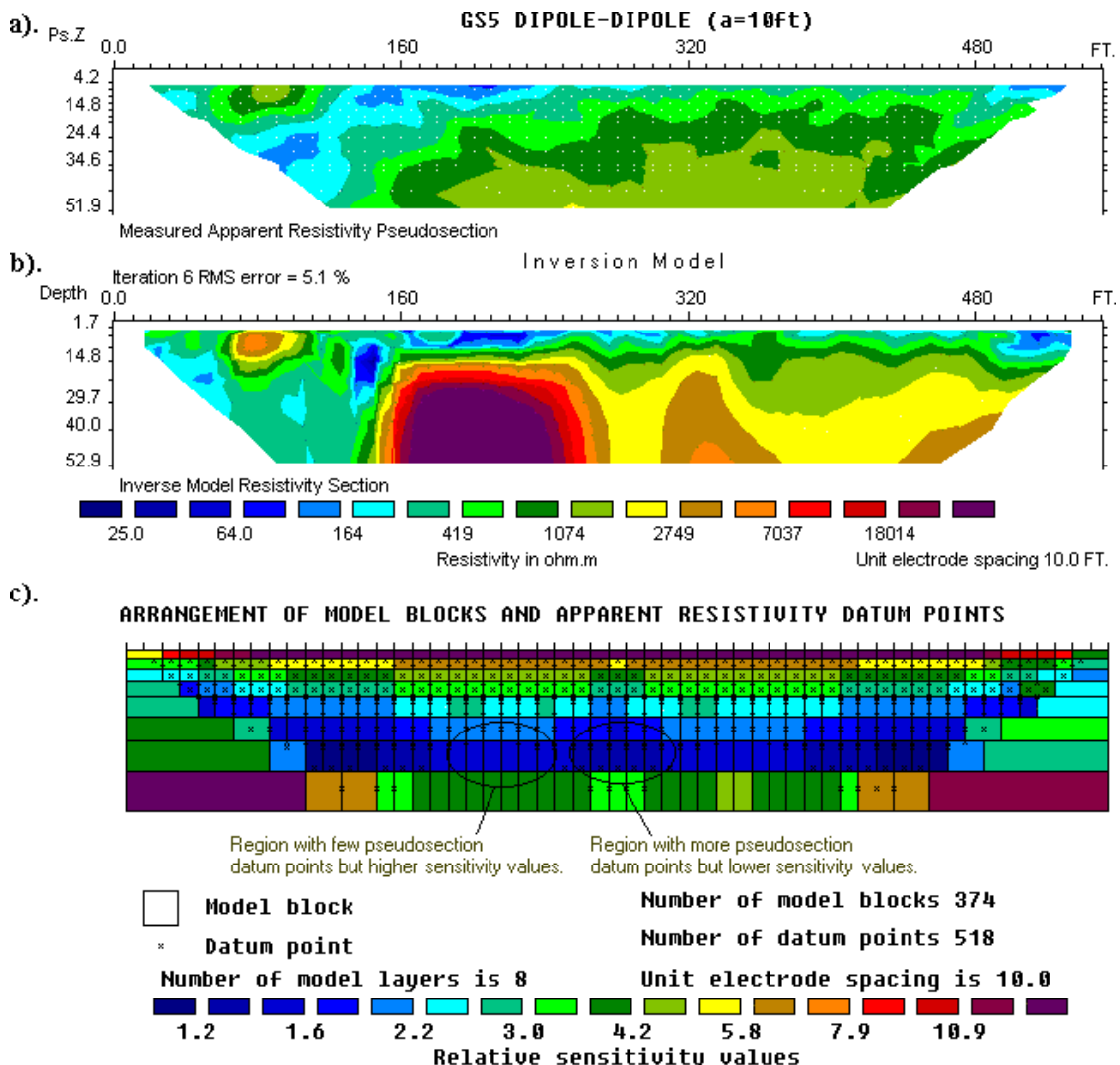


Figure 88. Mapping of holes in a clay layer, U.S.A. (a) Apparent resistivity pseudosection for the survey to map holes in the lower clay layer. (b) Inversion model and (c) sensitivity values of the model cells used by the inversion program.

7.5 Time-lapse water infiltration survey - U.K.

Resistivity imaging surveys have not only been carried out in space, but also in time! In some studies, the change of the subsurface resistivity with time has important applications. Such studies include the flow of water through the vadose (unsaturated) zone, changes in the water table due to water extraction (Barker and Moore, 1998), flow of chemical pollutants and leakage from dams (Johansson and Dahlin, 1996). The modifications to the inversion method to minimize variations across the different time models are described in Loke *et al.* (2014a).

A simple, but very interesting, experiment to map the flow of water from the ground surface downwards through the unsaturated zone and into the water table was described by Barker and Moore (1998). In this section, only some of the highlights of this experiment are described as an illustration of a time-lapse survey. This experiment was carried out in the Birmingham (England) area where forty thousand litres of water was poured on the ground surface using a garden hose over a period of 10 hours. Measurements were made before and during the irrigation of the ground surface, and after that for a period of about two weeks. Figure 89 shows the results of a survey carried out at the beginning of the experiment before the irrigation started. The inversion model (Figure 89b) shows that the subsurface, that consists of sand and gravel, is highly inhomogeneous. The water was poured out near the 24 meters mark on this line, and Figure 89c shows the inversion model for the data set collected after 10 hours of continuous irrigation. While the model resistivity values in the vicinity of the 24 meters mark are generally lower than the initial data set model in Figure 89b, the subsurface distribution of the water is not very clear from a direct comparison of the inversion models alone.

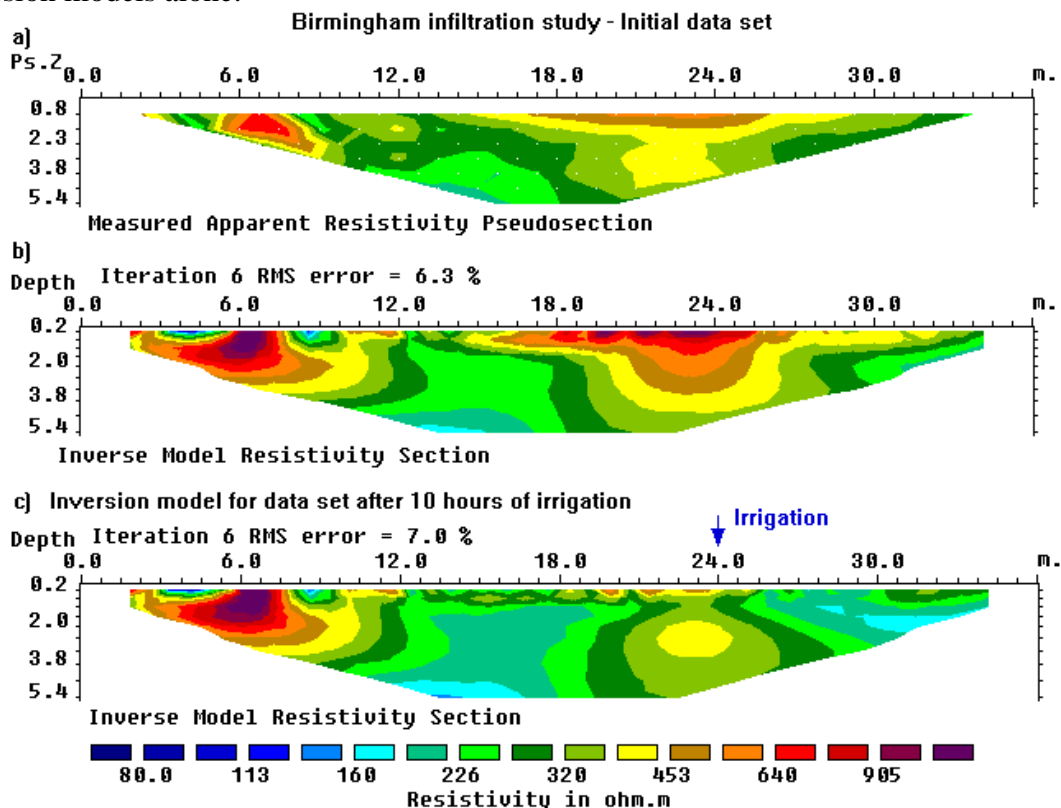


Figure 89. Water infiltration mapping, U.K. (a) The apparent resistivity and (b) inversion model sections from the survey conducted at the beginning of the Birmingham infiltration study. This shows the results from the initial data set that forms the base model in the joint inversion with the later time data sets. As a comparison, the model obtained from the inversion of the data set collected after 10 hours of irrigation is shown in (c).

The water distribution is more easily determined by plotting the percentage change in the subsurface resistivity of the inversion models for the data sets taken at different times (Figure 90) when compared with the initial data set model. The data set collected at 5 hours after the pumping began shows a reduction in the resistivity (of up to over 50 percent) near the ground surface in the vicinity of the 24 meters mark. The near-surface low resistivity zone reaches its maximum amplitude after about 10 hours when the pumping was stopped (Figure 90b). Twelve hours after the pumping was stopped, the low resistivity plume has spread downwards and slightly outwards due to infiltration of the water through the unsaturated zone. There is a decrease in the maximum percentage reduction in the resistivity values near the surface due to migration of the water from the near surface zone. This effect of the spreading of the plume becomes increasingly more pronounced after 24 hours (Figure 90d) and 36 hours (Figure 90e) due to further migration of the water. Note that the bottom boundary of the zone with approximately 20 percent reduction in the resistivity values tends to flatten out at a depth of about 3 meters (Figure 90e) where the plume from the surface meets the water table.

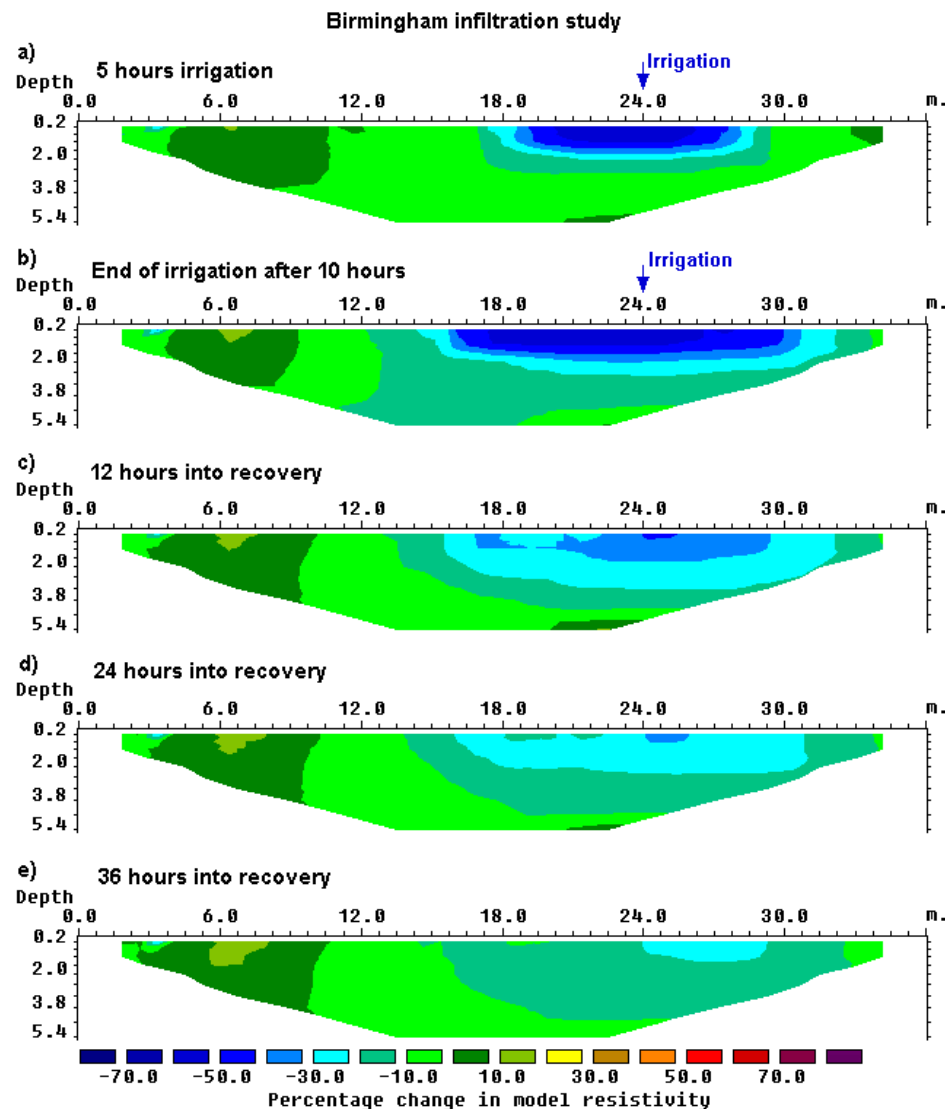


Figure 90. Time-lapse sections from the infiltration study. The sections show the change in the subsurface resistivity values with time obtained from the inversion of the data sets collected during the irrigation and recovery phases of the study.

7.6 Pumping test, U.K.

Resistivity measurements were made during a pumping test in the Hoveringham area of East Central England. The aquifer is a sand and gravel layer overlying mudstone. Figure 91 shows the initial apparent resistivity pseudosection, and model sections before pumping and after 220 minutes of pumping. Figure 92 that shows the relative change in the resistivity at 40, 120 and 220 minutes after the start of the pumping test.

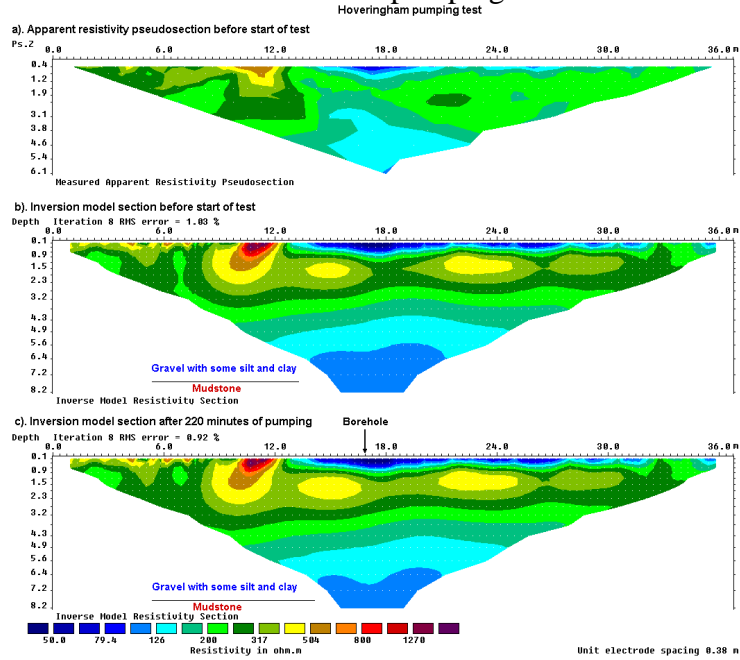


Figure 91. Hoveringham pumping test, U.K. (a) The apparent resistivity pseudosection at the beginning of the test. The inversion model sections at the (b) beginning and (v) after 220 minutes of pumping.

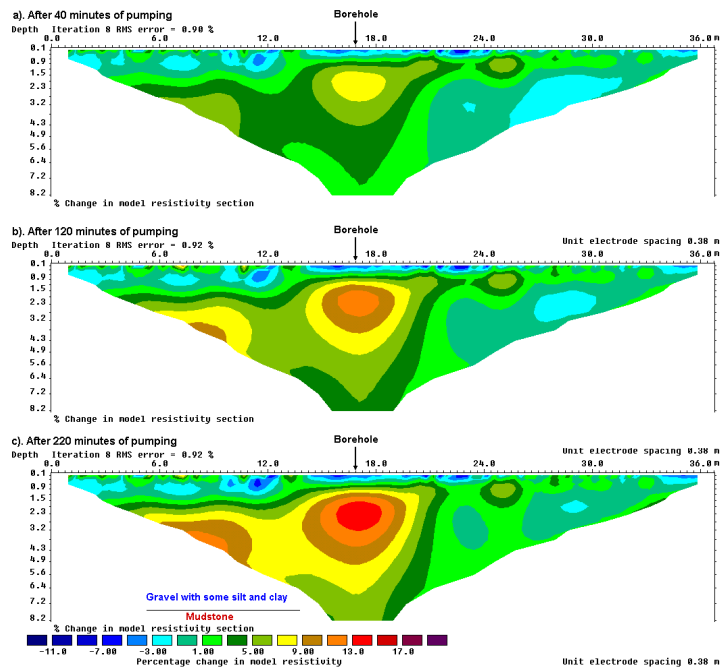


Figure 92. Percentage relative change in the subsurface resistivity values for the Hoveringham pumping test. To highlight the changes in the subsurface resistivity, the changes in the model resistivity are shown. Note the increase in the model resistivity below the borehole with time.

Figure 92 clearly shows the increase in the zone with higher resistivity values with time due to the extraction of the water. By using Archie's Law, and assuming the water resistivity does not change with time, we can estimate the change in the water saturation values. The decrease in the water saturation level within the aquifer, or desaturation values, is shown in Figure 93. As Archie's Law assumes that the conduction is due to the water content alone, the desaturation values are likely to be lower than the true values if there is significant clay content.

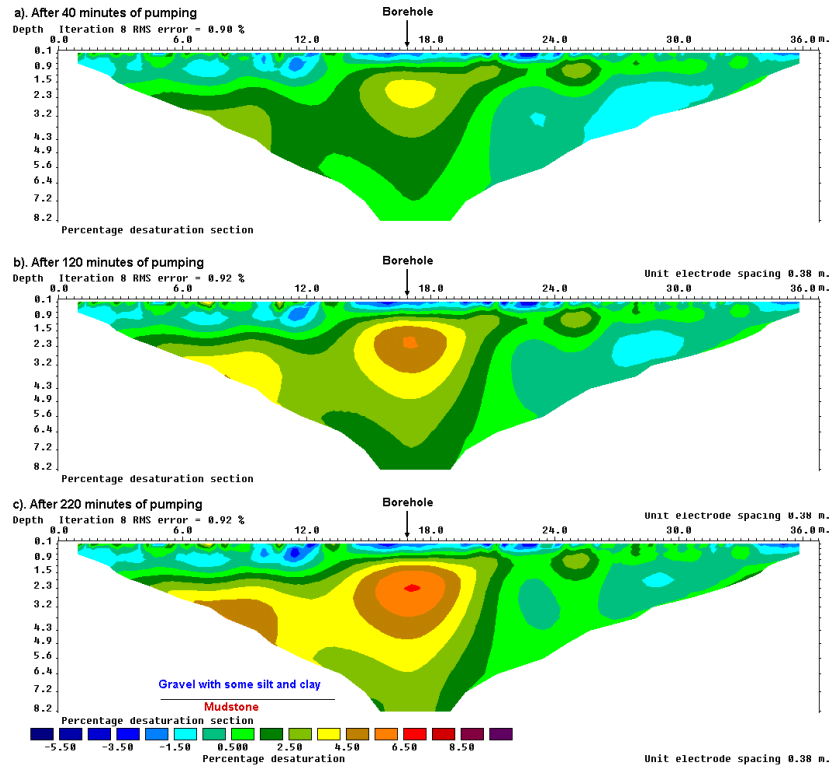


Figure 93. Use of Archie's Law for the Hoveringham pumping test. Sections showing the relative desaturation values obtained from the inversion models of the data sets collected during the different stages of the Hoveringham pumping test. Archie's Law probably gives a lower limit for the actual change in the aquifer saturation.

7.7 Wenner Gamma array survey - Nigeria

The Wenner Gamma array (Figure 4c) has a relatively unusual arrangement where the current and potential electrodes are interleaved. Compared to the Wenner Alpha and Beta arrays, the Wenner Gamma array is much less frequently used in field surveys. However, in some situations, there might be some advantage in using this array. The depth of investigation is significantly deeper than the Wenner Alpha array (0.59a compared to 0.52a, see Table 2), but the potential measured between the potential electrodes is only about 33% less than the Alpha array. In comparison, the voltage that would be measured by the Wenner Beta array is one-third that of the Alpha array which could be a serious disadvantage in noisy environments.

Figure 94a shows the Wenner Gamma array pseudosection from a groundwater survey in the Bauchi area of Nigeria (Acworth, 1981). In this region, groundwater is frequently found in the weathered layer above the crystalline bedrock. The weathered layer is thicker in areas with fractures in the bedrock, and thus such fractures are good targets for groundwater. In this area, the surveys were carried out with the Wenner Alpha, Beta and

Gamma arrays, together with electromagnetic profiling measurements using a Geonics EM34-3 system (Acworth, 1987). Here, only the result from the Wenner Gamma array data set is shown as an example.

To emphasize the boundary between the soil layer and the bedrock, the robust inversion option was used (section 4.3). The inversion model is shown in Figure 94b. The thickness of the lower resistivity weathered layer is generally about 10 to 20 meters. There is a narrow vertical low resistivity zone with a width of less than 20 meters below the 190 meters mark that is probably a fracture zone in the bedrock. A borehole well that was placed at the 175 meters mark that lies just at the edge of the fracture zone. It had yields that were somewhat lower than expected (Acworth, 1987). In such a situation, the 2D resistivity model would be useful to pinpoint the exact location of the center of the fracture zone to improve the yield from the borehole. The placement of the well was largely based on resistivity and EM profiling data, and many years before 2D resistivity inversion software and fast microcomputers were widely available.

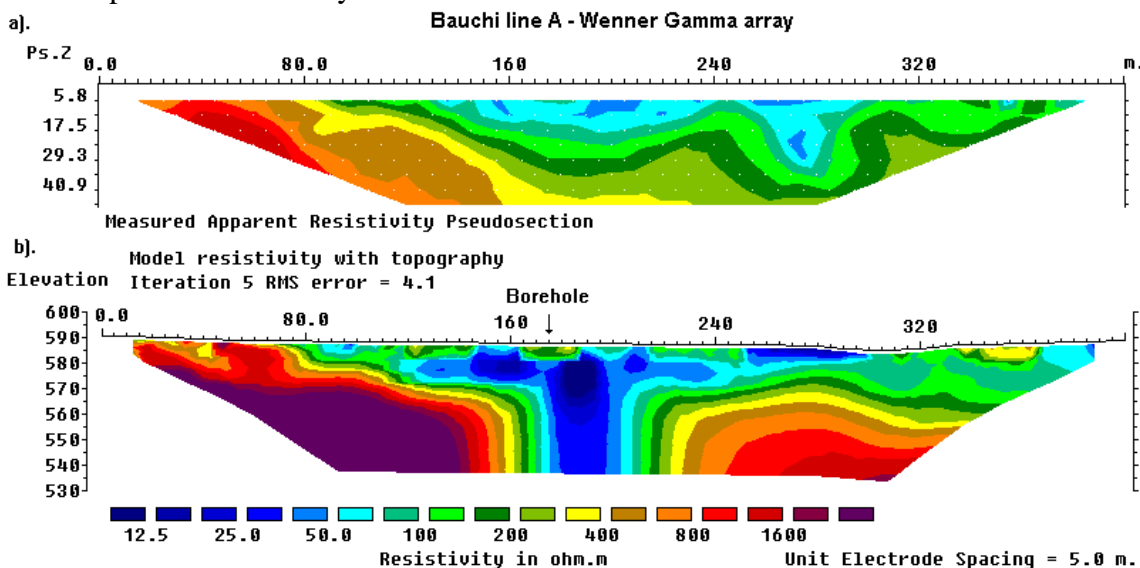


Figure 94. Groundwater survey, Nigeria. (a). Apparent resistivity pseudosection. (b) The inversion model with topography. Note the location of the borehole at the 175 meters mark.

As a final note, it is possible to invert data collected with the Wenner Alpha, Beta and Gamma arrays along the same line simultaneously with the RES2DINV program as a single data set. This can be done by using the "non-conventional array" option in the program where the positions of all the four electrodes in an array are explicitly specified. This might be an interesting method to combine the advantages of the different variations of the Wenner array.

7.8 Mobile underwater survey - Belgium

Contrary to popular belief, it is actually possible to carry out resistivity surveys underwater, even in marine environments. This example is one of the most unusual data sets that I have come across, and an interesting challenge for any resistivity imaging inversion software. It is not only the longest in physical length and number of electrode positions, but also uses an unusual highly asymmetrical non-conventional electrode arrangement collected by an underwater mobile surveying system. Mobile surveying systems have an advantage of faster surveying speed, but on land they suffer from the problem of poor ground contact (for the direct contact type) or low signal strength (for the electrostatic type). Please refer to section 2.3 for the details. An underwater environment provides an almost ideal situation for

a direct contact type of mobile system since there is no problem in obtaining good electrode contact!

Figure 95a shows the data from an eight kilometers survey line along a river. This survey was carried out by Sage Engineering of Belgium. The purpose of the survey was to map the near surface lithology of the riverbed where there were plans to lay a cable. The data set has a total of 7479 electrode positions and 6636 data points, whereas the inversion model used has 19936 cells. On a 3.2 Ghz Pentium 4 computer, it took slightly less than 2 hours to process this data set. On a newer PC, and using the appropriate software settings, it will probably takes less than 15 minutes (see section 4.8)!

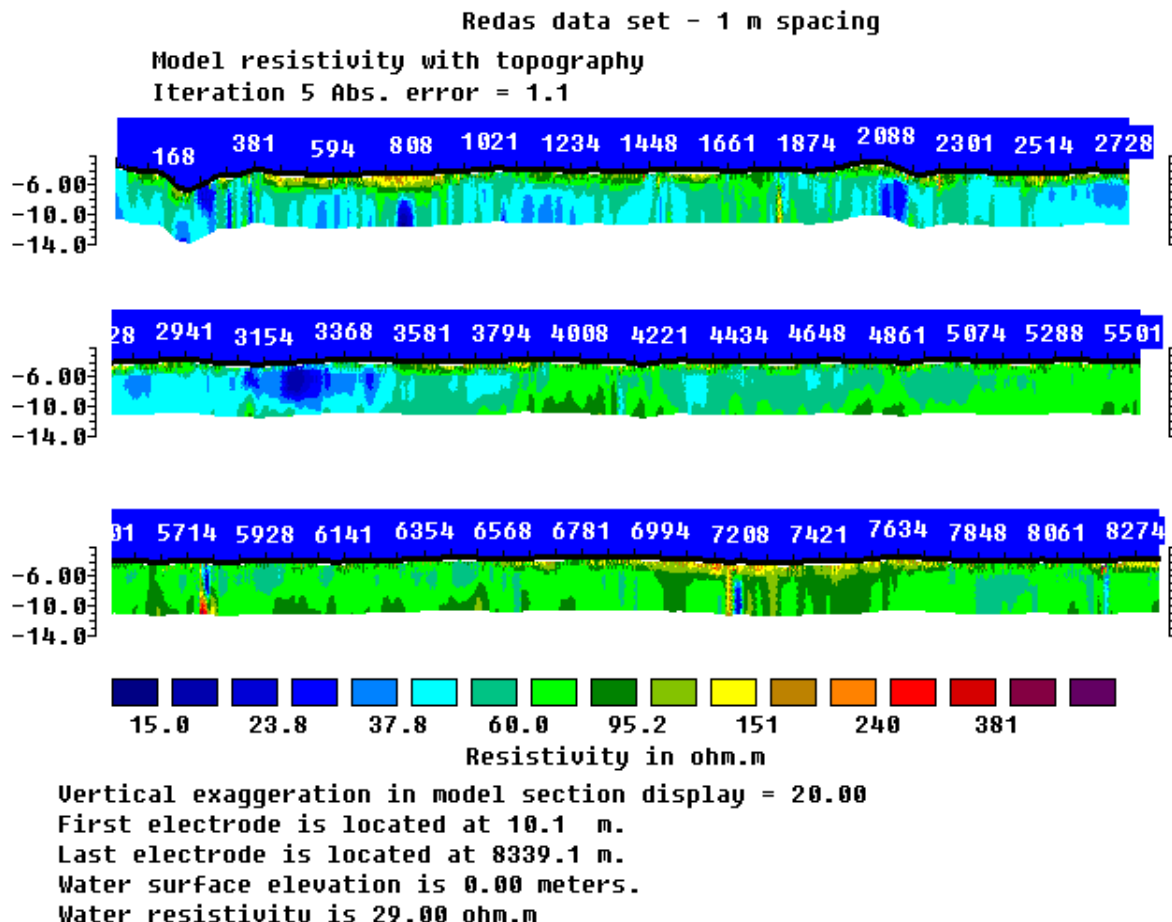


Figure 95. The inversion model after 4 iterations from an underwater riverbed survey by Sage Engineering, Belgium.

In the inversion model (Figure 95b), most of the riverbed materials have a resistivity of less than $120 \Omega\cdot\text{m}$. There are several areas where the near-surface materials have significantly higher resistivities of over $150 \Omega\cdot\text{m}$. Unfortunately, geological information in this area is rather limited. In the high resistivity areas, the divers faced problems in obtaining sediment samples. The lower resistivity materials are possibly more coherent sediments (possibly sand with silt/clay), whereas the higher resistivity areas might be coarser and less coherent materials.

7.9 Floating electrodes survey – U.S.A.

This survey was carried out along the Thames River in Connecticut, USA using a streamer floating on the water surface that was towed behind a boat. The steamer has 2 fixed current electrodes and 9 potential electrodes. Measurements were made with an 8-channel resistivity meter system. The water depth and conductivity were also measured during the survey. A dipole-dipole type of array configuration was used but some of the measurements used a non-symmetrical arrangement where the potential dipole length was different from the current dipole length. The apparent resistivity pseudosection from a survey line is shown in Figure 96a. The inversion model (Figure 96b) obtained when no special constraints were placed on the part of the model that falls within the water layer shows artefacts near the surface due to noise in the data. This model is fairly accurate when the material just below the river bottom has a high resistivity, but poor in areas with low resistivities. These problems do not occur in the model where the water layer resistivity was fixed during the inversion process (Figure 96c).

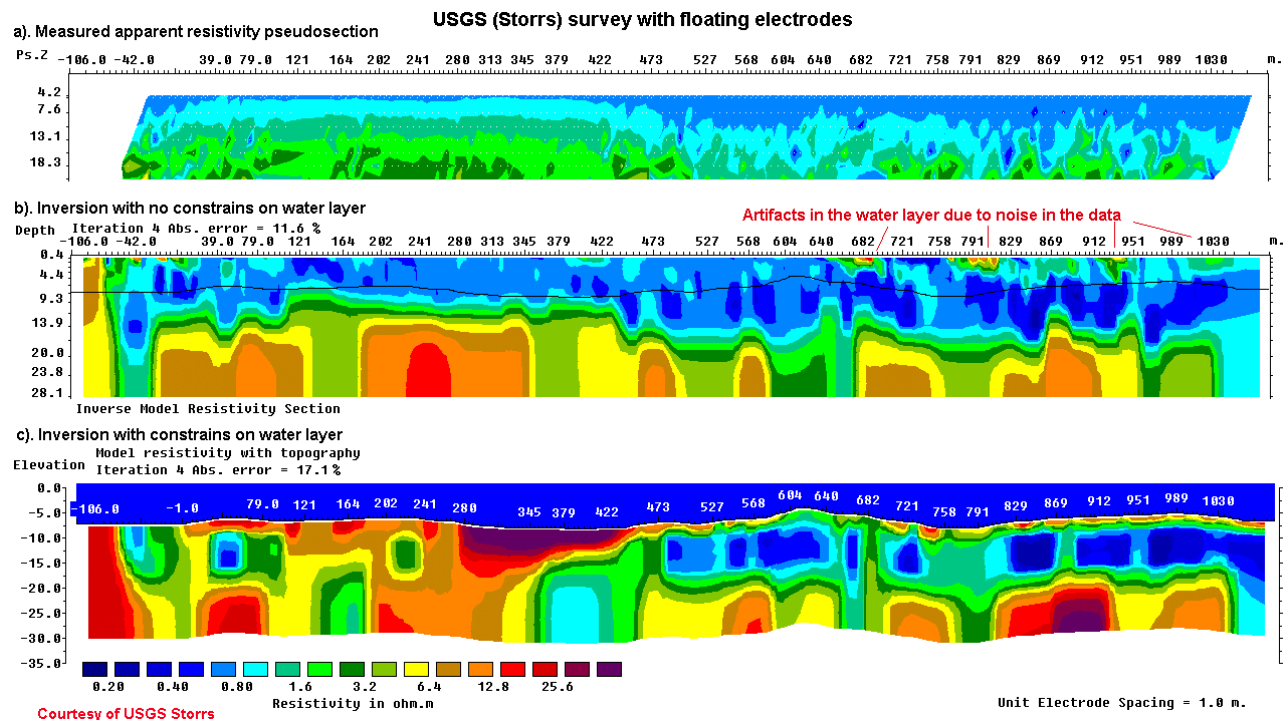


Figure 96. Thames River (CT, USA) survey with floating electrodes. (a) The measured apparent resistivity pseudosection. Inversion models obtained (b) without constraints on the water layer, and (c) with a fixed water layer.

7.10 Oil Sands, Canada

A new application for electrical and electromagnetic exploration methods is in the direct detection of hydrocarbons. It is well known that hydrocarbons have much higher resistivity values as compared to the surrounding sediments or sedimentary rocks, and thus ideal targets for electrical and EM based methods. One special form of hydrocarbon deposit that is ideal for the electrical imaging method is the oil sands in Canada (Kellett and Bauman, 1999). It is estimated that Canada has over 400 billion cubic meters (2.5 trillion barrels) of oil sands and heavy oil deposits. Commercial oil sands deposits are located at depths much shallower than conventional hydrocarbon reservoirs, so they can often be accurately mapped by conventional multi-electrode systems.

Figure 97a show the location of three major deposits in the Province of Alberta. The largest deposits are the Athabasca Oil Sands with over 200 Gm³ of reserves. The resistivity log across one of the oil sands bodies (Figure 97b) shows high resistivity values approaching 1000 ohm.m for the tar sands as compared to less than 30 ohm.m for the sediments, making the resistivity method a potentially good exploration approach. An example of a resistivity section obtained from a 2D survey (Figure 97c) shows prominent high resistivity zones associated with the oil sands.

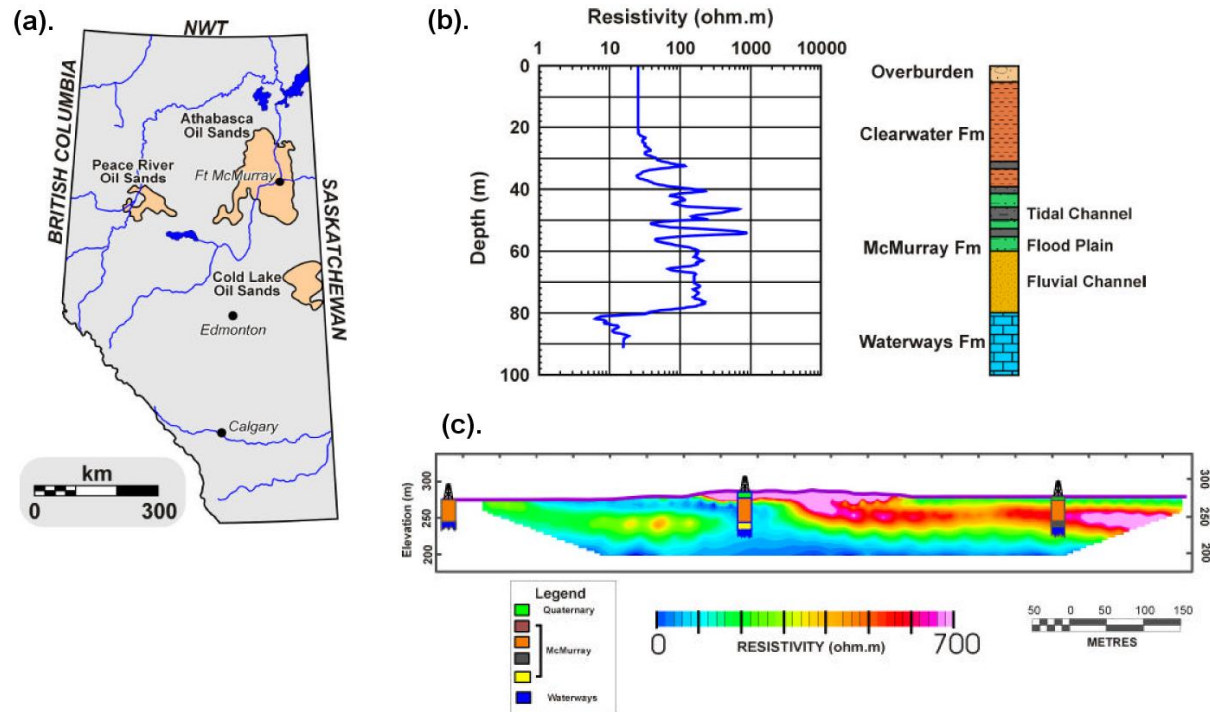


Figure 97. Survey to map oil sands, Alberta, Canada. (a) Location of major tar sands deposits in Alberta, Canada. (b) Example of resistivity log and geologic column of Athabasca oil sands. (c) 2-D resistivity model from imaging survey (Kellett and Bauman, 1999).

Besides these examples, 2-D imaging surveys have been carried for many other purposes such as the detection of leakage of pollutants from landfill sites, areas with undulating limestone bedrock, mapping of the overburden thickness over bedrock (Ritz *et al.*, 1999), leakage of water from dams, saline water intrusion in coastal aquifers, freshwater aquifers (Dahlin and Owen, 1998), monitoring of groundwater tracers (Nyquist *et al.*, 1999) and mapping of unconsolidated sediments (Christensen and Sorensen, 1994). The resistivity imaging method has also been used in underwater surveys in lakes and dams.

8 3-D electrical imaging surveys

8.1 Introduction to 3-D surveys

Since all geological structures are 3-D in nature, a fully 3-D resistivity survey using a 3-D interpretation model (Figure 6c) should in theory give the most accurate results. At the present time 3-D surveys is a subject of active research. However it has not reached the level where, like 2-D surveys, it is routinely used. The main reason is that the survey cost is comparatively higher for a 3-D survey of an area that is sufficiently large. There are two current developments that should make 3-D surveys a more cost-effective option in the near future. One is the development of multi-channel resistivity meters that enables more than one reading to be taken at a single time. This is important to reduce the survey time. The second development is faster microcomputers to enable the inversion of very large data sets (with more than 10,000 data points and survey grids with more than 1000 electrode positions) to be completed within a reasonable time.

8.2 Array types for 3-D surveys

The pole-pole, pole-dipole and dipole-dipole arrays are frequently used for 3-D surveys. This is because other arrays have poorer data coverage near the edges of the survey grid. The advantages and disadvantages of the pole-pole, pole-dipole and dipole-dipole arrays that were discussed in section 2.5 with regards to 2-D surveys are also valid for 3-D surveys.

8.2.1 The pole-pole array

Figure 98 shows one possible arrangement of the electrodes for a 3-D survey using a multi-electrode system with 25 nodes. For convenience the electrodes are usually arranged in a square grid with the same unit electrode spacing in the x and y directions. To map slightly elongated bodies, a rectangular grid with different numbers of electrodes and spacings in the x and y directions could be used. The pole-pole electrode configuration was commonly used for 3-D surveys, such as the E-SCAN method (Li and Oldenburg, 1992; Ellis and Oldenburg, 1994b). The maximum number of independent measurements, n_{max} , that can be made with n_e electrodes is given by

$$n_{max} = n_e(n_e - 1) / 2$$

In this case, each electrode is in turn used as a current electrode and the potential at all the other electrodes are measured. Note that because of reciprocity, it is only necessary to measure the potentials at the electrodes with a higher index number than the current electrode in Figure 99a. For a 5 by 5 electrodes grid, there are 300 possible measurements. For 7 by 7 and 10 by 10 electrodes grids, a survey to measure the complete data set would have 1176 and 4500 data points respectively. For commercial surveys, grids of less than 10 by 10 are probably not practical as the area covered would be too small.

It is can be very time-consuming (at least several hours) to make such a large number of measurements, particularly with a single-channel resistivity meters. To reduce the number of measurements required without seriously degrading the quality of the model obtained, an alternative measurement sequence is shown in Figure 99b. In this proposed "cross-diagonal survey" method, the potential measurements are only made at the electrodes along the x -direction, the y -direction and the 45 degrees diagonal lines passing through the current electrode. The number of data points with this arrangement for a 7 by 7 grid is reduced to 476 which is about one-third of that required by a complete data set survey (Loke and Barker, 1996b).

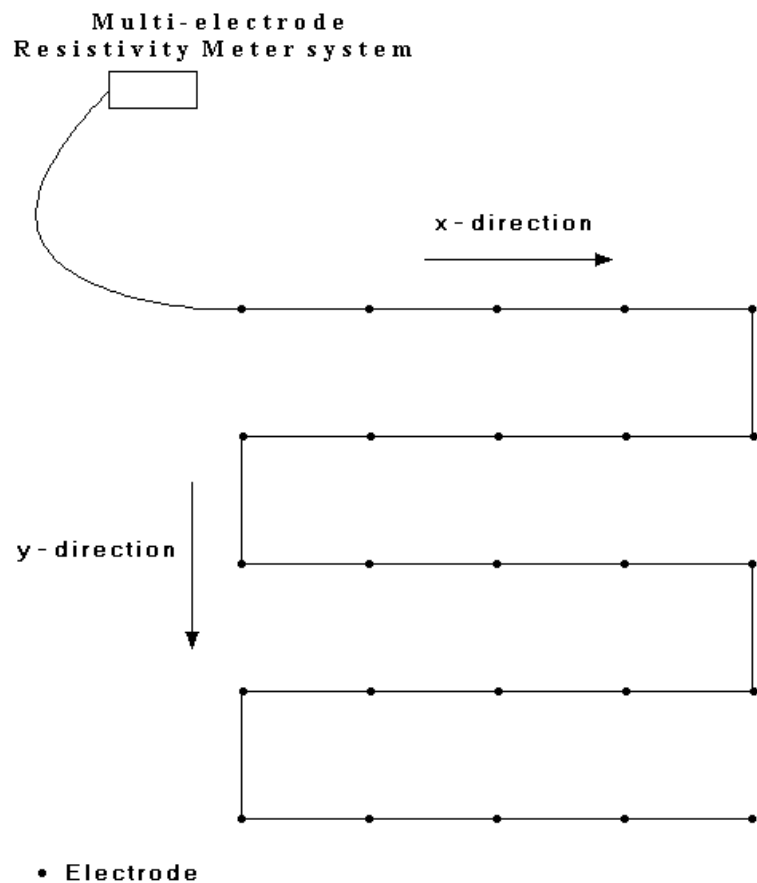


Figure 98. A simple arrangement of the electrodes for a 3-D survey.

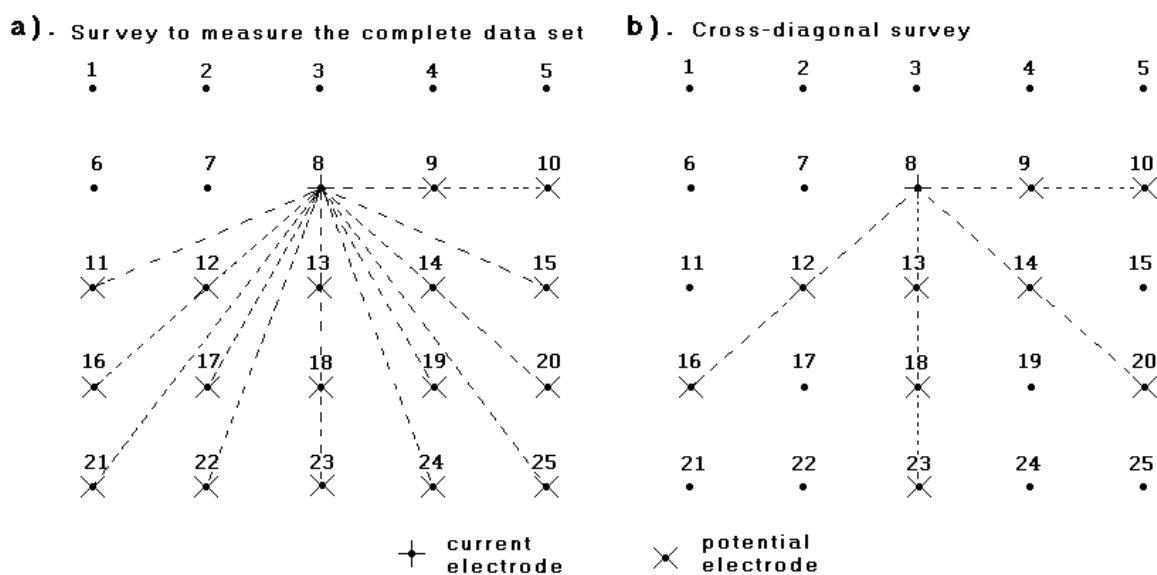


Figure 99. Two possible measurement sequences for a 3-D survey. The location of potential electrodes corresponding to a single current electrode in the arrangement used by (a) a survey to measure the complete data set and (b) a cross-diagonal survey.

In some cases, 3-D data sets are constructed from a number of parallel 2-D survey lines (section 8.3). Ideally there should be a set of survey lines with measurements in the x -direction, followed by another series of lines in the y -direction. The use of measurements in two perpendicular directions helps to reduce any directional bias in the data.

However, in some cases, only the data from a series of survey lines in one direction is available. This is particularly common if the surveys were originally conducted to provide 2-D images. Sometimes the spacing between the “in-line” electrodes is significantly smaller than the spacing between the lines. One important question is the maximum spacing between the lines that can be used for the data to be still considered “3-D”. A useful guide is the 3-D sensitivity plot. Figure 100 shows the sensitivity values on horizontal slices through the earth. The electrodes are arranged along the 0 and 1 meter marks along the x -axis. Near the surface, there is an approximately circular region with negative sensitivity values in the top two slices at depths of 0.07 and 0.25 meter. The zone with the largest sensitivity (using the 4 units sensitivity contour line as a guide) extends in the y -direction to slightly over half the electrode spacing. This means to get a complete 3-D coverage, if the measurements are only made in the x -direction, the spacing between the lines should not be much more than the smallest electrode spacing used.

The papers by Bentley and Gharibi (2004) and Gharibi and Bentley (2005) give a fairly comprehensive discussion on constructing 3-D data sets from 2-D survey lines.

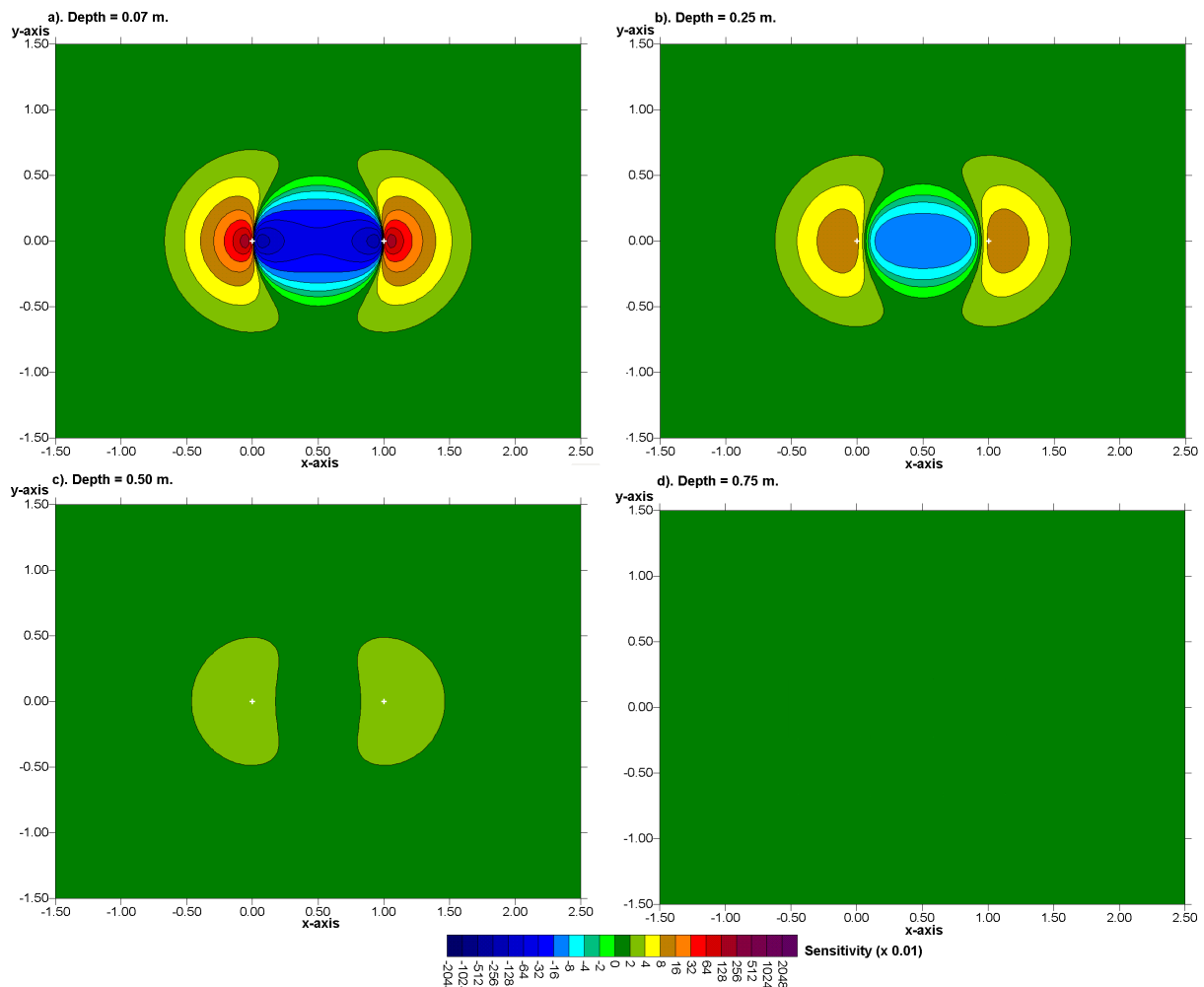


Figure 100. 3-D sensitivity plots for the pole-pole array. The plots are in the form of horizontal slices through the earth at different depths.

The pole-pole array has two main disadvantages. Firstly it has a much poorer resolution compared to other arrays. Subsurface structures tend to be smeared out in the final inversion model. The second disadvantage, particularly for large electrode spacings, is that the second current electrode and potential electrode must be placed at a sufficiently large distance from the survey grid. Both disadvantages have been discussed in detail in Section 2.5.7. Park and Van (1991) who used this array for a field experiment found that about 15% of the measurements did not satisfy reciprocity because the contributions from the remote electrodes were significant. In general, this probably affects the readings with the larger spacings.

8.2.2 The pole-dipole array

This array is an attractive alternative to the pole-pole array for surveys with medium and large survey grids (12 by 12 and above). It has a better resolving power than the pole-pole array (Sasaki, 1992), and is less susceptible to telluric noise since both potential electrodes are kept within the survey grid. Compared to the dipole-dipole array, it has a significantly stronger signal strength. Although it has one “remote” electrode (the C2 electrode), the effect of this electrode on the measurements is much smaller compared to the pole-pole array (section 2.5.8). As the pole-dipole array is an asymmetrical array, measurements should be made with the “forward” and “reverse” arrangements of the electrodes (Figure 29). To overcome the problem of low signal strength for large values of the “ n ” factor (exceeding 8), the “ a ” spacing between the P1-P2 dipole pair should be increased to get a deeper depth of investigation with a smaller “ n ” factor. The use of redundant measurements with overlapping data levels to increase the data density can in some cases help to improve the resolution of the resulting inversion model (section 2.5.9).

Figure 101 and Figure 102 show the sensitivity patterns for this array with the dipole separation factor “ n ” equal to 1 and 4 respectively. There is prominent area with negative sensitivity values between the C1 and P1 electrodes (located at 0.0 and 0.5 meter along the x -axis). The plots are arranged such that the array length (in this case the distance between the C1 and P2 electrodes) is set at 1.0 meter for both “ n ” factors. For a larger “ n ” factor, the area of negative sensitivities between the C1 and P1 electrodes becomes larger and extends to a greater depth. The array is more sensitive to structures off the array axis (i.e. in the y -direction) when “ n ” is equals to 1. The area with the higher sensitivity values extends to about 0.8 times the array length (Figure 101), or 1.6 times the unit electrode spacing. When the “ n ” factor is larger (Figure 102), the array is more sensitive to off-axis structures near the P1-P2 dipole. Note also the negative sensitivity values to the right of the P2 electrode.

If the 3-D survey is carried out with a series of parallel lines, and the cross-line measurements are not made, the distance between the lines should preferably be within two to three times the inline unit electrode spacing. This is to ensure that the subsurface material between the lines is adequately mapped by the in-line measurements.

8.2.3 The dipole-dipole, Wenner and Schlumberger arrays

The dipole-dipole array can be recommended only for grids that are larger than 12 by 12 due to the poorer horizontal data coverage at the sides. The main problem that is likely to be faced with this array is the comparatively low signal strength. Similar to 2-D surveys, this problem can be overcome by increasing the “ a ” spacing between the P1-P2 dipole to get a deeper depth of investigation as the distance between the C1-C2 and P1-P2 dipoles is increased. Also, the use of overlapping data levels is recommended (section 2.5.9).

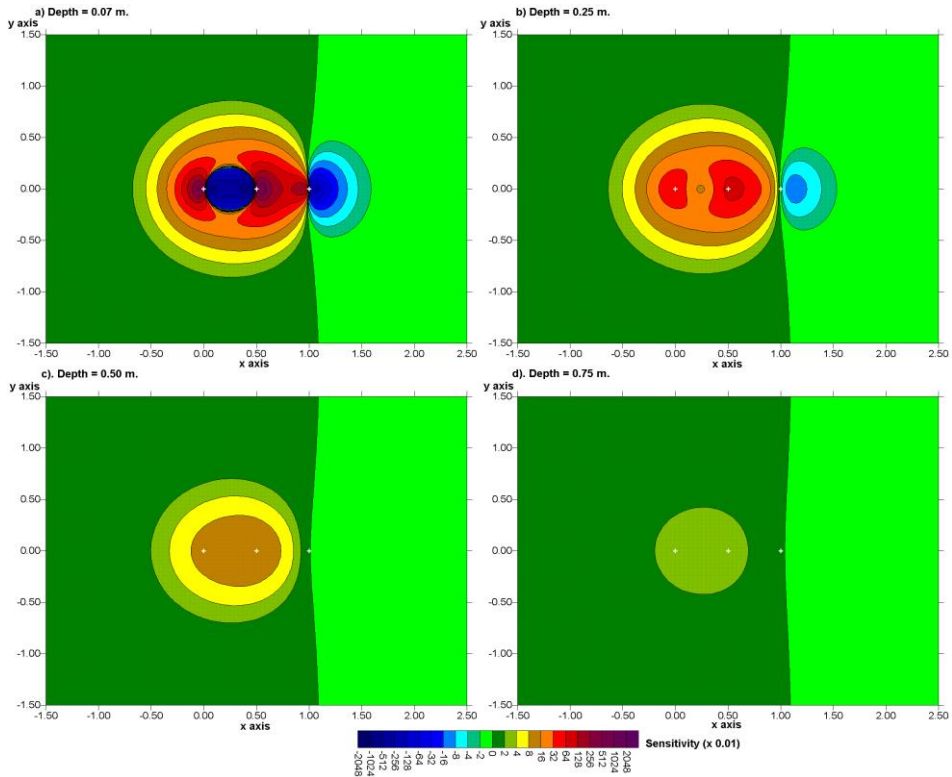


Figure 101. 3-D sensitivity plots for the pole-dipole array with $n=1$ in the form of horizontal slices through the earth at different depths. The C1 electrode is the leftmost white cross.

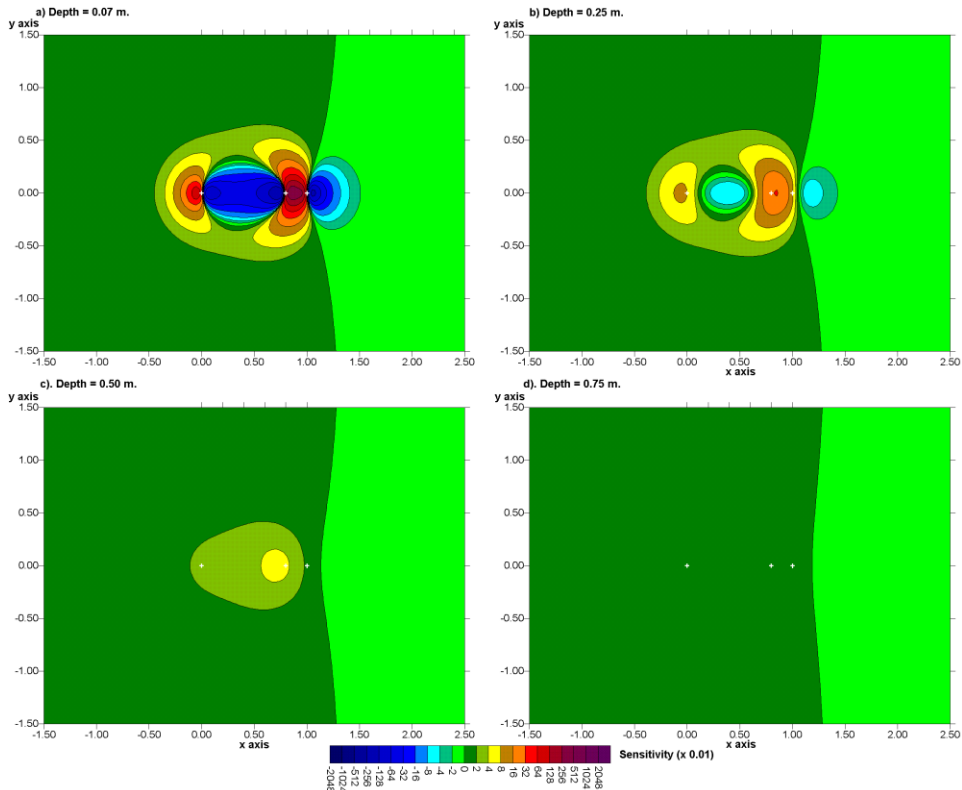


Figure 102. 3-D sensitivity plots for the pole-dipole array with $n=4$ in the form of horizontal slices through the earth at different depths.

Figure 103 and Figure 104 shows the sensitivity patterns for the dipole-dipole array when the “ n ” factor is equal to 1 and 4 respectively. The sensitivity values have small but negative values outside the immediate vicinity of the array. Another interesting feature is that the sensitivity contours tend to be elongated in the y -direction, particularly for the larger “ n ” value. The 4 unit sensitivity contour extends to about 0.6 times the array length in the y -direction, or about 1.8 times the unit electrode spacing. This means that the array is more sensitive to structures off the array axis compared to the pole-pole and pole-dipole arrays. This feature is troublesome in 2-D surveys, but might be advantageous in 3-D surveys.

The off-axis elongation of the sensitivity contours agrees with the observation by Dahlin and Loke (1997) that the dipole-dipole array is more sensitive to 3-D effects compared to other common arrays. This factor is important when the dipole-dipole array is used in 2-D imaging surveys where it is assumed that the subsurface geology is 2-D. In many cases, 3-D data sets for the dipole-dipole arrays are constructed from a number of parallel 2-D survey lines, particularly from previous surveys. Due to the elongated sensitivity pattern, the dipole-dipole array can probably tolerate a larger spacing between the survey lines (to about three times the inline unit electrode spacing) and still contain significant 3-D information.

In closing this section on four electrodes arrays, the sensitivity patterns for the Wenner alpha (Figure 105), Schlumberger (Figure 106) and Wenner gamma arrays (Figure 107, the Wenner beta is the dipole-dipole with a “ n ” value of 1 as shown in Figure 101) are shown. The sensitivity contours for the Wenner alpha array, outside of the immediate vicinity of the electrodes, are elongated in the direction of the line of electrodes. This means that the Wenner alpha array is less sensitive to off-line structures than the dipole-dipole array, i.e. it is less sensitive to 3-D. This agrees with empirical observations by Dahlin and Loke (1997). The sensitivity pattern for the Wenner-Schlumberger array (Figure 106) is similar to that for the Wenner alpha array except for a slight bulge near the center of the array. The sensitivity patterns for the Wenner gamma array (Figure 107) show characteristic bulges near the C1 and C2 electrodes that were observed earlier in the 2-D sensitivity sections (Figure 23). Thus it is expected to be more sensitive to 3-D structures near the C1 and C2 electrodes.

8.2.4 Summary of array types

For relatively small grids of less than 12 by 12 electrodes, the pole-pole array has a substantially larger number of possible independent measurements compared to other arrays. The loss of data points near the sides of the grid is kept to a minimum, and it provides better horizontal data coverage compared to other arrays. This is an attractive array for small survey grids with relatively small spacings (less than 5 meters) between the electrodes. However, it has the disadvantage of requiring two “remote” electrodes that must be placed at a sufficiently large distance from the survey grid. The pole-dipole array is an attractive option for medium size grids. It has a higher resolution than the pole-pole array and it requires only one remote electrode and is much less sensitive to telluric noise. For surveys with large grids, particularly when there is no convenient location for a remote electrode, the dipole-dipole array can be used. The electrodes for 3-D surveys are frequently arranged in a rectangular grid. However, the RES3DINV resistivity and I.P. inversion program can also handle survey layouts with an arbitrary distribution of the electrodes.

In large 3-D I.P. surveys, it has become popular to use the offset version of the pole-dipole and dipole-dipole arrays to cover a large area rapidly. The C1 current electrode (or C1-C2 current dipole) is placed on a separate line parallel to the line with the potential receivers. An example of this type of survey is described in section 8.12.4.

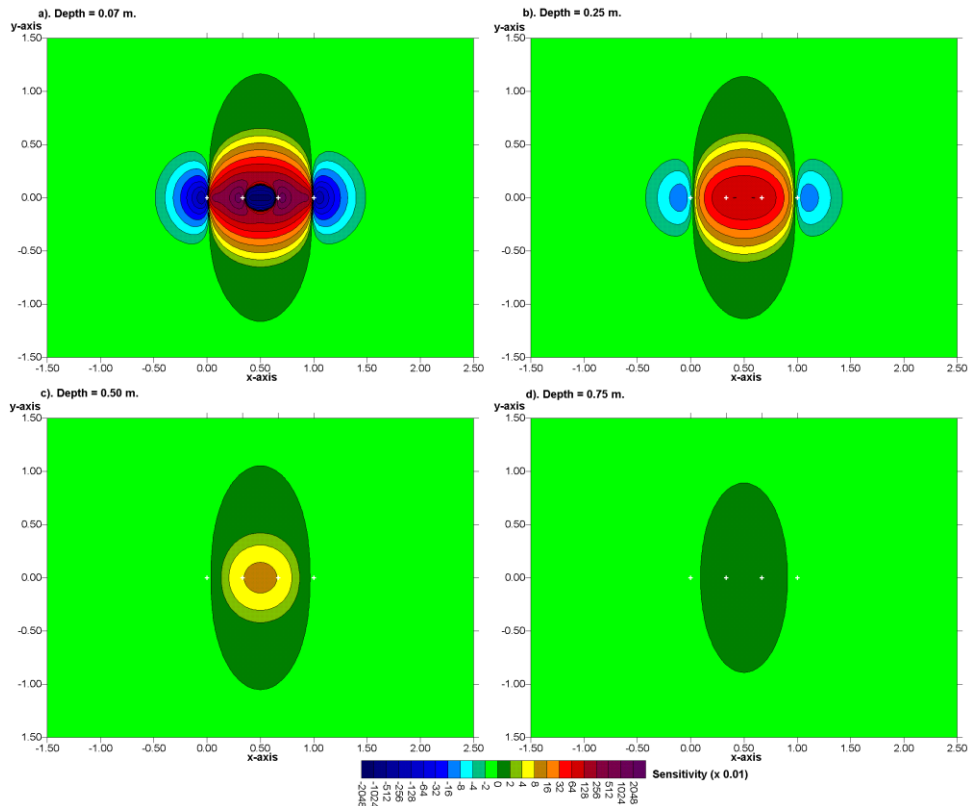


Figure 103. 3-D sensitivity plots for the dipole-dipole array with $n=1$ in the form of horizontal slices through the earth at different depths. The C2 electrode is the leftmost white cross.

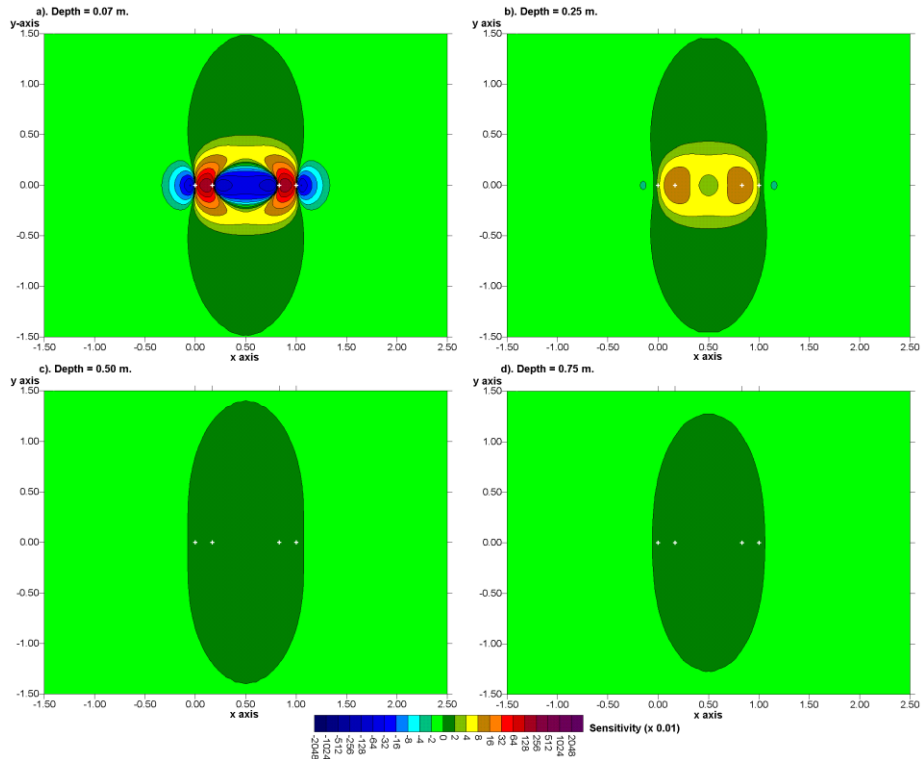


Figure 104. 3-D sensitivity plots for the dipole-dipole array with $n=4$ in the form of horizontal slices through the earth at different depths. The C2 electrode is the leftmost white cross.

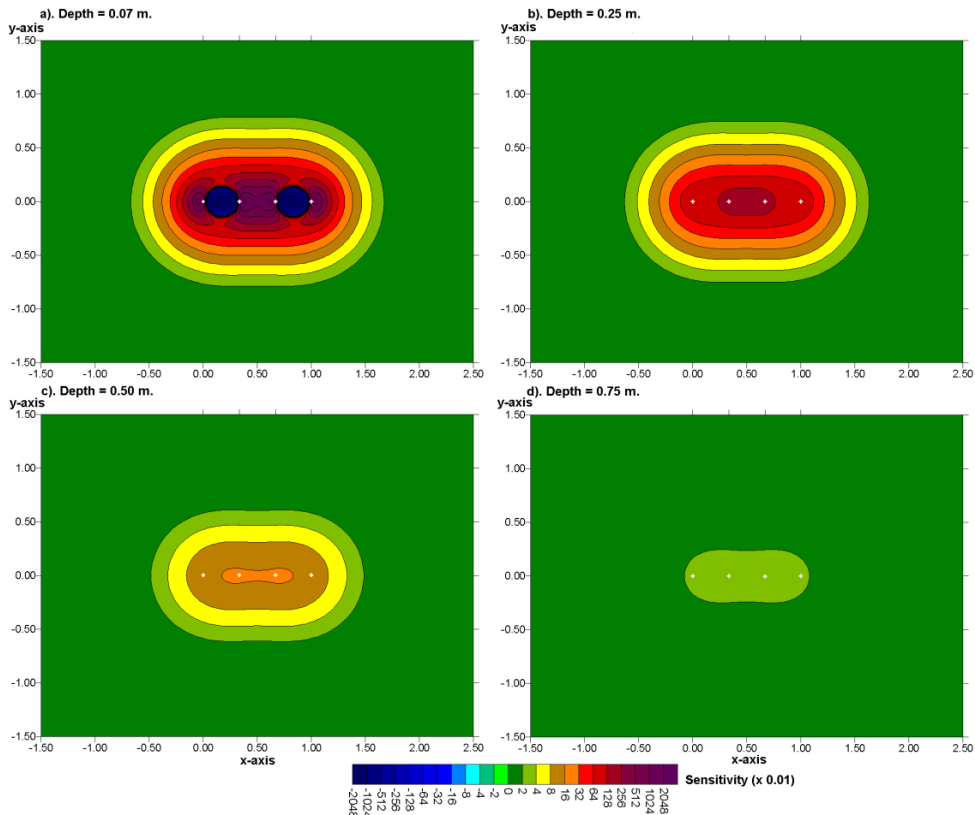


Figure 105. The 3-D sensitivity plots for the Wenner alpha array at different depths.

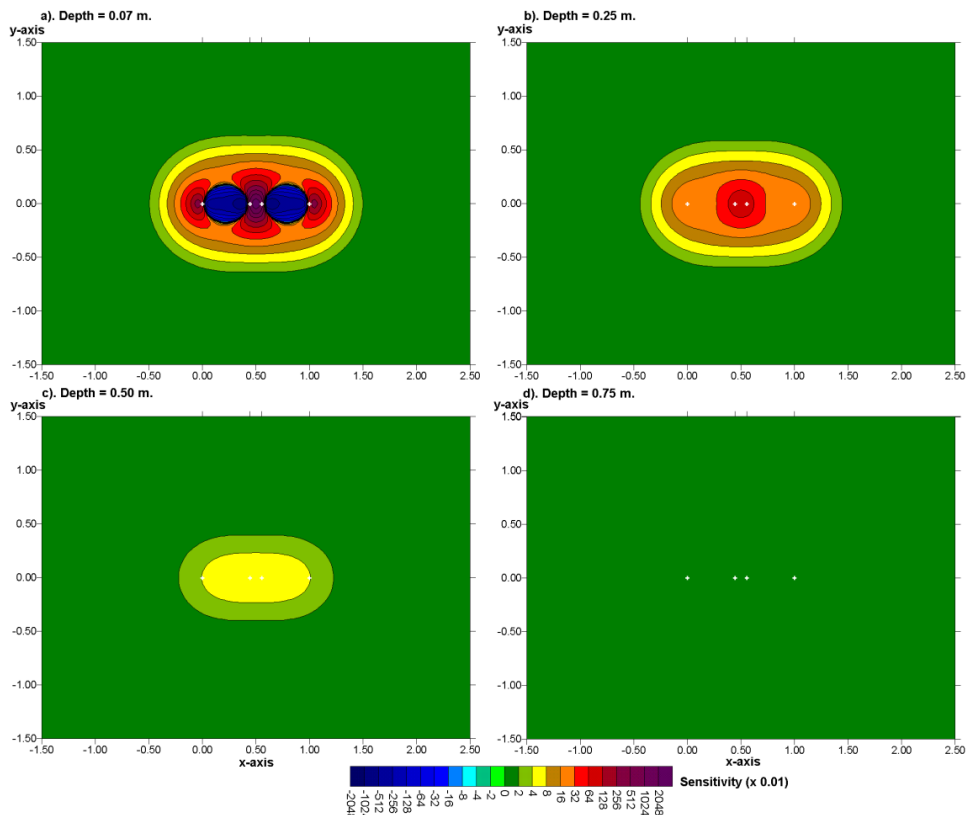


Figure 106. The 3-D sensitivity plots for the Wenner-Schlumberger array with the $n=4$ at different depths.

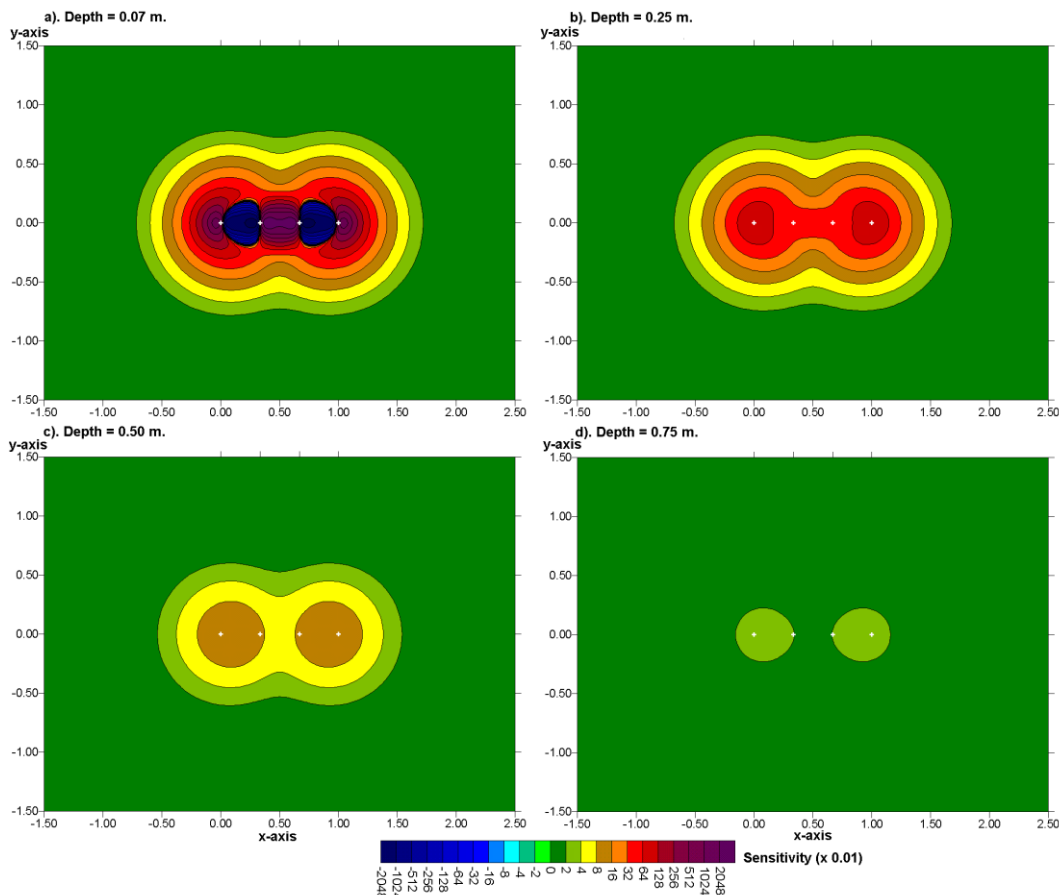


Figure 107. The 3-D sensitivity plots for the Wenner gamma array at different depths.

8.3 3-D roll-along techniques

Most commercial 3-D surveys will probably involve grids of at least 16 by 16 in order to cover a reasonably large area. A 16 by 16 grid will require 256 electrodes which is more than that available on many multi-electrode resistivity meter systems. One method to survey such large grids with a limited number of electrodes is to extend the roll-along technique used in 2-D surveys to 3-D surveys (Dahlin and Bernstone, 1997). Figure 108 shows an example of a survey using a multi-electrode resistivity-meter system with 50 electrodes to survey a 10 by 10 grid. Initially the electrodes are arranged in a 10 by 5 grid with the longer lines orientated in the x -direction (Figure 108a). Measurements are made primary in the x -direction, with some possible measurements in the diagonal directions. Next the entire grid is moved in the y -direction so that the 10 by 5 grid now covers the second half of the 10 by 10 grid area. The 10 by 5 grid of electrodes is next orientated in the y -direction (Figure 108b).

The example data file PIPE3D.DAT was obtained from a survey using such a roll-along technique. It was carried out with a resistivity-meter system with only 25 nodes with the electrodes arranged in an 8 by 3 grid. The long axis of this grid was orientated perpendicularly to two known subsurface pipes. The measurements were made using three such 8 by 3 sub-grids so that the entire survey covers an 8 by 9 grid. For each 8 by 3 sub-grid, all the possible measurements (including a limited number in the y -direction) for the pole-pole array were made. In this survey, the second set of measurements in the y -direction (as in Figure 108b) was not carried out to reduce the survey time and also because the pipes have an almost two-dimensional structure.

For practical reasons, the number of field measurements in some surveys might be even less than the cross-diagonal technique. Another common approach is to just make the

measurements in the x - and y - directions only, without the diagonal measurements. This is particularly common if the survey is made with a system with a limited number of independent electrodes, but a relatively large grid is needed. A roll-along procedure using only 3 parallel cables is described in Dahlin and Bernstone (1997).

In some cases, measurements are made only in one direction. The 3-D data set consists of a number of parallel 2-D lines. The data from each 2-D survey line is initially inverted independently to give a series of 2-D cross-sections. The measured apparent resistivity values from all the lines can also be combined into a 3-D data set and inverted with RES3DINV to give a 3-D picture. While the quality of the 3-D model is expected to be poorer than that produced with a complete 3-D survey, such a “poor man’s” 3-D data set could reveal major resistivity variations across the survey lines (see also section 8.5). Until multi-channel resistivity instruments are widely used, this might be the most cost-effective solution to extract some 3-D information from 2-D surveys. This arrangement might be particularly useful for surveys with the dipole-dipole array that can tolerate larger spacings between the survey lines.

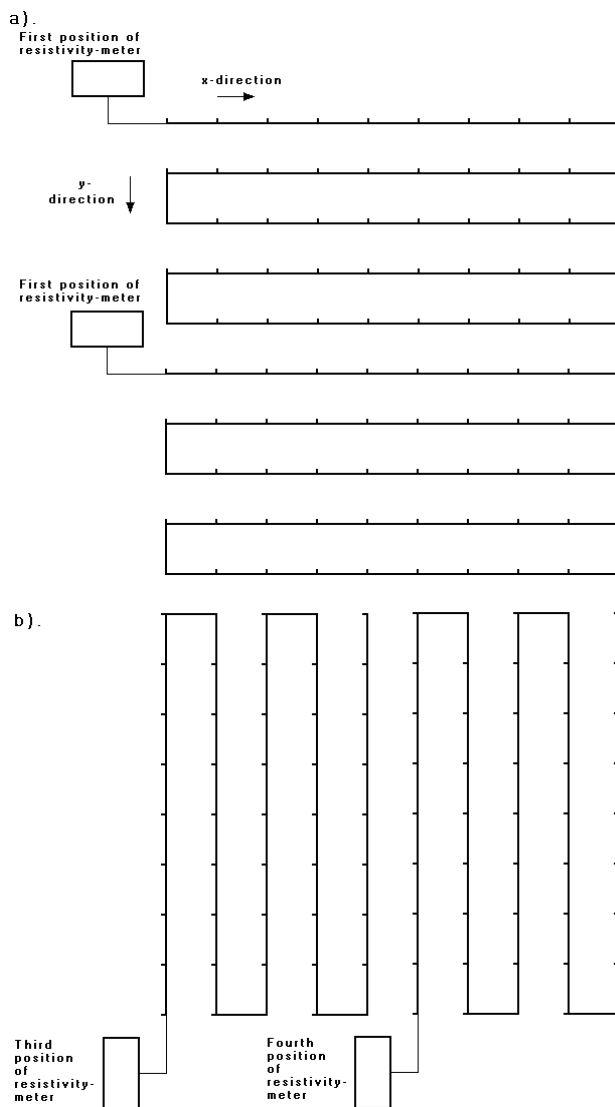


Figure 108. Using the roll-along method to survey a 10 by 10 grid with a multi-electrode system with 50 nodes. (a) Surveys using a 10 by 5 grid with the lines orientated in the x -direction. (b) Surveys with the lines orientated in the y -direction.

8.4 A 3-D forward modeling program

In the interpretation of data from 2-D resistivity imaging surveys, it is assumed that the subsurface geology does not change significantly in the direction that is perpendicular to the survey line. In areas with very complex geology, there could be significant variations in the subsurface resistivity in this direction (i.e. the geology is 3-D), which could cause distortions in the lower sections of the 2-D model obtained (please refer to section 4.7).

The 3-D resistivity forward modeling program, RES3DMOD.EXE, enables you to calculate the apparent resistivity values for a survey with a rectangular grid of electrodes over a 3-D structure. This is a Windows based program that can be used from within Windows XP/Vista/7/8/10. To take a look at the operation of the program, use the “File” option followed by “Read model data” to read in the file BLOCK11.MOD, which has a 11 by 11 survey grid. After that, click the “Edit/Display” option.

To modify the 3-D model, click the “Edit resistivity model” option. In this option, you can change the resistivity of the 3-D cells in the mesh used by the finite-difference method (Dey and Morrison, 1979b) to calculate the apparent resistivity values. To quit from the “Edit” mode, press the Q or the Esc key. To calculate the apparent resistivity values, click the “Calculate” option. To take a look at the apparent resistivity pseudosections, click the “Display apparent resistivity” option. You can choose to display the apparent resistivity values in the form of horizontal pseudosections, or as vertical pseudosections as used in 2-D surveys. Displaying the vertical pseudosections will give you an idea of the effect of a 3-D structure on the measurements in a 2-D survey. In a study made by Dahlin and Loke (1997), the dipole-dipole array was found to be the most sensitive to 3-D effects while the Wenner array was the least sensitive.

The RES3DMOD program also has an option to save the apparent resistivity values into a format that can be accepted by the RES3DINV inversion program. As an exercise, save the apparent resistivity values as a RES3DINV data file for one of the models, and later carry out an inversion of this synthetic data set.

Table 12. 3-D forward modeling examples

Data set and purpose	Things to try
PRISM2.MOD – This is a 3-D model used to generate the pseudosections shown in Figure 67.	(1). Read in the file, and then run the “Calculate” step to calculate the potential values. This is a relatively large model file, so you might want to collect some coffee while the computer is running. (2). Next choose the “Display apparent resistivity” option under the “Edit/Display” menu. Try first with pole-pole array, and take a look at the pseudosections. (3). Next try with other arrays.
BLOCK15.MOD – A 15 by 15 grid model with several rectangular prisms.	(1). Read in the file, and then run the “Calculate” step to calculate the potential values. (2). Next choose the “Display apparent resistivity” option under the “Edit/Display” menu. Take a look at the pseudosections for a few arrays. (3). Try using the “Edit model” option to change the model, and then recalculate the potential values. Check out the effect of your changes on the apparent resistivity pseudosections.

Figure 109a show an example of a 3-D model with a 15 by 15 survey grid (i.e. 255 electrodes). The model, which consists of four rectangular prisms embedded in a medium with a resistivity of 50 $\Omega\cdot\text{m}$, is shown in the form of horizontal slices through the earth. The apparent resistivity values for the pole-pole array (with the electrodes aligned in the x -direction) are shown in the form of horizontal pseudosections in Figure 109b. Note the low resistivity block with a resistivity of 10 $\Omega\cdot\text{m}$ near the centre of the grid that extends from a depth of 1.0 to 3.2 meters. For measurements with the shorter electrode spacings of less than 4 meters this block causes a low resistivity anomaly. However, for electrode spacings of greater than 6 meters, this low resistivity prism causes a high resistivity anomaly! This is an example of “anomaly inversion” which is caused by the near-surface zone of negative sensitivity values between the C1 and P1 electrodes (Figure 100).

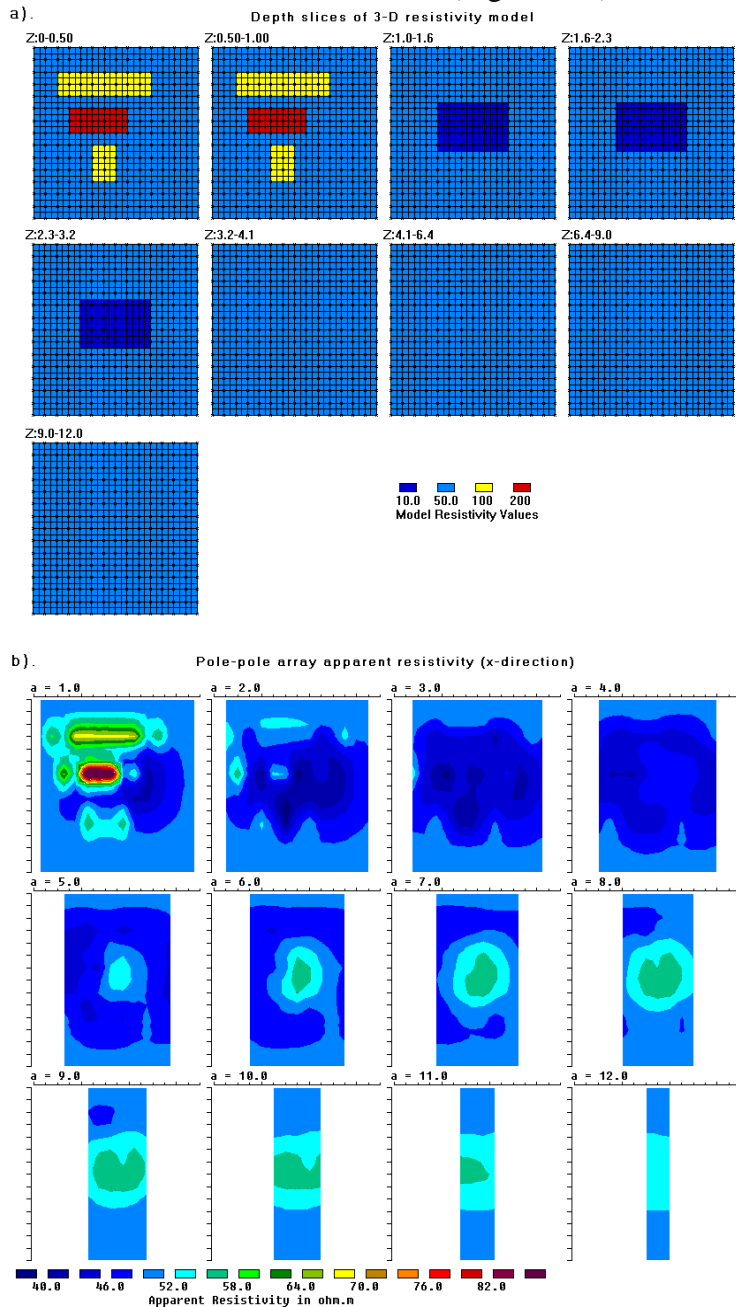


Figure 109. A 3-D model with 4 rectangular prisms in a 15 by 15 survey grid. (a) The finite-difference grid. (b) Horizontal apparent resistivity pseudosections for the pole-pole array with the electrodes aligned in the x -direction.

8.5 3-D inversion algorithms and 3-D data sets

Two interesting questions that sometimes arise, particularly in non-academic circles, is the definition of a 3-D inversion algorithm and what constitutes a 3-D data set. The first question can be easily answered, but the second is less clear.

A defining feature of a 3-D algorithm inversion algorithm is that it allows the model resistivity values to vary in all three directions, i.e. in the x -, y - and z -directions. This is in contrast to 2-D inversion where the subsurface resistivity is assumed to vary only in the x - and z -directions but constant in the y -direction; and in 1-D inversion where the resistivity is only allowed to change in the z -direction. The inversion model used by the RES3DINV program consists of independent rectangular cells (Figure 110) where the model values are allowed to vary in all three directions simultaneously, so it is uses a true 3-D inversion algorithm. Note that a model constructed from a series of 2-D inversions along parallel lines is not a true 3-D inversion model.

Another defining characteristic of a 3-D inversion algorithm is the use of a 3-D forward modeling subroutine, such as the 3-D finite-difference and finite-element methods (Dey and Morrison, 1979b; Silvester and Ferrari, 1990), to calculate the model apparent resistivity and Jacobian matrix values.

A more difficult question is what constitutes a “3-D” data set. At present there is no generally accepted definition of a 3-D data set. While the inversion algorithm used to invert the data set is 3-D, whether the data set contains significant 3-D information is another matter. It was stated in section 2.2 that to get a good 2-D model for the subsurface the data coverage must be 2-D as well. For a 2-D survey, measurements are made with different electrode spacings and at different horizontal locations to obtain such a 2-D coverage. However, the degree of data coverage needed before a data set can be considered “3-D” is less clear. Using the pole-pole survey as an example, the following classification system is proposed for 3-D data sets. They are listed in decreasing order of 3-D information content.

Category 1 - An ideal 3-D survey with the electrodes arranged in a rectangular grid, and with measurements in all possible directions (such as in Figure 99a), i.e. along the grid lines as well as at different angles to the grid lines.

Category 2 – The electrodes are arranged in a rectangular grid. All the measurements along the grid lines (i.e. in the x - and y -directions) but only a limited number of measurements at an angle to the grid lines(such as along the 45 degree diagonals for square grids as shown in Figure 8.2b) are made. The ROOTS7.DAT data file is such an example of a survey with limited measurements in the angular directions. In this case, the survey was carried out 49 electrodes in a 7 by 7 grid and 468 measurements were made. A “complete” 3-D data set would have 1176 measurements.

Category 3 – Measurements are only made in the two directions along the grid lines, i.e. in the x - and y -directions, and no measurements at an angle to the grid lines are made. This measurement sequence is frequently used when there are insufficient nodes in the multi-electrode system to cover the entire survey area at a single time. One possible measurement sequence is shown in Figure 108. The data for the sludge deposit field example (Dahlin and Bernstone 1997) in section 8.7.2 falls under this category.

Category 4 – Measurements in only one direction (for example the x -direction) along a series of parallel 2-D survey lines. This situation is common for data from old surveys, particularly I.P. surveys for mineral deposits. For this type of data set, a series of 2-D inversions is usually first carried out. The 3-D inversion is then used on a combined data set with the data from all the survey lines in an attempt to gleam new information out of old data, and to see whether 3-D effects are significant (i.e. whether the results from the 2-D inversions are valid). The success of the 3-D inversion partly depends on the spacing between the lines and the type of array used (section 8.2). As a general rule, the spacing between the lines should

not be more than twice the unit electrode spacing along the lines.

While ideally the data should be of Category 1 or at least Category 2 so that some angular data is available, the RES3DINV program will also accept data that falls under Categories 3 and 4. The accuracy of the 3-D models obtained from the Categories 3 and 4 data types will be lower than the Categories 1 and 2 data types, and will greatly depend on the spacing between the lines and the type of array used. However, even for the Category 4 data type, the results from the 3-D inversion should provide a useful indicator on whether 3-D effects are significant. This can provide a check on the validity of the results obtained from independent 2-D inversions of the different survey lines.

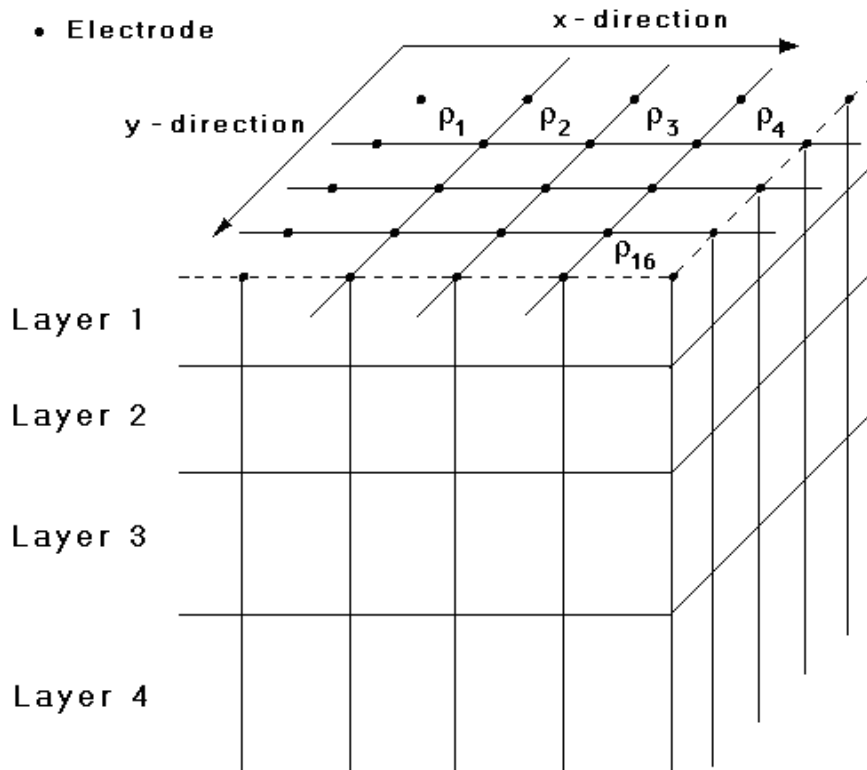


Figure 110. The model used in 3-D inversion.

8.6 A 3-D inversion program

3-D inversion of field data set can be carried out in a similar way using the smoothness-constrained least-squares method used for the 2-D inversion. The model used to interpret the 3-D data set is shown in Figure 110. The subsurface is divided into several layers and each layer is further subdivided into a number of rectangular cells. A 3-D resistivity inversion program, RES3DINV, is used to interpret the data from 3-D surveys. This program attempts to determine the resistivity of the cells in the inversion model that will most closely reproduce the measured apparent resistivity values from the field survey. Within the RES3DINV program, the thickness of the layers can be modified by the user.

Please refer to the instruction manual (RES3DINV.PDF) for the RES3DINV program for the data format. The set of files that comes with the RES3DINV program package has a number of field and synthetic data files. You can carry out an inversion of some of these files to get a feel of how the program works.

Table 13. 3-D inversion examples

Data set and purpose	Things to try
PIPE3D.DAT – A field survey data file where a roll-along technique was used. The total grid size is 9 by 8.	(1). Read in the file, and then run the “Carry out inversion” step. (2). After that, take a look at the results using the “Display” window.
ROOTS7.DAT – A “cross-diagonal survey” data set using a 7 by 7 survey.	(1). Read in the file, and then invert the data set. (2). Try using the “Robust inversion” option, and see whether there is a significant change in the results.
ROOT7_REMOTE.DAT – The same data set with the location of the C2 and P2 electrodes included.	Try inverting this data file and see whether the remote electrodes have a significant effect of the results.
BLOCKS11T.DAT – A synthetic data set with topography. It has a 11 by 11 grid.	(1). Read in the file, and then invert the data set. (2). Invert again using the “Robust inversion” option.

8.7 Banding effects in 3-D inversion models

Many 3-D field data sets are constructed by combining a series of parallel 2-D survey lines. Ideally the distance between the lines should be about the same as the distance between adjacent electrodes in each line. However, in most cases, the distance between the lines can be two or more times larger than the inter-electrode spacing along the lines. This can lead to a ‘banding’ or ‘herring-bone’ effect with the structures aligned along the two axes of the survey grid, particularly if the l_1 -norm or blocky inversion method is used. Figure 111 shows several alternative models for a survey over the Vetlanda landfill site in Sweden that consists of 11 parallel 2-D lines with 63 electrodes positions along each line (Rosqvist *et al.*, 2009). The pole-dipole array was used. The spacing between the lines is twice the unit electrode spacing along the lines. Only the first 6 layers (that are most affected by the banding effect) of the inversion models are shown. The model using the standard inversion settings (Figure 111a) shows severe banding effects, particularly in the low resistivity zone in the top two layers. This is reduced, particularly in the topmost layer, by using a higher damping factor for the topmost layer (Figure 111b).

The normal horizontal roughness filter used has components in the x and y directions only (Figure 112b). Thus it has a tendency to produce structures aligned along the x and y directions. Since the model cells have sides that are aligned in the same direction as the survey grid lines, the structures in the inversion models tend to have edges that are aligned in the same directions as the survey lines. To reduce this effect, the roughness filter used is modified so that it has components in the diagonal directions (Farquharson, 2008) as well in the x - y plane (Figure 112d). Figure 111c shows the inversion model produced when this modification is made to the horizontal roughness filter, while the vertical roughness filter is still only applied between the model cell and the cells immediately above and below it. The prominent banding effect in the low resistivity region in the top two layers of the model (Figure 111c) is greatly reduced using this horizontal diagonal filter.

Applying the diagonal filter components in the horizontal direction but not in the vertical direction can lead to a bias (in the horizontal direction) in the shape of the structures produced. To remove this bias, the diagonal components are also applied to the vertical roughness filter as well in the x - z and y - z planes. The model produced with the diagonal components in the horizontal and vertical directions is shown in Figure 111d. The banding effect is no longer discernable in this model.

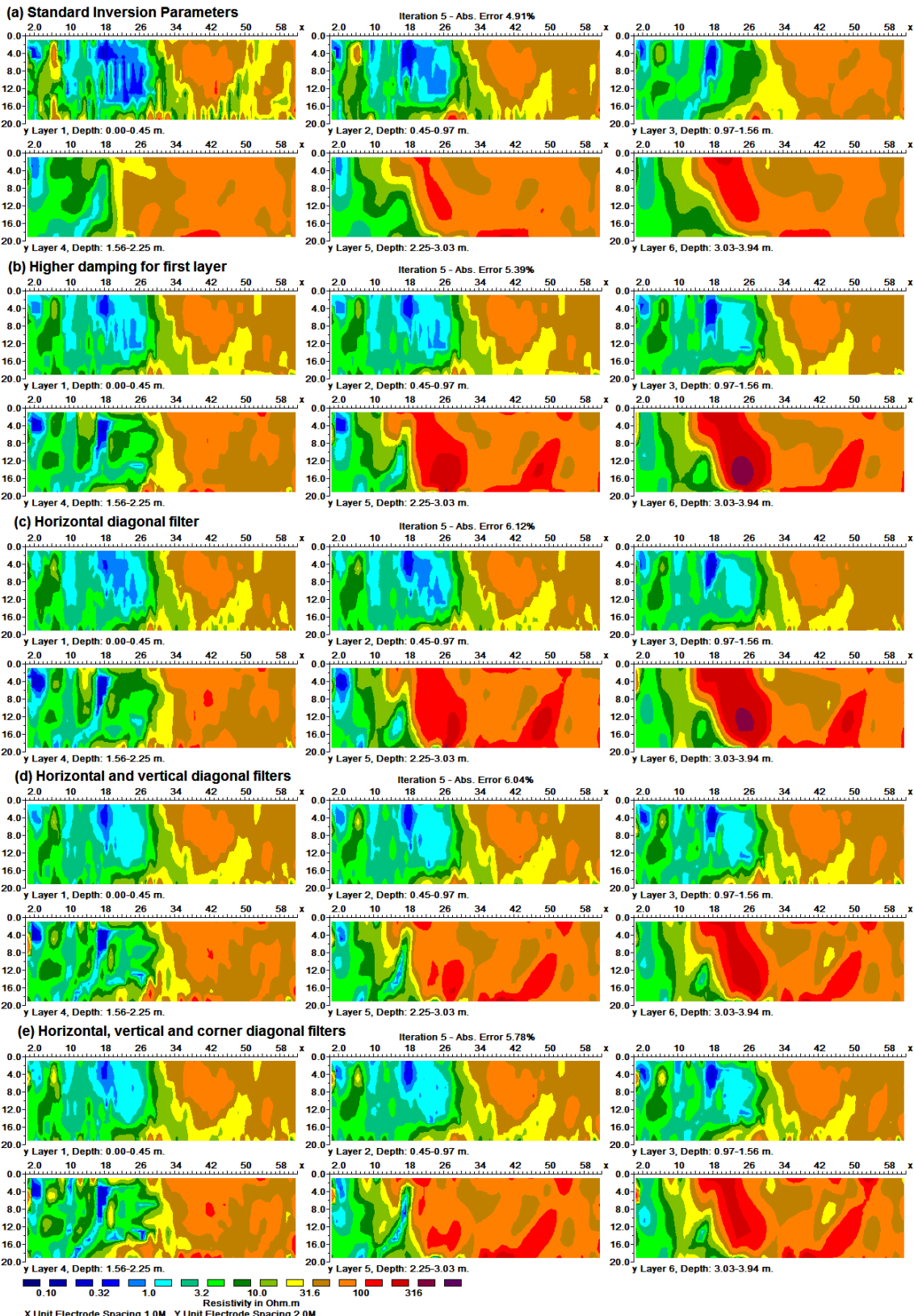


Figure 111. Inversion models for the Vetlanda landfill survey data set. (a) Using standard inversion settings. (b) With a higher damping factor for the topmost layer. (c) Using diagonal roughness filter in the horizontal (x - y) directions. (d) Using diagonal roughness filters in the vertical (x - z and y - z) directions as well. (e) Using the roughness filter in all directions.

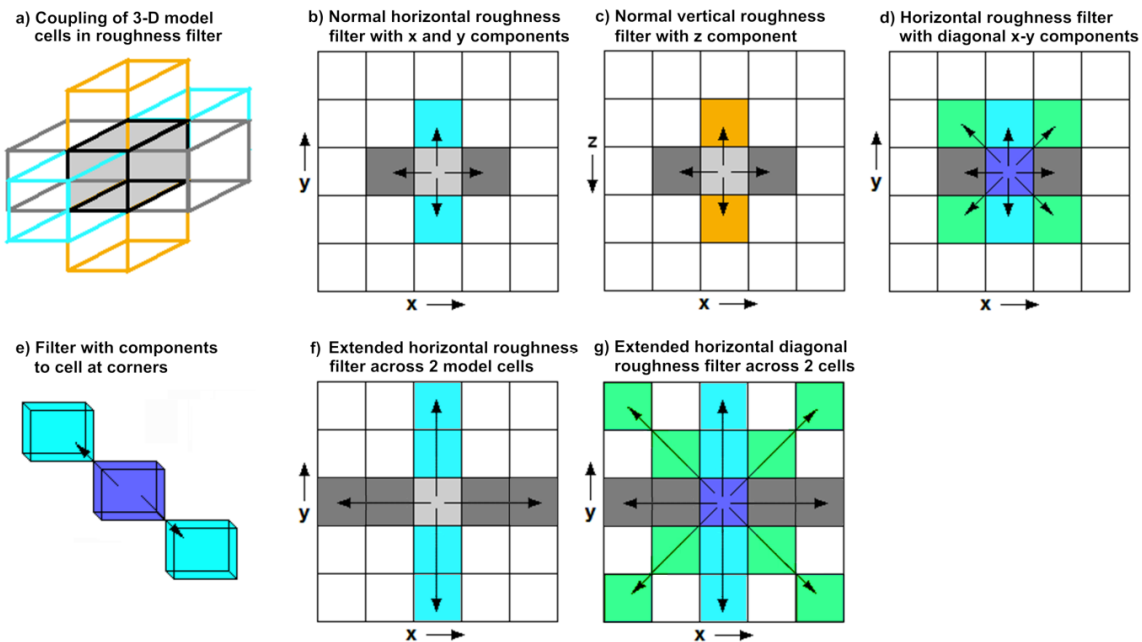


Figure 112. Types of 3-D roughness filters. (a) With components in the x - and y - directions only for the horizontal filter. (b) With components in the diagonal directions in the x - y plane for the horizontal filter. (c) Applying the roughness filter with the corner model cells as well. Only two (out of eight) corner cells are shown.

In the final model, the diagonal components for the roughness filter are also applied between the model cell and the cells adjacent to the corners of the cell (Figure 112e). Except for the cells at the surface, bottom and sides of the model grid, there are eight such corner neighboring cells surrounding each cell. The roughness filter is now applied between each interior model cell and all the 26 cells surrounding it. The resulting inversion model shown is in Figure 111e. In theory, this should reduce any bias in shape of the structures from the alignment of model cells grid (Farquharson, 2008; Loke and Dahlin, 2010).

The model in Figure 111 has model cells with widths of 1 meter in the x direction and 2 meters in the y direction, i.e. elongated in the y direction. This is because the model discretization follows the spacing between the electrode positions. It is possible the banding in the y direction is partly caused by the model cells being elongated in the y direction. A possible alternative method to reduce the banding is to use model cells that are of the same widths in both directions, i.e. a selective model refinement in the y direction. This doubles the number of model cells as well as the number of nodes in the finite-difference grid. Figure 113 shows the inversion models using cells of 1 meter length in both the x and y directions. The inversion model with the standard inversion settings (Figure 113a) does not exhibit the prominent banding in the y direction (Figure 111a). Instead there is a slight banding in the x direction in the top two layers with clustering of very low or high resistivity values along the survey lines. This feature is removed when a higher damping factor is used for the first layer (Figure 113b). The boundary of the low resistivity zone (marked by the light blue color) between x distances of 15 to 27 meters in the top three layers in this model shows a 'stepped' pattern aligned in the x or y direction. This is probably due to the use of a roughness filter with components in these directions (Figure 112b). This feature is removed when the roughness filter with diagonal components is used (Figure 112d) that does not bias the structure in the x and y directions (Figure 113c). The inversion model with the diagonal filter components in the z direction as well (Figure 113d) is also free of the 'stepped' boundary pattern.

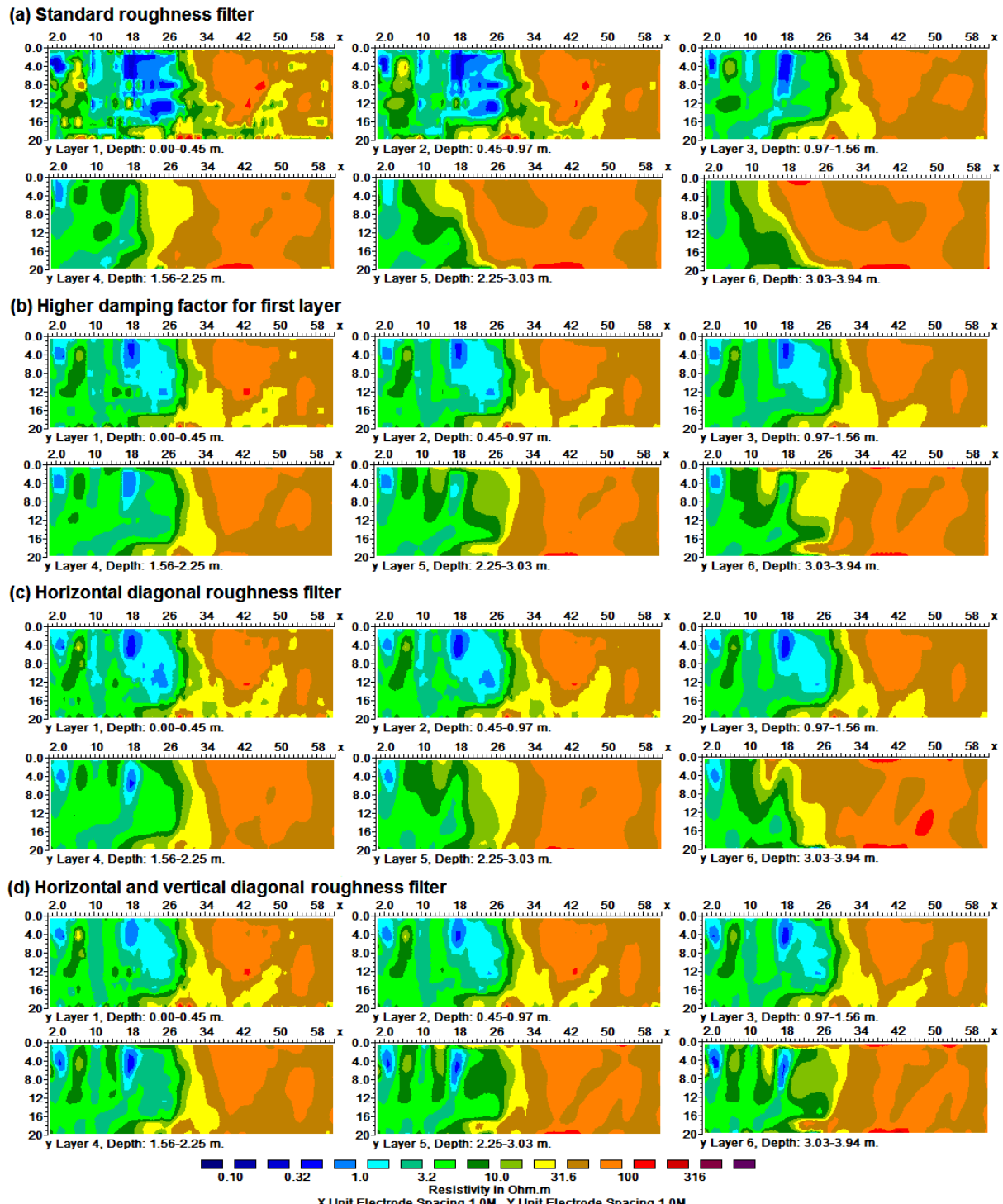


Figure 113. Inversion models for the Vetlanda landfill survey data set using model cells of equal lengths in the x - and y - directions. (a) Using standard inversion settings. (b) With a higher damping factor for the topmost layer. (c) Using diagonal roughness filter in the horizontal (x - y) directions. (d) Using diagonal roughness filters in the vertical (x - z and y - z) directions as well.

8.8 The use of long electrodes in 3-D surveys

It is normally assumed that the dimensions of the electrodes used are much smaller than the spacing between them so that they can be considered as ‘point’ electrodes. In some situations, the length of the electrode is sufficiently long such that it has to be taken into

account. One situation where this arises is when a metallic well casing is used as an electrode. The resistivity of the metal well casing is much lower than the surrounding medium, so the potential on the surface of the casing is essentially constant. The use of such ‘long’ electrodes has been the subject of several papers (Schenkel and Morrison, 1994; Singer and Strack, 1998; Ramirez et al., 2003; Daily et al., 2004). Many of these studies involve deep surveys where the measurements are made using the metal cased wells as electrodes. One situation of interest for environmental and engineering surveys is the use of both point and long electrodes in a survey where existing metal wells can be used as the long electrodes (Rucker *et al.*, 2007, 2010). It is well known that well-to-well measurements involving vertical ‘long’ electrodes only have poor vertical resolution. However, measurements between a ‘point’ and a ‘long’ electrode have better vertical resolution. It might even help when the long electrode extends below the target of interest.

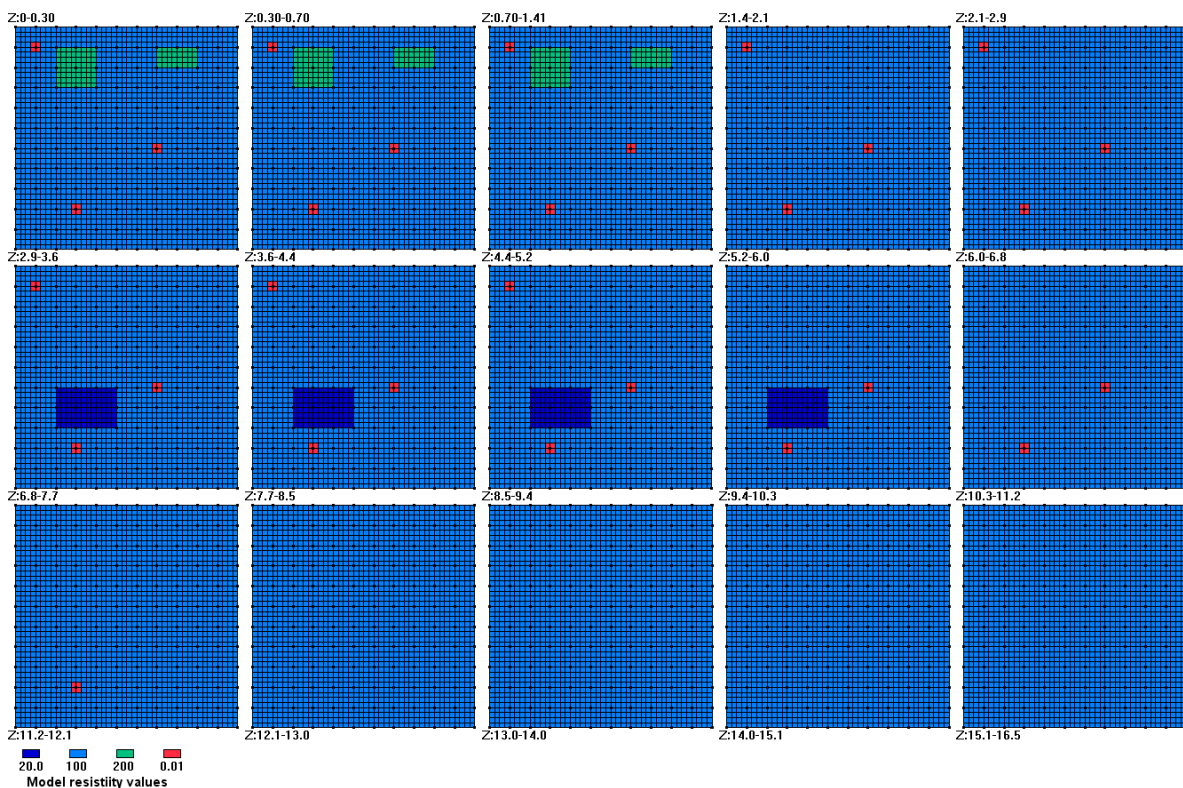


Figure 114. Synthetic model for long electrodes survey. 3-D model using cells of low resistivity ($0.01 \Omega\text{-m}$) that are marked in red to simulate cased wells.

Figure 114 shows a model with a low resistivity block of $20 \Omega\text{-m}$ at a depth of 2.9 to 6.0 meters. The maximum length of the block is 3 meter that is less than its average depth, thus it will be a difficult target for normal surveys with point electrodes on the surface. Figure 115a shows the inversion model for a pole-pole survey data set using the cross-diagonal measurement sequence (Figure 99) using only point electrodes on the surface. Another data set was generated for the same model with three of the point electrodes converted into long electrodes. This was done by assigning a very low resistivity value to the cells around the point electrode, as marked by the red cells in Figure 114. Two of the long electrodes extend below the low resistivity block. The inversion model for the data set using the combination of point and long electrodes (Figure 115b) shows slightly better resolution for the low resistivity block. The lowest resistivity achieved in model is about $77 \Omega\text{-m}$ (Figure 115b) which is lower

than the value of $83 \Omega\text{m}$ achieved by the model for the data set using only surface point electrodes (Figure 115a).

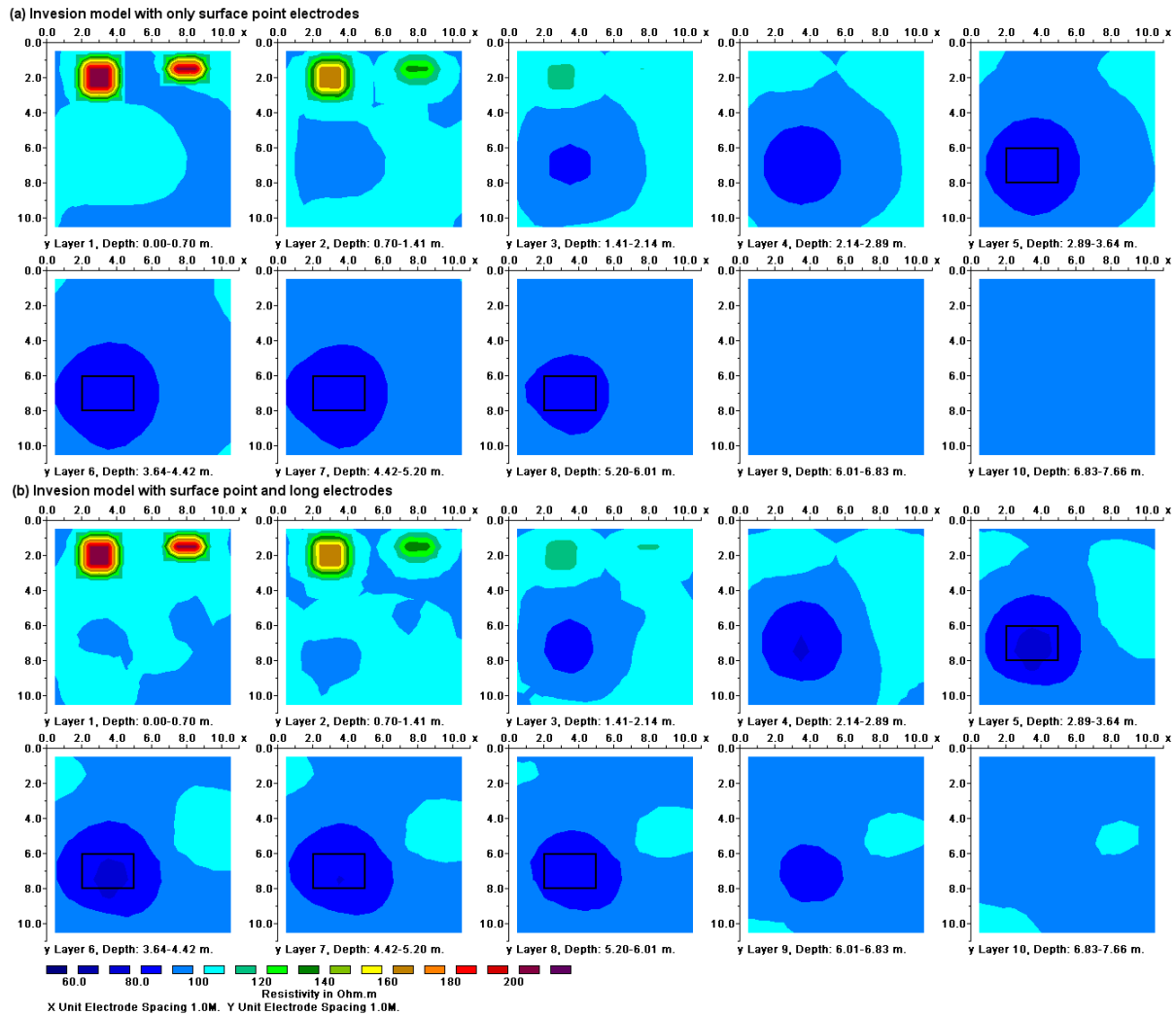


Figure 115. Comparison of inversion models using point electrodes with and without long electrodes. (a) Inversion model for pole-pole data set using only surface point electrodes. (b) Inversion model for pole-pole data set using 121 point and 3 long electrodes.

8.9 Data grid formats and model discretizations

8.9.1 Types of surveys and model grids

There has been a trend over the years to reconcile theory with practice. Initially, 3-D models assume a simple situation where the electrodes used in the survey have uniform spacing in both the x and y directions (Figure 116a). This situation was sufficient in simple research setups, and easy for computer programming. However, over the years, more complex data formats were developed so that more complex field situations could be accommodated. The next step is to allow for a situation where the electrodes are still arranged in a rectangular grid, but the distance between the survey lines is not constant (Figure 116b). However, due to physical obstructions, it is sometimes not possible to run straight survey lines. The trapezoidal data grid format allows for small deviations from straight survey lines (Figure 116c). However, it still assumes each line has the same number of electrodes in the x or y directions. To convert the 3-D of field data set into a resistivity model for the subsurface, we divide the subsurface into a number of blocks. The three data grid formats tie the (x,y)

positions of the corners of the model blocks to the electrode positions. In more complex surveys, the survey lines might be in different directions with different numbers of electrodes. A common situation encountered in mineral surveys is data collated from different survey campaigns at different times over the same prospect. This results in a data set with survey lines running in different directions. The fourth grid format (Figure 116d) is so far the most general and designed to handle almost any electrode distribution. The (x,y) positions of the model blocks are now independent of the electrode positions. A non-uniform rectangular grid is used to set up the (x,y) corners of the model blocks so that a finer grid can be used where there are more electrode positions. In the future, more complex mathematical models might have to be used so that it more closely matches the field situation. One modification is to handle surveys where the lines are not orientated north-south or east-west. This requires a simple data coordinate reorientation. Another possible situation is where the length of the survey lines vary across the survey area.

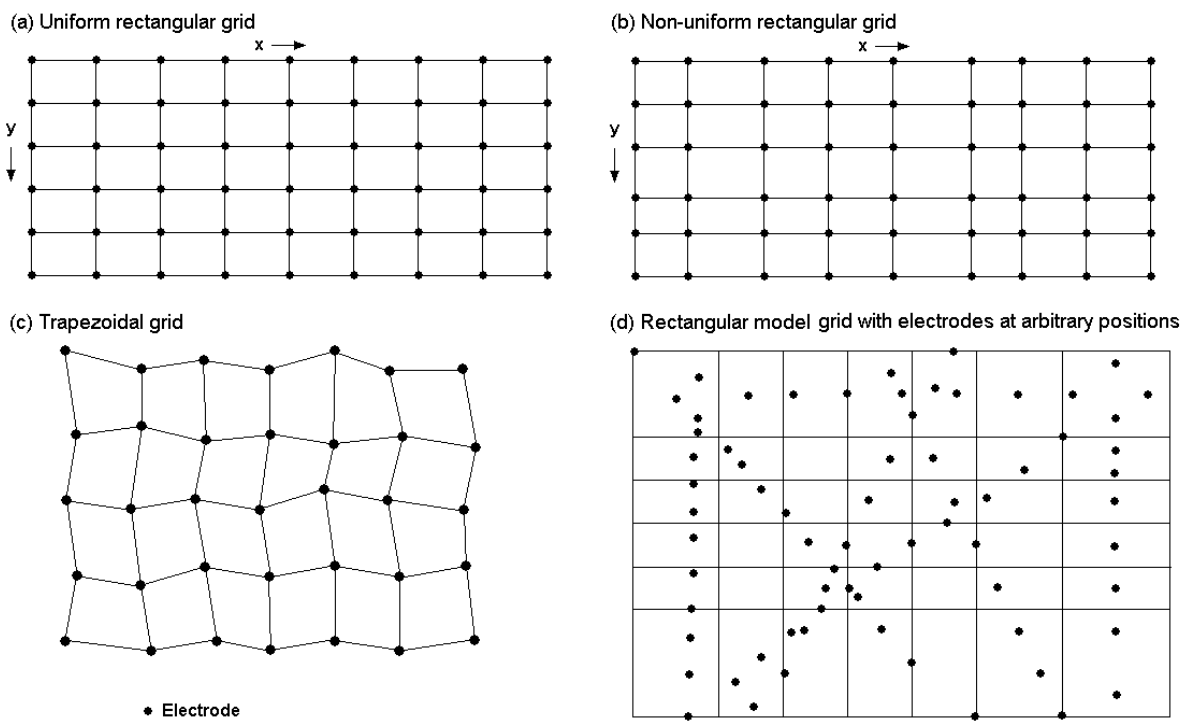


Figure 116. 3-D data grid formats.

8.9.2 Model grid optimization for large surveys with arbitrary electrodes positions

The data format that separates the model grid from the survey electrodes positions (Figure 116d) has made it possible to model data from very complex survey layouts. This flexibility comes at the price of higher computer memory requirements. Thus this option is only available in the 64-bit RES3DINVx64 program. In this section, we will take a closer look at the finite-difference and finite-element mesh used and ways to optimize it so as to reduce the memory required.

Firstly, the program subdivides each model cell by four mesh lines in both the x and y directions (Figure 117). When the electrode falls on a node location (at the intersection of the x and y mesh lines), it can be directly modeled by that node. There are two alternatives to model the effect of an electrode at an arbitrary position with the finite-difference and finite-element methods when it does not fall on a mesh node. The first is to calculate the potential at the electrode by interpolating the potentials (Figure 117a) at the four nearest nodes in the

mesh (and similarly replace a single current electrode node by four equivalent current sources). The second method moves the nearest node to the location of the electrode using a distorted finite-element mesh (Figure 117b). For both methods, it is important that two electrodes used in the same array are sufficiently far apart in the mesh setup used. Figure 118a shows a problem when a current electrode is close to a potential electrode in the same array when the interpolation method is used. Both the current and potential electrodes will share a common node if they are too close together. To avoid this problem, there should be at least two mesh lines between the two electrodes so that they do not share a common node (Figure 118b).

It is possible to avoid the situation in Figure 118a by using smaller model cells. However, using small model cells will increase the number of nodes in the finite-difference or finite-element mesh. It will also increase the total number of model cells in the inversion model. Both of this will increase the computer memory and time required for the inversion of the data set. It might be necessary to make some adjustments to the model grid specified to obtain the optimum balance.

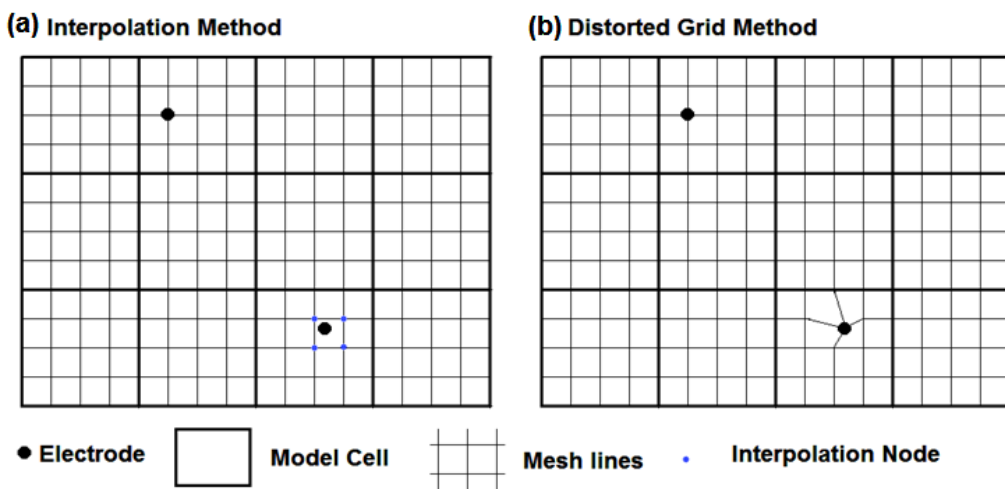


Figure 117. Methods to model the effect of an electrode using the finite-difference and finite-element methods.

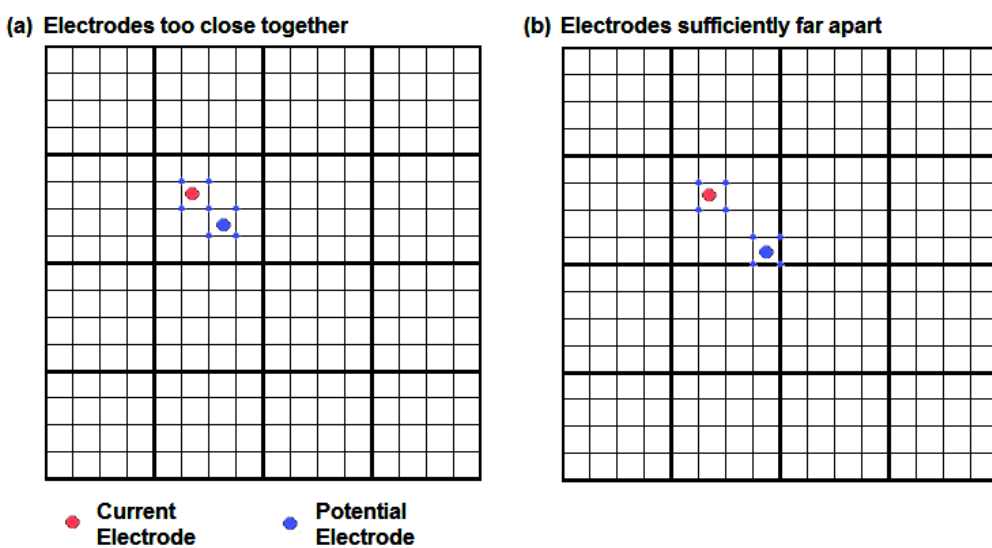


Figure 118. The use of an appropriate mesh spacing to obtain sufficient accuracy for electrodes in the same array that close together.

To illustrate this, we used the data from a survey at the Hanford site in Washington state, USA where the waste material was stored in trenches and concrete cribs (Rucker *et al.*, 2007). Different resistivity survey phases were carried out using 2-D lines (Figure 119). The distribution of the electrodes does not fit into a simple rectangular grid. The first attempt to model the data uses a model grid with cell widths of 5 meters. This produced a model grid with 125x98 lines in the *x*-*y* directions. The inversion model had 16 layers that gave a total of 192448 model cells. While the inversion of the data set could be carried out on a PC with 24 GB RAM, there were a number of electrode that were too close in the mesh, as marked by the light blue points in the grid display (Figure 120a). The next model grid has cell widths of 4 meters (Figure 8.23b). This eliminated electrodes that were less than 2 mesh lines apart, but this produced a model grid with 156x122 lines in the *x*-*y* directions. The inversion model has 300080 cells, and the finite-difference mesh had more than 1.5 million nodes and the PC with 24 GB RAM was not able to run the inversion. The third model grid with cell widths of 4 meters in the *x*-direction where the electrodes were close together (on the right side of the mesh) and 5 meters elsewhere. This gave a model grid with 136x98 lines. The model has 209520 cells that could be handled by the PC with 24 GB RAM. The final inversion model obtained using this model grid setup is shown in Figure 121. The linear features in the second to fifth layers are due to the trenches and concrete cribs. The leakage zones are marked by the prominent low resistivity zones in the fifth and deeper layers. Note that the bottom left corner of all the layers show relatively less resistivity variation compared to the other sections. This is basically due to the fact it has no data coverage as the survey lines do not cross this section.

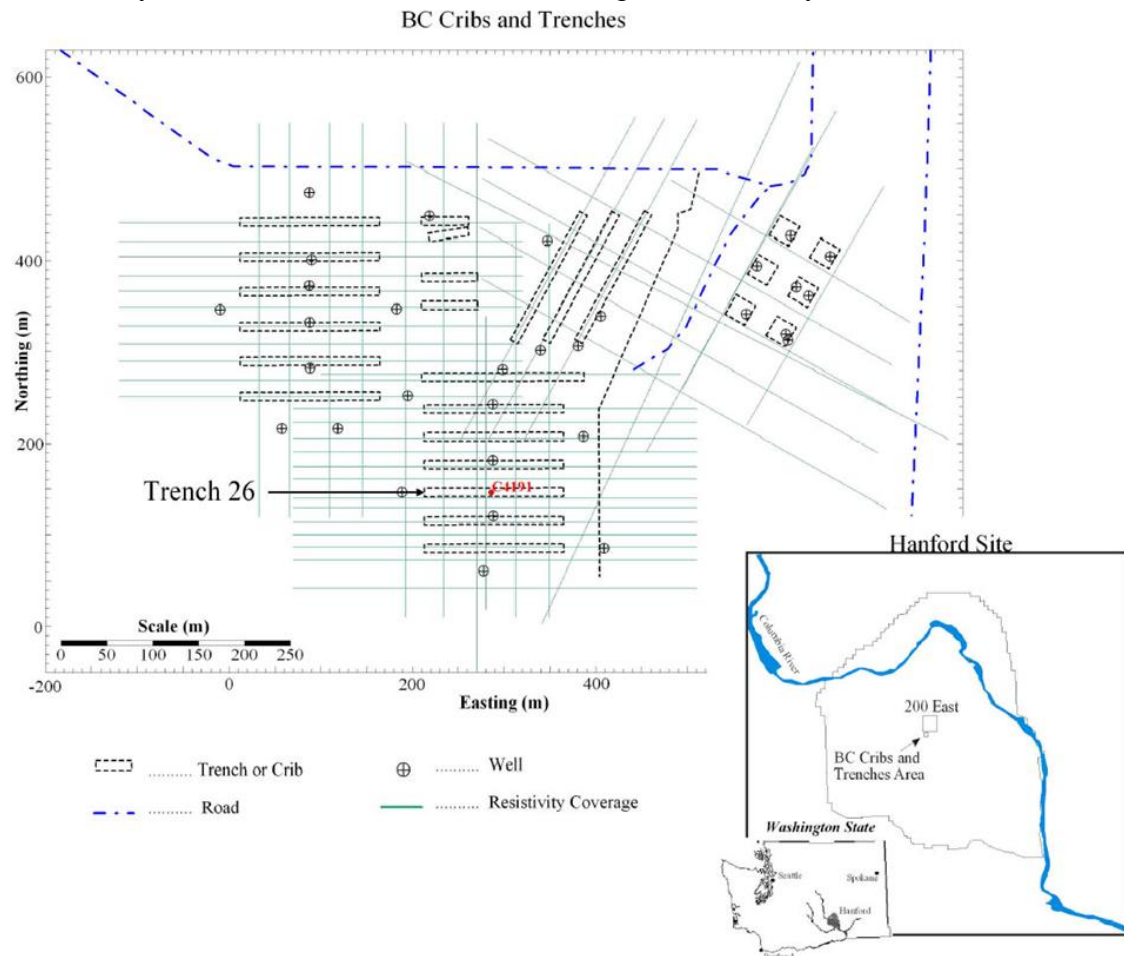


Figure 119. Map with survey lines and infrastructure at the Hanford site.

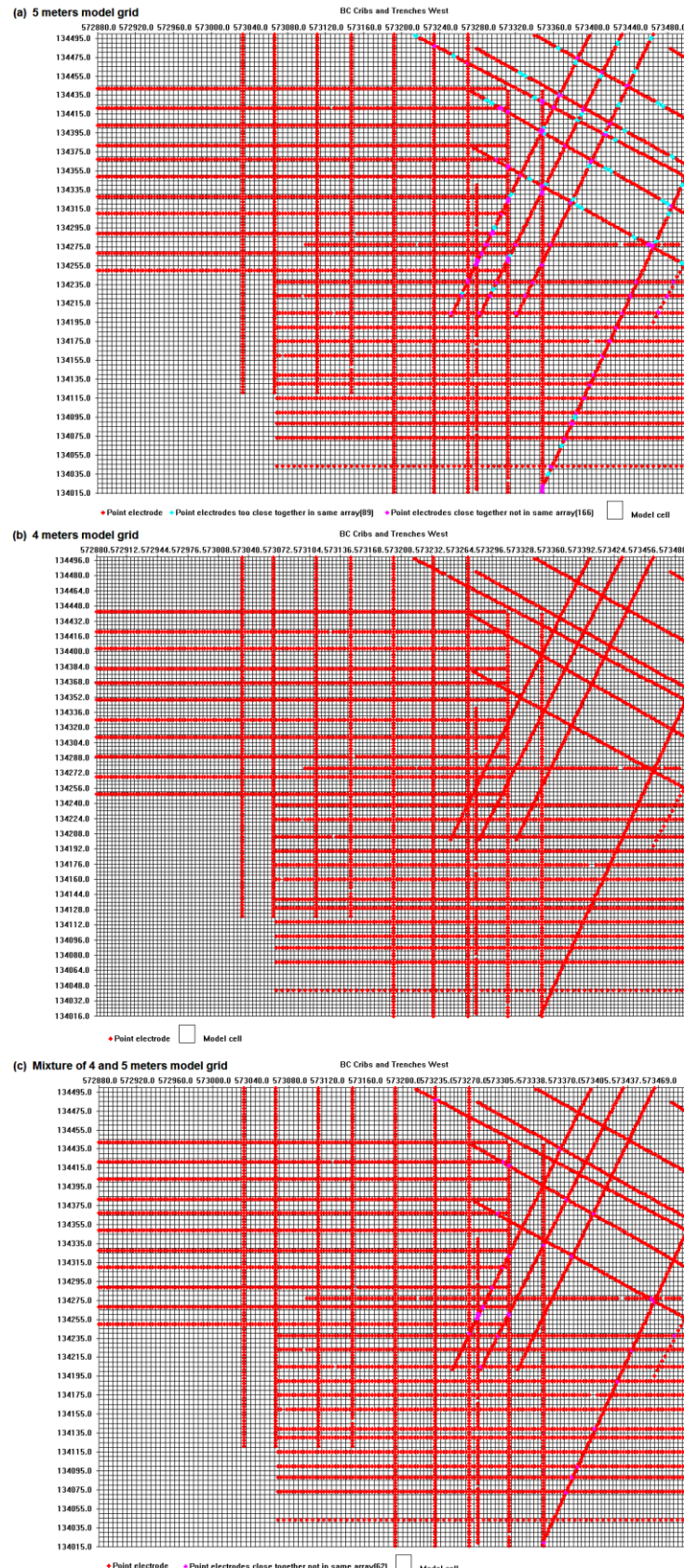


Figure 120. Types of model grids for the Hanford survey data set. (a) Using a 5 meters spacing model for the entire area. (b) Using a 4 meters spacing model for the entire area. (c) Using a mixture of 4 and 5 meters spacing model grid.

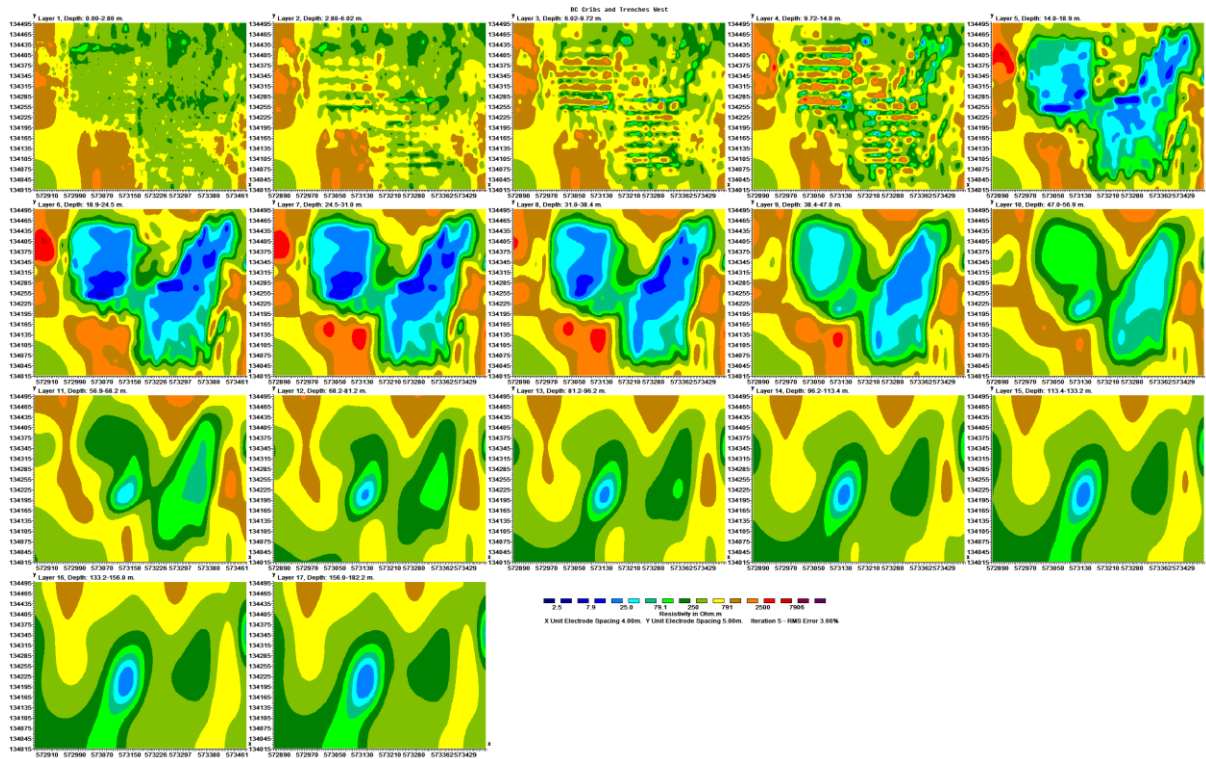


Figure 121. Inversion model for Hanford survey site.

8.10 3-D array optimization – grids and perimeters

In a previous section (section 4.9.4), a method to generate optimized arrays for 2-D surveys using the model resolution was discussed. As 3-D surveys might involve hundreds to thousands of electrode positions, the use of similar array optimization techniques might appear to be an intractable problem. However by using a combination of improvements in the array optimization algorithm, advances in computer hardware and improved numerical algorithms (Loke *et al.*, 2015a) together with a novel method to generate the test arrays (Loke *et al.*, 2013b), this is now possible. The key to the use of the array optimization method is to take advantage of the fact that practical field survey have limitations in the number of electrodes that be accessed at the same time due to equipment limitations. Most field equipment have less than 100 nodes, certainly less than the thousands of possible electrode positions in a 3-D field survey. One example is shown in Figure 122 with 3 cables with 21 electrodes each (Dahlin *et al.*, 2002). A larger area can be surveyed by moving the setup in the *y* direction using a roll-along method, such as the 21 by 17 survey grid used by Dahlin *et al.* (2002). Although the final survey grid has 357 electrodes, not all possible combinations of the electrodes can be used. This greatly reduces the size of the possible array combinations. As an example of the improvements possible using optimized arrays, the results for a synthetic test model used in Loke *et al.* (2013b) is shown in Figure 123. The model consists of three rectangular blocks with resistivity of 1000 ohm.m at different depths embedded in a homogeneous medium of 100 ohm.m. The survey grid consists of 8 lines with 21 electrodes each. The inline electrode spacing is 1 meter while the distance between the lines is 2 meters. The first data set consists of the inline Wenner-Schlumberger and dipole-dipole arrays where the geometric factor is less than 2262 m. The second data set was created by the ‘Compare R’ array optimization method. Voltage dependent Gaussian random noise (Zhou and Dahlin, 2003) with an amplitude of 1 milli-ohm was added to the resistance values before they were converted into apparent resistivity values. The L1-norm method was used for both the data

misfit and model roughness (Loke *et al.*, 2003) in the inversion of this data. The L-curve method was used to estimate the optimum inversion damping factor. Figure 123 shows the inversion models for the conventional arrays (with 3152 data points) and the optimized data (3154 data points) sets. The optimized data set has slightly more points to maintain symmetry in the array configurations used. The top two blocks are poorly resolved by the conventional arrays data set (Figure 123a) compared to the optimized data set (Figure 123b). The width of the topmost block anomaly is twice the actual size while its maximum resistivity is less than 240 ohm.m. In comparison, the optimized arrays inversion model has a maximum resistivity of about 640 ohm.m and the correct width. The optimized arrays also achieve significantly higher resistivity values at the locations of the second and the third blocks. Note that although the data misfit for the optimized data set (0.66%) is slightly higher than that for the conventional data set (0.34%) due to the higher average geometric factor of the optimized arrays, the model resolution is better.

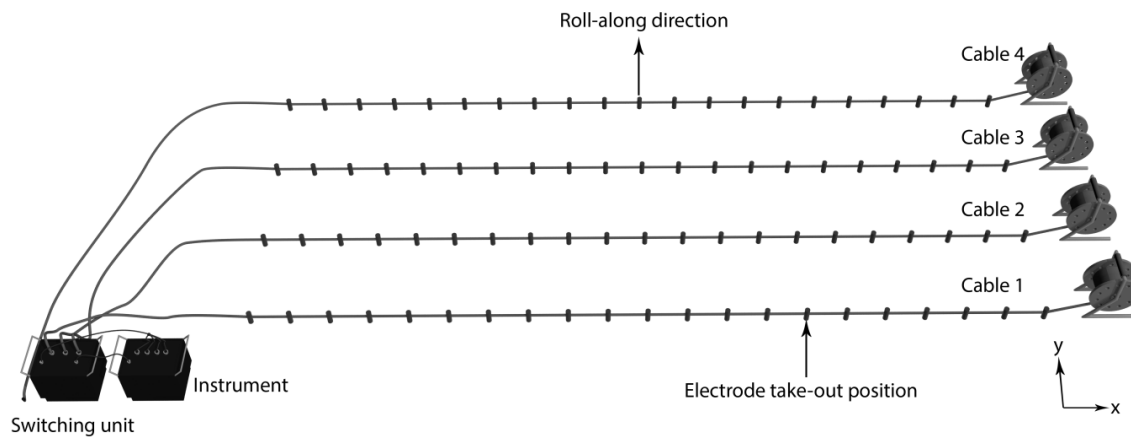


Figure 122. Arrangement of survey lines using a 3 cable system with the Abem SAS instrument.

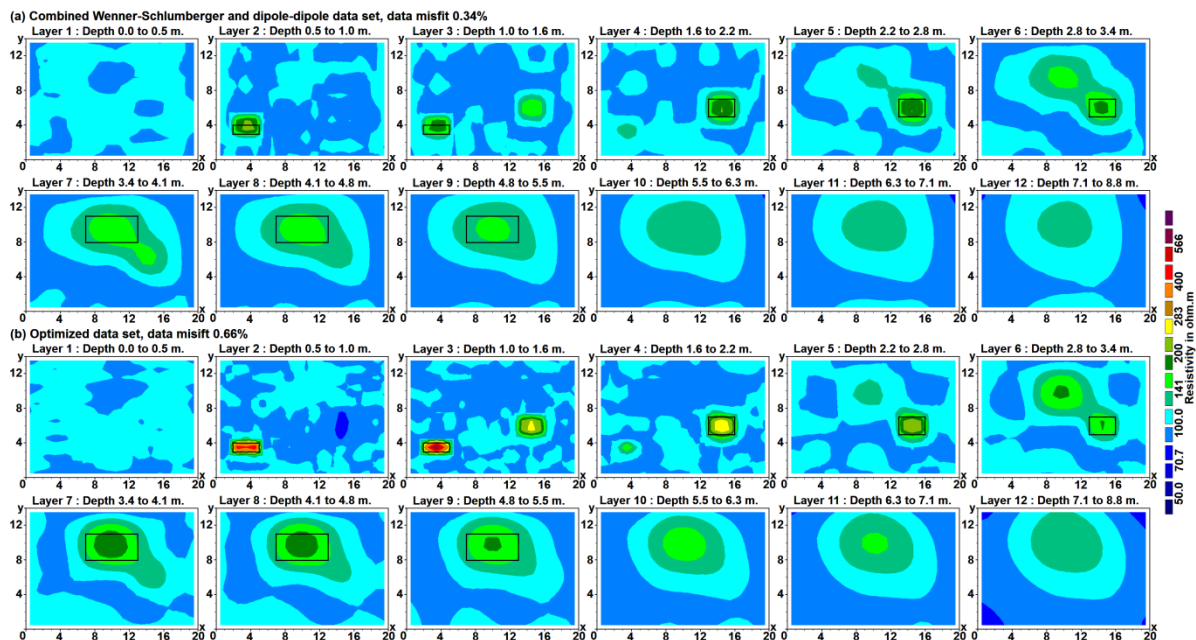


Figure 123. Inversions model for (a) combined Wenner-Schlumberger and dipole-dipole data set, (b) optimized data set. The actual positions of the blocks are marked by black rectangles.

An interesting special case of a 3-D survey is when the electrodes are confined to the perimeter of the survey area (Tejero-Andrade *et al.*, 2015). The arrays used for such surveys are commonly based on heuristic rules, and very often designed for a perimeter with sharp corners such as a rectangle (Baker *et al.*, 2001), and might not be applicable for perimeters with smooth shapes such as a circle. An algorithm to generate optimized arrays for perimeters of any shape is described in Loke *et al.* (2015d). As an example, for a survey with 40 electrodes arranged in a square perimeter, the comprehensive data set has nearly 180 thousand arrays. Figure 124a shows model resolution plots for the first 6 layers for the comprehensive data set that shows the maximum possible resolution for this survey setup. The highest resolution values are in the first layer near the electrodes and decrease rapidly with depth and towards the centre of the survey region. The resolution sections for the ‘conventional’ arrays consisting of the ‘L and Corner’ arrays (Tejero-Andrade *et al.*, 2015) with 946 data points have much lower resolution values, particularly in the deeper layers (Figure 124b). The optimized arrays generated by the ‘Compare R’ method with the same number of data points have significantly higher resolution values (particularly in the 5th layer), although the resolution values are well below that of the comprehensive data set (Figure 124c). Figure 125 shows model resolution sections in a vertical plane across the middle of the area. It more clearly shows that the optimized arrays have higher resolution values than the conventional arrays particularly at the middle and at depth. This is clearly shown by the relative model resolution sections calculated using the ratio of the resolution of the data set with that of the comprehensive data set (lower row of sections in Figure 125). The ‘conventional’ arrays clearly has lower resolution values near the center of the survey region and at depth. The larger optimized data set with 2000 data points has an average resolution of 0.091 compared to 0.111 for the comprehensive data set with almost 100 times more arrays.

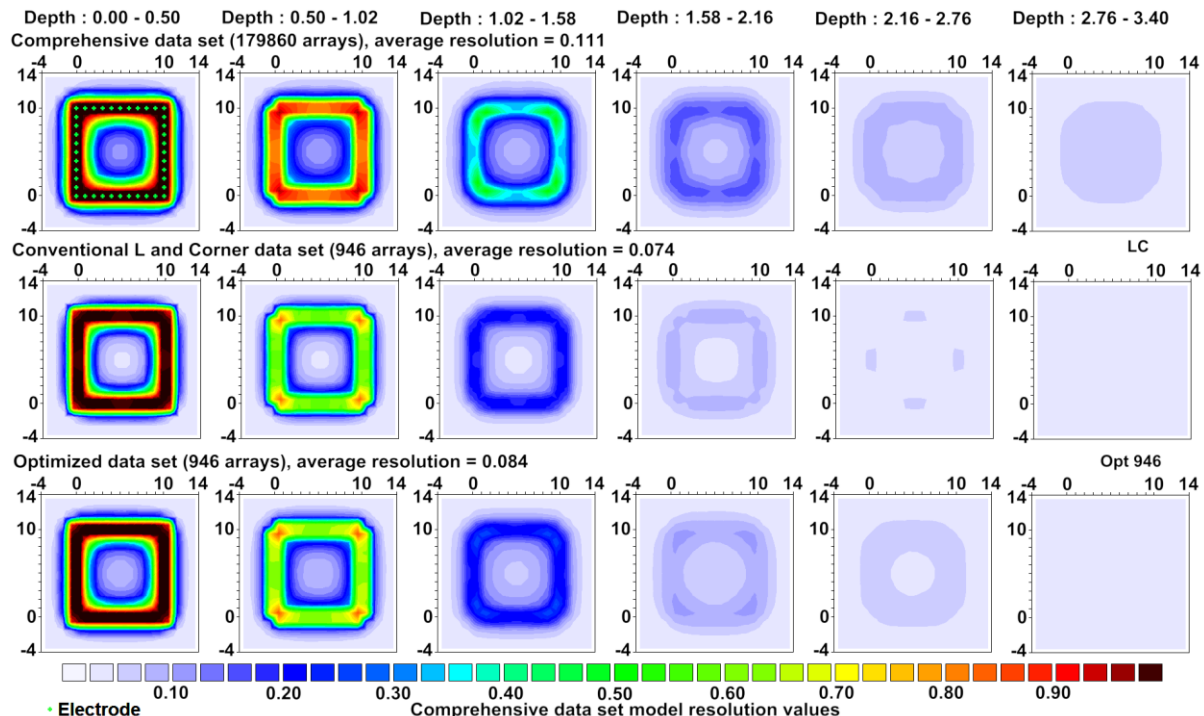


Figure 124. Horizontal sections showing the model resolution for the (a) comprehensive data set, (b) standard arrays and (c) optimized arrays. The electrode positions are marked by small green crosses in the top layer in (a).

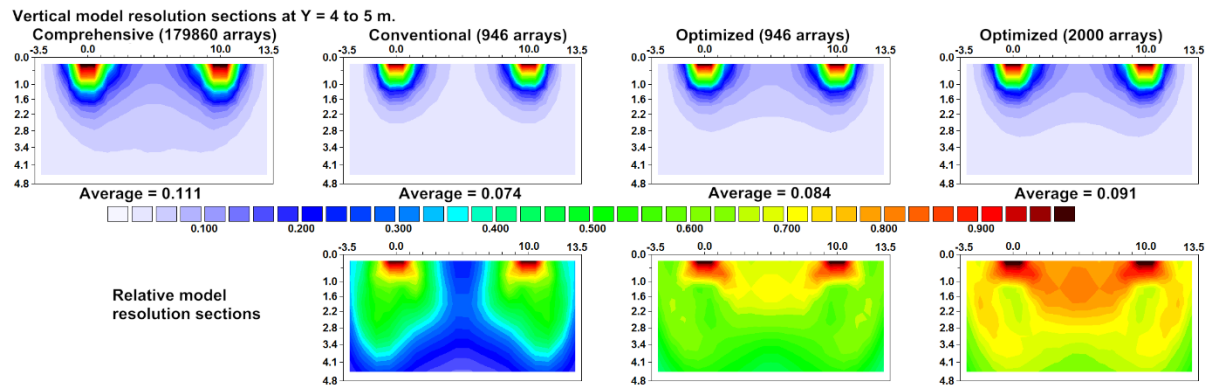


Figure 125. Vertical cross-sections showing the model resolution for the comprehensive, ‘standard’, small and large optimized data sets.

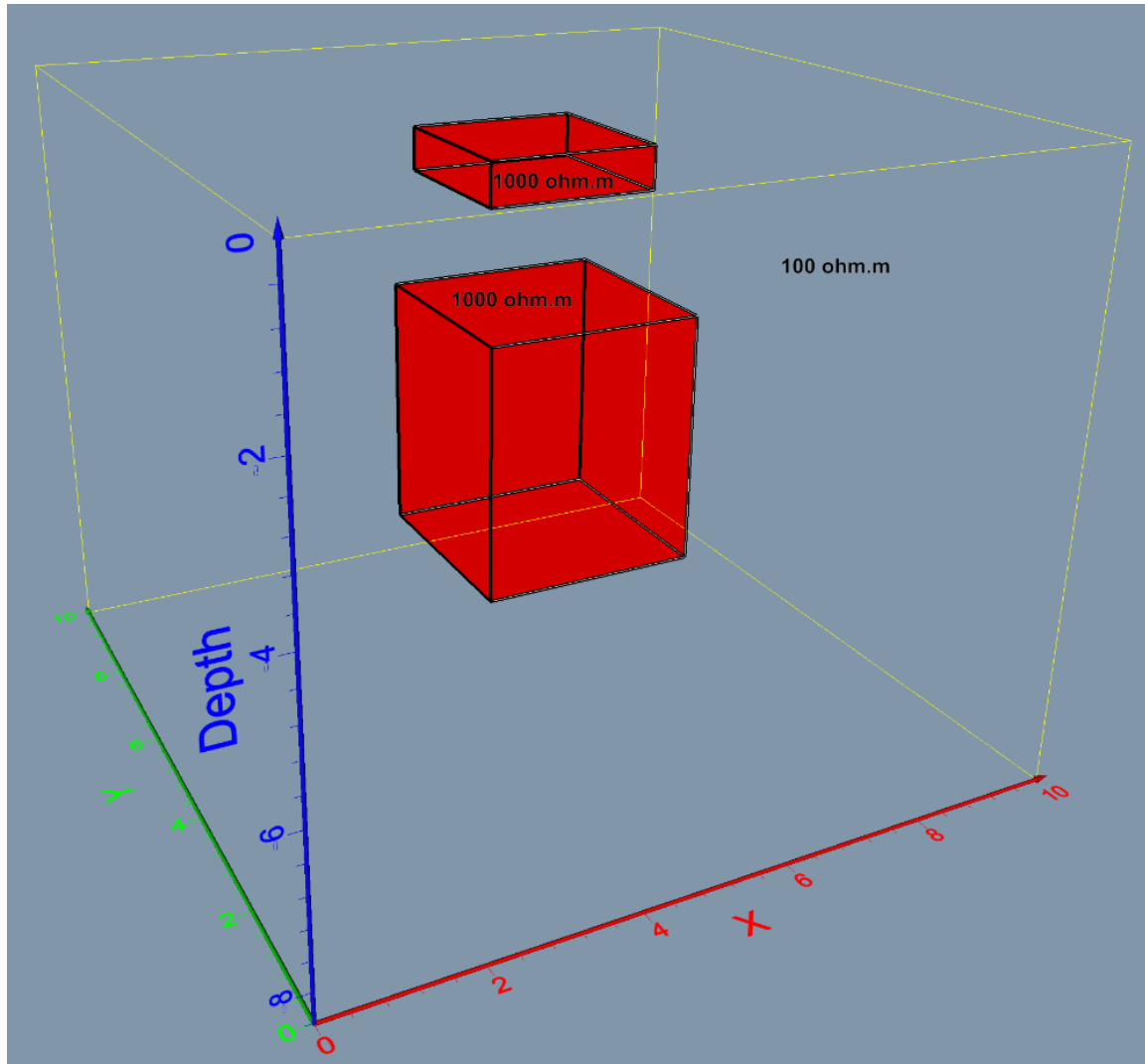


Figure 126. The synthetic test model with two 1000 ohm.m rectangular blocks (marked by black rectangles) embedded in a 100 ohm.m background medium.

To illustrate the performance of the different arrays, a test model consisting of two high resistivity rectangular blocks of 1000 ohm.m embedded within a 100 ohm.m medium (Figure 126) was used. The first test data set consists of the conventional ‘L and Corner’ arrays (Tejero-

Andrade *et al.*, 2015) with the maximum geometric factor set at 4147 m that gives 946 data points. Gaussian random noise (Zhou and Dahlin, 2003) with a mean amplitude of 1 milliohm was added to the calculated resistance values before they were converted to apparent resistivity. The 'L and Corner' arrays model (Figure 4a) detects the blocks with maximum resistivity values of about 110 ohm.m but the shape of the deeper block is not clearly defined. The smaller optimized data set model has a higher maximum value of about 119 ohm.m for the deeper block (Figure 4b) with the maximum anomaly value that is closer to the true position in the upper part of the block. However the top edge of the block is not well resolved with a small artifact that extends to the surface. The poor vertical resolution is expected from the PSF plot (Figure 3e). The model for the larger optimized set with 2000 data points (Figure 4c) shows higher values of 115 and 124 ohm.m at the positions of the top and bottom high resistivity blocks. Although the optimized data sets have higher models misfits (1.5%) compared to the 'L and Corner' arrays (0.5%) due to higher average geometric factors of the arrays used, the deeper block is better resolved in the inversion models. The array optimization program took 616 seconds to generate the data set with 2000 arrays.

Despite being able to detect the larger block near the center of the survey grid, the optimized data sets cannot clearly resolve the top of this structure. It was also observed by Tejero-Andrade *et al.* (2015) that it was not possible to resolve the top of the structures used in their synthetic models tests. Figure 128 shows plots of the point-spread-function (PSF) values (Oldenborger and Routh, 2009) for a model cell at different depths located near the center of the square for the comprehensive data set. All the PSF plots have a predominantly vertical pattern. The regions with significant PSF values are spread out about 2 m laterally but about 4 m vertically. As the comprehensive data set contains all the possible arrays, this indicates any survey with the electrodes confined to the perimeter will be able to resolve horizontal boundaries better than vertical boundaries. When the depth of the model cell is less than 2 m (or less than half the distance from the nearest electrode) the highest PSF values occur near the surface. This is the reason the anomalies in the inversion models reach the surface although the actual top boundary of the structure is deeper. The maximum value of the PSF plot for the cell at 3.08 m depth (Figure 128e) is located below the surface closer to the actual depth of the cell. Thus for depths of more than half the distance from the nearest electrode the maximum model anomaly value is expected to be below the surface although detecting the structure will more difficult due to the loss of resolution with depth.

An example with a survey on a circular perimeter is next used to illustrate the general nature of the array optimization algorithm. The array optimization algorithm has the advantage over heuristic rules (based on a particular perimeter shape) the same technique can be used regardless of the shape of the perimeter. Figure 129 shows the model resolution sections for a survey perimeter with 40 electrodes in a circle. As expected, the resolution decreases towards the center of the survey area. The test model has two rectangular blocks of 10 ohm.m in a 100 ohm.m medium (Figure 130). The two blocks are detected in the inversion model for the smaller optimized data set with 946 data points (Figure 130a). However, the top and bottom boundaries of the deeper block are now well resolved. There is a slight improvement with the larger optimized data set (Figure 130b). The left boundary of the top block and the bottom boundary of the lower block are better resolved.

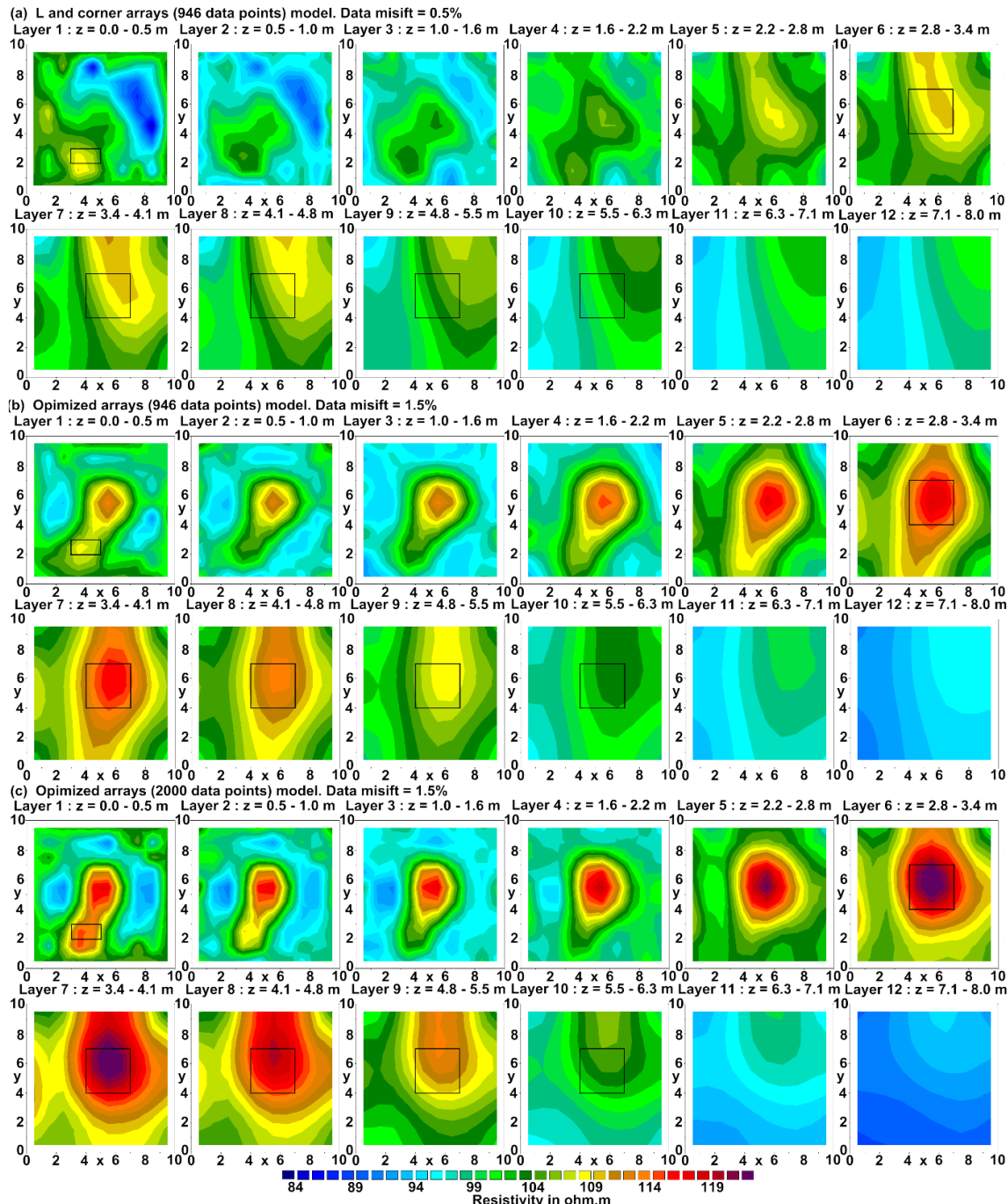


Figure 127. The inversion models for the synthetic model with two 1000 ohm.m rectangular blocks (marked by black rectangles) embedded in a 100 ohm.m background medium.

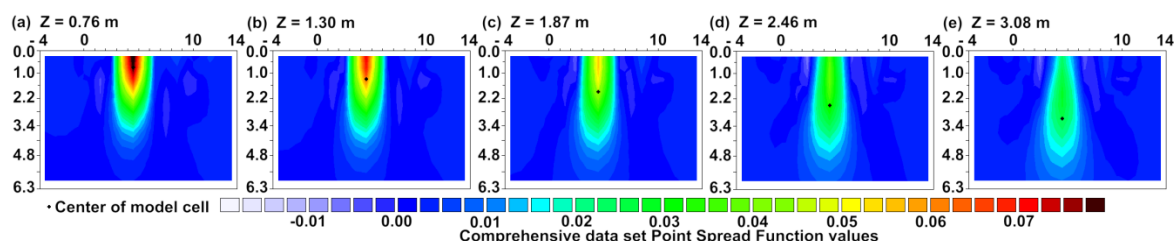


Figure 128. Comprehensive data set point-spread-function plots on a vertical x-z plane located at $y=4.5 \text{ m}$ for a model cell at different depths with centre at $x=4.5\text{m}$ and $y=4.5\text{m}$.

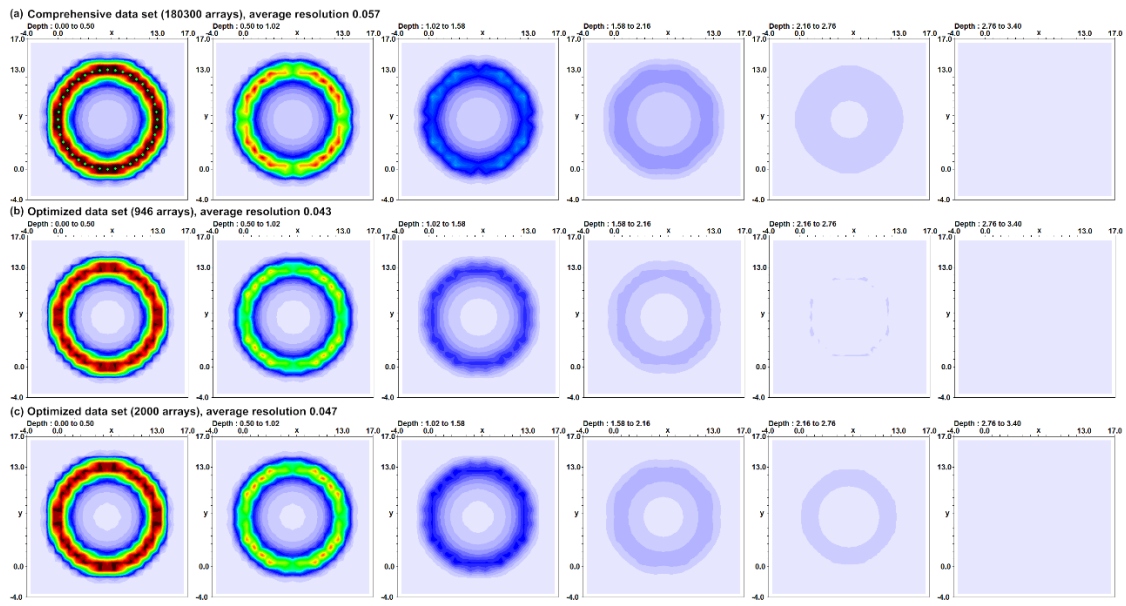


Figure 129. Model resolution sections with circular perimeter for (a) comprehensive data set with 180300 arrays, optimized data sets with (b) 946 and (c) 2000 arrays.

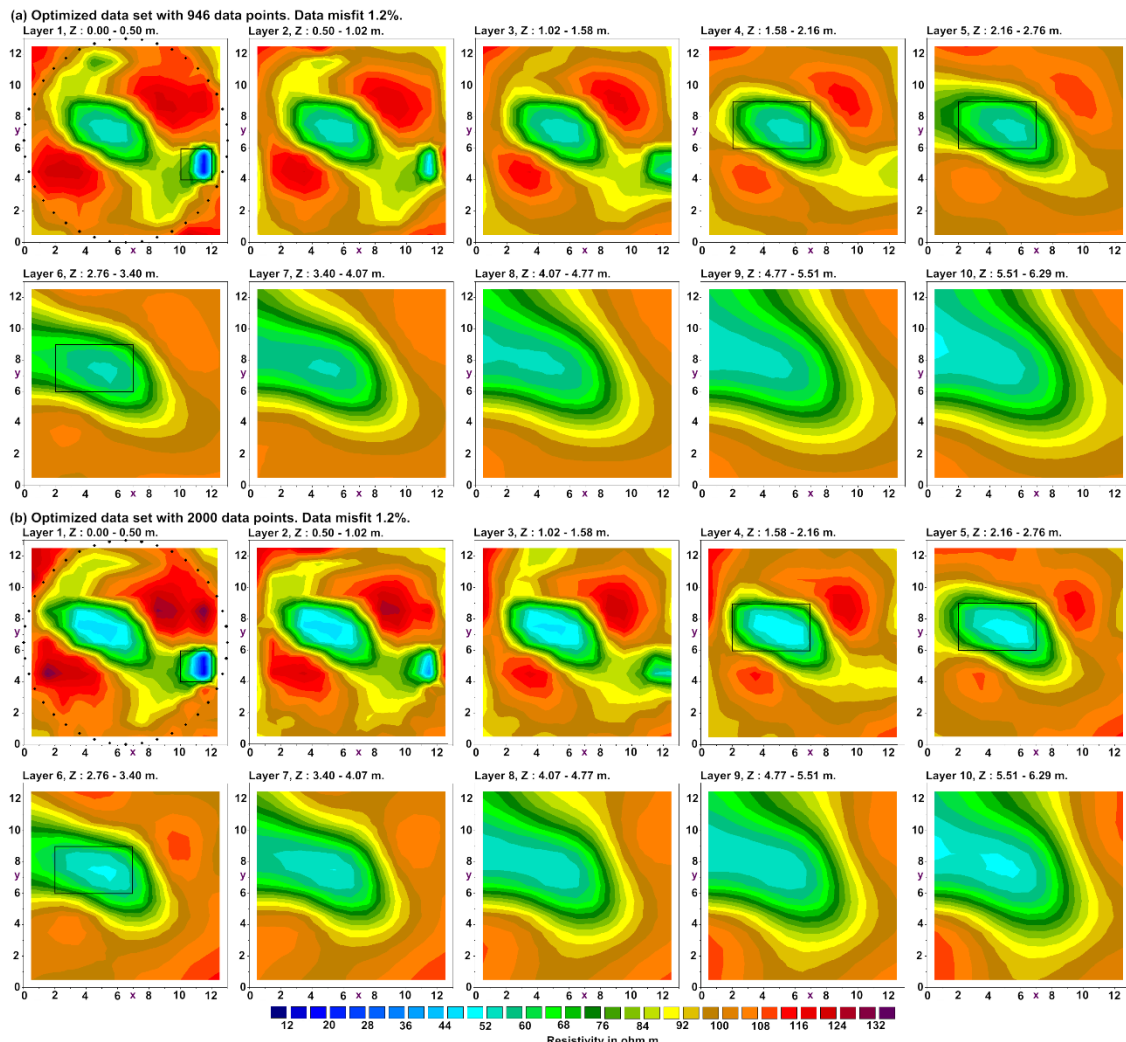


Figure 130. Inversion results for survey with a circular perimeter using optimized arrays with (a) 946 and (b) 2000 data points.

8.11 Unstable arrays and the geometric factor relative error

It has become increasingly popular in large scale mineral exploration surveys to use the offset pole-bipole or bipole-bipole type of arrays that greatly reduces the survey time and cost (White *et al.*, 2001). The current and potential electrodes are laid out on separate lines. This not only reduces EM coupling in I.P. surveys, but reduces the number of times the current electrodes (with associated heavy current generator) have to be moved. One problem that has arisen with this type of layout that is gives rise to 'unstable' arrays where the two potential electrodes almost lie on an equipotential contour line. Usually it is sufficient to use the geometric factor to identify 'unstable' arrays that are likely to have very low potentials. Arrays with very large geometric factors will have very low potentials, and thus likely to be very noisy. However it has been found that arrays with acceptable geometric factors but with electrodes on different lines can also be 'unstable' (Loke *et al.*, 2014c). A similar situation occurs for cross-borehole surveys where the current and potential electrodes are located in different boreholes (Wilkinson *et al.*, 2008). In mineral exploration surveys, the current transmitter is usually not linked to the potential measuring units, thus the sign of the measured potential cannot be determined. It is usually assumed the measured potential (and thus apparent resistivity) is positive. So a situation can arise where the field array has a positive apparent resistivity value, but the calculated apparent resistivity value might be negative. Numerical methods, such as the finite-difference and finite-element methods, have finite accuracy. For some array configurations, the theoretical potential difference might be smaller than the error in the finite-difference or finite-element forward modeling method. Thus the forward modeling routine might give a negative apparent resistivity value. Although it is possible to carry out an inversion using the apparent resistivity instead of the logarithm of the apparent resistivity, using the logarithm is preferable as it scales the apparent resistivity values that can have a very large linear range.

The geometric factor relative error was proposed by Wilkinson *et al.* (2008) to identify cross-borehole arrays that are likely to be unstable. This gives the sensitivity of the array to errors in the position of the electrodes. The geometric factor K for any four electrode array located on the ground surface is given by

$$K = 2\pi/H, \quad H = \left[\frac{1}{r_{AM}} - \frac{1}{r_{AN}} - \frac{1}{r_{BM}} + \frac{1}{r_{BN}} \right]. \quad (8.1)$$

The current electrodes are denoted by A and B , while the potential electrodes are M and N . r_{AM} is the distance between A and M . The sensitivity (s) of the geometric factor to errors in the positions of the electrodes (Loke *et al.*, 2014c) is given by

$$s^2 = \left(\frac{\partial K}{\partial A} \right)^2 + \left(\frac{\partial K}{\partial B} \right)^2 + \left(\frac{\partial K}{\partial M} \right)^2 + \left(\frac{\partial K}{\partial N} \right)^2. \quad (8.2)$$

The geometric factor relative error is then defined to be

$$R_E = s / K. \quad (8.3)$$

Note while s is independent of the unit electrode spacing (such as the ' a ' spacing for the Wenner array) R_E depends on the unit electrode spacing. To avoid this dependency, it is proposed that a normalized geometric factor is used in the calculation of R_E . In this case, the geometric is calculated where the electrode distances are divided by the unit electrode spacing. If a finite-difference or finite-element mesh with 4 nodes between adjacent electrode positions is used, it is found that using an upper limit of about 5 for R_E is usually sufficient to filter out the offset type of arrays that are likely to give negative calculated apparent resistivity values. If an even finer mesh is used, such as 8 nodes between adjacent electrode spacings, a higher upper limit can be used at the expense of longer calculation times and greater computer memory requirements.

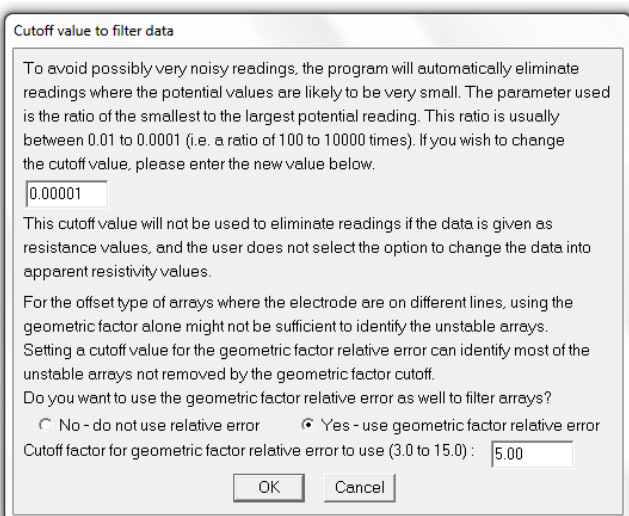
In terms of use in actual field data inversion, the user defined model grid option (probably with the arbitrary electrodes format) is likely to be used with the Res3dinvx64 program. This has the flexibility to adjust the x and y model grid spacings to fit the unit electrode spacing used in the field survey. The model grid spacing should not be larger than the unit electrode spacing used in the survey, and 4 nodes between adjacent model grid lines should be used for the maximum accuracy. To effectively use more than 4 nodes between adjacent electrode positions in the mesh, the user defined grid option allows using a grid spacing that is smaller than the unit electrode spacing. As an example, if a 50 meters electrode spacing was used in the survey, and a model grid with 25 meter spacing is used, the finite-element mesh will effectively have 8 nodes between adjacent electrode positions.

In designing the array configurations for a field survey, the geometric factor as well as geometric factor relative error can be used to avoid arrays that are likely to be unstable. The potential values measured by such unstable arrays are likely to be very small (and thus overwhelmed by telluric noise), or very sensitive to errors in the electrode positions (this could be a significant issue in field surveys in rugged and forested terrains), such that the data measured is not meaningful and does not contribute significantly to resolving the subsurface geology. This should be used to curb extreme field survey designs in an attempt to maximize the data collection speed or coverage. In one data set I have come across, the arrays used have geometric factors ranging from about 800 to 300 million m. Obviously measurements using arrays with very large geometric factors are likely to be too noisy to be useful.

In selecting arrays to be used for field surveys, the following filtering steps are suggested to eliminate arrays that are likely to be unstable.

- 1). Set an upper geometric factor limit, and remove arrays that exceed this limit. Arrays with very large geometric factors will have very low potentials, and thus data from such arrays might be too noisy to be useful. The upper geometric factor will depend on the characteristics of equipment used (maximum current, signal processing features to improve signal-to-noise ratio etc.) and the survey environment. A variation of this is to set a limit of the ratio of the maximum geometric factor to the minimum geometric factor of the arrays in the data set to reflect the dynamic range of signals that can be detected by the instrument.
- 2). Set an upper limit for the geometric factor relative error. This is to eliminate the offset type of arrays that might have a reasonable geometric factors but likely to be unstable. A value of 4 to 10 can be used for most data sets.

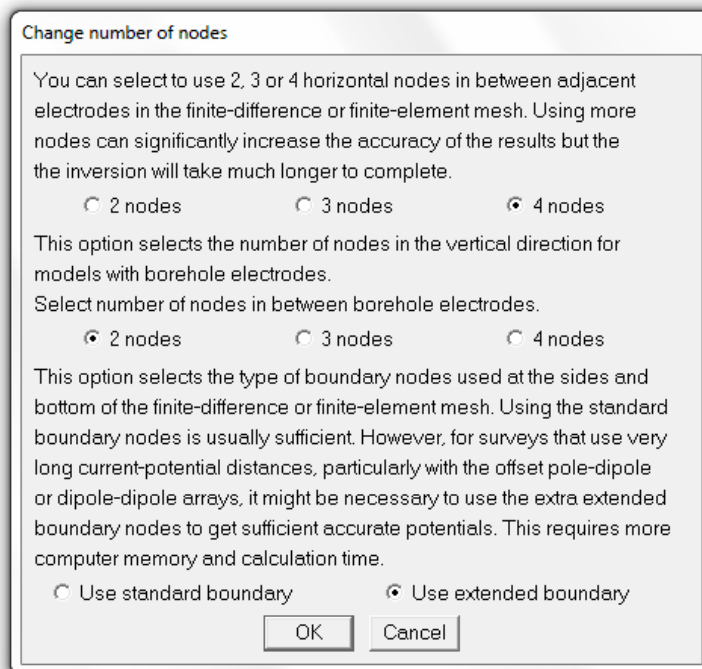
In the Res3dinvx64 program, the above filtering methods are set using the ‘File-Cutoff factor to filter data’ option. The following dialog box is shown on selecting this option.



Setting a value of 0.0001 for the geometric factor cutoff value allows the maximum geometric factor to be 10,000 times the minimum geometric factor in the data points selected. This is probably higher than the dynamic range of most resistivity-meter systems. For the geometric factor relative error, a cutoff value of about 5 seems to work for most data sets.

3). Conduct a homogeneous earth model test using a finite-difference modeling program, such as RES3DMODx64. In this case, calculate the apparent resistivity values for the proposed array configurations for a homogeneous numerical model, such as with a resistivity of 100 ohm.m. In theory, the calculated apparent resistivity values should be the same as the model resistivity value. If the calculated apparent resistivity value differs by more than 20% from the model value, the array is likely to be unstable. In any case, the forward modeling routine used in the inversion cannot provide reasonably accurate apparent resistivity values for such arrays, so a numerical interpretation is not viable using such data points.

In relation to this, some of the offset type of arrays used in 3-D surveys also use very long distances between the current electrodes and potential dipole. This results in arrays with very low potentials which are particularly sensitive to the boundary conditions used in the finite-difference or finite-element forward modeling routine. In some cases, the small inaccuracies in the boundary conditions can cause a net negative potential to be calculated which in turn results in negative apparent resistivity values. One method to reduce the small errors in the boundary conditions is to use more buffer nodes near the edges of the mesh used. In the Res3dinvx64 program, this is selected using the ‘Change Settings – Forward Modeling Settings – Change number of nodes’ option that brings up the dialog box shown below.



Using an extended boundary increases the number of nodes in the mesh, and thus increases the computer time and memory required for the inversion of the data set. To satisfy these requirements, a multi-core CPU and 64-bit system is required.

8.12 Not on firm foundations – inversion with shifting electrodes in 2-D and 3-D

It is implicitly assumed that the positions of the electrodes used in 2-D or 3-D surveys are accurately known when interpreting the data set. In recent years, there has been significant developments in geoelectrical monitoring surveys to detect temporal changes in the subsurface (Chambers *et al.*, 2014; Perrone *et al.*, 2014), such as mapping of gas flows

from landfills (Loke *et al.*, 2014a) and the monitoring of unstable slopes (Supper *et al.*, 2014). The measurements are repeated a number of times using the same set of electrodes. The electrode positions are measured at the start of the campaign and possibly also at regular intervals. However, ground movements sometimes occur between the times of electrode positions measurements. Thus the electrode positions might not be accurately known for some data sets, making it necessary to determine the shifts in the electrode positions from the resistivity data itself (Wilkinson *et al.*, 2015). A method was presented by Kim (2014) where both the subsurface resistivity and electrodes positions are unknown variables to be determined by the least-squares optimization method. The least-squares optimization equation (for a 2-D problem) is modified to the following form.

$$[\mathbf{G}_i^T \mathbf{R}_d \mathbf{G}_i + \lambda_i \mathbf{V}^T \mathbf{R}_m \mathbf{V}] \Delta \mathbf{q}_i = \mathbf{G}_i^T \mathbf{R}_d \mathbf{g}_i - \lambda_i \mathbf{V}^T \mathbf{R}_m \mathbf{V} \mathbf{q}_{i-1} \quad (8.4)$$

$$\text{where } \mathbf{q} = \begin{pmatrix} \mathbf{r} \\ \mathbf{x} \\ \mathbf{z} \end{pmatrix}, \mathbf{G} = \begin{pmatrix} \mathbf{J} \\ \mathbf{X} \\ \mathbf{Z} \end{pmatrix}, \mathbf{V} = \begin{pmatrix} \mathbf{W} \\ \alpha \mathbf{W}_x \\ \beta \mathbf{W}_z \end{pmatrix}.$$

The combined Jacobian matrix \mathbf{G} consists of \mathbf{J} (the model resistivity sensitivity values), \mathbf{X} and \mathbf{Z} (the sensitivity values for the changes in the x and z electrode positions) matrices. λ is a damping factor vector and \mathbf{g} is the data misfit vector. \mathbf{q} is the model parameters vector consisting of \mathbf{r} (model resistivity) and \mathbf{x} and \mathbf{z} (electrode position) vectors. $\Delta \mathbf{q}_i$ is the change in the model parameters. \mathbf{W} is the resistivity spatial roughness filter term. \mathbf{W}_x and \mathbf{W}_z are the roughness filters for the electrode position vectors. \mathbf{R}_d and \mathbf{R}_m are weighting matrices used by the L1-norm inversion method (Loke *et al.*, 2003). α and β are the relative damping factor weights for the shifts in the electrode positions.

Kim (2014) used the perturbation method (McGillivray and Oldenburg, 1990) to calculate the spatial Jacobian matrices \mathbf{X} and \mathbf{Z} . For a survey line with e electrodes it will be necessary to recalculate the potentials by resolving the finite-element capacitance matrix equation $2e$ times. While this is possible for 2-D problems, it becomes impractical for 3-D problems where the forward modeling routine is about two to three orders of magnitude slower. Furthermore, it is necessary to calculate the partial derivatives in 3 directions (x, y, z). A much faster method using a modification of the adjoint-equation approach (McGillivray and Oldenburg, 1990) to calculate the \mathbf{X} and \mathbf{Z} Jacobian matrices is described in Loke *et al.* (2015c). For 3-D problems, the adjoint-equation method is one to two orders of magnitude faster than the perturbation method. For 3-D problems, it is probably three orders of magnitude faster. A very large value of the spatial damping factors (α and β) of about 100 was also used by Kim (2014) to reduce distortions in the electrode positions caused by near-surface resistivity variations. However, it was found that using such large values for the α and β damping factors tend to reduce the accuracy of the recovered electrode positions as well (Loke *et al.*, 2015c).

A homogeneous half space is commonly used as the starting model for the optimization algorithm. In a time-lapse survey the initial positions of the electrodes are usually accurately measured, and can be treated as fixed parameters in the inversion of the initial data set. The temporal changes in the subsurface resistivity are usually much less than the spatial variations (Loke *et al.*, 2014a). Thus the inversion model of the initial data set provides a good starting model for the later time data sets. Loke *et al.* (2015c) modified the inversion algorithm to use the model from a previous survey as the starting model which essentially eliminated distortions in recovered positions of the x and z electrodes caused by near-surface resistivity variations. Figure 131 shows a synthetic 2-D model used to illustrate the effect of shifts in the electrode positions without the need to use large values for the spatial damping factors. The initial model has 31 electrode positions with a uniform 1 m

spacing on a flat surface (Figure 131a). Figure 131b shows the perturbed model with four changes. The electrode at the 5.0 m mark is shifted 0.3 m. to the right. The electrode at the 17.0 m mark is shifted 0.4 m. upwards. A 70 ohm.m prism (depth of 1.0 m to the top) is added between the two existing prisms, and the 20 ohm.m low resistivity prism is extended downwards by 0.73 m. The measured data consists of dipole-dipole arrays with the '*a*' dipole lengths ranging from 1 to 4 m., and the '*n*' factor ranging from 1 to 6. This gives a total of 415 data points. Gaussian random noise (Zhou and Dahlin, 2003) with a mean amplitude of 2.5 milliohm was added to the data before they were converted to apparent resistivity values. The average noise level for the data set is about 1.0%. Figure 131b shows the inversion models obtained assuming the electrodes are equally spaced on a flat surface. The model for the perturbed data set has significant distortions (Figure 131b) below the electrode at the 5m mark which has shifted horizontally, as well as below the 17 m mark that has shifted vertically. Figure 131c shows the inversion model obtained when the electrodes are allowed to shift. The model obtained from the inversion of the initial data set shown in Figure 131a was used as the starting model. The distortions in the model have been removed and the data misfit of 1.0% is close to the noise added. Note the upwards shift in the electrode at the 17 m mark that matches shift in the synthetic model. In this inversion the spatial relative damping factors α and β were set at 1.0.

Figure 132 shows a 3-D example with shifted electrodes. The synthetic model has two blocks of 20 and 400 ohm.m in a 100 ohm.m medium below a survey grid with 17 by 15 electrodes at 1 m apart. The electrode at (x,y) location of (2,2) was were shifted 0.3 m horizontally in the x-direction, while the electrode at (10,4) was shifted 0.3 m in the y-direction. The electrode at (12,12) was shifted upwards by 0.4 m. The model with fixed electrodes shows artifacts at the positions of the shifted electrodes in the top two layers (Figure 132a) which are removed in the model where the electrodes are allowed to move (Figure 132b) during the data inversion.

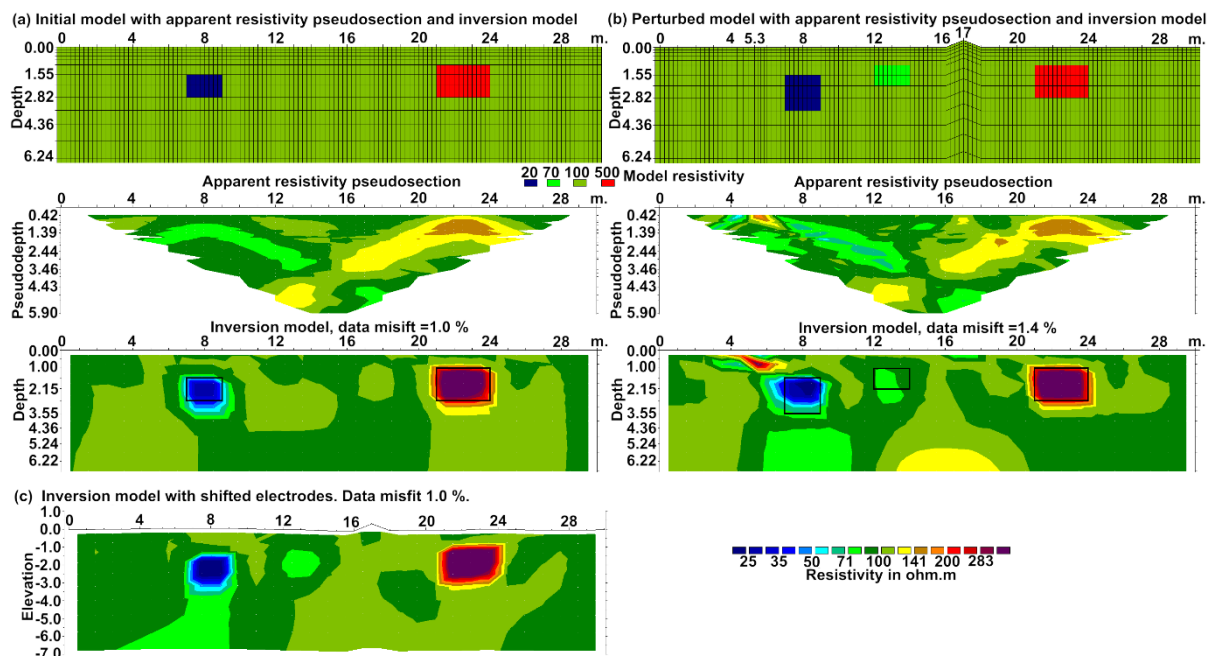


Figure 131. The (a) initial and (b) perturbed synthetic test models with apparent resistivity pseudosections and inversion models assuming a constant electrode spacing and flat surface. (c) The inversion model obtained with the algorithm that allows the electrodes to shift.

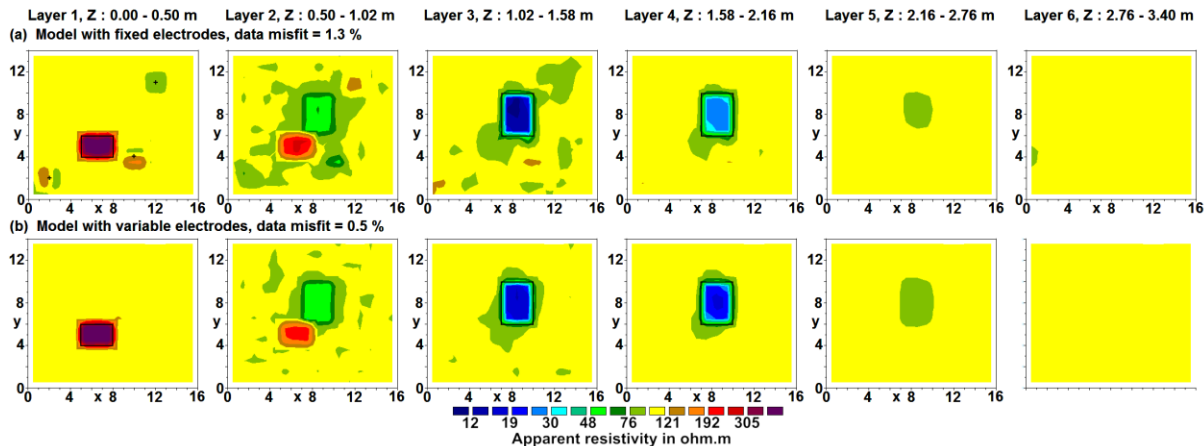


Figure 132. Example of electrode shifts in a 3-D model. (a) Inversion model with fixed electrodes. The shifted electrodes are marked by small black cross in the top layer. (b) Inversion model where electrodes are allowed to shift.

8.13 Examples of 3-D field surveys

In this section, we will take a look at the results from a couple of 3-D field surveys over areas with complex geology.

8.13.1 Birmingham field test survey - U.K.

This field test was carried out using a multi-electrode system with 50 electrodes commonly used for 2-D resistivity surveys. The electrodes are arranged in a 7 by 7 grid with a unit spacing of 0.5 meter between adjacent electrodes (Figure 133a). The two remote electrodes were placed at more than 25 meters from the grid to reduce their effects on the measured apparent resistivity values. To reduce the survey time, the cross-diagonal survey technique was used. The subsurface is known to be highly inhomogenous consisting of sands and gravels. Figure 133b shows the horizontal sections of the model obtained at the 6th iteration. The two high resistivity zones in the upper left quadrant and the lower right corner of Layer 2 are probably gravel beds. The two low resistivity linear features at the lower edge of Layer 1 are due to roots from a large sycamore tree just outside the survey area. The vertical extent of the gravel bed is more clearly shown in the vertical cross-sections across the model (Figure 133c). The inverse model shows that the subsurface resistivity distribution in this area is highly inhomogenous and can change rapidly within a short distance. In such a situation a simpler 2-D resistivity model (and certainly a 1-D model from conventional sounding surveys) would probably not be sufficiently accurate. This is a rather small data set with 468 data points and 324 model cells where the inversion on a modern PC with a hex-core CPU took just 10 seconds!

Figure 134 shows the use of the L-curve method (Farquharson and Oldenburg, 2004) to estimate the optimum damping factor (section 1.4) in the inversion of this data set. The L-curve method estimates the data misfit and model roughness for a large range of damping factor values such as starting from one-hundredth to 100 times a trial value. The shape of the curve obtained by plotting the model roughness versus the data misfit usually has an 'L' shape with a distinct corner (Figure 134a). The damping factor value that corresponds to the maximum curvature point of this curve is then chosen as the optimum damping factor value (Figure 134b).

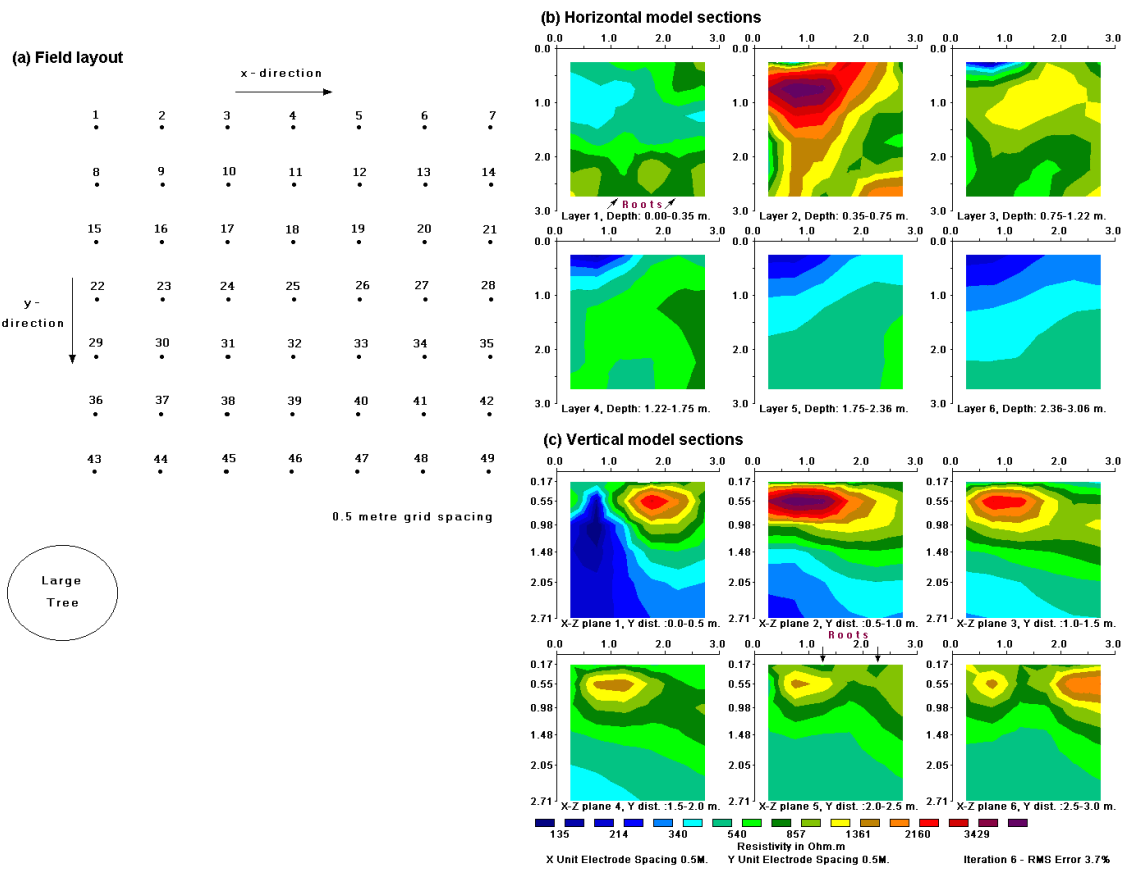


Figure 133. (a) Arrangement of electrodes in the Birmingham 3-D field survey. (b) Horizontal and (c) vertical cross-sections of the model obtained from the inversion of the Birmingham field survey data set. The locations of observed tree roots on the ground surface are also shown.

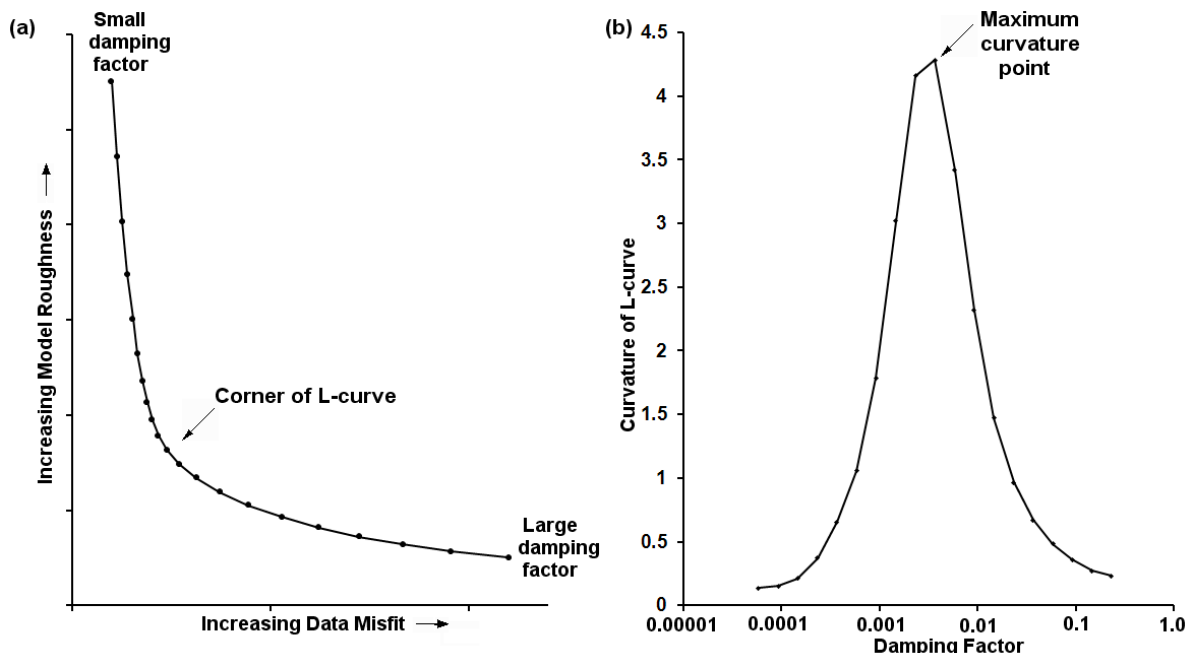


Figure 134. Example L-curve plots. (a) A plot of the model roughness versus the data misfit

for the Birmingham survey data set for a number of damping factor values. (b) A plot of the curvature of the curve in (a) for the different damping factor values. The ‘optimum’ damping factor is at the maximum curvature point.

8.13.2 Sludge deposit - Sweden

This survey covers a 21 by 17 grid by using a 3-D roll-along method (Dahlin and Bernstone, 1997). To reduce the survey time, a number of parallel multi-electrode cables were used (Figure 122). This survey was carried out at Lernacken in Southern Sweden over a closed sludge deposit. Seven parallel multi-electrode cables were used to cover a 21 by 17 grid with a 5 meters spacing between adjacent electrodes. There were a total number of 3840 data points in this data set.

The maximum spacing is chosen so that the survey will map structures to the maximum depth of interest (section 2.5.2). In this case, the maximum spacing was 40 meters compared to the total length of 100 meters along a line in the x-direction. In this survey, the cables were initially laid out in the x -direction, and measurements were made in the x -direction. After each set of measurements, the cables were shifted step by step in the y -direction until the end of the grid. In surveys with large grids, such as in this example, it is common to limit the maximum spacing for the measurements.

The model obtained from the inversion of this data set is shown in Figure 135. The former sludge ponds containing highly contaminated ground water show up as low resistivity zones in the top two layers (Dahlin and Bernstone, 1997). This was confirmed by chemical analysis of samples. The low resistivity areas in the bottom two layers are due to saline water from a nearby sea. Figure 136 shows a 3-D view of the inversion model using the Slicer-Dicer 3-D contouring program.

An interesting more recent 3-D survey over a landfill site is described in Chambers et al (2006).

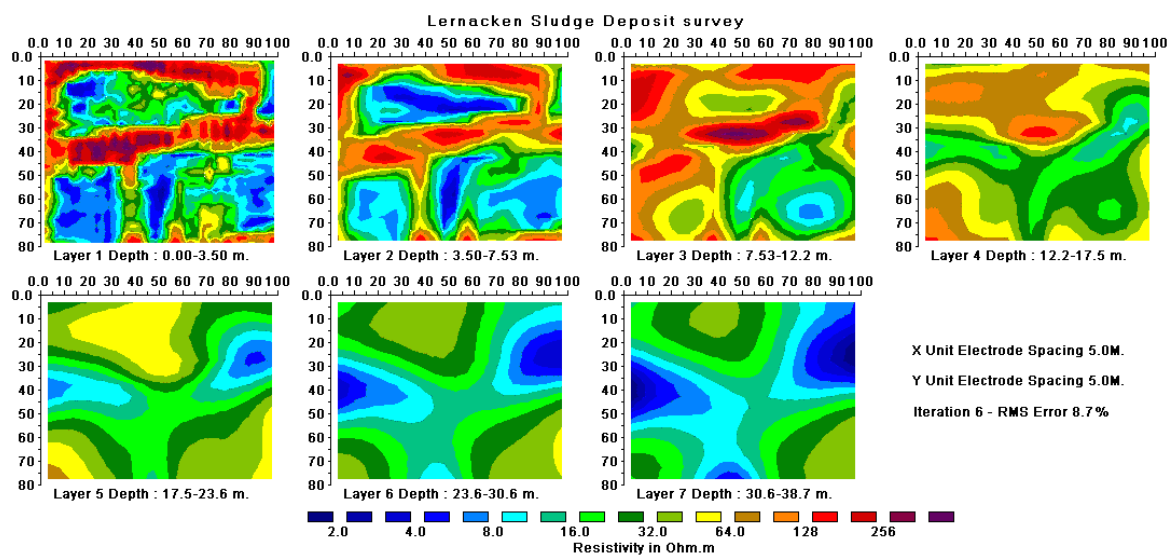


Figure 135. The 3-D model obtained from the inversion of the Lernacken Sludge deposit survey data set displayed as horizontal slices through the earth.

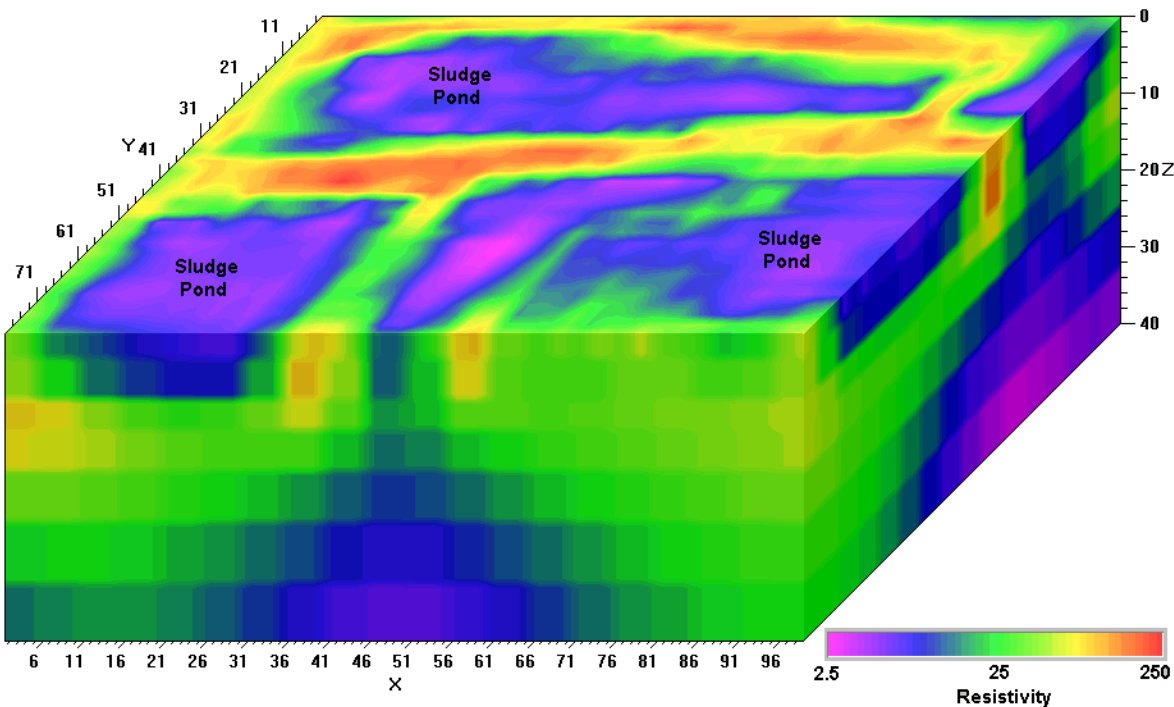


Figure 136. A 3-D view of the model obtained from the inversion of the Lernacken Sludge deposit survey data set displayed with the Slicer/Dicer program. A vertical exaggeration factor of 2 is used in the display to highlight the sludge ponds. Note that the color contour intervals are arranged in a logarithmic manner with respect to the resistivity.

8.13.3 Aquatic survey - Panama

This is an unusual example from an aquatic survey along the Panama Canal (Figure 137). Dredging of the canal is necessary to expand it to accommodate larger vessels. The cost of the dredging greatly depends on the nature of sub-bottom sediments and bedrock. A detailed aquatic survey was thus conducted to determine the nature of the sediments and bedrock. This survey was conducted using a streamer cable pulled behind a boat (Noonan and Rucker, 2011; Rucker and Noonan, 2013). A series of quasi-parallel 2-D surveys lines were used that were nominally spaced 25 meters apart. The dipole-dipole array with an electrode spacing of 15 meters and a total cable length of 170 meters was used. This arrangement gave a depth of investigation of up to about 25 meters. The water depth was about 15 to 17 meters. The survey was conducted along several lines running along the axis of the canal. Auxiliary data such as GPS, water bathymetry and resistivity were also measured during the survey. Unlike land surveys, it is not possible to keep the lines straight in a mobile aquatic survey. One section of the survey area with the 2-D lines is shown in Figure 138. Thus conventional 2-D inversion of each individual line did not give sufficiently accurate results, as a 2-D model assumes that the line is straight. Furthermore, a 2-D model assumes that the geological structures are 2-D and the line is perpendicular to the strike of the structures. The data from the different 2-D lines were then collated into a single 3-D data file. The arbitrary electrodes data format (section 8.9) was used to accommodate the non-regular arrangement of lines. As there is usually an abrupt change in the resistivity between the water and the sub-bottom materials, a sharp boundary corresponding to the water bottom at a depth of about 15 to 17 meters was added and the resistivity of the first layer (corresponding to the water column) was set at 67 ohm.m. The inversion model shows significant variations in the sub-bottom materials (the last 3 sections in Figure 139). The lowest resistivity material generally corresponds to moderately soft tuff, intermediate resistivity to moderately hard agglomerate

and high resistivity to hard andesite (Noonan and Rucker, 2011). Overall, the results of the 3-D inversion model agreed more closely with the known geology from drill-cores than individual 2-D inversion models. The example in Figure 139 has 13655 data points and 6006 model cells. The inversion of this medium sized data set took about 13 minutes on a PC with an Intel i7 970 hex-core CPU and 24GB RAM.

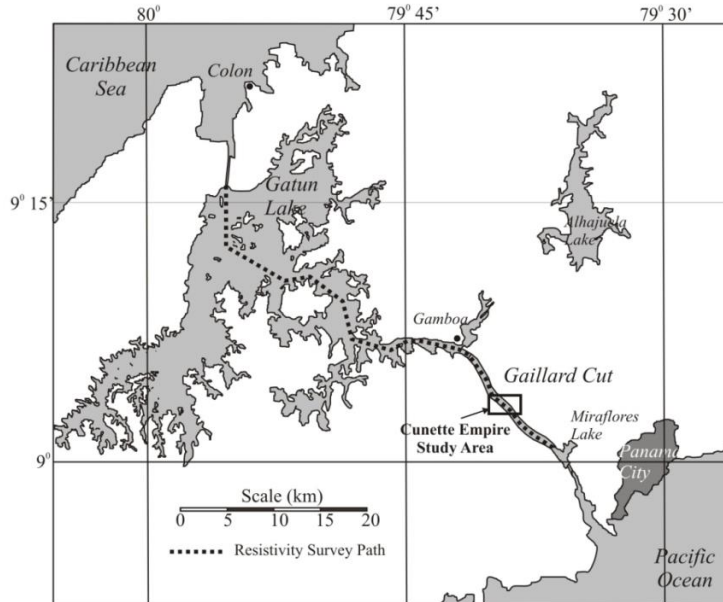


Figure 137. Map of the Panama Canal region with the survey area marked (Noonan and Rucker, 2011).

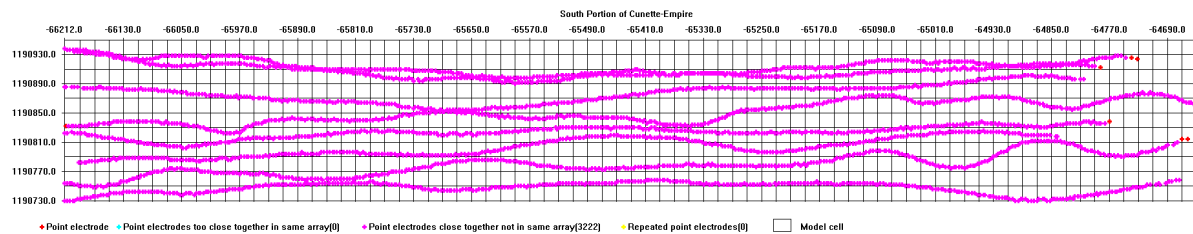


Figure 138. The model grid used for the Panama Canal floating electrodes survey with 20 by 20 meters cells. The location of the electrodes along the surveys lines are shown as colored points.

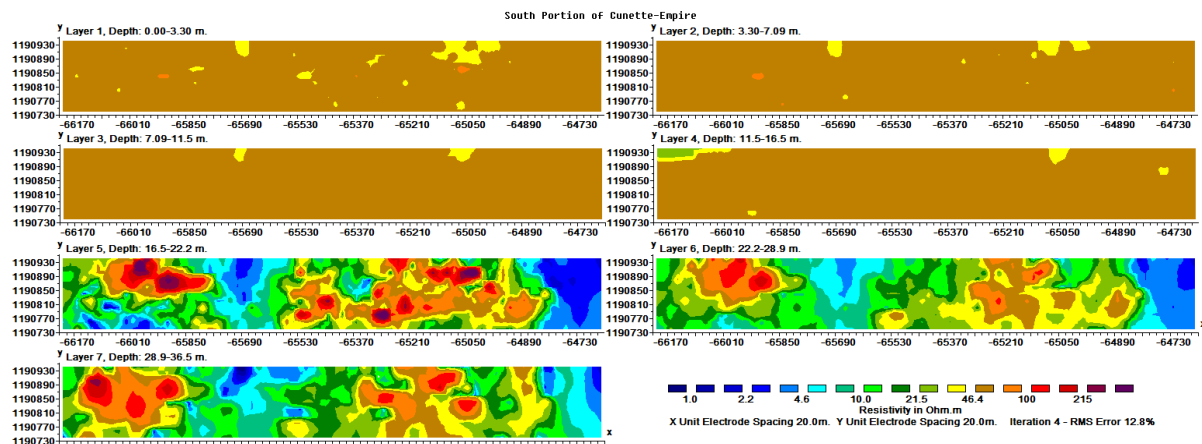


Figure 139. The inversion model for the Panama Canal floating electrodes survey. The first 4 layers correspond to the water column.

8.13.4 Copper Hill - Australia

This is an interesting example of a 3-D resistivity and IP survey provided by Arctan Services Pty. and Golden Cross Resources, Australia. Copper Hill is the oldest copper mine in NSW, Australia. An earlier survey was conducted in 1966 using mapping, rock chip sampling, an I.P. survey and 7 drill-holes (Chivas and Nutter, 1975; White *et al.*, 2001). Copper porphyry with minor gold and palladium mineralization were found to occur in structurally controlled fractures and quartz veins. However, due to the very complex geology (Figure 140), large differences in ore grades were found in drill-holes that were less than 200 meters apart. To map the ore deposit more accurately, a new 3-D resistivity and I.P. survey using the offset pole-dipole array was used. The survey covered a large (1.6 x 1.1km) area using a series of 1.6 km lines with a spacing of 25m between adjacent electrodes. Figure 141 shows the arrangement of the transmitter and receiver lines. Currents of up to 7 Amps were used. The entire survey took 10 days giving a total of over 7000 measurements. Further details about the survey layout and procedures used to improve the data quality as well as to reduce the survey time are described in the paper by White *et al.* (2001). Other interesting information about the mineralization at the Copper Hill area is available at the Golden Cross Resources Ltd. web site www.reflections.com.au/GoldenCross/.

The data was inverted with the RES3DINV program that produced a 3-D resistivity and I.P. model for the area. The 3-D I.P. model that shows the location of the mineralized zones more clearly is shown in Figure 142. The inversion model output from the RES3DINV program was rearranged into a VRML format that could be read by a 3-D visualization program (please contact Arctan Services for the details) that enables the user to display the model from any direction.

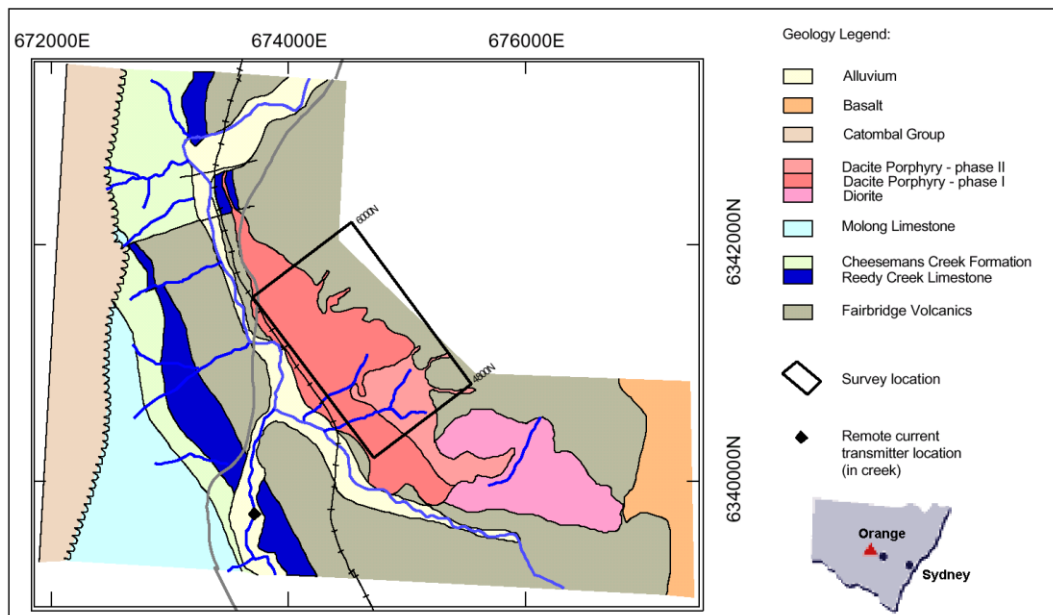


Figure 140. Geological map of the Copper Hill area (White *et al.* 2001).

The 3-D I.P. model in Figure 142 shows two en-echelon north-south trends and two approximately east-west trends forming an annular zone of high chargeability. The results from existing drill-holes that had targeted the shallower part of the western zone agree well with the resistivity and IP model. A drill-hole, CHRC58, intersected a 217m zone with 1.7 g/t gold and 0.72% copper coincided well with an IP zone of greater than 35mV/V. The lower boundary of the western zone with high chargeability coincides well with low assay results from existing drill-holes. The eastern zone with high chargeability and resistivity values do

not outcrop on the surface and very little drilling has penetrated it. Further surveys, including drilling, is presently being carried out.

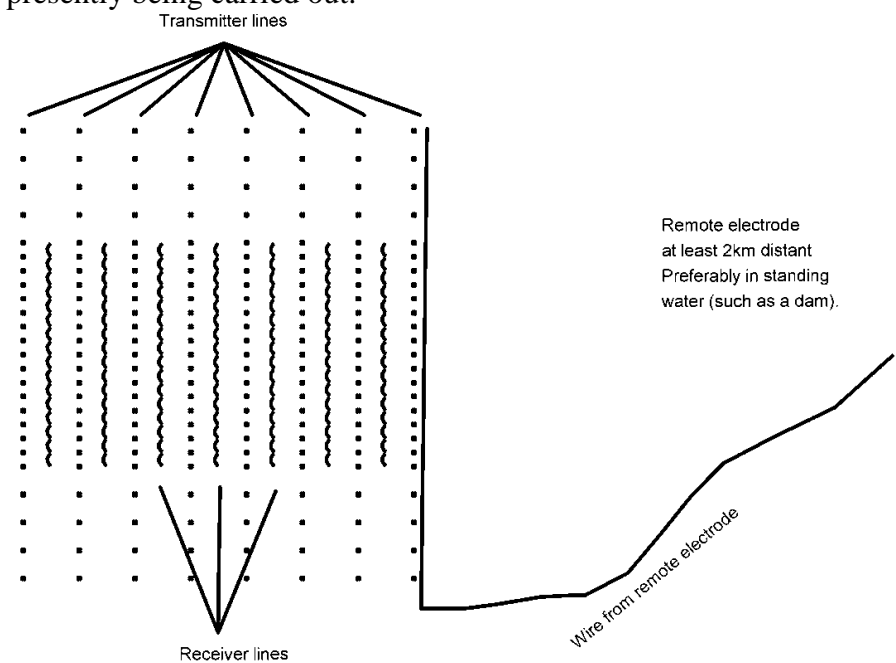


Figure 141. Electrodes layout used for the 3-D survey of the Copper Hill area.

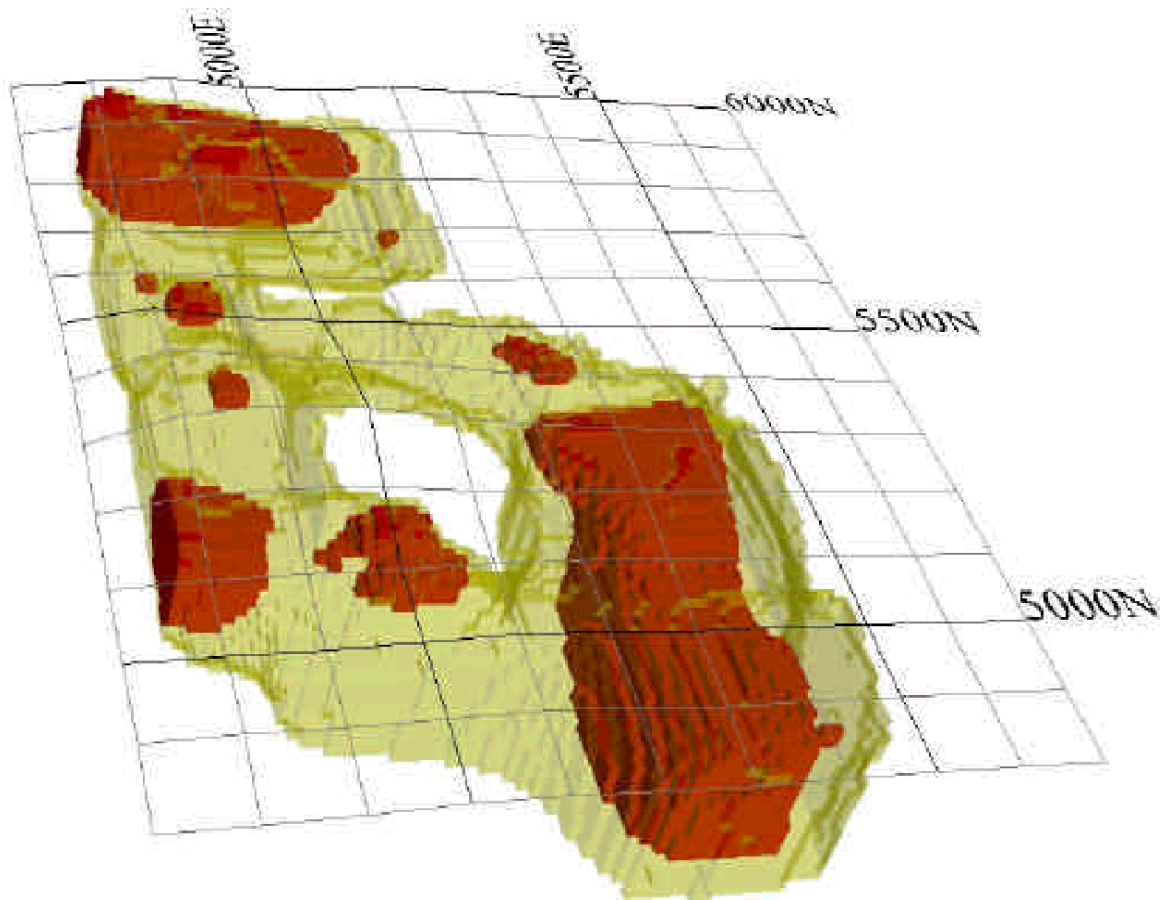


Figure 142. The I.P. model obtained from the inversion of the Copper Hill survey data set. Yellow areas have chargeability values of greater than 35 mV/V, while red areas have chargeability values of greater than 45 mV/V (White *et al.*, 2001).

8.13.5 Athabasca Basin – Canada

The Athabasca basin in northern Saskatchewan (Figure 143) has over 30 deposits and it is the richest uranium region in the world. It produces about 21% of the world's uranium (Raemakers *et al.*, 2006). The uranium ore is typically found in sandstones overlying metamorphic basement where it fills reactivated fault zones. The objective of the survey is to detect the low resistivity alteration zone associated with the uranium deposit (Figure 144). The survey area is a challenging environment with dry surface sand with a very thin humus layer that makes good electrical contact difficult. With temperatures of minus 40°C in winter, laying out long survey lines to achieve the required depth penetration of more than 500 meters require tremendous efforts. The example in this section comes from Bingham *et al.* (2006) where some interesting choices were made in the survey design. The pole-pole array was used to reach the required depth of penetration with the limited survey line lengths that were available. While the pole-pole array has the poorest resolution (for depths within reach of the other arrays), here it is choice between POOR resolution or NO resolution at depths of up to 700 m. Figure 145 shows an example of one of the survey results for the resistivity at a depth of about 200 meters. A 3-D data set was constructed by collating data from parallel 2-D survey lines. The inversion model shows a prominent narrow low resistivity zone that corresponds to the alteration zone.

The advantages and disadvantages of the pole-pole array is a matter of some debate, particularly for deep surveys. Besides deep uranium surveys, it has also been used for other mineral surveys by some companies (see for example the www.geofisicos.com.pe web site). While there are many advocates of this array, others point out to its poor resolution compared to other arrays (assuming these arrays used a sufficient long survey line to get the same penetration depth). The pole-pole array offers field advantages of much shorter measurement arrays and the ability to penetrate deeper than any other array for the same survey line length, although there is the extra effort of maintaining two infinites (David Bingham, pers. comm., 2009). The pole-dipole array has also been used for uranium exploration in the Athabasca basin, and the 2-D and 3-D resistivity surveys played a significant role in the discovery of a very large deposit (Donald Carriere, pers. comm., 2009) at Wheeler River near the existing McArthur River deposit.

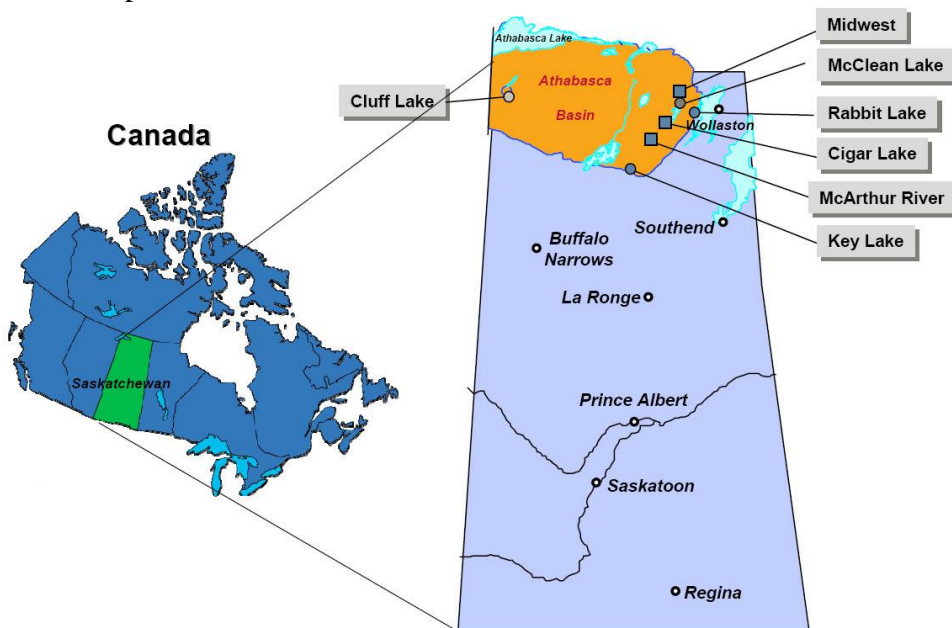


Figure 143. Location of uranium mines in the Athabasca basin, Saskatchewan (Bingham *et al.*, 2006).

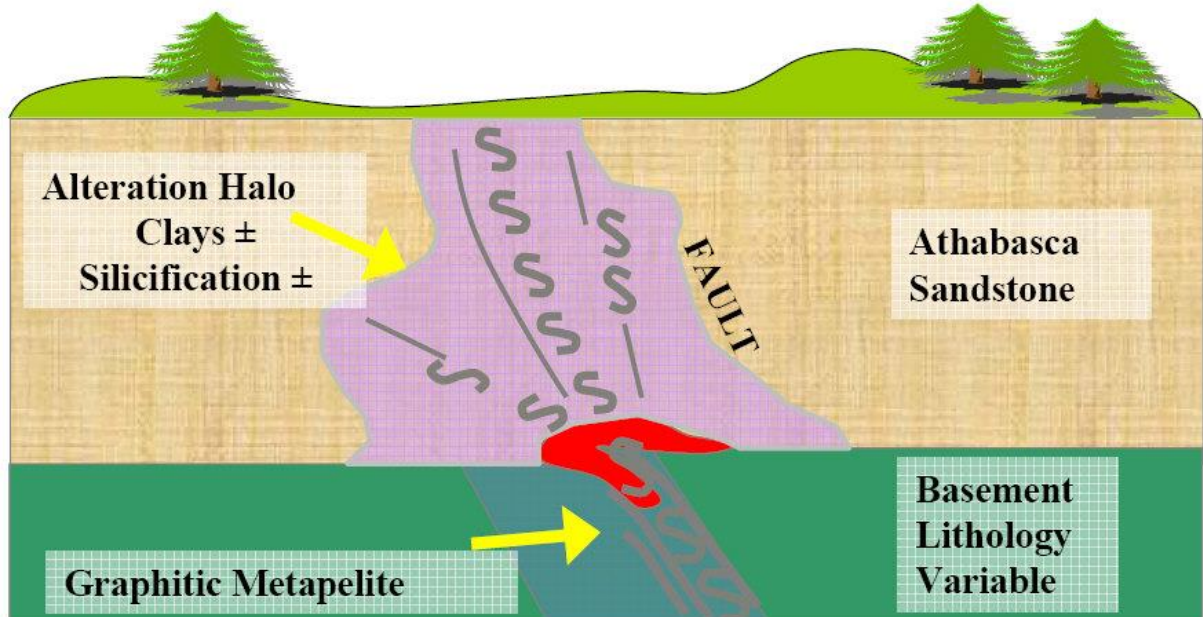


Figure 144. Geological model of uranium deposit (Bingham *et al.*, 2006).

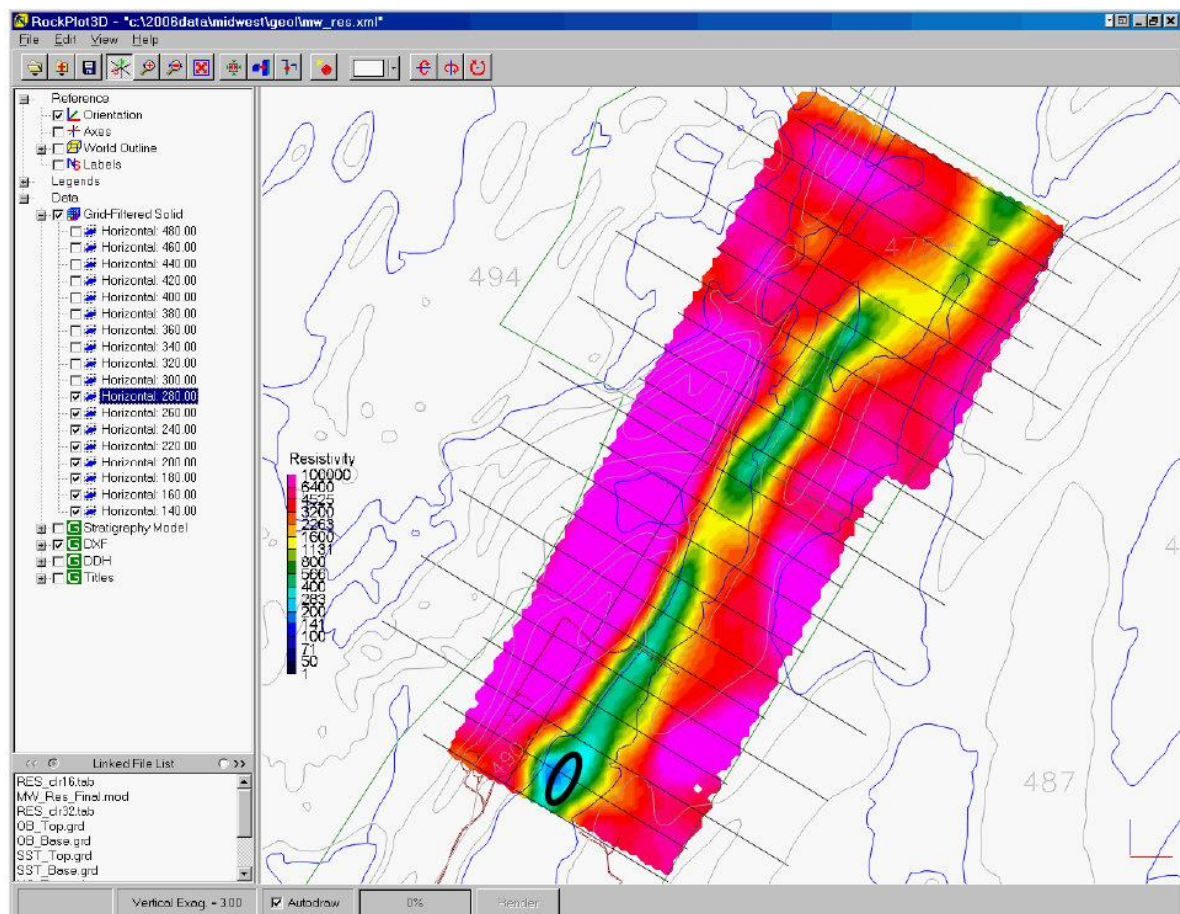


Figure 145. Example of inversion model from the Midwest deposit area showing the resistivity at a depth of about 200 meters (Bingham *et al.*, 2006).

8.13.6 Cripple Creek and Victor Gold Mine, Colorado – USA

This example illustrates the tremendous progress made in the resistivity method over the last 25 years, for simple 1-D models to 3-D models with complex variations in both space and time (Loke *et al.*, 2014a) using an unusual electrode layout. The survey was made during a secondary recovery of gold operation by injecting sodium cyanide solution into ore rock piles after surface leaching had ceased at the Cripple Creek and Victor Gold Mine in Colorado, USA (Figure 146a) in September 2011 (Rucker *et al.*, 2014). Resistivity measurements were made to monitor the flow of the solution so as to optimize gold recovery. The measurements were made using 48 electrodes on the ground surface arranged in a radial pattern (Figure 146b), 94 electrodes along six boreholes and 8 long electrodes using steel-case injection wells (Rucker *et al.*, 2014). Each snapshot took 14 minutes to complete, and a total of 780 snapshots were acquired. The positions of the electrodes together with the surface topography are shown in Figure 146c. Due to the use of a radial layout, the data coverage is very sparse towards the edges of the model grid (Figure 146b). As the resistivity distribution within the ore heap is highly inhomogeneous, the change in the resistivity is used to monitor the flow of the solution.

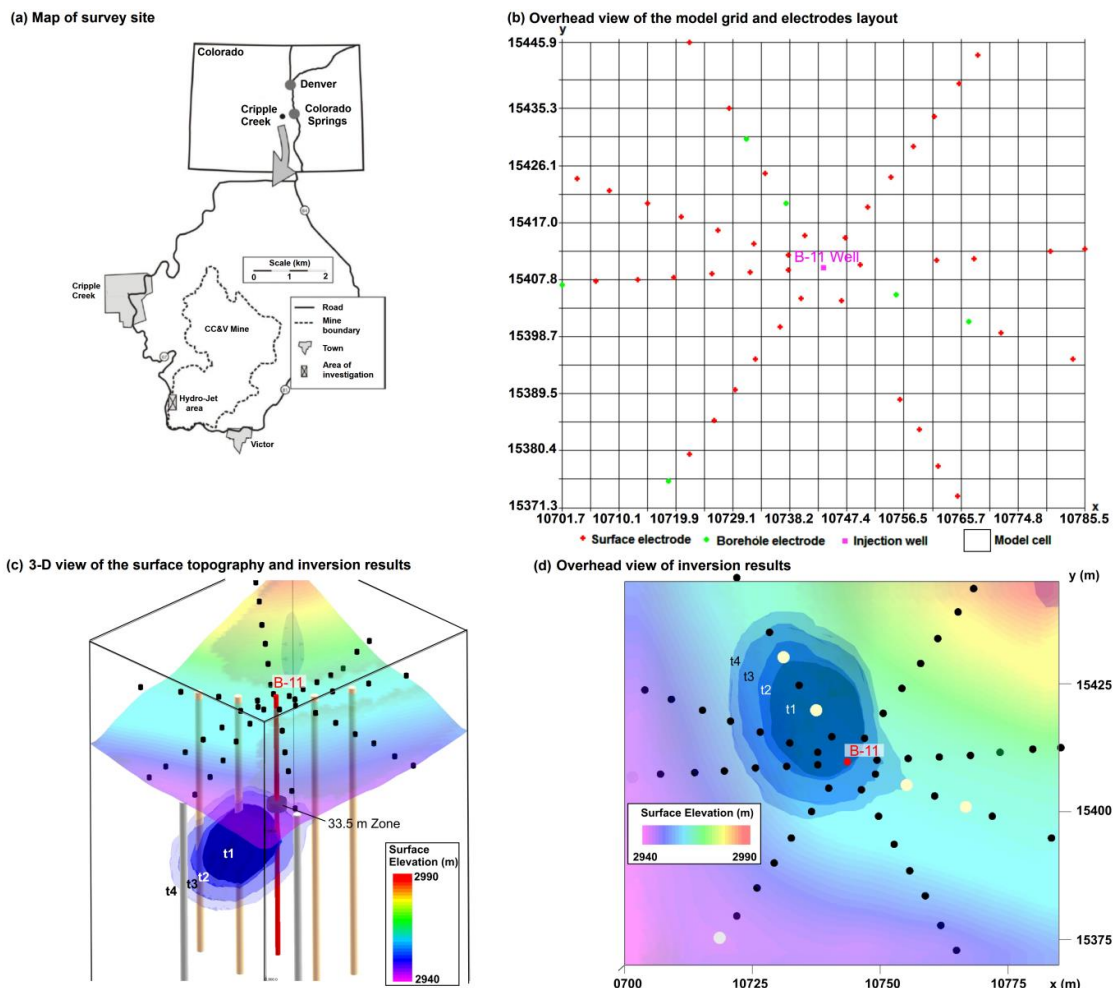


Figure 146. A complex time-lapse field survey example. (a) Map of Cripple Creek survey site. (b) Overhead view of the inversion model grid with electrodes layout. (c) Iso-surface contours for the -4% resistivity change at different times after the injection of the sodium cyanide solution (that started at 2.8 hours from the first data set in snapshots used). $t_1 = 1.1$ hours, $t_2 = 2.4$ hours, $t_3 = 3.7$ hours, $t_4 = 4.9$ hours. (d) Overhead view of iso-surfaces.

Figure 146c,d shows the results from one series of measurements in the form of iso-surface contours for the -4% change in the resistivity at different times. Note the area with the largest change is located to the north of the well. This is probably due to differences in the subsurface permeability and structural nonuniformities within the heap created during end-dump construction (Rucker *et al.*, 2014). The heap was built up over the past 20 years by trucks dumping fresh ore over the edge of older ore.

8.13.7 Burra copper deposit, South Australia : Model reliability determination

This example is used to illustrate different methods of determining model reliability. The Burra copper deposit in South Australia (Figure 147a) was discovered in 1845 and mining started in 1848 and ceased in 1877. It was at one time the largest copper mine in Australia. It was reopened in 1971 and closed again in 1981. The primary ore is probably chalcopyrite, with significant amounts of malachite, azurite, cuprite, chrysocolla and native copper. Figure 147c shows some of the lines from a 1966 I.P. survey. Because of urban development and consequent restricted access for any new survey lines, a re-interpretation of the data was carried using modern 3-D inversion methods to glean more information from it (Loke *et al.*, 2013b). There is highly uneven data coverage. A model with a uniform grid using 50x50 meter cells (in the x-y directions) is used (Figure 147c).

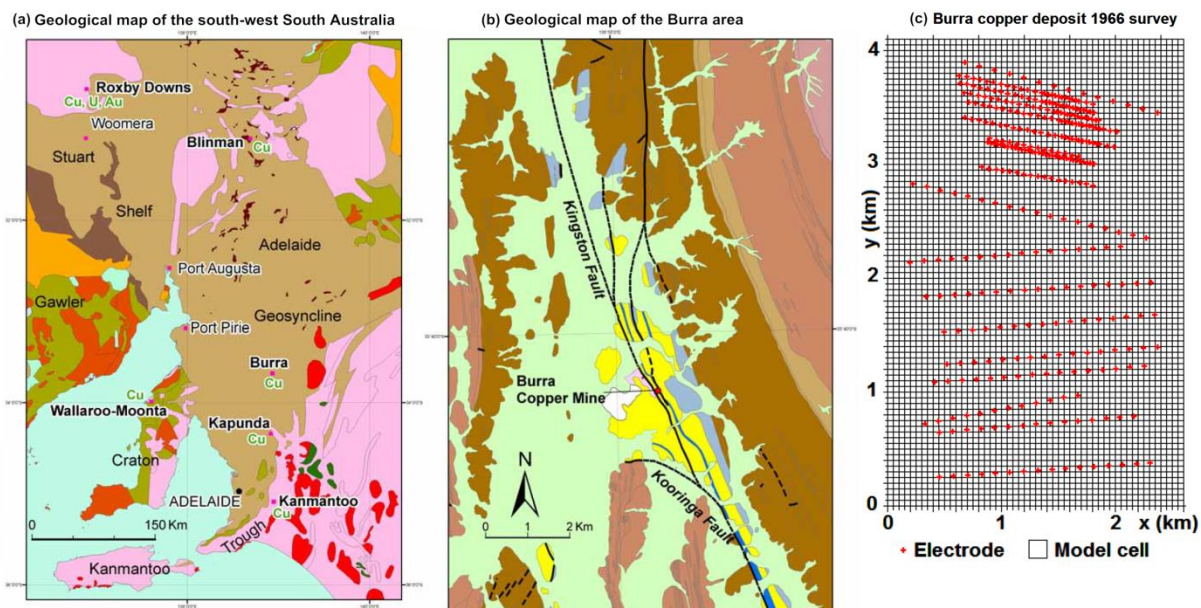


Figure 147. Geological map of (a) south-west South Australia, (b) the Burra area, and (c) a plot of survey electrodes and model cells layout.

The resistivity model (Figure 148a) shows a prominent north-south low resistivity linear feature near the 1.8 km mark (*x*-axis) that corresponds to the Kingston Fault. The I.P. anomaly (Figure 148b) in the northern part of the fault zone at depths of 100 to 200 meters corresponds to the Eagle deposit prospect. The nature of the I.P. anomaly towards the bottom-left edge of the deeper layers is uncertain as there is not much data coverage there. However it lies in the Kingston Fault zone (Figure 147b) with reports of pyrites in a nearby bore.

Figure 149 show plots of the model resolution calculated using the resistivity and I.P. Jacobian matrices, and the VOI using the model resistivity values. If a cutoff value of about 50 is used for the resistivity resolution index (Figure 149a), the maximum depth of

investigation is about 200 m. Not surprisingly, the highest resolution values are concentrated near the survey lines, particularly around the group of shorter spacing lines in the northern third of the survey area. This pattern is more pronounced in the I.P. resolution plots (Figure 149b). The I.P. resolution sections have a shallower maximum depth of investigation than the resistivity sections. This was confirmed by similar calculations for synthetic models with more uniform data coverage. The VOI sections give a maximum depth of investigation of about 200 m. in the southern half of the area below the longer survey lines (Figure 149c). The VOI plot show a more complex pattern with local artefacts at several places and does not always increase monotonically with depth (Figure 150c). The I.P. anomaly in the northern half of the survey area lie in a region with higher resolution (and generally low VOI) values, so it is likely to be real. The southern I.P. anomaly lie in a region with low resolution (and high VOI) values, so its nature from the data alone is uncertain without independent confirmation.

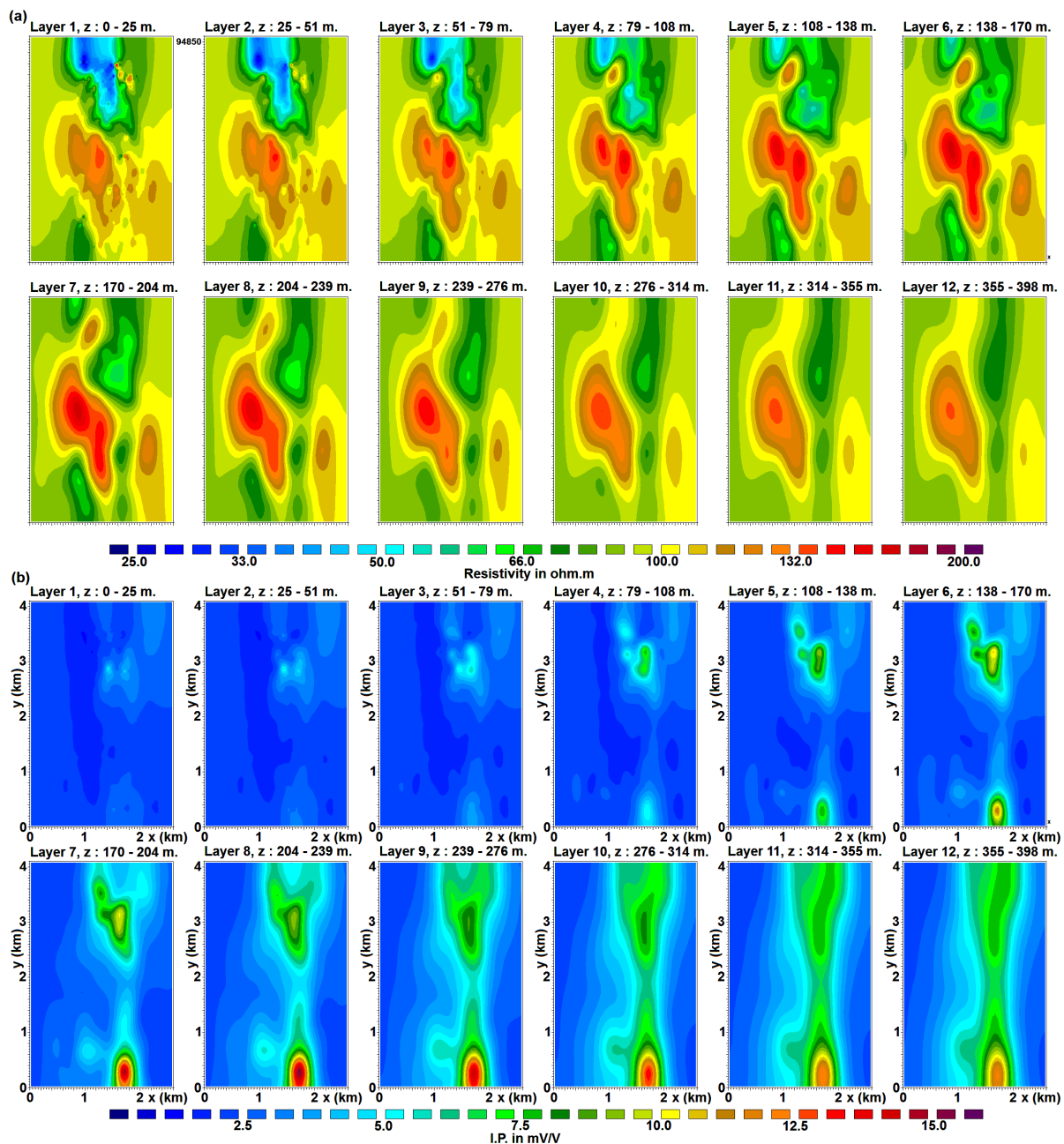


Figure 148. Burra survey (a) resistivity and (b) I.P. inversion model layers.

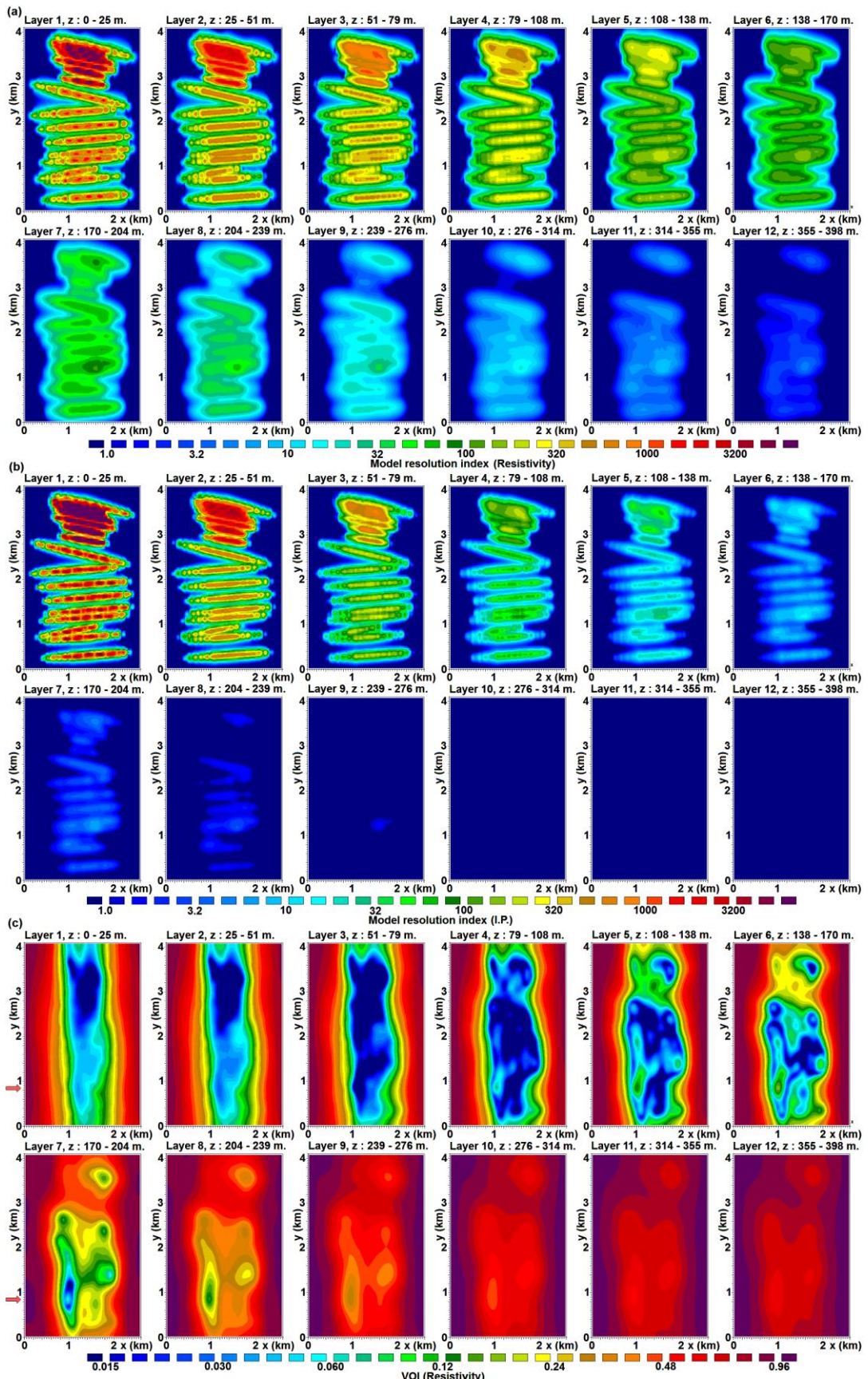


Figure 149. The model (a) resistivity and (b) I.P. resolution index, and (c) VOI values. The red arrows at the left side of (c) shows the position of the vertical slice shown in Figure 150.

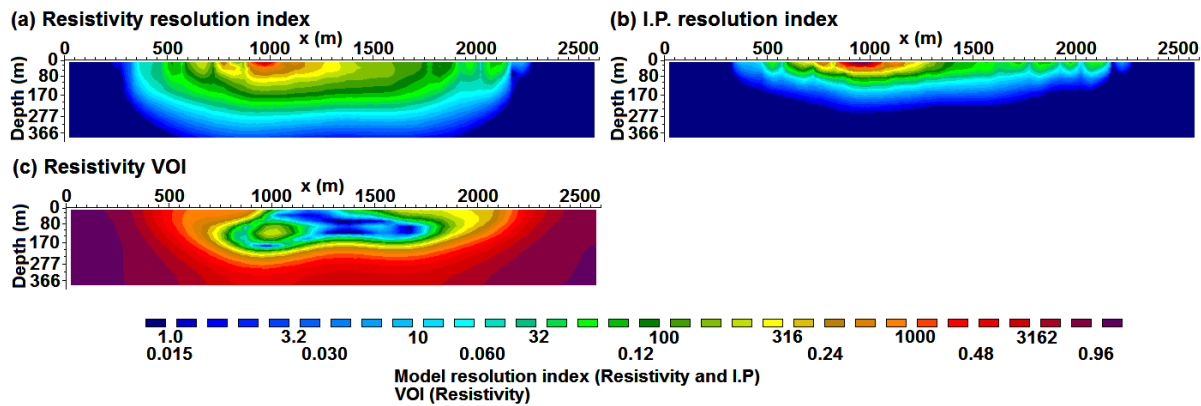


Figure 150. Vertical cross-sections of the (a) resistivity model resolution index, (b) I.P. resolution index and (c) VOI in the X-Z plane 0.8 km north of the origin.

Some remarks about model reliability estimation - Some method of assessing the reliability of the inversion results should be used. The sensitivity method (section 4.4) is the simplest but it is difficult to pick a consistent cutoff value. The DOI/VOI method can be used for any data set where it is possible to carry out an inversion. This plot normally has sharp boundaries that make it easier to pick out the region with ‘reliable’ model values. A cut-off value of about 0.1 is usually used. However it is susceptible to local artefacts possibly caused by the local optimization inversion method used. The model resolution method is more robust and less affected by the inversion settings used. However it is computationally more demanding which limits the size of the problem it can handle. Unlike the DOI/VOI plot, it shows a gradational change in the resolution values that makes it more difficult to select a cut-off value.

8.14 Closing remarks on the 3-D method

A characteristic feature of 3-D surveys is the large number of electrode positions and measurements. To achieve a sufficiently wide coverage at a lower cost, commercial surveys are usually carried out using a series of 2-D parallel lines using multi-channel systems. For fast computer inversion of very large survey grids, a multi-core CPU with at least 8 GBs of RAM is needed. Recent advances in both software and hardware have now made 3-D surveys and computer modeling within reach of small service companies. The future probably lies in parallel survey techniques (using multi-channel systems) and parallel computing techniques (using multi-core CPUs). The new 64-bit versions of Windows have greatly increased the amount of usable RAM (in theory up to 192 GB, but in practice 16 to 64 GB on most off-the-shelf modern PCs) and consequently the size of the data sets that can be processed. The extra memory space is essential for the new inversion techniques for 3-D time-lapse surveys where up to 100 data sets measured at different times at the same survey site using the same equipment setup (Loke *et al.*, 2011b, 2014a). The limiting factor now is the computer processing time. This challenge will be met by future 8-core and 16-core CPUs (and GPUs with hundreds of cores) together with innovative programming techniques to extract the maximum performance from the available computer hardware (Loke *et al.*, 2010b).

Acknowledgments

Dr. Torleif Dahlin of Lund University in Sweden kindly provided the Odarslov Dyke, Lernacken and Vetlanda data sets. The Grundfor data set was provided by Dr. Niels B. Christensen of the University of Aarhus in Denmark and Dr. Torleif Dahlin. The Rathcroghan data set was kindly provided by Dr. Kevin Barton and Dr. Colin Brown from data collected by the Applied Geophysics Unit of University College Galway, Ireland. Many thanks to Richard Cromwell and Rory Retzlaff of Golder Assoc. (Seattle) for the survey example to map holes in a clay layer. Dr. Andrew Binley of Lancaster University kindly provided the interesting cross-borehole data set. The Bauchi data set was provided by Dr. Ian Acworth of the University of New South Wales, Australia. The Redas river survey data set was kindly provided by Jef Buckinx of Sage Engineering, Belgium. Mr. Julian Scott and Dr. R.D. Barker of the School of Earth Sciences, University of Birmingham provided the Clifton, the Tar Works and the 3-D Birmingham survey data sets. Slicer/Dicer is a registered trademark of Visualogic Inc. I would like to thank Paul Bauman and WorleyParsons Canada for permission to use the figures for the Athabasca oil sands case history. I would like to thank David Bingham and Grant Nimeck of Areva Resources Canada Inc. for permission to use the figures for the Athabasca uranium deposit case history. The challenging Hanford, Panama Canal and Cripple Creek surveys data set were provided by Dale Rucker of HydroGeophysics Inc. (USA). I would like to thank Kim Frankcombe and Phoenix Copper for the Burra data set. Last, but not least, permission from Arctan Services Pty. and Gold Cross Resources to use the Copper Hill 3-D example is gratefully acknowledged.

References

- Acworth, R.I., 1981. The evaluation of groundwater resources in the crystalline basement of Northern Nigeria. Ph.D. thesis, Univ. of Birmingham.
- Acworth, R. I., 1987, The development of crystalline basement aquifers in a tropical environment: *Quarterly Journal Engineering Geology*, **20**, 265-272.
- Alumbaugh, D.L. and Newman, G.A., 2000. Image appraisal for 2-D and 3-D electromagnetic inversion. *Geophysics*, **65**, 1455-1467.
- Tejero-Andrade, A., Cifuentes-Nava, G., Chávez, R., Lopez-Gonzalez, A. and C. Delgado-Solorzano , 2015. L- and CORNER-arrays for 3D electric resistivity tomography : an alternative for geophysical surveys in urban zones. *Near Surface Geophysics*, **13**, 335-367.
- Aristodemou, E and Thomas-Betts, A, 2000. DC resistivity and induced polarisation investigations at a waste disposal site and its environments. *Journal of Applied Geophysics*, **44** (2-3), 275-302
- Auken, E., and Christiansen, AV., 2004. Layered and laterally constrained 2D inversion of resistivity data. *Geophysics*, **69**, 752-761.
- Baker, H.A., Djeddi, M., Boudjadja, A.G. and K. Benhamam, 2001. A different approach in delineating near surface buried structures. EAGE 63rd Conference & Technical Exhibition.
- Barker, R.D., 1978. The offset system of electrical resistivity sounding and its use with a multicore cable. *Geophysical Prospecting*, **29**, 128-143.
- Barker, R.D., 1989. Depth of investigation of collinear symmetrical four-electrode arrays. *Geophysics*, **54**, 1031-1037.
- Barker R.D., 1992. A simple algorithm for electrical imaging of the subsurface. *First Break* **10**, 53-62.
- Barker R.D., 1996. The application of electrical tomography in groundwater contamination studies. EAGE 58th Conference and Technical Exhibition Extended Abstracts, P082.
- Barker, R. and Moore, J., 1998. The application of time-lapse electrical tomography in groundwater studies. *The Leading Edge*, **17**, 1454-1458.
- Bauman, P., 2005. 2-D resistivity surveying for hydrocarbons – A primer. *CSEG Recorder*, April, 25-33.
- Bentley, L.R. and Gharibi, M., 2004. Two- and three-dimensional electrical resistivity imaging at a heterogeneous remediation site. *Geophysics*, **69**, 674-680.
- Bernstone, C. and Dahlin, T., 1999. Assessment of two automated electrical resistivity data acquisition systems for landfill location surveys : Two case histories. *Journal of Environmental and Engineering Geophysics*, **4**, 113-122.
- Bingham, D., Nimeck, G., Wood, G. and Mathieson, T., 2006. 3D resistivity in the Athabasca basin with the pole-pole array. 1 day workshop - Geophysical methods and techniques applied to uranium exploration. SEG Annual General Meeting 2006, New Orleans.
- Blome, M., Maurer, H. and Greenhalgh, S., 2011. Geoelectric experimental design — Efficient acquisition and exploitation of complete pole-bipole data sets. *Geophysics*, **76**, F15-F26.
- Carpenter, E.W. and Habberjam, G.M., 1956. A tri-potential method of resistivity prospecting. *Geophysical Prospecting*, **29**, 128-143.
- Chambers , J.E., Kuras, O., Meldrum, P.I., Ogilvy, R.O. and Hollands, J., 2006. Electrical resistivity tomography applied to geologic, hydrogeologic, and engineering investigations at a former waste-disposal site. *Geophysics*, **71**, B231-B239.
- Chambers J E, Wilkinson P B, Weller A L, Ogilvy R D, Meldrum P I, and Caunt, S, 2007. Mineshaft imaging using surface and crosshole 3D electrical resistivity tomography: A case history from the East Pennine Coalfield, UK. *Journal of Applied Geophysics*, **62**, 324-337.

- Chambers, J.E., Gunn, D.A., Wilkinson, P.B., Meldrum, P.I., Haslam, E., Holyoake, S., Kirkham, M., Kuras, O., Merritt, A. and Wragg, J., 2014. 4D electrical resistivity tomography monitoring of soil moisture dynamics in an operational railway embankment, *Near Surface Geophysics*, **12**, 61-72.
- Chivas, A.R. and Nutter, A.H., 1975. Copper Hill porphyry-copper prospect. Knight, S.L. (ed.), *Economic geology of Australia and Papua New Guinea vol. I. Metals*: Australasian Institute of Mining and Metallurgy Monograph No. 5, p. 716-720.
- Christensen N.B. and Sorensen K.I., 1994. Integrated use of electromagnetic methods for hydrogeological investigations. *Proceedings of the Symposium on the Application of Geophysics to Engineering and Environmental Problems*, March 1994, Boston, Massachusetts, 163-176.
- Claerbout, J.F. and Muir, F., 1973. Robust modeling with erratic data. *Geophysics*, **38**, 826-844.
- Constable, S.C., Parker, R.L. and Constable, C.G., 1987. Occam's inversion : A practical algorithm for generating smooth models from electromagnetic sounding data. *Geophysics*, **52**, 289-300.
- Dahlin, T., 1996. 2D resistivity surveying for environmental and engineering applications. *First Break*, **14**, 275-284.
- Dahlin, T., 2000. Short note on electrode charge-up effects in DC resistivity data acquisition using multi electrode arrays. *Geophysical Prospecting*, **48**, 181-187.
- Dahlin, T. and Bernstone, C., 1997. A roll-along technique for 3D resistivity data acquisition with multi-electrode arrays, Procs. SAGEEP'97 (Symposium on the Application of Geophysics to Engineering and Environmental Problems), Reno, Nevada, March 23-26 1997, vol 2, 927-935.
- Dahlin, T. and Loke, M.H., 1997. Quasi-3D resistivity imaging-mapping of three dimensional structures using two dimensional DC resistivity techniques. *Proceedings of the 3rd Meeting of the Environmental and Engineering Geophysical Society*. 143-146.
- Dahlin, T. and Loke, M.H., 1998. Resolution of 2D Wenner resistivity imaging as assessed by numerical modelling, *Journal of Applied Geophysics*, **38**, 237-249.
- Dahlin, T. and Owen, R., 1998. Geophysical investigations of alluvial aquifers in Zimbabwe. *Proceedings of the IV Meeting of the Environmental and Engineering Geophysical Society (European Section)*, Sept. 1998, Barcelona, Spain, 151-154.
- Dahlin, T., Bernstone, C. and Loke, M.H., 2002, A 3D resistivity investigation of a contaminated site at Lernacken in Sweden. *Geophysics*, **60**, 1682-1690.
- Dahlin, T. and Zhou, B., 2004, A numerical comparison of 2D resistivity imaging with ten electrode arrays, *Geophysical prospecting*, **52**, 379-398.
- Dahlin, T. and Zhou, B., 2006, Gradient array measurements for multi-channel 2D resistivity imaging, *Near Surface Geophysics*, **4**, 113-123.
- Dahlin, T. and Leroux, V., 2012. Improvement in time-domain induced polarisation data quality with multi-electrode systems by separating current and potential cables. *Near Surface Geophysics*, **10**, 545-565.
- Dahlin, T. and Loke, M.H., 2015. Negative Apparent Chargeability in Time-domain Induced Polarisation Data. *Journal of Applied Geophysics*, in press.
- Daily, W. and Owen, E, 1991. Cross-borehole resistivity tomography. *Geophysics*, **56**, 1228-1235.
- Daily, W., Ramirez, A., Newmark, R. and Masica, K., 2004. Low-cost reservoir tomographs of electrical resistivity. *The Leading Edge*, May 2007, 272-280.
- Daniels F. and Alberty R.A., 1966. *Physical Chemistry*. John Wiley and Sons, Inc.
- deGroot-Hedlin, C. and Constable, S., 1990. Occam's inversion to generate smooth, two-

- dimensional models form magnetotelluric data. *Geophysics*, **55**, 1613-1624.
- Day-Lewis, F.D., Singha K. , and Binley A., 2005. The application of petrophysical models to radar and electrical resistivity tomograms: resolution dependent limitations. *Journal of Geophysical Research*, **110**, B08206, doi: 10.1029/2004JB003569, 17 p.
- Dey A. and Morrison H.F. 1979a. Resistivity modelling for arbitrary shaped two-dimensional structures. *Geophysical Prospecting* **27**, 106-136.
- Dey A. and Morrison H.F., 1979b. Resistivity modeling for arbitrarily shaped three-dimensional shaped structures. *Geophysics* **44**, 753-780.
- Edwards L.S., 1977. A modified pseudosection for resistivity and induced-polarization. *Geophysics*, **42**, 1020-1036.
- Ellis, R.G. and Oldenburg, D.W., 1994a, Applied geophysical inversion: *Geophysical Journal International*, **116**, 5-11.
- Ellis, R.G. and Oldenburg, D.W., 1994b. The pole-pole 3-D DC-resistivity inverse problem : a conjugate gradient approach. *Geophys. J. Int.*, **119**, 187-194.
- Farquharson, C.G., and D.W. Oldenburg, 1998. Nonlinear inversion using general measures of data misfit and model structure, *Geophysical Journal International*, **134**, 213-227.
- Farquharson, C.G., and D.W. Oldenburg, 2004. A comparison of automatic techniques for estimating the regularization parameter in non-linear inverse problems. *Geophysical Journal International*, **156**, 411-425.
- Farquharson, C.G., 2008. Constructing piecewise-constant models in multidimensional minimum-structure inversions. *Geophysics*, **73**, K1-K9.
- Fox, R.C., Hohmann, G.W., Killpack,T.J. and Rijo, L., 1980, Topographic effects in resistivity and induced polarization surveys. *Geophysics*, **45**, 75-93.
- Gerard, R. and Tabbagh, A., 1991. A mobile four electrodes array and its application to electrical survey of planetary grounds at shallow depths. *J. Geophys. Res.*, **96** (B-3), 4117-4123.
- Gharibi, M. and Bentley, L.R., 2005. Resolution of 3-D electrical resistivity images from inversions of 2-D orthogonal lines. *Journal of Environmental and Engineering Geophysics*, **10**, 339-349.
- Golub, G.H. and van Loan, C.F., 1989. Matrix computations. The John Hopkins Un. Press.
- Gouet, O., 2007. Projet de classement au titre des articles L.341-1 et suivants du Code de l'Environnement De L'ÎLE D'OLÉRON. Report, Ministère de l'Écologie et du Développement Durable, Département de la Charente-Maritime, Poitiers, 84p.
- Griffiths, D.H. and Turnbull, J., 1985. A multi-electrode array for resistivity surveying. *First Break* **3** (No. 7), 16-20.
- Griffiths D.H., Turnbull J. and Olayinka A.I. 1990, Two-dimensional resistivity mapping with a computer- controlled array. *First Break* **8**, 121-129.
- Griffiths D.H. and Barker R.D.,1993. Two-dimensional resistivity imaging and modelling in areas of complex geology. *Journal of Applied Geophysics*, **29**, 211-226.
- Hallof, P.G., 1990. Reconnaissance and detailed geophysical results, Granite Mountain Area Pershing County, Nevada. in Fink, J.B., McAlister, E.O., Sternberg, B.K., Wieduwilt, W.G. and Ward, S.H. (Eds), 1990, Induced polarization : Applications and case histories : Investigations in Geophysics No. 4, SEG, 325-353.
- Harro D. and Kruse S. 2013. Improved imaging of covered karst with the multi-electrode resistivity implant technique. 13th Sinkhole Conference, NCKRI Symposium 2, Carlsbad, New Mexico, 7 pp.
- Holcombe, J. and Jirack, G., 1984. 3-D terrain corrections in resistivity surveys. *Geophysics*, **49**, 439-452.
- Inman, J.R., 1975. Resistivity inversion with ridge regression. *Geophysics*, **40**, 798-817.
- Johansson, S. and Dahlin, T., 1996. Seepage monitoring in an earth embankment dam by

- repeated resistivity measurements. European Journal of Engineering and Geophysics, **1**, 229-247.
- Jung, H.K., Min, D.J., Lee, H.S., Oh, S. and Chung, H., 2009. Negative apparent resistivity in dipole-dipole electrical surveys. *Exploration Geophysics*, **40**, 33-40.
- Keller G.V. and Frischknecht F.C., 1966. Electrical methods in geophysical prospecting. Pergamon Press Inc., Oxford.
- Kellett, R.L. and Bauman, P.D., 1999. Electrical resistivity imaging of oil sand horizons : A modern slant on an old technique. Komex International Ltd.
- Kemna, A., Rakers, E. and Binley, A., 1997. Application of Complex Resistivity Tomography to Field Data from a Kerosene Contaminated Site, In: Proc. 3rd Meeting of the Environmental and Engineering Geophysics Society, Aarhus, 8-11, September, 1997, p151-154.
- Kenma, A., Binley, A., Ramirez, A. and Daily, W., 2000. Complex resistivity tomography for environmental applications. *Chemical Engineering Journal*, **77**, 11-18.
- Kim, J.H., Yi, M.J., Park, S.G., Kim, J.G., 2009. 4D inversion of DC resistivity monitoring data acquired over a dynamically changing earth model. *Journal of Applied Geophysics*, **68**, 522-532.
- Koefoed O., 1979. Geosounding Principles 1 : Resistivity sounding measurements. Elsevier Science Publishing Company, Amsterdam.
- LaBrecque, D.J., Miletto, M., Daily, W., Ramirez, A. and Owen, E., 1996. The effects of noise on Occam's inversion of resistivity tomography data. *Geophysics*, **61**, 538-548.
- Li Y. and Oldenburg D.W. 1992. Approximate inverse mappings in DC resistivity problems. *Geophysical Journal International* **109**, 343-362.
- Lines L.R. and Treitel S. 1984. Tutorial : A review of least-squares inversion and its application to geophysical problems. *Geophysical Prospecting*, **32**, 159-186.
- Loke, M.H., 1994. The inversion of two-dimensional resistivity data. Unpubl. PhD thesis, Un. Of Birmingham.
- Loke, M.H., 1999. Time-lapse resistivity imaging inversion. Proceedings of the 5th Meeting of the Environmental and Engineering Geophysical Society European Section, Em1.
- Loke, M.H., 2000. Topographic modelling in resistivity imaging inversion. 62nd EAGE Conference & Technical Exhibition Extended Abstracts, D-2.
- Loke, M.H. and Barker, R.D., 1995. Least-squares deconvolution of apparent resistivity pseudosections. *Geophysics*, **60**, 1682-1690.
- Loke M.H. and Barker R.D., 1996a. Rapid least-squares inversion of apparent resistivity pseudosections using a quasi-Newton method. *Geophysical Prospecting*, **44**, 131-152.
- Loke M.H. and Barker R.D., 1996b. Practical techniques for 3D resistivity surveys and data inversion. *Geophysical Prospecting*, **44**, 499-523.
- Loke, M.H. and Dahlin, T., 2002. A comparison of the Gauss-Newton and quasi-Newton methods in resistivity imaging inversion. *Journal of Applied Geophysics*, **49**, 149-162.
- Loke, M.H., Acworth, I. and Dahlin, T., 2003. A comparison of smooth and blocky inversion methods in 2D electrical imaging surveys. *Exploration Geophysics*, **34**, 182-187.
- Loke, M.H. and Dahlin, T., 2010. Methods to reduce banding effects in 3-D resistivity inversion. *Procs. 16th European Meeting of Environmental and Engineering Geophysics*, 6 - 8 September 2010, Zurich, Switzerland, A16.
- Loke, M.H., Wilkinson, P. and Chambers, J., 2010a. Fast computation of optimized electrode arrays for 2D resistivity surveys. *Computers & Geosciences*, **36**, 1414-1426.
- Loke, M.H., Wilkinson, P. and Chambers, J., 2010b. Parallel computation of optimized arrays for 2-D electrical imaging. *Geophysical Journal International*, **183**, 1202-1315.
- Loke, M.H., 2011. Electrical resistivity surveys and data interpretation. in Gupta, H (ed.), Solid Earth Geophysics Encyclopaedia (2nd Edition) "Electrical & Electromagnetic"

- Springer-Verlag, 276-283.
- Loke, M.H., Chambers, J.E. and Kuras, O., 2011a. Instrumentation, electrical resistivity. in Gupta, H (ed.), Solid Earth Geophysics Encyclopaedia (2nd Edition) "Electrical & Electromagnetic", Springer-Verlag, 599-604.
- Loke, M.H., Dahlin, T. and Leroux , V., 2011b. Constrained time-lapse inversion of 3-D resistivity surveys data. Near Surface 2011 - 17th European Meeting of Environmental and Engineering Geophysics Leicester, UK, 12-14 September 2011, F06.
- Loke, M.H., Chambers, J.E., Rucker, D. F., Kuras, O. and Wilkinson, P. B., 2013a. Recent developments in the direct-current geoelectrical imaging method. *Journal of Applied Geophysics*, **95**, 135-156.
- Loke, M.H., Frankcombe, K. and Rucker, D.F., 2013b. The inversion of data from complex 3-D resistivity and I.P. surveys. 23rd International Geophysical Conference and Exhibition, 11-14 August 2013 - Melbourne, Australia, 79.
- Loke, M.H., Dahlin, T., Rucker, D.F., 2014a. Smoothness-constrained time-lapse inversion of data from 3-D resistivity surveys. *Near Surface Geophysics*, **12**, 5-24.
- Loke, M.H., Wilkinson, P. B., Chambers, P. B. and Strutt, M., 2014b. Optimized arrays for 2-D cross-borehole electrical tomography surveys. *Geophysical Prospecting*, **62**, 172-189.
- Loke, M.H., P. B. Wilkinson, P.B., Uhlemann, S.S., Chambers, J.E. and Oxby, L. S., 2014c. Computation of optimized arrays for 3-D electrical imaging surveys. *Geophysical Journal International*, **199**, 1751-1764.
- Loke, M.H., P. B. Wilkinson, P.B., Chambers, J.E., Uhlemann, S.S. and Sorensen, J.P.R, 2015a. Optimized arrays for 2-D resistivity survey lines with a large number of electrodes. *Journal of Applied Geophysics*, **112**, 136-146.
- Loke, M.H., Kiflu, H., Wilkinson, P.B., Harro, D. and Kruse, S., 2015b. Optimized arrays for 2-D resistivity surveys with combined surface and buried arrays. *Near Surface Geophysics*, **13**, 505-517.
- Loke, M.H., Wilkinson, P.B. and J.E. Chambers, 2015c. Rapid Inversion of Data from 2-D and from 3-D Resistivity Surveys with Shifted Electrodes. Near Surface Geoscience Conference, Turin, Italy, 6-10 September 2015,We 21 B11.
- Loke, M.H., Wilkinson, P.B.,Tejero-Andrade, A. and Kruse, S., 2015d. Optimized Arrays for Resistivity Measurements Confined to the Perimeter of a Survey Area. Near Surface Geoscience Conference, Turin, Italy, 6-10 September 2015,We 21 B16.
- Marescot, L. and Loke, M.H., 2003.Using the depth of investigation index method in 2D resistivity imaging for civil engineering surveys. SAGEEP 2003. Denver, USA.
- McGillivray, P.R. and Oldenburg, D.W., 1990. Methods for calculating Frechet derivatives and sensitivities for the non-linear inverse problem : A comparative study. *Geophysical Prospecting*, **38**, 499-524.
- Menke, W., 1984. Geophysical data analysis : Discrete inverse theory. Academic Press Inc.
- Merrick, N.P., 1997. A new resolution index for resistivity electrode arrays. *Exploration Geophysics*, **28**, 106-109.
- Nelson, G.D. and Van Voorhis, G.D., 1973, Letter to the editor regarding the paper "Complex resistivity spectra of porphyry copper mineralization". *Geophysics*, **38**, 984.
- Niederleithinger, E., 1994, Use of high resolution geomagnetics, 2D-DC-geoelectrics and induced polarisation in environmental investigations. Paper presented at SAGEEP '94, Boston, USA.

- Nimmer, R. E., Osiensky, J. L., Binley, A. M. & Williams, B. C. (2008) Three-dimensional effects causing artifacts in two-dimensional, cross-borehole, electrical imaging. *Journal of Hydrology*, **359**, 59-70.
- Noonan, G. and D.F., Rucker, 2011. Panama Canal Expansion Project: How Marine Electrical Resistivity was Used in Support of Canal Dredging. SAGEEP 2011, Annual meeting of the Environmental and Engineering Geophysical Society, Charleston, SC. April 10-14, 2011.
- Nyquist, J.E., Bradley, J.C. and Davis, R.K., 1999. DC resistivity monitoring of potassium permanganate injected to oxidize TCE in situ. *Journal of Environmental & Engineering Geophysics*, **4**, 135-148.
- Olivar, A., de Lime, L. and Sharma, M.M., 1990. A grain conductivity approach to shaly sandstones. *Geophysics*, **55**, 1347-1356.
- Olayinka, A.I. and Yaramanci, U., 2000, Use of block inversion in the 2-D interpretation of apparent resistivity data and its comparison with smooth inversion: *Journal of Applied Geophysics*, **45**, 63-82.
- Oldenborger, G.A., Routh, P.S. and Knoll, M.D., 2005. Sensitivity of electrical resistivity tomography data to electrode position errors. *Geophys. J. Int.*, **163**, 1–9.
- Oldenburg D.W and Li Y. 1994. Inversion of induced polarization data. *Geophysics*, **59**, 1327-1341.
- Oldenburg, D.W. and Li., Y., 1999. Estimating depth of investigation in dc resistivity and IP surveys. *Geophysics*, **64**, 403-416.
- Park, S.K. and Van, G.P. 1991. Inversion of pole-pole data for 3-D resistivity structures beneath arrays of electrodes. *Geophysics*, **56**, 951-960.
- Pazdirek, O. and Blaha, V., 1996. Examples of resistivity imaging using ME-100 resistivity field acquisition system. EAGE 58th Conference and Technical Exhibition Extended Abstracts, Amsterdam.
- Panissod, C., Dabas, M., Hesse, A., Jolivet, A., Tabbagh, J. and Tabbagh, A., 1998. Recent developments in shallow depth electrical and electrostatic prospecting using mobile arrays. *Geophysics*, **65**, 1542-1550.
- Pelton, W.H., Ward, S.H., Hallof, P.G., Sill, W.R. and Nelson, P.H., 1978. Mineral discrimination and the removal of inductive coupling with multifrequency IP. *Geophysics*, **43**, 588-609.
- Perrone, A., Lapenna, V. and Piscitelli, S., 2014. Electrical resistivity tomography technique for landslide investigation: A review. *Earth-Science Reviews*, **135**, 65–82.
- Ramaekers, P., Thomas, D., Cutts, C., Gandhi, S., Delaney, G. and Olson, R., 2006. Unconformity associated uranomim deposits. 1 day workshop - Geophysical methods and techniques applied to uranium exploration. SEG Annual General Meeting 2006, New Orleans.
- Ramirez, A., Newmark, R. and Daily, W., 2003. Monitoring carbon dioxide floods using electrical resistance tomography (ERT) : Sensitivity studies. *Journal of Environmental and Engineering Geophysics*, **8**, 187-208.
- Ritz, M., Parisot, J.-C., Diouf, S., Beauvais, A. and Dione, F., 1999. Electrical imaging of lateritic weathering mantles over granitic and metamorphic basement of eastern Senegal, West Africa. *Journal of Applied Geophysics*, **41**, 335-344.
- Rosqvist, R., Leroux, V., Dahlin, T., Svensson, M., Måansson, C-H. and Lindsjö, M., 2009. Detektering av gas i deponier med resistivitet (in Swedish), Rapport SGC 208-1102-7371, ISRN SGC-R-208-SE, Svenskt Gastekniskt Center, Malmö, 66p.
- Roy, A. and Apparao, A, 1971. Depth of investigation in direct current methods. *Geophysics*, **36**, 943-959.
- Rucker, D.F., Levin, M.T. and Myers, D.A., 2007. Imaging beneath Hanford's Tank Farms

- with electrical resistivity geophysics - An innovative approach. WM '07 Conference, Feb. 25-March 1, 2007, Tuscon, AZ.
- Rucker, D., Loke, M.H., Levitt, M.T. and Noonan, G.E., 2010. Electrical Resistivity Characterization of an Industrial Site using Long Electrodes. *Geophysics*, **75**, WA95-WA104.
- Rucker, D.F. and Loke, M.H., 2012. Optimized geoelectrical monitoring with three-dimensional arrays, Proceedings SEG-AGU Hydrogeophysics Workshop, 8–11 July 2012, Boise, Idaho, USA.
- Rucker, D.F. and Noonan, G.E., 2013. Using marine resistivity to map geotechnical properties: a case study in support of dredging the Panama Canal. *Near Surface Geophysics*, **11**, 625-637.
- Rucker, D.F., Crook, N., Winterton, J., McNeill, M., Baldyga, C. A., Noonan, G. and Fink, J. B., 2014. Real-time electrical monitoring of reagent delivery during a subsurface amendment experiment. *Near Surface Geophysics*, **12**, 151-163.
- Sasaki, Y. 1992. Resolution of resistivity tomography inferred from numerical simulation. *Geophysical Prospecting*, **40**, 453-464.
- Scott, J.B.T., Barker, R.D. Peacock, S., 2000. Combined seismic refraction and electrical imaging. Procs. 6th Meeting of the European Association for Environmental and Engineering Geophysics, 3-7 Sept. 1997, Bochum, Germany, EL05.
- Seaton, W.J. and Burbey, T.J., 2000. Aquifer characterization in the Blue Ridge physiographic province using resistivity profiling and borehole geophysics : Geologic analysis. *Journal of Environmental & Engineering Geophysics*, **5**, no. 3, 45-58.
- Schenkel, C.J. and Morrison, H.F., 1994. Electrical resistivity measurement through metal casing. *Geophysics*, **59**, 1072-1082.
- Shima, H., 1992. 2-D and 3-D resistivity imaging reconstruction using crosshole data. *Geophysics*, **55**, 682-694.
- Shima, H., Sakashita, S. and Kobayashi, T., 1996. Developments of non-contact data acquisition techniques in electrical and electromagnetic explorations. *Journal of Applied Geophysics*, **35**, 167-173.
- Silvester P.P. and Ferrari R.L., 1990. Finite elements for electrical engineers (2nd. ed.). Cambridge University Press.
- Smith, T., Hoversten, M., Gasperikova, E. and Morrison, F., 1999. Sharp boundary inversion of 2D magnetotelluric data. *Geophysical Prospecting*, **47**, 469-486.
- Singer, B.S. and Strack, K.M., 1998. New aspects of through-casing resistivity theory, *Geophysics*, **63**, 52-63.
- Slater, L., Binley, A.M., Zaidman, M.D. and West, L.J., 1997, Investigation of vadose zone flow mechanisms in unsaturated chalk using cross-borehole ERT. Proceedings of the EEGS European Section 3rd Meeting, Aarhus, Denmark, 17-20.
- Slater, L., Binley, A.M., Daily, W. and Johnson, R., 2000. Cross-hole electrical imaging of a controlled saline tracer injection. *Journal of Applied Geophysics*, **44**, 85-102.
- Sorenson, K.I., 1994: The Ellog auger drilling method. Proceedings of the symposium on the application of geophysics to engineering and environmental problems, Boston, Massachusetts. - Environmental and Engineering Geophysical Society, 985-994.
- Sorenson, K., 1996. Pulled Array Continuous Profiling. *First Break*, **14**, 85-90.
- Spiegel, R.J., Sturdivant, V.R. and Owen, T.E., 1980, Modeling resistivity anomalies from localized voids under irregular terrain. *Geophysics*, **45**, 1164-1183.
- Spies, B.R. and Ellis, R.G., 1995. Cross-borehole resistivity tomography of a pilot-scale, in-situ vitrification test. *Geophysics*, **60**, 1313-1325.
- Stewart M. and Parker J. 1992. Localization and seasonal variation of recharge in a covered karst aquifer system, Florida, USA, in *Hydrogeology of Selected Karst Regions*, H.

- Palos and W. Back, eds. *International Contributions to Hydrogeology* **13**, International Association of Hydrogeologists.
- Stummer, P., Maurer, H. and Green, A., 2004. Experimental design: Electrical resistivity data sets that provide optimum subsurface information. *Geophysics*, **69**, 120-129.
- Sugimoto, Y., 1999. Shallow high-resolution 2-D and 3-D electrical crosshole imaging. *The Leading Edge*, **18**, 1425-1428.
- Sumi, F., 1965. Prospecting for non-metallic minerals by Induced Polarization. *Geophysical Prospecting*, **14**, 603-616.
- Summer, J.S., 1976. Principles of induced polarization for geophysical exploration. Elsevier Scientific Publishing Company.
- Supper, R., Ottowitz, D., Jochum, B., Römer, A., Pfeiler, S., Kauer, S., Keuschnig, M. and Ita, A., 2014. Geoelectrical monitoring of frozen ground and permafrost in alpine areas: field studies and considerations towards an improved measuring technology. *Near Surface Geophysics*, **12**, 93-115.
- Telford, W.M., Geldart, L.P. and Sheriff, R.E., 1990. *Applied Geophysics* (second edition). Cambridge University Press.
- Tong, L. and Yang, C., 1990. Incorporation of topography into two-dimensional resistivity inversion. *Geophysics*, **55**, 354-361.
- Vanhala, H., Soininen, H. and Kukkonen, I., 1992. Detecting organic chemical contaminants by spectral-induced polarization method in glacial till environment. *Geophysics*, **57**, 1014-1017.
- Vanhala, H. and Peltoniemi, M., 1992. Spectral IP studies of Finnish ore prospects. *Geophysics*, **57**, 1545-1555.
- Van Voorhis, G.D. Nelson, P.H. and Drake, T.L., 1973. Complex resistivity spectra of porphyry copper mineralization. *Geophysics*, **38**, 49-60.
- Waddell, J. and Barton, K., 1995. Seeing beneath Rathcroghan. *Archaeology Ireland*, Vol. **9**, No. 1, 38-41.
- Weller, A., Seichter, M. and Kampke, A., 1996. Induced-polarization modelling using complex electrical conductivities. *Geophys. J. Int.*, **127**, 387-398.
- Weller, A., W. Frangos, and M. Seichter, 2000. Three-dimensional inversion of induced polarization data from simulated waste, *J. Appl. Geophys.*, **44**, 67-83.
- Weller, A., Breede, K., Slater, L. and Nordsiek, S., 2011. Effect of changing water salinity on complex conductivity spectra of sandstones. *Geophysics*, **76**, F315-F327.
- White, R.M.S., Collins, S., Denne, R., Hee, R. and Brown, P., 2001. A new survey design for 3D IP modelling at Copper hill. *Exploration Geophysics*, **32**, 152-155.
- Wilkinson P.B., Chambers J.E., Meldrum P.I., Ogilvy R.D. and Caunt S., 2006a. Optimization of array configurations and panel combinations for the detection and imaging of abandoned mineshafts using 3D cross-hole electrical resistivity tomography. *Journal of Environmental and Engineering Geophysics* **11**, 213-221.
- Wilkinson, P.B., Meldrum, P.I., Chambers, J.C., Kuras, O. and Ogilvy, R.D., 2006b. Improved strategies for the automatic selection of optimized sets of electrical resistivity tomography measurement configurations. *Geophys. J. Int.*, **167**, 1119-1126.
- Wilkinson, P. B., Chambers, J. E., Lelliott, M., Wealthall, G. P. and Ogilvy, R. D., 2008. Extreme Sensitivity Of Crosshole Electrical Resistivity Tomography Measurements To Geometric Errors. *Geophysical Journal International*, **173**, 49-62.
- Wilkinson, P.B., Loke, M.H., Meldrum, P.I., Chambers, J.E., Kuras, O., Gunn, D.A., Ogilvy, R.D., 2012, Practical aspects of applied optimized survey design for electrical resistivity tomography, *Geophysical Journal International*, **189**, 428-440.
- Wilkinson, P.B., Uhlemann, S., Chambers, J.C., Meldrum, P. I. and Loke, M.H., 2015. Development and testing of displacement inversion to track electrode movements on

- 3D Electrical Resistivity Tomography monitoring grids. *Geophysical Journal International*, **200**, 1566-1581.
- Witherly, K.E. and Vyselaar, J., 1990. A geophysical case history of the Poplar Lake Copper-Molybdenum deposit, Houston Area, British Columbia. In Fink, J.B., McAlister, E.O., Sternberg, B.K., Wieduwilt, W.G. and Ward, S.H. (Eds), 1990, Induced polarization : Applications and case histories : Investigations in Geophysics No. 4, Soc. Expl. Geophys.
- Wolke, R. and Schwetlick, H., 1988, Iteratively reweighted least squares algorithms, convergence analysis, and numerical comparisons: SIAM Journal of Scientific and Statistical Computations, **9**, 907-921.
- Wynn, J.C., Grosz, A.E. and Carlson, V.L., 1990. Induced-polarization response of some titanium-bearing placer deposits in Southeastern United States. In Fink, J.B., Sternberg, B.K., McAlister, E.O., Wieduwilt, W.G. and Ward, S.H. (Eds.), Induced polarization – Applications and case histories. Investigations in Geophysics No. 4, SEG, 280-303.
- Zhao, J.X., Rijo, L. and Ward, S.H., 1986. Effects of geoelogeic noise on cross-borehole electrical surveys. *Geophysics*, **51**, 1978-1991.
- Zhdanov, M.S. and Keller, G.V., 1994. The geoelectrical methods in geophysical exploration. Elsevier, Amsterdam.
- Zhou, B. and Greenhalgh, S.A., 1997. A synthetic study on cross-hole resistivity imaging with different electrode arrays. *Exploration Geophysics*, **28**, 1-5.
- Zhou, B. and Greenhalgh, S.A., 2000. Cross-hole resistivity tomography using different electrode configurations. *Geophysical Prospecting*, **48**, 887-912.
- Zhou B. and Dahlin, T., 2003, Properties and effects of measurement errors on 2D resistivity imaging surveying, *Near Surface Geophysics*, **1**, 105-117.
- Zonge, K.L. and Wynn, J.C., 1975. Recent advances and applications in complex resistivity measurements. *Geophysics*, **40**, 851-864.